THE APPLICATION OF PLASMA IMMERSION ION IMPLANTATION TO SHEEP SHEARING COMBS

John H. Watkins, B.E. (Mech.)

Materials Engineering Group,
Department of Chemical Engineering,
The University of Adelaide, Australia.

A dissertation submitted
to the University of Adelaide
in fullfilment of the requirements
for the degree Doctor of Philosophy

August, 1995

CONTENTS

TABLE OF FIGURES

Chapter 1

-

Chapter 2

Chapter 3

Chapter 4

XW10 steel after 350°C PIII treatment.

Chapter 5

Chapter 6

Chapter 7

Appendices

ABSTRACT

Detailed observations were made of the microstructural changes occurring near the surface of a Cr-Mo-V alloy tool steel rod (Assab XW10) which had been subjected to nitrogen ion implantation at 350°C by the Australian Nuclear Science and Technology Organization (ANSTO) using the Plasma Immersion Ion Implantion (PIII) technique which they developed at their Lucas Heights Research Laboratories in Sydney, NSW. Using a newly developed specimen preparation technique, transmission electron microscope studies were carried out at depths beneath the surface of the nitrogen ion implanted rods varying from 5 - 400 μm. These microstructural observations were correlated with microhardness measurements and showed the presence of a series of well defined layers beneath the surface: I - IV.

Layer I (0 - 10 μm) contained two finely dispersed carbo-nitrides, MX (M_4X_3) and M_2X plates (X = C, N; M = Cr, Mo, V, Fe) in tempered martensitic laths. Coarse Fe_4N precipitates that were precipitation hardened by fine MX spheres reinforced the lath boundaries. However, the hardness this layer (1100 HV_{25g} at 5 μm) was less than the peak value which could be explained by an enlarged ferrite grain size. There was a notable absence of the primary carbides, $M_{23}C_6$ and M_7C_3, in this layer. Layer II (10 - 20 μm), showing the peak hardness (1500 HV_{25g}), had a ferrite grain size close to the bulk material and contained a third fine precipitate (CrN) which interlocked with the MX and M_2X platelets. The primary carbides were still not found, but complex structured CrN spheroidal precipitates were identified with the same morphology as the original primary carbides. Layer III (20 - 40 μm) had intermediate hardness (1100 HV_{25g}) with no fine CrN precipitates or coarse Fe_4N but the primary carbides gradually emerged while the coarse CrN spheroids disappeared. Layer IV (40 - 100 μm) showed ever decreasing hardness with coarse Fe_3C sheets containing primary carbides. The

microstructure of the material deeper than 100 μm (650 HV_{25g}) was consistent with a treatment temperature of 350°C containing only fine Fe_3C precipitates within α-Fe laths and smooth surfaced primary carbides.

Mathematical modelling of the PIII process was carried out to investigate the variations of temperature with time and depth beneath the surface. Simulations of the present implantation found that the surface temperature rose by only 2.2°C at the end of a 50 μs ion pulse and rapidly equilibrated with the bulk material. Thus, temperature variations did not seem responsible for the apparent grain growth that occurred in the surface layer. However, the concentration of vacancies near the surface resulting from the ion implantation process was suggested to be above the level necessary for the recrystallization of ferrite and the decomposition of primary Cr-carbides.

To estimate nitrogen penetration during implantation, the limitations of conventional (Fick's) diffusion modelling from a pulsed nitrogen source were explored. It was found that, in the present case, the sparsity of ions striking the surface of the rod and low diffusivity of nitrogen invalidated pulse by pulse treament. Nevertheless, the diffusion from an averaged flux from the combination of many thousands of pulses was modelled. That simulation showed that Fick's diffusion of nitrogen could not reasonably explain the TEM observations of the nitride rich layer: the nominal dose was suggested to be too low, while the nitrogen diffusivity was also too low.

The industrial application of this new treatment to the combs and cutters used in sheep shearing handpieces was investigated. Full evaluation of the technique as applied to combs could not be carried out because of equipment delays at ANSTO. However, the requirements to apply PIII to combs were clearly delineated: 1) manufacture combs from a high quality secondary hardening tool steel; and 2) use a comb sharpening process which does not damage the metallurgical structure of the surface of the comb.

The wear damage on conventional shearing combs resulting from shearing use were examined in detail to form a basis to evaluate surface modified combs. Abrasive wear of the ground face by grit was once again found to be the primary cause of loosing

wool fibre severance. Wear of the rake faces (edge faces of comb teeth) was examined for the first time since it has immediate relevance to the survival of hardened surface layers applied to combs. Abrasion by grit caught between comb and cutter cutting edges were suggested as the primary mechanism for rake face wear. Further, a model of the conditions where wool fibre severance breaks down through wear of the cutting edges was proposed based on the rotation of wool fibres around the cutting edges (cf. a sheet metal guillotine). This model could reasonably predict the critical wear parameters.

Studies on earlier failures of WC-Co "D-gun" coated combs showed that the development of fatigue cracks in the η phase resulted in a loss of integrity of the coating which prematurely degraded the cutting edges of the combs.

DECLARATION

This thesis contains no material which has been accepted for the award of any other degree or diploma in any University.

To the best of my knowledge and belief, this thesis contains no material previously published or written by another person, except where due reference is made in the text of the thesis.

I consent to this thesis being made available for photocopying and loan if applicable if accepted for the award of the degree.

John H. Watkins

August, 1995

ACKNOWLEDGMENTS

I would like to sincerely thank Prof. D.R. Miller, my academic supervisor, for his guidance and encouragement, and for the wonderful opportunity to work on such a diverse project.

Special appreciation goes to Mr. Huw Rosser and the staff of CEMMSA (Centre of Electron Microscopy and Microstructural Analysis of South Australia) for use of their facilities and interest in my work. Thanks to Dr. Peter Miller of the CSIRO (Commonwealth Scientific Industrial Research Organization) Materials Research Laboratories, Melbourne, for his expertise in obtaining microanalysis data from their 300 kV A.E.M.. All Plasma Immersion Ion Implantation was conducted by Dr. George Collins and Dr. John Tendys at the Lucas Heights Research Laboratories of ANSTO (Australian Nuclear Science and Technology Organisation). Dr. R.J. Finch performed the microhardness tests presented in Chapter 3. The shearing trials of sheep shearing combs presented in Chapter 6 were undertaken in a team environment which consisted of Prof. D.R. Miller, the author and Dr. R.J. Finch.

I am grateful to the Australian Wool Corporation for providing me with a postgraduate research studentship which enabled me to conduct my research unhindered. I also thank the consortium of ANSTO, CSIRO Division of Applied Physics, Metal Manufacturers Ltd. (Woolongong, Aust.) and the University of Adelaide (D.R. Miller) who secured the funds for this research through a Government Industrial Research and Development (GIRD) grant from the Commonwealth Department of Industry, Technology and Commerce (DITAC).

I thank my family and friends for their patience and support. I especially thank my father because he showed me this dream so young.

Chapter 1

INTRODUCTION

1.1 GENERAL.

The current research program focuses on the application of Radio Frequency Plasma Immersion Ion Implantation (PIII) to two tool steels. The primary aims of this work were to determine the effectiveness of the PIII process in enhancing the surface properties of a secondary hardening tool steel proposed for commercial shearing comb manufacture, and to elucidate the mechanisms by which this occurred. Substantial enhancement of the surface properties and extreme modifications to the steel adjacent to the surface were indeed observed. Techniques of analytical transmission electron microscopy and scanning electron microscopy were employed to map changes in the microstructure across the modified surface layer. Comparisons were made, as part of this study, into structure and property changes which could be induced into this same steel by a commercial nitriding process. In order to provide a basis for understanding these changes, mathematical modelling of the thermal effects caused by this ion implantation process was undertaken. The conventional steel used in shearing comb manufacture was not examined in such detail since that steel responded poorly to surface treatment due to its low thermal stability.

In addition, studies were made on the application of PIII technology to a commercial problem: the short service life of sheep shearing tools. Detailed examinations of wear damage on unimplanted shearing combs were made to provide a basis to surface treat combs.

1.2 HISTORICAL BACKGROUND.

This project was initiated in the Materials Engineering Group at the University of Adelaide by Prof. D.R. Miller, after his involvement in both the ion implantation of materials using the PIII process, and investigations into the surface modification of sheep shearing tool steels.

In 1985, D.R. Miller and T. Zujic investigated the failure mechanism of thermally sprayed coatings on shearing combs. Their work suggested not only that fatigue was responsible for the breakdown of these coatings, but also that ceramic coatings, of this kind, may be inappropriate for use in shearing combs. Next, as part of a four-organization consortium[†] , D.R. Miller initiated a research program to determine the specific property and structure changes induced by PIII on, amongst other materials, the steel used in shearing comb manufacture. Through the efforts of this consortium, a Government Industrial Research and Development (GIRD) grant (No. 15023) was awarded in December, 1988, from the Commonwealth Department of Industry, Technology and Commerce (DITAC). Since there was no provision for postgraduate student funding for the present thesis, an application was made to the WRDC (Wool Research and Development Council) of the Australian Wool Corporation in October, 1988. In March 1989, a Studentship was awarded to the author of this thesis by the WRDC. During part of this time, R.J. Finch worked as a Research Officer on the GIRD grant project. Later, in 1993, R.D. Young was employed as a Research Officer, through an AWC grant, to investigate alternative methods to resharpen shearing combs.

1.3 PLASMA IMMERSION ION IMPLANTATION.

For many decades industry has benefitted from treating iron-based engineering components which are subject to wear, by nitriding processes. Particular applications have been in cases where the untreated service life is short, or when the manufacturing cost of the component is high compared to the material cost. Commercially available

---

† ANSTO (Australian Nuclear Science and Technology Organization); CSIRO (Commonwealth Scientific Industrial Research Organization) Div. Applied Phys; Metal Manufacturers Ltd., Woolongong, Australia.

nitriding treatments for steels have evolved in recent years from "pack cyaniding" to "gas nitriding" to "ion nitriding" along with increased efficiency and decreased environmental impact. However, a persisting limitation of these conventional treatments is the slow gas/metal absorption kinetics at the component surface. This dictates that the process temperature be a minimum of around 500°C for steels, to overcome the activation energy for nitrogen absorption, usually resulting in undesirable softening of the hardened steel beneath the modified surface layer (even in secondary hardening steels: Chapter 3) .

Recently, a solution to this problem has been found by applying ion implantation technology, a process developed for semiconductor manufacture nearly thirty years ago. This process is able to inject nitrogen directly into the component surface from a particle accelerator source. However, the relatively high cost of this technology and the "line-of-sight" restrictions have not afforded it general appeal in the manufacturing community.

Nevertheless, in the last ten years, two new processes have emerged which are based on the ion implantation principle. They could be described as hybrids of traditional nitriding and ion implantation, using a nitrogen plasma generated around the component to implant nitrogen into the entire surface simultaneously by high voltage pulses. One of these processes is Plasma Immersion Ion Implantation (PIII) [1], which is under development at the A.N.S.T.O. Lucas Heights Research Laboratories and, in this investigation, has been used for relatively high temperature implantation of tool steels, e.g., above 200°C. Research efforts made by the previously mentioned consortium have demonstrated that PIII can offer significant advances over conventional surface hardening treatments. Not only has the rapid growth of nitride-rich surface layers been seen at substantially lower temperatures, but also, surface layers with higher peak hardness can develop, and higher substrate hardness can be retained: see Chapter 3. Another plasma based ion implantation project, termed Plasma Source Ion Implantation (PSII) is currently under research at the University of Wisconsin, Madison, also with interesting results [2]. However, it is understood that

neither process has reached the point of commercial introduction as a surface treatment alternative.

Implantation trials on type H13 steel, a secondary hardening tool steel, first demonstrated that rapid development of a deep hardened surface layer (e.g., 50 μm) could be achieved by the PIII process [3]. Earlier trials on a low alloy, high carbon steel proved unsuccessful for reasons given in Chapter 3. These experiments emphasized that the effects of the PIII process on the microstructure of materials were not clearly understood. Therefore, the principle objective of the present study was to determine the precise nature of the microstructural changes induced in the surface of a secondary hardening tool steel by the PIII process (Chapter 4).

Microhardness measurements on cross-sections of the modified surface layers in H13 steel, and later XW10 steel, showed that sharp hardness gradients existed beneath the treated surface. As will be shown in Chapter 4, the important microstructural features in the hardened layers had dimensions of only 10 x 100 nm, so the important advantages offered by analytical transmission electron microscopy (TEM) were needed to characterize such fine microstructures. For example, by using the diffraction capabilities of the TEM, the habit planes and crystallographic orientation relationships between these fine particles and their matrix, essential to understand the hardening mechanisms, could be examined.

Substantial experimental difficulties are usually encountered when attempting to prepare electron transparent cross-sections of thick surface layers (> 5 μm) with sharp hardness gradients. A new TEM specimen preparation technique was developed which enabled the previous experimental difficulties to be overcome, as described in Appendix 3. Extensive TEM experiments were then conducted to record the crystallography, composition and geometry of all phases throughout the surface layer with the highest peak hardness developed during PIII experiments in XW10 tool steel.

1.4 SHEEP SHEARING.

The shearing of sheep is a major industry in Australia that has long been plagued by short cutting tool life. These tools have a relatively high maintenance cost due to their rapid wear. For this reason, shearing is a rigorous environment in which to evaluate the performance of PIII surface treatments on steels. The aim of this work was to investigate the how to apply the PIII process to shearing tools, and to test surface modified tools in a sheep shearing environment.

Standard shearing tools consist of a thirteen tooth comb and a four-toothed cutter [4]. The comb is clamped in a handpiece and manually guided next to the skin of the sheep while the cutter oscillates over the comb in an arc, creating a scissoring action which severs the dense 10 - 20 μm diameter wool fibers in the fleece. The cutting edges must remain in close proximity, as they scissor, to fracture the small diameter wool fibers. Since the tools invariably wear, this close proximity becomes impossible after a period of use, and the tools must frequently be withdrawn from operation to be sharpened. Abrasive wear has been cited as the principle mechanism which leads to the loss of fiber severance. Therefore, by increasing the wear resistance of the critical surfaces of the tools, additional wool severance life in-between sharpening is anticipated.

Of the tools, shearing combs were selected for PIII treatment, in preference to cutters, as a conventional comb is more expensive, will usually survive longer before sharpening is required, and offers more surface area to treat. However, implanting the surface of combs that are in direct contact with cutters was not thought to be worthwhile, because the resulting modified surface layers would be progressively removed during sharpening. In fact, during shearing use, some wear of the mating face of the comb is desirable. Nevertheless, as shown in Chapter 7, the edge faces of comb teeth were found to be critical areas to limit wear damage. In this case, a sharpening process could rejuvenate the comb's cutting edges without sacrificing the enhanced surface properties on the edge faces.

In the course of these studies, questions were raised about conventional technologies used to manufacture and operate shearing tools. As mentioned above, the most promising PIII surface treatment results were obtained for secondary hardening tool steels. Early shearing trials using implanted "silver" steel, a low alloy, high carbon steel used in conventional comb manufacture, could not show the potential benefits of PIII treatment. Thus special combs, manufactured from XW10 steel by Sunbeam Australia, Pty. Ltd., were treated by the PIII process and prepared for shearing trials. However, due to some unusually large chromium carbides present in the initial microstructure of the steel, the thin tips of many comb teeth did not have adequate toughness to resist fracture during rigorous shearing use. This problem could not be rectified during the period of the author's research because the PIII equipment suffered fire damage and was inoperational for all of 1992. Nevertheless, other research was conducted to help introduce ion implantation to shearing combs.

Damage to the ion implanted edge surfaces of comb teeth was anticipated if the aggressive sharpening method presently used on conventional combs was used to sharpen modified combs. The research group of Miller, Young and Watkins developed and tested an alternative sharpening process, although it is not reported here.

The principle direction of the author's research on shearing combs was to characterize the wear processes that lead to the breakdown of wool fiber severance in conventional combs. The specific aims of this study were to suggest the critical wear processes, and to create data by which future shearing experiments on modified combs could be evaluated. To this end, detailed analyses of the wear patterns resulting from controlled shearing experiments were made. In order to explain some wear features and to further understand comb/cutter edge interactions, modelling of the interaction of grit and wool fibers with a pair of cutting edges was undertaken. A subsidiary goal of this project was to investigate alternatives to PIII treatment for the improvement of shearing comb life. To this end, failure analysis of a thermally sprayed WC/Co coating on a standard comb was undertaken [presented at the International Conference on Surface Engineering, Adelaide, Australia, 12-14 March, 1991 (Appendix 7)].

Chapter 2

PLASMA IMMERSION ION IMPLANTATION AS A SURFACE MODIFICATION TECHNIQUE

2.1 INTRODUCTION.

As mentioned in § 1.3, ion implantation as a means of surface treating steels on an industrial scale has moved from the conceptual stage, with experiments using ion beam implanters, towards a realistic process through the introduction of PIII and PSII technology. The need for an alternative surface hardening process has been long-standing because of the relative inefficiency of conventional nitriding processes.

The main limitation of gas nitriding and its later development, plasma nitriding [5], is the way in which the nitrogen enters the components surface: these processes rely on relatively slow gas/metal surface chemistry to eventually absorb nitrogen before it is available for diffusion within the metal lattice [6]. This absorption tends to be an equilibrium process, with the surface saturation of nitrogen limiting the nitriding rate, dictating higher treatment temperatures to achieve a reasonable rate. Thus, a typical treatment to gain a 50 μm wear resistant surface on H13 steel is 30 hours at 500°C, resulting in a retained substrate hardness of 635 HV_{200g} [7]. Ion nitriding, which uses a small D.C. bias on the component, offers an improvement, albeit, not dramatic.

In the last 20 years, ion implantation has been extensively developed for the doping of semiconductors, a process which uses an ion beam to inject atoms directly into surfaces of materials. For semiconductor processing, this technique relies on precise control of the ion beam, ion species and energy level, and stringent cleanliness. Numerous research efforts have been made to expand this technology into the surface

treatment a myriad of other materials (pure metals, common alloys, plastics, etc.). To obtain uniform coverage of the workpiece from a single ion beam, the beam can be rastered across the surface. As a potential surface treatment for steels, the major advance of ion implantation is that it overcomes the equilibrium nature of conventional treatments by injecting nitrogen directly into the surface of a component.

Initially, research efforts on nitriding of iron concentrated on room temperature implantation because of traditional practices in semiconductor manufacture. Later, because of the limited penetration depths of ions achievable at these temperature, e.g., 100 nm for 50 keV nitrogen into α-Fe (see Chapter 5), some implantation experiments were done between room temperature and 300°C [8-12], but total diffusion depths of nitrogen have usually not exceeded 1 μm. The use of much higher accelerating voltages have also been studied, but normally result in undesirable radiation damage to the surface.

The limitations of implanting nitrogen through an ion beam are: 1) the relatively high cost of ion accelerators; 2) obtaining a uniform ion dose with a discrete ion beam; and 3) the restricted supply of ions to the surface. Nevertheless, target manipulators have been designed to obtain uniform ion beam coverage on non-planar components, and some commercial ion implanters are in use.

Notwithstanding this, a consequence of the large amount of research that has been done on "line-of sight" implantation is the fundamental understanding gained of the processes that occur during ion implantation. This is of great importance to the development of the new plasma based nitriding treatments.

As explained in the next section, the use of nitrogen plasmas as the ion source has sparked interest in the surface hardening field as this type of ion source surrounds the target which can overcome line of sight restrictions and high unit costs of conventional ion implantation. Conrad *et al.*, in Madison, Wisconsin, USA, first investigated these techniques under the name of Plasma Source Ion Implantation (PSII) [2]. A group at ANSTO, Lucas Heights, Australia, has been developing a related process, Plasma Immersion Ion Implantation (PIII) [1]. The PIII process constitutes a significant

advance over both traditional nitriding treatments and ion beam techniques, as diffusion depths of 50 μm have been observed with this treatment in significantly shorter times and lower process temperatures.

2.2 PRINCIPLES AND OPERATION OF THE PIII PROCESS.

The PIII process and equipment have been previously described by Collins *et al.* [13]. However, a brief description is given here for completeness.

The key features of the PIII equipment are: 1) the ability to implant nitrogen ions into the entire surface of a target simultaneously; 2) a high regeneration rate of nitrogen ions in the plasma surrounding the target through the injection of radio frequency waves, allowing a minimum of ion depletion during typical pulsed treatments; 3) implantation of the ions in discrete pulses by applying a large negative potential across the target and grounded wall of the working vessel; 4) control over the target temperature by modulating the pulse duration and frequency; 5) uniformly high implantation rates of the ions irrespective of the surface orientation**. Thus, in principle, a high nitrogen concentration can be maintained within the workpiece surface at all times during processing, at any desired workpiece temperature (NB. at or below the temperature range used in conventional nitriding treatments).

The PIII equipment, Figure 2.1, consists of a vessel connected to a vacuum system, a high voltage power supply and pulse modulator, a radio frequency generator and antenna, and various diagnostic apparatus. The workpiece is located near the centre of the vessel and is supported by a shielded conducting rod attatched to the pulse modulator. The vessel is evacuated and then filled with nitrogen gas to a pressure of ~ $1x10^{-3}$ mbar. A plasma of primarily N_2^+ ions and electrons is continuously generated by the injection of R.F. waves into the chamber: typically 250 W of R.F. power at 12 - 13 MHz which gives a plasma density of around $1x10^{10}$ cm^{-3}. The ion life in the plasma, e.g., before recombination with electrons, is of the order of 10^{-6} s. Energetic

---

** N.B. there is an increased rate of implantation in the vicinity of sharp edges: see Watterson [92].

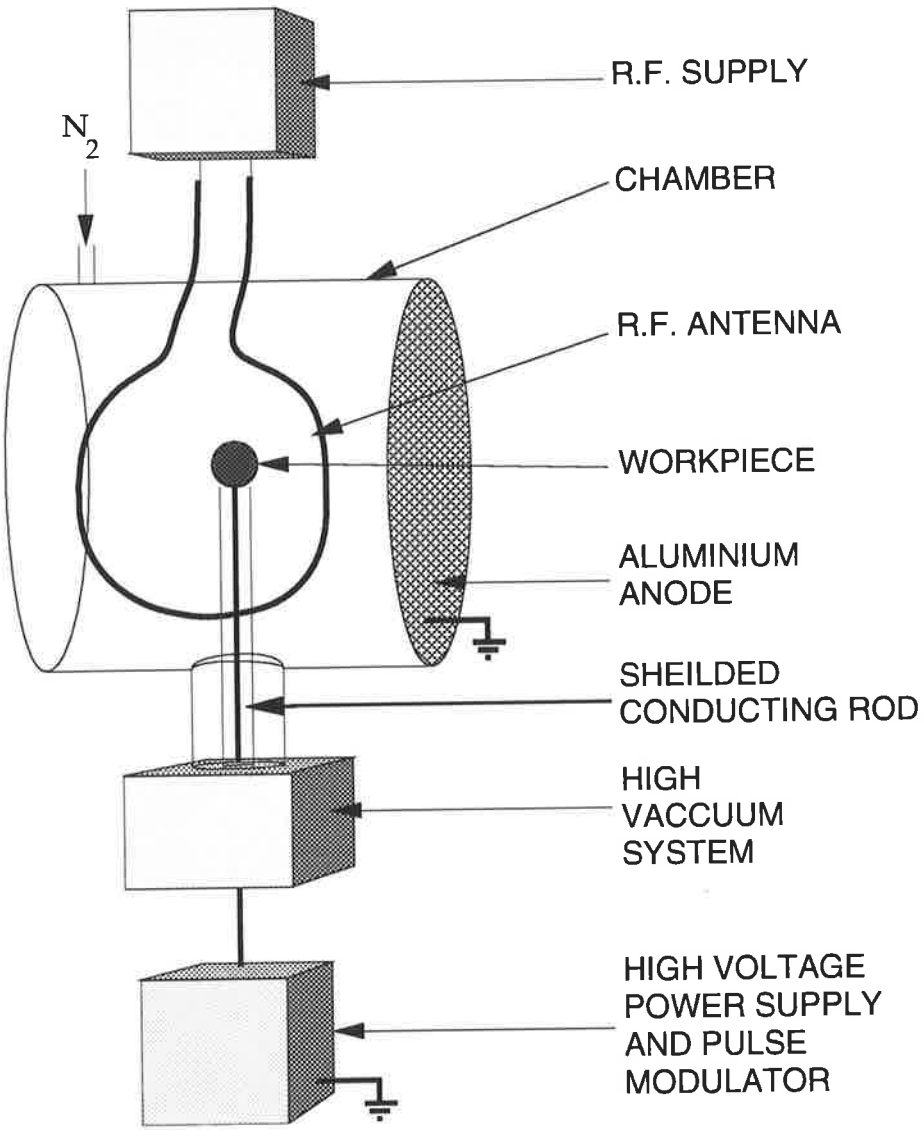

Figure 2.1: A schematic diagram of the Plasma Immersion Ion Implantation (PIII) equipment

electrons liberated from the ionization process play a significant role in maintaining the plasma density. The R.F. antenna is located outside the chamber if the vessel is made from borosilicate glass, or inside if the vessel is steel.

The workpiece is biased to a large negative potential (~50 kV) in discrete pulses; The pulse bias, pulse duration pulse frequency and plasma density are controllable during the implantation process. These parameters determine the heat flux injected into the workpiece which occurs through the energy transfer between the high speed ions and the target lattice. This heat input must be balanced by a heat extraction process to avoid overheating of the workpiece. When the heat input is balanced by heat loss, a stable processing temperature is reached. For the experiments in this thesis, temperature control was achieved by varying the pulse frequency alone, while heat was extracted from the workpiece through a conduction and radiation path, achieving stable temperatures within 10 minutes of starting the treatment. An infra-red pyrometer was used to measure the target temperature during implantation. However, the specimen rod had a low emmissivity polished metal surface which prevents pyrometric measurement at these temperatures. To overcome this, the temperature of graphite painted radiating blocks was measured, as discussed further in Chapter 5.

During the high voltage pulses, the electrons are repelled from the target surface, while the nitrogen ions are attracted, albeit at a much slower rate due to their mass difference. This particle motion leads to the development of a stable plasma sheath between the workpiece and the plasma, typically 80 mm thick. The plasma remains close to neutral potential (*i.e.*, the grounded wall) while the sheath becomes increasingly positive towards the target. The plasma is thought to conduct at least as well as pure copper, hence, completes the electrical circuit to the aluminium plate in the end wall of the vessel, which is at ground potential. The diagnostic equipment used in these experiments to characterize the plasma parameters consisted of a Langmuir probe, to measure plasma density, and a capacitive probe to measure the sheath thickness.

The principle difference between PIII and PSII is in the method of plasma generation: instead of an unconfined, inductively coupled R.F. plasma, PSII uses a

conventional filament discharge with an array of permanent magnets on the chamber wall to attempt to partially confine the secondary electrons responsible for plasma regeneration. The advantage of R.F. plasma generation is that this method has a uniform and high ionization rate and hence can sustain high ion fluxes into the target without substantial local depletion of ions in the plasma when treating complex target geometries [1].

2.3 MODIFICATION OF SURFACES BY ION IMPLANTATION.

In addition to precipitation and interstitial diffusion that occur in conventional nitriding processes, ion implantation causes a number of effects in a shallow layer at the target surface. These additional effects are principally caused by the collisions between the energetic ions and the target lattice as the ions slow down. The depth of influence of these collisions can be much greater than the initial implantation depth of the ions through the production and diffusion of lattice defects. The importance of defects is strongly dependent on the nature of the target material and temperature, and the ion species, ion energy, etc.

For room temperature implantation of say 50 kV N_2^+ ions into pure iron, the maximum depth of penetration of the ions is ~ 100 nm. Here, the diffusion rate of N in iron is so low that the N atoms remain in their lattice site unless involved in knock-on collisions from subsequent implanted ions. The features of this shallow layer have been described in some detail, and include: ion concentration and energy release distributions with depth, vacancy formation, ionization of target atoms, etc. . The results of these interactions of ions with the substrate are predictable by conventional theory and have been modelled into computer packages, e.g., TRIM (see Chapter 5).

However, a layer of this depth as a surface hardening treatment is of little significance to most engineering components. A more realistic depth might be 10's of micrometers, so the next step is to look at implantation at higher temperatures where mass diffusion becomes significant, e.g., T > 200°C for steels. Modified layers of increased thickness have been achieved with both PSII and PIII [14,15]. Above room

temperature, a number of additional processes may be occurring, namely, precipitation and radiation effects.

Within the target, radiation effects have a significant influence on the distributions of elements in and beyond the implanted range of the ions [16,17]. Radiation effects include Radiation Enhanced Diffusion (RED), Radiation Induced Segregation (RIS), Radiolytic Decomposition of Precipitates (RDP), sputtering and ion beam mixing. These effects increase with increasing temperature, through the mobility of defects and atoms, and with increasing dose, through the introduction of more defects. Radiation induced amorphization has also been observed but not at elevated temperatures (e.g., > 200°C) where the defect mobility is great enough to allow reordering to occur. Sputtering can preferentially remove atoms from the surface layer, hence it not only increases the defect production, but can also change the near-surface composition.

The main defects introduced by ion implantation are vacancies and interstitials. In unimplanted metals, vacancies are usually only found in low density, even near the melting point, while interstitials are typically not present in metals due to their high activation energy of formation. However, collision cascades which occur during implantation, produce a considerable quantity of interstitials and a greater than normal density of vacancies. As vacancies are the primary mechanism for solute diffusion in alloys, excess vacancy concentrations increase the diffusion coefficients of these atoms considerably, e.g., RED. This allows phase transformations to occur at lower than usual temperatures, such as precipitation or decomposition of metastable phases. The interaction of like defects produces agglomerates such as vacancy clusters (voids) and interstitial ordering (dislocation lines and loops), e.g., RIS. However, interstitials and vacancies annihilate each other and can also be lost to sinks such as dislocations, grain boundaries and the surface.

One other effect is the preferential diffusion of introduced defects or interstitial atoms in particular crystal orientations: termed channelling. However, with a large diffusion depth in a fine grained polycrystalline target, this effect is averaged out for diffusion depths much greater than the grain size.

2.4 DETECTION AND CHARACTERIZATION OF SURFACE MODIFICATIONS.

There are two fundamental methods of determining the effects of ion implantation on surfaces: quantifying changes in the mechanical properties and characterizing changes in the surface chemistry and microstructure.

The following outlines a variety of techniques used in the field of ion implantation to detect changes in metal surfaces.

2.4.1 Measurement of Mechanical Property Changes.

Investigating the effects of ion implantation on the mechanical properties of materials has been approached in two ways: 1) controlled laboratory testing of simple systems to determine the change in a single property; and 2) *in situ* testing of standard industrial components to find the overall performance of the treatment. Laboratory tests include finding the wear, corrosion and fatigue resistance, and the changes in microhardness and surface friction.

Because of their immediate relevance to the practical problem of shearing comb evaluation, hardness and wear testing techniques are discussed.

2.4.1.1 *Hardness Measurement Techniques:*

Recording the changes in hardness of an implanted surface can be a rapid method to prove the effectiveness of a surface treatment, e.g., for quality control in a production situation. The bulk hardness, e.g., well beneath the modified surface layer, serves as the reference for determining the effectiveness of the surface treatment. Due to the limited depth of microstructural modification achievable with room temperature ion implantation, microhardness or nanoindentation [18] hardness measurements have been made from a direction normal to the implanted surface. These techniques are essentially non-destructive for all but the most critical applications, but can yield ambiguous results. However, with the deeper modified layers that can be generated during high temperature, high dose implantation, measurements of the micro- or nano-hardness with depth beneath the surface can be made on polished cross-sections of the

material, *i.e.*, microhardness-depth profiling. This latter technique can be a far more powerful tool in characterizing the macrostructural changes caused by implantation. Both Knoop and Vickers microhardness techniques have been used to evaluate ion implantation treatments. Vickers has the advantage over Knoop tests that hardness values are not so sensitive to load (recorded hardness increases with decreasing load but is most sensitive below 100 g) [19].

The main limitation of microhardness-depth techniques is that the hardness at the very surface is impossible to measure because indentations must be a minimum of 2.5 diameters away from the surface to be a valid test. Therefore, measurements close to the surface must be made with very low loads, bearing in mind the load sensitivity.

2.4.1.2 ***Techniques of Wear Testing:***

Wear tests on ion implanted specimens are usually conducted using the unimplanted specimens of the same material as the experimental control group. The wear performance is evaluated by measuring either the wear rate, that is the specimen mass removed per unit time, or the wear life, *i.e.*, the survival time of a specimen before it becomes inoperational. Tests can also be characterized by the wear mode, e.g., abrasive versus adhesive.

Laboratory wear testing of N-implanted steels has been reviewed by McHargue [20]. Pin-on-disc type wear tests have virtually been the standard test among researchers in the field of the ion implantation of metals. The pin-on-disc equipment consists of an abrader rod, typically 3 mm in diameter, pressing normally against a rotating disc, e.g., 25 mm in diameter; the implantation is performed on the disc surface which contacts the end of the rod. The load, lubrication rate, lubricant type, rotational speed and test duration are the test variables. The volume worn away is calculated either directly, by measuring the weight lost from each component, or by measuring the depth worn away across the wear track. Variations to this procedure have included cutting radial slots into the surface of the disc and reciprocating the motion. Measurements of friction have sometimes been reported.

Because of the specific nature of the wear environment of sheep shearing tools, as described in Chapters 6 and 7, pin-on-disc wear testing was thought to be an inappropriate evaluation method for implantation trials on shearing comb steels. However, the alternative evaluation method of *in situ* testing of shearing combs, are not without potential problems.

The limitation of *in situ* tests of say, a shearing comb, is that many environmental parameters, that directly affect the wear behavior, can change between tests or not be measurable. These parameters can include: the local temperature, the size distribution of third body abrasive particles, the lubrication, the surface texture and the contact pressure. *In situ* tests on ion implanted components have included metal cutting processes such as blanking of sheet materials such as steels and polymers and erosive abrasion. Conrad *et al.* [2] have reviewed field trials of ion implanted components.

2.4.2 Detection of Changes in the Surface Chemistry.

Changes in the composition and distribution of elements and compounds across shallow surface layers can be found by a number of techniques which can be either destructive or non-destructive, depth selective or not depth selective. Not withstanding, common features of all methods are that observations are made using either photons or subatomic particles: a requirement because the scale of micro-structural feature being analysed is typically sub-micron.

Conventional implantation has been performed between liquid nitrogen temperatures through to 200°C, *i.e.*, without significant diffusion of the ions after initial implantation. Layers obtained by this process are typically 100 – 200 nm thick and occasionally up to 1 μm. For this reason researchers in this field have concentrated on short range detection of surface layers.

Techniques used for determining the distribution of elements within a surface include the non-destructive tests: Nuclear Reaction Analysis (NRA) and Rutherford Backscattering Spectroscopy (RBS); and the destructive tests: Secondary Ion Mass

Spectroscopy (SIMS), Ion Scattering Spectroscopy (ISS), Auger Electron Spectroscopy (AES) and Glow Discharge Spectroscopy (GDS) which employ sputter etching to gain depth information.

NRA [21] profiles the implanted nitrogen by detecting surface emissions produced by nuclear resonant reactions $^{14}N(\alpha,\gamma)^{18}F$; $^{14}N(d,p)$; $^{14}N(d,\alpha)$ ^{12}C and $^{15}N(p,\alpha\gamma)^{12}C$. This technique gives information up to 100 nm below the surface with ~ 5 nm resolution. It has been used to monitor the redistribution of nitrogen in the substrate by implanting only one isotope and detecting both [12].

RBS has good detection of transition metals by the monitoring of back-scattered electrons from reactions of typically 2 MeV He^{2-} ions with atomic nuclei in the surface. This technique gives information up to 150 nm below the surface with good resolution.

The destructive tests find the relative proportions of the near surface elements by analysing energy spectra. Profiles of these elements with depth are obtained by progressive sputter etching of the surface. SIMS, ISS, AES and GDS [22] are used to detect light elements, e.g., C, N and O whilst AES is also used for heavier elements, e.g., Fe, Cr, etc. The sputtering beam is usually ionized argon which typically has sputtering rates of 25 nm/s for steel [22].

The compounds present in the surface have been detected by the non-destructive tests of X-ray Diffraction (XRD), Conversion Electron Mössbauer Spectroscopy (CEMS) and X-ray Photo-electron Spectroscopy (XPS) (destructive).

XRD [23] typically uses Cu-Kα radiation to show the compounds present by measuring the lattice spacings from diffracted X-rays. This technique is made depth selective up to 100 nm by using the glancing angle technique (0.3 – 1.0°). However, it requires a flat surface area of ~ 1 cm^2 in order to accumulate a sufficient X-ray count to analyse, which can make detection difficult in many standard engineering components. Moreover, XRD can suffer from ambiguous phase identification because first, many x-ray reflections for individual phases have un-measurable intensities, and second, peaks from different phases can overlap when the microstructure is composed of several unknown phases.

CEMS [23] measures the chemical states of transition elements and can differentiate between the various nitrides and allotropes and solid solutions of iron. It is not depth selective or destructive and has a range of up to 100 nm.

XPS measures the binding energy of near surface atoms and hence the composition. It is qualitative and can be made depth selective by sputter etching.

2.4.3 Characterization of Microstructural Changes.

Scanning electron microscopy (SEM) and optical microscopy (OM) allow gross characterization of ion implanted materials with relatively thick modified layers. However, structural changes induced by ion implantation usually occur on a scale below the limit of resolution of these techniques (see Chapter 4). Therefore, transmission electron microscopy (TEM) is the only technique able to yield structural information, e.g., the size, shape and distribution of phases, in implanted surface layers. TEM studies on ion implanted materials have included observing pre-thinned foils (~ 100 nm) which have been subsequently implanted [24-26]. Cross-sectional TEM (XTEM) has been rarely reported [25,27] due to the difficulties of preparing thin areas of the very edge of cross-sections (see Appendix 3) but is essential for observing deeply modified layers.

2.5 PREVIOUS INVESTIGATIONS OF PIII AND PSII.

Tendys *et al.* have used a number of experimental techniques to investigate the effects of the PIII process [1,3,8,13,28,29]. The techniques used have been: metallography, NRA using the $^{14}N(d,\alpha)^{12}C$ reaction, Glancing Angle XRD, micro-hardness tests, pin on disc wear tests, and CEMS. The metals treated have been primarily iron and steels under a range of temperatures and doses. Specific results for PIII from Tendys *et al.* are discussed in Chapter 4.

Conrad *et al.* have used a variety of methods to evaluate the PSII process [2,15,30-33], which include: pin on disc wear testing, field trials of treated components, microhardness testing, RBS, SIMS, XPS, AES, TEM, and computer modelling.

Materials investigated have been steels (types 5160 and M2), a titanium alloy (Ti-6Al-4V), Incoloy, Invar alloys, polymers, and ceramics.

Chapter 3

MECHANICAL PROPERTIES OF PIII TREATED STEELS

3.1 INTRODUCTION.

It was explained in the previous chapter that the PIII process has the potential to effectively nitride steels under conditions not realistic in conventional treatments. As the PIII process had not previously been investigated for the surface treatment of tool steels, experiments were undertaken to characterize the mechanical response of selected steels to the PIII treatment.

Initial tests were designed to establish both the maximum hardness developed in the nitride rich surface layer in several tool steels, and the rate of growth of that layer over a range of PIII process conditions. Since C and N diffusion rates in steels are strongly temperature dependent, the workpiece temperature during PIII treatment was considered as the primary variable in this investigation. Interstitial diffusion rates are not only critical in the rate of growth of nitride-rich layers [6,34], but also in the breakdown of primary hardening effects, such as decomposition of martensite, and the agglomeration of fine carbide precipitates [35]. Thus, the selected steels were implanted over a range of specimen temperatures from 200 - 500°C, while the ion dose was set at a level known to cause significant change in the microstructure, *i.e.*, ~10^{18} /cm^2.

The choice of steels was initially those steel presently used in the manufacture of shearing combs, type K510 (high carbon, low alloy), and of wire drawing dies, type H13 (low carbon, secondary hardening) with compositions given in Table 3.1.

Later, a third steel, type XW10, was added to the test program to replace K510 which responded poorly to PIII treatment. The selection of XW10 was based on two considerations. First, high carbon steels have better resistance to wear in aggressive abrasive environments, e.g., sheep shearing; Second, precipitation hardening characteristics in a steel are essential to offset the effects of processing at elevated temperatures, e.g., > 200°C [36], where the nitride rich surface layer can grow to a substantial depth, e.g., 50 μm, within a moderate time, e.g., several hours.

Table 3.1: Composition (wt%) of the steels selected for PIII and GN treatments:

Steel	Fe	Cr	C	Mn	Si	Mo	V
K510 (Bohler)	bal	0.7	1.2	0.3	0.2	-	0.1
H13 (ASSAB)	bal	5.0	0.4	1.0	0.4	1.0	1.5
XW10 (ASSAB)	bal	5.3	1.0	0.6	0.2	1.1	0.2

Due to the relationship between hardness and wear resistance, microhardness profiling with depth beneath the implanted surface was used as the first indicator of microstructural change. This technique has the advantage that it can be performed rapidly and in the laboratory. The gross microstructural features of implanted cross-sections were characterized using optical- and scanning electron microscopy. These observations are reported in the next chapter (§ 4.3) with the TEM results.

As one of the main factors in the survival of sheep shearing combs is wear resistance, and as in situ testing can suffer from un-measurable changes in important parameters, laboratory wear testing of PIII treated steels was considered. However, as mentioned in Chapter 2, the standard pin-on-disc wear test was inappropriate for evaluating the effectiveness of PIII treatments on shearing comb steels. A new wear test was designed which could test implanted rods under reciprocating motion and localized contact stresses, a situation closer to wear in the shearing environment. However, this work was not completed in the period of candidacy because of time spent on other topics covered in this thesis. Controlled *in situ* testing of combs in sheep shearing use is reported instead (Chapter 6).

The toughness of shearing comb steels at the end of the manufacturing process was found to be critical for the survival of the comb in shearing use (Chapter 6). Fractures occurred in several of the thin sections in the vicinity of the comb tooth tips. For this reason, special attention should be given to future grades of steel selected to manufacture shearing combs.

3.2 HEAT TREATMENT PRIOR TO IMPLANTATION.

Each of the steels under investigation requires a different heat treatment to obtain an acceptable balance between the retained hardness, for wear resistance, and toughness, for fracture resistance of the thin comb teeth.

Each steel was heat treated according to the manufacturer's recommendations for high wear resistance and some toughness: see Appendix 1. Precautions were taken to avoid decarburization during solution treatment, *i.e.*, all specimens were sealed in silica tubes that had been evacuated then filled with argon. Immediately after solution treatment, the specimens were quenched by fracturing the silica tubes in oil. The heat treatment of specially made shearing combs (Sunbeam, Australia) was also performed in an inert atmosphere.

The differences in the tempering characteristics of types K510 and XW10 steels are illustrated in Figures 3.1, while the bulk hardnesses of XW10 steel before implantation is shown in Figure 3.2.

3.3 PIII TREATMENTS OF SELECTED TOOL STEELS.

The objective of these experiments was to find a PIII nitriding temperature which gave the highest peak hardness in the modified surface layer, with minimal softening of the substrate. A further aim was to develop hardening to a significant depth (for shearing combs: Chapter 7) within a moderate treatment time, e.g., 50 μm within 3 hours. This depth of hardening was selected so that comparisons could be made with conventional nitriding treatments of similar depth. To achieve control of the specimen

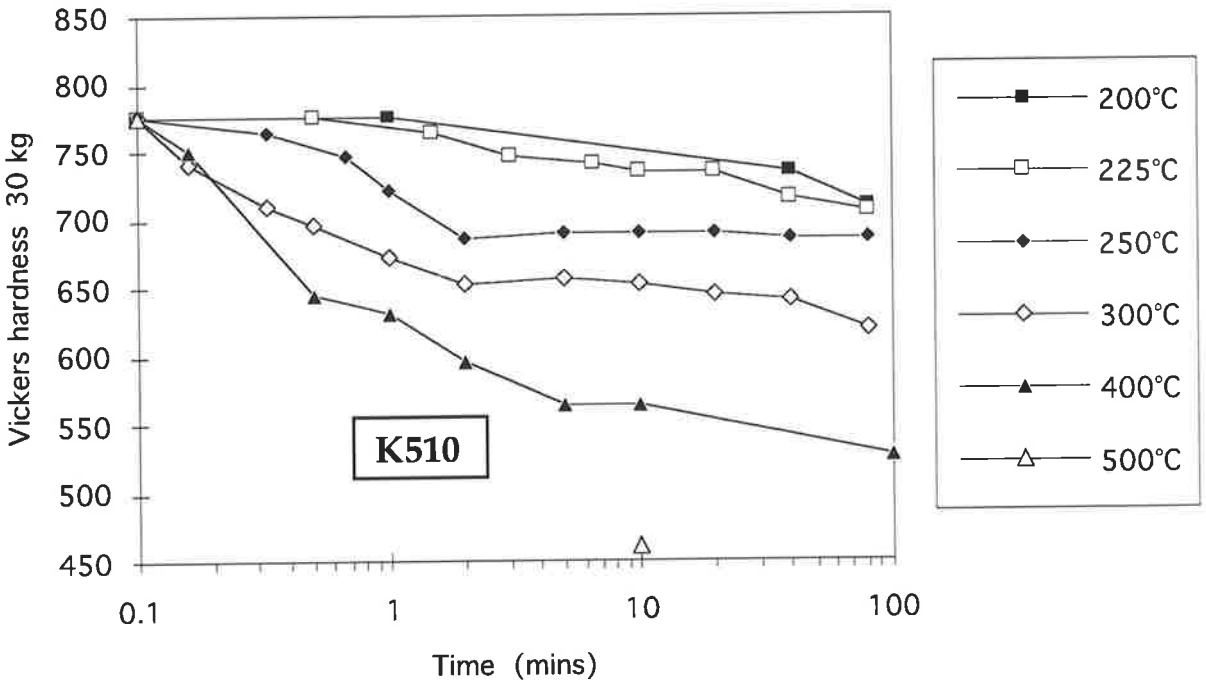

(a)

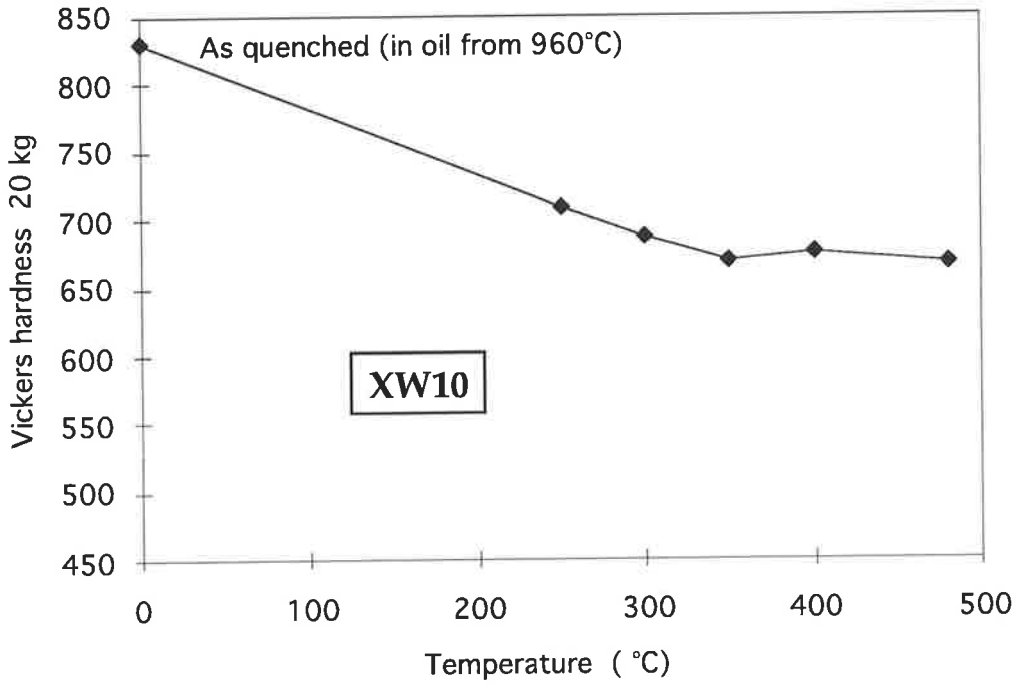

(b)

Figure 3.1: Thermal stability of shearing comb steels from the quenched condition:
(a) "silver" steel (K510) in salt baths, 200<T<400°C, and furnace, T>400°C;
(b) XW10 steel in salt baths (2x1hour), 200<T<400°C, and furnace, T>400°C)

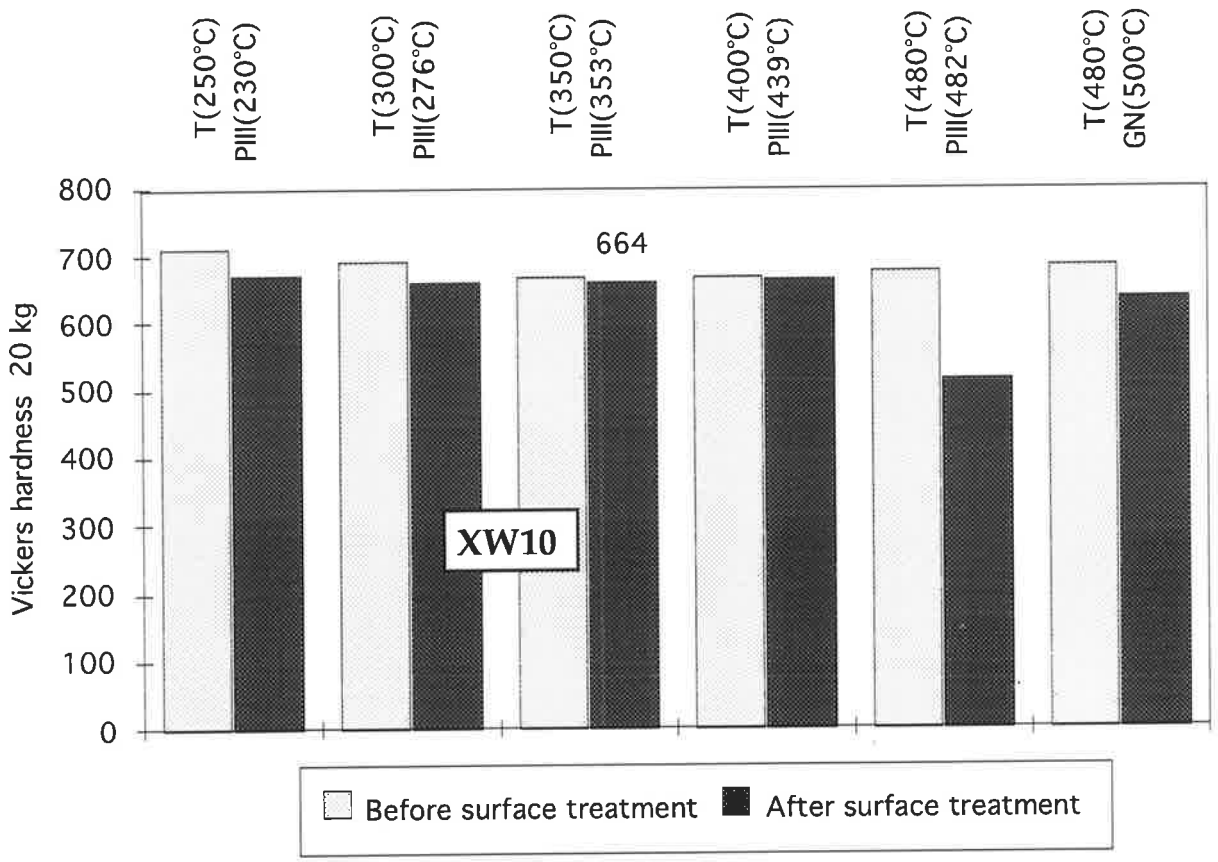

Figure 3.2: Bulk hardness in XW10 steel before and after surface treatment by either PIII or gas nitriding (GN). The initial hardness resulted from the individual quenching and tempering treatments given to each specimen (chosen to maximise the final hardness: Appendix 1), while the final hardness after surface treatment resulted from the additional tempering received during either PIII or gas nitriding (GN).

temperature, the PIII process variables were adjusted as described in Chapter 2, for the given specimen configuration.

A standard specimen geometry was chosen for all of the nitriding treatments in this thesis, *i.e.*, a 50 mm long, 2 mm diameter rod. Implantation was performed on the equipment at the ANSTO Lucas Heights Research Laboratories, Australia by the PIII research team of Dr. John Tendys, Dr. George Collins and Dr. Ron Hutchings. Their suggestions and collaboration were crucial to the success of these investigations.

Other conventional nitriding treatments were performed on the same grades of steel by a commercial gas nitriding specialist. Process conditions were chosen to obtain a hard surface layer that is recommended for wear resistance.

Details of the nitriding treatments, both PIII and conventional, of the three steels under investigation are given in Appendix 1.

3.4 CHANGES IN HARDNESS INDUCED BY SURFACE TREATMENTS.

Both the bulk hardness and the change in microhardness with depth beneath the treated surface of PIII and GN rods were recorded as described in Appendix 2. These bulk hardness and microhardness measurements were made by R.J. Finch in the course of the GIRD project, but are discussed here due to their immediate relevance to the other studies in this thesis.

3.4.1 Bulk Hardness Changes in the Substrate.

During high temperature implantation (or gas nitriding), microstructural changes can take place from thermal effects, above the changes induced by the nitrogen addition. These changes can include tempering of martensitic substrates (all steels) and precipitation hardening (secondary hardening steels only). The hardness of the material well beneath the modified surface layer (e.g., 0.5 mm) is a result of the thermal treatment alone, and therefore can be used as a datum to gauge the extent of further microstructural changes induced by the PIII and gas nitriding processes in their surface layers.

Figure 3.2 illustrates the effects of thermal treatment received during surface treatments on type XW10 steel. Note that because a constant ion dose was chosen for these experiments (§ 3.3), the time that each specimen was held at the PIII process temperature was not constant, but was reduced for increasing process temperature. This is an important consideration in view of the time and temperature dependence of microstructural transformations. Comparing the bulk hardness of PIII treated rods after heat treatment and after surface treatment, the 230, 276, 353 and 439°C effects are consistent with extensions of the tempering processes at those temperatures. That is, temper softening (martensite decomposition) was noticeable in the 230, 276 and 353°C specimens, while precipitation hardening is suggested in the 439°C specimen. Moreover, detailed microstructural studies on the specimen implanted at 353°C (Chapter 4) confirmed that the tempering received during the PIII treatment only caused martensite decomposition. Note that precipitation hardening is only expected above 400°C for XW10 steel at these temperatures and times (Fig. 3.1(b)). The excessive softening of the 480°C PIII substrate compared to the 500°C gas nitrided substrate suggests that the accuracy of the temperature measurement during PIII treatments above 439°C is questionable.

On the other hand, thermal treatments which occurred during PIII treatments on K510 steel had disasterous effects on the substrate microstructure. Substantial softening of the entire cross-section took place for PIII treatments above 200°C, as expected from the separate heat treatment studies that were conducted, Figure 3.1(a). The relevance of these effects to the shearing comb application are that only low temperature PIII treatments are possible if wear resistance is to be retained.

3.4.2 Microhardness Changes across N-Containing Surface Layers.

Figures 3.3 and 3.4 show the microhardness-depth measurements on surface treated XW10 and H13 steels. As illustrated by Figs. 3.3, the PIII treatments done at or below 300°C have little effect on the micro-hardness/depth profile of either H13 or XW10 steels. These small variations are most likely a result of heat treatments given

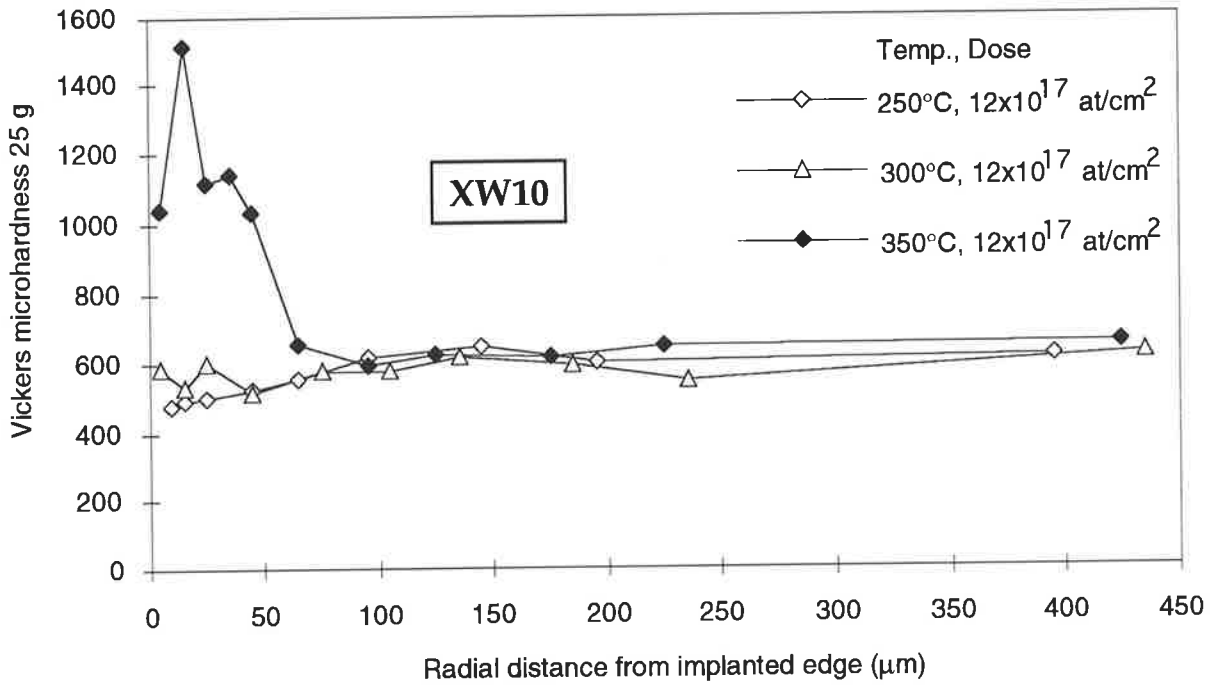

(a)

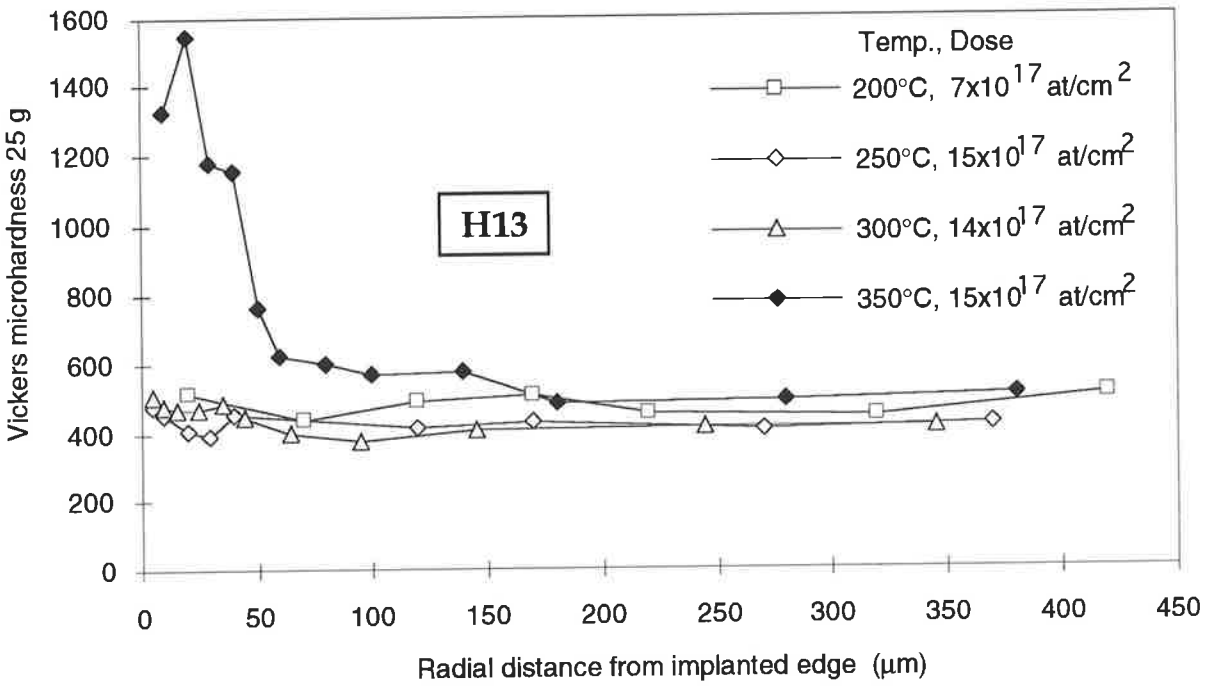

(b)

Figure 3.3: Transverse microhardness profiles for PIII treated XW10 (a) and H13 (b) steels showing treatment temperatures ≤350°C. For either steel, implantation temperatures less than 350°C had little effect on the hardness. However, at an implantation temperature of 350°C, substantial near surface hardening was found in both steels.

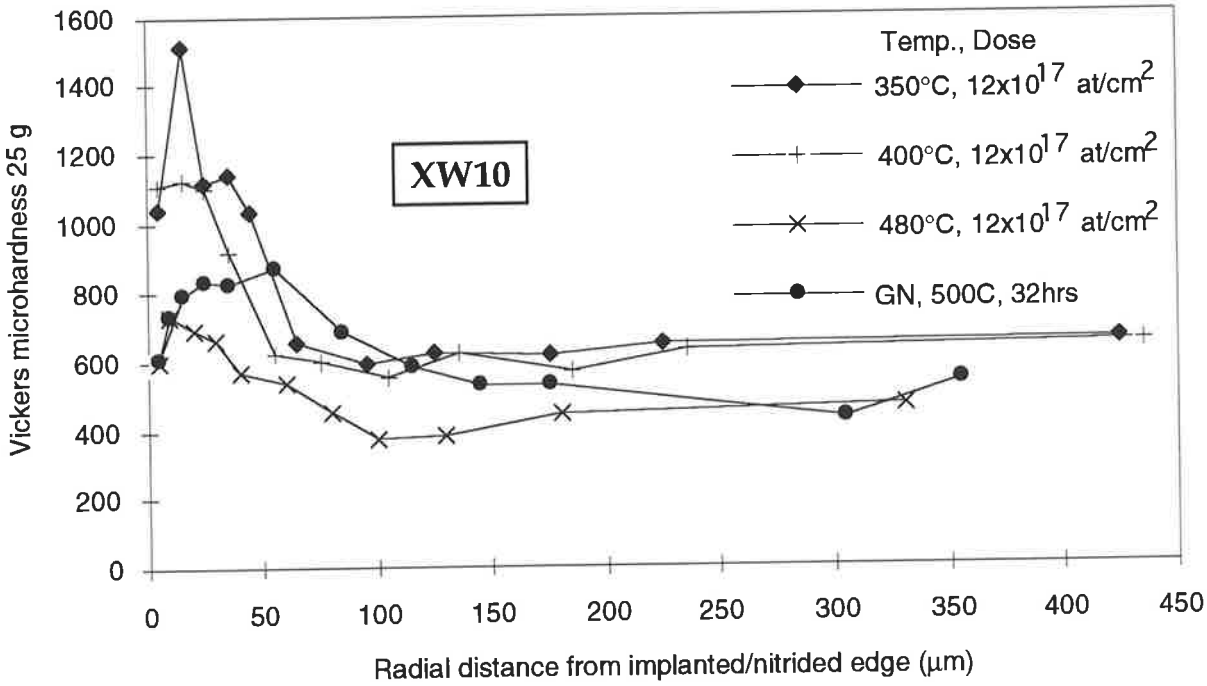

(a)

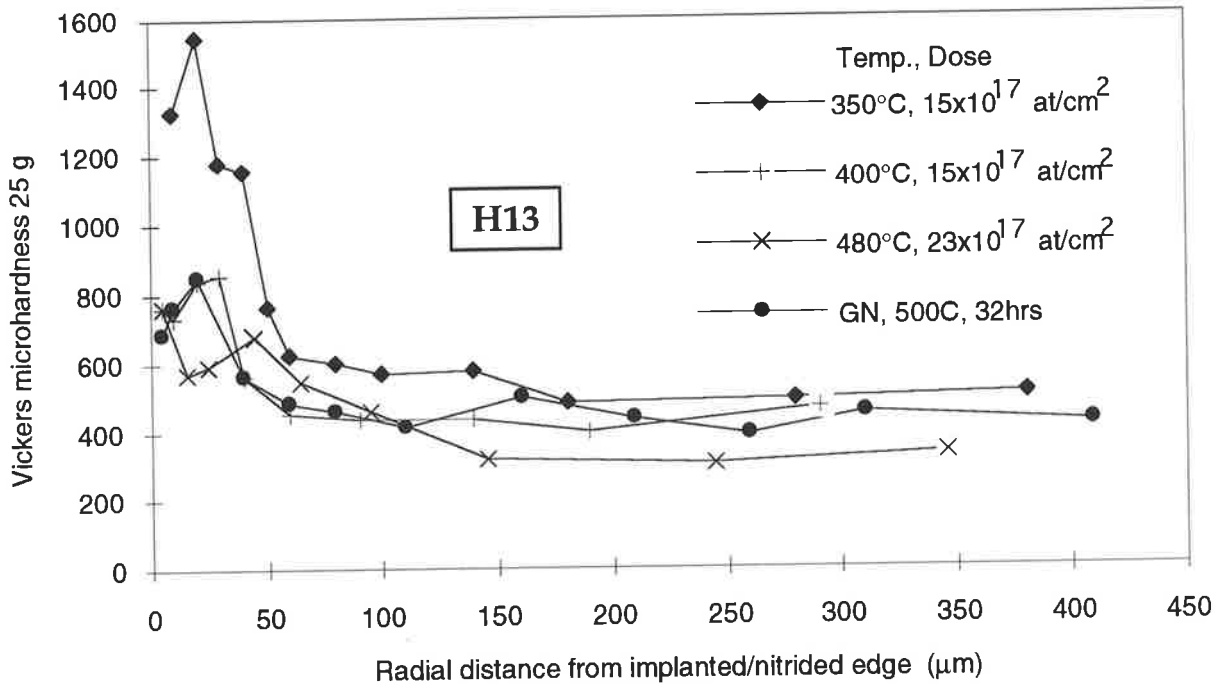

(b)

Figure 3.4: Transverse microhardness profiles for PIII treated XW10 (a) and H13 (b) steels showing treatment temperatures ≥350°C. For either steel, implantation temperatures greater than 350°C had deleterious effects on the hardness. Gas nitriding under commercial conditions did not perform as well as the 350°C PIII treatment.

prior to implantation. In particular, the reducing hardness towards the surfaces of the XW10 steel rods is perhaps due to slight decarburization during the initial heat treatment process.

However, the results from the 353°C PIII treatment of the precipitation hardening steels greatly contrasts the traditional 500°C GN treatment: Figure 3.4. There is a dramatically higher hardness over a 50 μm surface band in both XW10 and H13 steels, showing a peak hardness of ~1500 HV_{25g}. Both hardness profiles at this process temperature have the same form, e.g., the surface hardness (5 μm) substantially lower than the peak value; the peak hardness at ~ 15 μm; a narrow plateau (~ 20 - 25 μm); and a diffusion tail (~ 25 - 60 μm). H13 steel appears to have a secondary diffusion tail from ~ 50 - 175 μm.

The similarities between the 353°C PIII hardness profiles of these two steels suggests that the carbon content (Table 3.1) of these secondary hardening steels has less effect on the growth rate of the nitride rich surface layer during PIII treatment than during gas nitriding treatment at 500°C. The substantially slower growth during gas nitriding could be explained in terms of the low solubility of carbon in α-Fe, which in turn, allows only a slow rate of nitrogen absorption into the surface under those equilibrium conditions. However, the PIII treatment evidently overcomes these absorption restrictions by forced injection of nitrogen. This creates an artificially high interstitial concentration just under the surface that forces inward diffusion of C and N. Nevertheless, carbon does influence the microstructural development during nitriding treatments, as discussed in § 4.6.2, and as indicated by the secondary diffusion band in the lower carbon steel (H13).

The effects on the hardness of implanting H13 and XW10 at temperatures above 353°C are shown in Figs. 3.4. Type H13 appears to be more sensitive to processing temperature than XW10 as XW10 has a higher peak hardness and shows a diffusion tail. However, the shallower diffusion tail in XW10 resulting from 400°C PIII compared to the 353°C profile indicates that the inward diffusion of nitrogen is being blocked, perhaps by a stable surface band of precipitates. This effect is not found in the

corresponding H13 specimen, once again suggesting that the carbon content influences the diffusion process. Once again, the substantially reduced hardness beneath the hardened layer in the 480°C PIII treatment suggests that the nominal treatment temperature was not correct.

The gas nitriding results are typical for these materials and treatments [6].

3.5 CONCLUSIONS.

It is clear from comparisons of the PIII processing times and temperatures with the microhardness profiles, that under near optimum conditions, the PIII treatment develops a harder surface layer in a much shorter time and at a lower temperature than possible with conventional gas nitriding. The reasons why this is so are examined in the next two chapters.

It appears that secondary hardening tool steels are suitable materials to gain the strong benefits of the PIII treatment, whereas, lower alloy steels are not, consistent with the experience of gas nitriding.

One problem anticipated with the application of PIII treatments to shearing combs and other components which require strong wear resistence, is the relatively soft surface layer (0 - 10 μm) which was found to develop in 350°C PIII treated XW10 steel. This issue is discussed in the context of the shearing comb wear mechanisms (Chapter 7).

Chapter 4

MICROSTRUCTURAL CHANGES IN XW10 STEEL AFTER PIII TREATMENT

4.1 INTRODUCTION.

The previous chapter described the changes in the physical properties, especially hardness, induced by PIII. To provide an understanding of the dramatic hardness increase near the implanted surface and to define the requirements for mathematical modelling of PIII (Chapter 5), detailed studies of the microstructure of the 350°C PIII XW10 steel were undertaken. For reference, the microstructures of the XW10 steel in the as received, solution treated and quenched, and quenched and tempered at 350°C (Q&T) conditions were determined. Following PIII treatment at 350°C of the steel in the Q&T condition, the microstructural changes as a function of depth beneath the ion implanted layer, were characterised.

Optical- and scanning electron metallography provide valuable methods of detecting gross changes in the microstructure, but in order to reveal the detailed changes brought about by PIII, high resolution transmission electron microscopy (TEM) with its associated analytical capabilities must be employed.

The preparation of TEM specimens which permit the microstructure of a material to be studied immediately beneath a surface whose properties have been changed by a process such as ion implantation, present special problems. In the current investigation, a new approach has been adopted which provides a reliable and reproducible method of preparing electron transparent thin transverse sections of the ion implanted rod over

the depth range from 5 μm to 120 μm beneath the implanted surface. The experimental details of this technique are described in Appendix 3.

As it is often difficult to determine the composition of some carbides and nitrides by conventional electron diffraction in the TEM, successful use was made of the techniques of electron energy loss spectroscopy (EELS) and high resolution energy dispersive X-ray analysis (XEDS). These compositional analyses were performed by Dr. Peter Miller at CSIRO Australia, Division of Materials Science and Technology, Clayton, Victoria, using their analytical transmission electron microscope.

4.2 PREVIOUS MICROSTRUCTURAL INVESTIGATIONS OF ION IMPLANTED AND NITRIDED STEELS.

Despite the evidence that the microstructural changes which most influence the hardness of nitrided layers occur on the scale of 10's of nanometers (§ 4.2), relatively few TEM studies have been made on nitrided or ion implanted martensitic Cr-Mo-V tool steels. Cross-sectional TEM (XTEM) studies with well defined, depth selective microstructural characterization are even more scarce [25,27]. The microstructural changes induced by implantation depend on the composition and initial microstructure of Fe alloys.

McHargue [20] reviewed the early research on nitrogen ion implanted steels (< 1 μm diffusion depths). In pure α-Fe, α''-$Fe_{16}N_2$, γ'-Fe_4N, ε-Fe_3N, ζ-Fe_2N and ε-Fe_2N_{1-x}, as well as some $Fe_x(C,N)$ compounds reportedly precipitate for implantation temperatures below 300°C [11,12,21,23,25,37-45]. The formation of Fe-N phases has been established by Kopcewicz *et al.* [46] who constructed a phase diagram for Fe-N phases in pure iron as a functions of implantation temperature and nitrogen dose. They reported that in the 350 - 400°C range with high doses (> $6x10^{17}$ at/cm^2), γ'-Fe_4N and ε_3- $Fe_{3-x}N$ were stable precipitates, although deeper (>1 μm) microstructures were not reported.

Regarding ion implantation of steels, Fayeulle [48] observed 3 - 5 nm nitrides in an ion implanted γ-Fe-Cr alloy. Fayeulle *et al.* [24] observed plan view specimens of an annealed Fe-31 wt% Cr alloy that had been implanted at room temperature with 40 keV

nitrogen. They found ε-$Fe_{2+x}N$, $(Cr,Fe)_{2+x}N$ and $Cr_2(C,N)$ nitrides in matrices of α'-martensite and γ-(Fe,N) solid solution.

Kozubowoski *et al.* [26] studied the room temperature 100 keV nitrogen ion implantation into a martensitic stainless steel (AISI 403) using plan view TEM specimens. They found finely dispersed α"-$Fe_{16}N_2$ oriented with the tetragonal unit cell parallel to the α-Fe cubic axes, and $(Fe,Cr)_2N_{1-x}$ nitrides oriented with the (001) planes parallel to the {110} type planes.

Other researchers [49] have performed TEM on back-thinned plan-view specimens of Ti and Ti+N implanted H13 steel (300-400°C). TiN, TiC, Fe_2Ti and Fe_3N were observed in this shallow surface layer with a peak Vickers hardness of 1150 (unknown load) obtained after post-implantation annealing at 500°C for 20 min.

Hutchings *et al.* [3] suggested using XRD that Fe_2N_{1-x} was on the very surface of 350°C PIII treated type H13 steel, and that a diffusion band existed beneath that surface compound layer.

Regarding the nitriding of steels, Philips and Seybolt [47] conducted investigations on the early stages of the ion nitriding of annealed Fe-M-C alloys (M=transition metal). Their principle findings were: (a) the main hardening mechanism was the formation of fine alloy nitride platelets on the {001} α-Fe planes; (b) these fine nitride precipitates were resistant to coarsening during post nitriding annealing at temperatures up to 650°C; (c) the coarser carbides that formed during tempering (in the heat treatment process) partially dissolved during nitriding; and (d) coarse primary carbides of Cr and Ti did not significantly alter the nitriding behavior of the matrix.

Ozbaysal *et* al. [7] investigated the ion nitriding of AISI-H13, -D2, -D3 and -M2 steels and reviewed the previous work on the nitriding of Fe-Cr-C alloys. They found: (a) fine partially coherent alloy nitrides were responsible for the peak hardness which was directly proportional to the Ti, V or Mo content of the steel, and inversely proportional to the alloy precipitate size; (b) the nitride size range was 10 - 40 nm; (c) θ-Fe_3C formed in the prior austenite grain boundaries ahead of the hardened nitride zone; (d) Cr-carbides transformed into Cr-nitrides in the outer nitrided layer; (e) the nitriding

rate was directly proportional to the carbon content of the steel; and (f) that there was a diffuse transition from the case to the core microstructure.

Another feature commonly reported [6] after conventional nitriding treatments is that a 0 - 5 μm "compound layer" often forms at the surface of components, consisting of γ'- Fe_4N and/or ε- $Fe_{2-3}N$. The composition of this layer determines the resistance of the surface to wear and fatigue: having no compound layer is generally considered desirable for the best wear and fatigue properties. The (Fe,N) layer appears to form because of the slow diffusion rate of nitrogen into the bulk material, while the layer composition is determined by the temperature, the nitrogen activity at the surface and the steel's composition.

From these studies, the general conclusions are firstly that the peak surface hardening (~ 1000 - 1200 HV) in these materials occurs through the production of finely dispersed alloy nitrides in the α-matrix of the steel. Secondly, whether the steel has a martensitic or a ferritic matrix or whether there are primary carbides or not does not seem to influence the peak hardness of these tool steels. Thirdly, the growth rate of nitrogen rich surface layer is controlled by the carbon content: higher carbon content implies a lower growth rate.

4.3 MACROSCOPIC OBSERVATIONS OF PIII AND GAS NITRIDED XW10 STEEL.

The micrographs of the whole modified surface layers that developed in the 350°C PIII and 500°C gas nitrided specimens (Figures 4.1 and 4.2) illustrate some immediate differences between these two treatments and compare with the microhardness profiles (Figures 3.3).

The light microscope revealed two distinct bands in the 0 - 20 μm PIII layer: a 10 μm poorly etching band on the outer surface, and a 10 μm deeply etching band immediately beneath: Fig. 4.1(a). Beyond these there was a 60 μm band with an etching gradient towards the lightest etching bulk material. For future references, these bands will be termed Zones I, Zone II and Zone III (NB. Zone III is later shown by TEM

Figure 4.1(a): XW10 Steel, 350°C PIII: - (OM of 2% nital etched axial cross-section) Shows the entire PIII modified layer: A, surface of 2 mm diameter rod; B, band of peak hardness (15 μm); C. diffusion tail (25-100 μm); D, reference substrate (>100 μm); and E, a coarse Cr carbide retained from the heat treatment process.

Figure 4.1(b): XW10 Steel, 500°C Gas nitrided: - (OM of 2% nital deeply etched axial cross-section). Shows the entire GN modified layer: A, surface of 2 mm diameter rod; B, band of peak hardness (60 μm); and C, diffusion tail (60-140 μm).

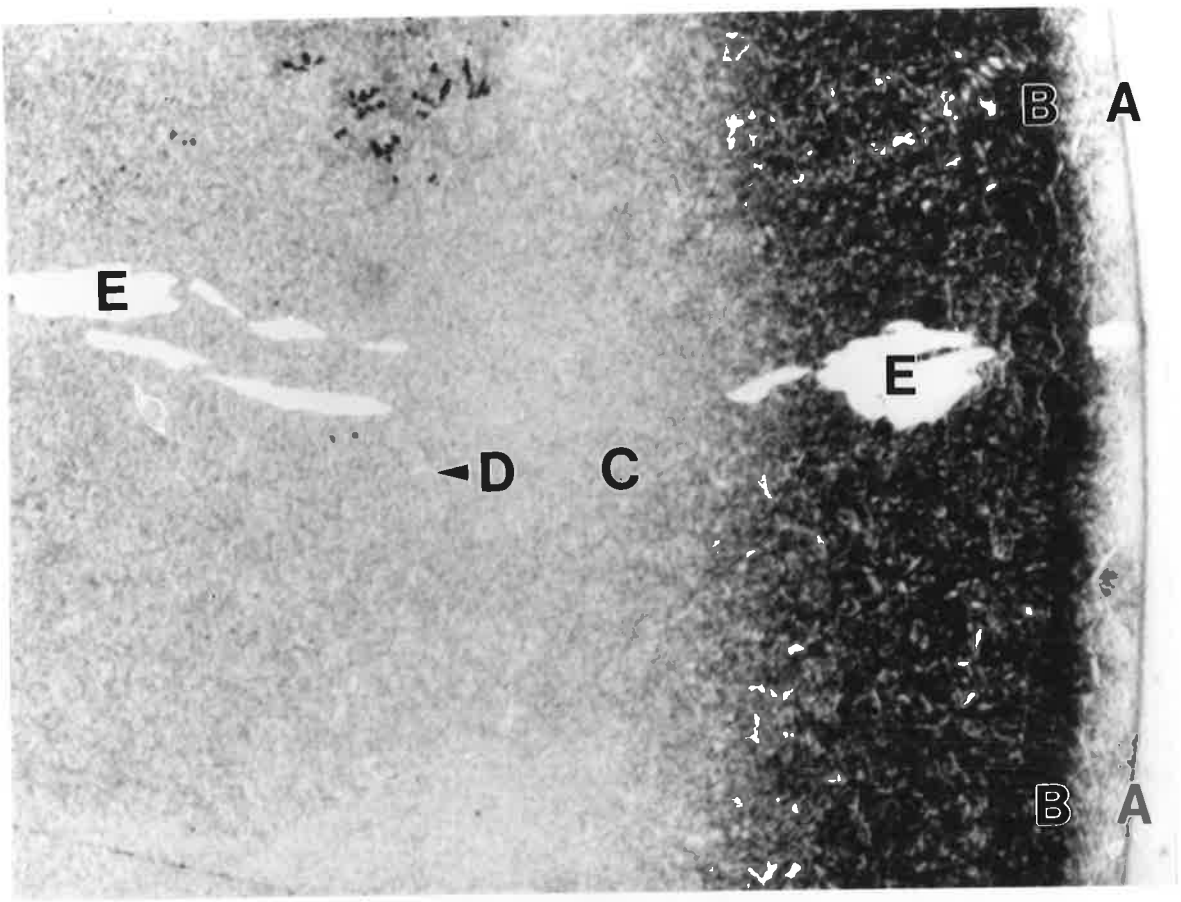

(a)

20μm

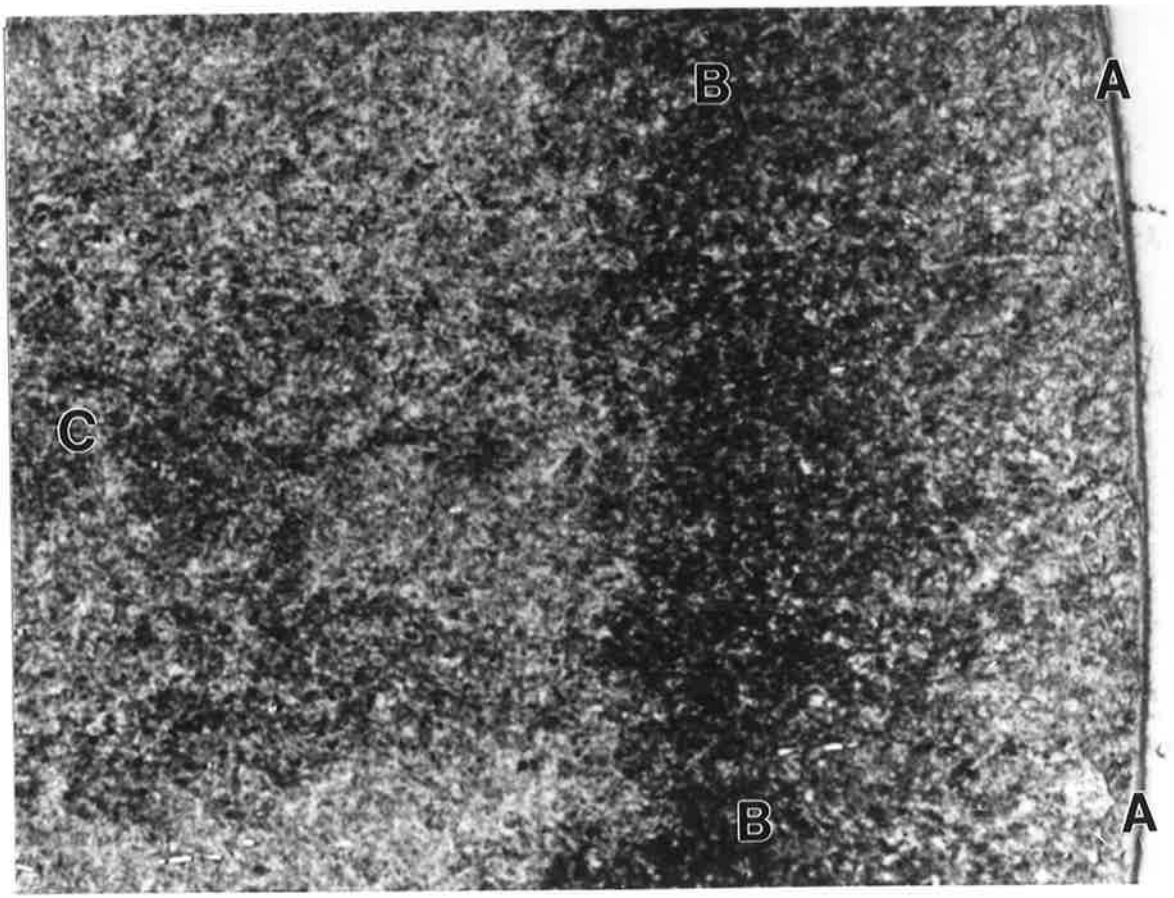

(b)

20μm

Figure 4.2(a): XW10 Steel, 350°C PIII: - (SEI of 2% nital etched axial cross-section): A, surface of 2 mm diameter rod; B, fine Fe_4N precipitate sheets in the grain boundaries of matrix laths with no primary carbides apparent; C, coarse Fe_3C precipitate sheets in the prior austenite grain boundaries; D, primary carbides; and E, band of peak hardness (15 μm).

Figure 4.2(b): XW10 Steel, 500°C Gas nitrided: - (SEI of 2% nital deeply etched axial cross-section): A, surface of 2 mm diameter rod; B, primary carbides; C,coarse Fe_3C sheets in prior austenite grain boundaries.

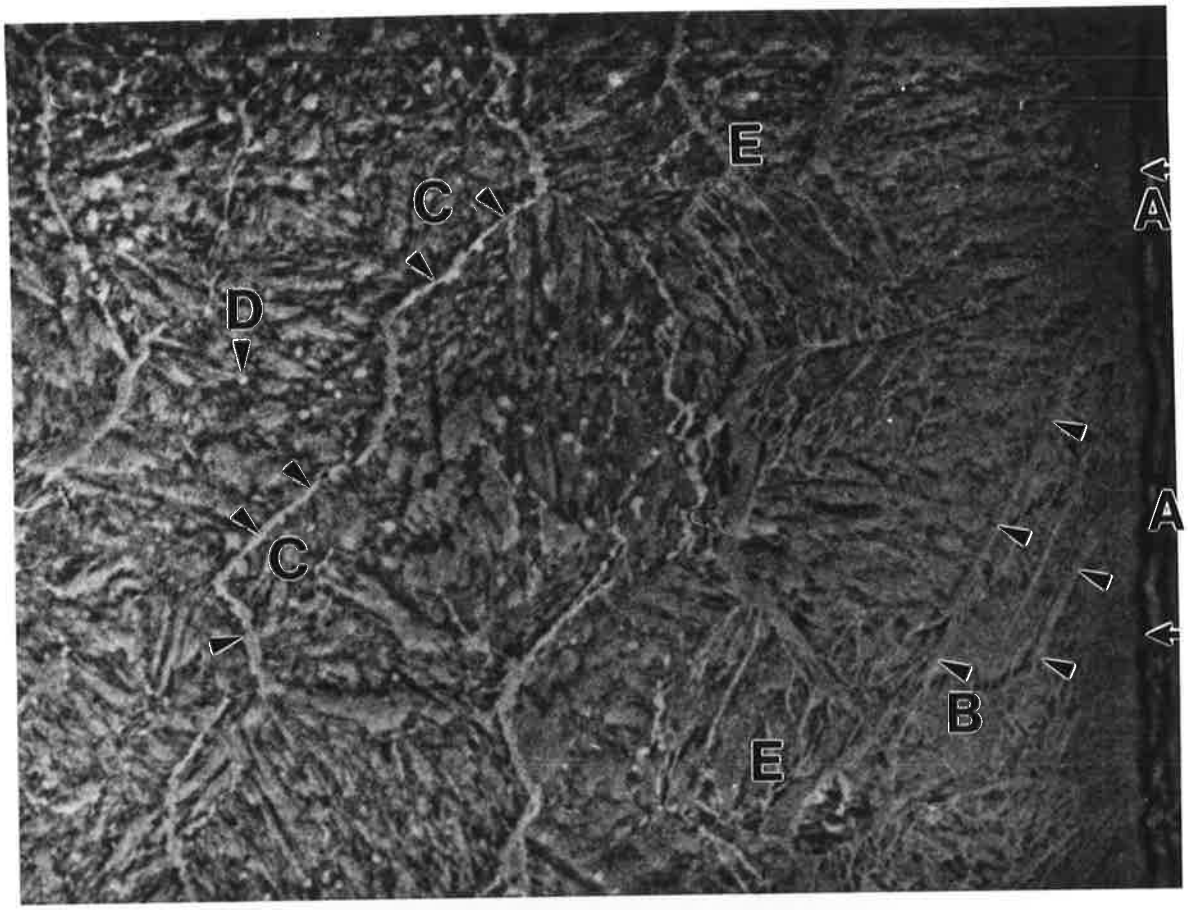

(a)

5μm

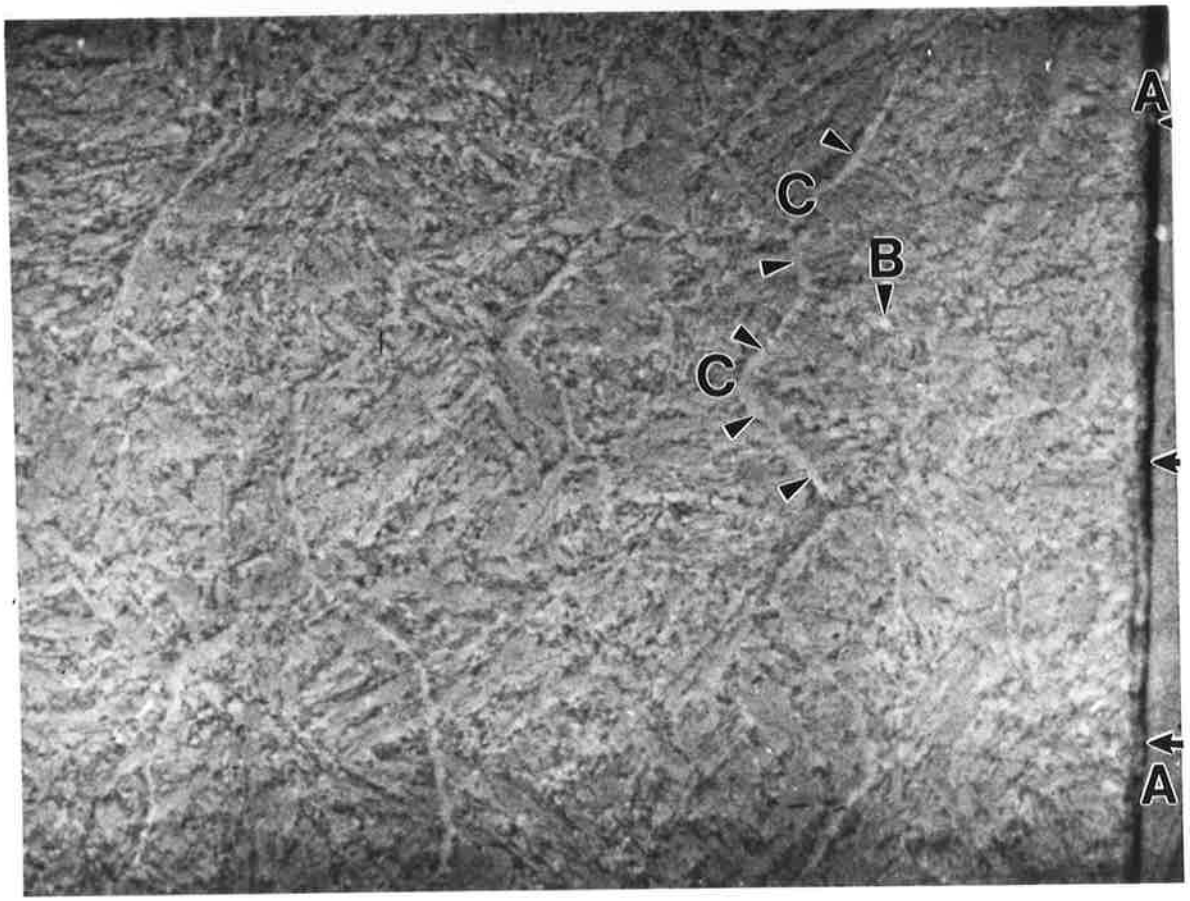

(b)

5μm

techniques to be more conveniently described as two bands: Zones III and IV). Comparing these bands with the microhardness profile, the peak hardness corresponds with the centre of Zone II, while the depth at which the bulk hardness is reached corresponds to the edge of Zone III. The gas nitrided layer, Fig. 4.1(b) had a much flatter and smoother variation in the etching characteristic compared to the PIII layer, which supports the differences in the hardness profiles(Figures 3.3). For this treatment, once again, the darkest etching band coincided with the peak hardness (60 μm).

Under closer inspection in the SEM, Fig. 4.2(a), Zone I of the PIII layer was apparently composed of elongated laths separated by slender precipitate sheets, later identified as Fe_4N, appearing as the lighter coloured phase, while there seemed to be an absence of primary carbides. Zone III looked quite similar to the bulk microstructure apart from long irregular precipitate sheets, later identified as Fe_3C, oriented roughly parallel with the surface of the rod. The occurrence of these sheets were found to be independent of the position on the circumference of the rod and were often 20 μm in length. These depths of these sheets beneath the implanted surface was not constant, but as will be shown later, followed the superstructure of the prior austenite grain and subgrain boundaries (§ 4.5.5). Zone II appeared to be the transition between Zones I and III, showing diminishing primary carbides and slender Fe_4N sheets. Zone II often contained the highest density of the coarser Fe_3C sheets found in the modified layer.

In general, the gas nitrided specimen had microstructures across the modified layer that differed from the appearance of its bulk material only by the presence of similar coarse Fe_3C sheets as described above. These sheets did not exist as frequently or in the same density as found in the PIII specimen. Primary carbides could be observed up to the rod's surface. Unlike the PIII specimen, the gas nitrided specimen had a discontinuous compound layer on the surface some 5 μm thick.

4.4 TRANSMISSION ELECTRON MICROSCOPY OF XW10 STEEL BEFORE PIII TREATMENT.

(See Appendix 1 for details of the heat treatment)

4.4.1 The As Received Condition (Fully Annealed).

As shown in Fig. 4.3(a), in the fully annealed condition, the microstructure of the steel consisted of 0.2 - 1.5 μm carbides embedded in an α-Fe matrix. The carbides were identified as types $M_{23}C_6$ and M_7C_3, by SAD analyses, although $M_{23}C_6$ was found more often. SEM images of the microstructure in this condition (expanded regions similar to Figs. 4.3) were digitised and subjected to quantitative image analysis using the "NIH Image" software using methods reported by Easterling [50]. This revealed that the primary carbides had a volume fraction of 25%, Fig. 4.4. Some massive M_7C_3 carbides up to 30 μm in size were observed, Fig. 4.1(a), and were a feature of this steel that persisted through all subsequent processing.

4.4.2 The Solution Treated and Quenched Condition.

The quenched matrix, Fig. 4.3(b), consisted of both lath and twinned plate type martensites, Fig. 4.5. The prior austenite grain size was approximately 5 - 10 μm.

The twinned plate structure is shown in Fig. 4.6(a): a martensite plate and its twin both in the [113] orientation and mirrored in the $(112)_{Martensite}$ plane, as observed by Thomas [51]. The images (b) and (c) show the $(110)_{Martensite}$ and $(110)_{Twin}$ reflections from this area. Streaking observed in the SADP, (d), is explained by the limited dimensions of the twins in the <112> directions (~ 20 nm).

Image analysis of the primary carbides after solution treatment and quenching, Fig. 4.3(b) and 4.4, showed that their volume fraction had been reduced to 7%. As these were mainly Cr/Fe carbides, a corresponding rise in the Cr content in the matrix would be expected, which was supported by XEDS observations showing ~5 wt% Cr in the matrix: see Appendix 4. The remaining carbides were located primarily at the prior

austenite grain boundaries, e.g., Fig. 4.3(b), with some smaller carbides at junctions of martensite lath blocks. Both types of the original complex carbides were seen.

Less than the predicted 5% retained austenite [52] was found, a likely result of stress relief induced transformation that can occur during specimen preparation.

4.4.3 The Quenched and 350°C Double Tempered Condition.

Before implantation, a uniform distribution of primary carbides was observed, essentially unchanged from the quenched condition, Fig. 4.7. In addition, a fine dispersion of θ-Fe_3C plate precipitates could now be seen in the b.c.c ferrite matrix, Fig. 4.8. Numerous references exist to explain the behavior of secondary hardening steels during heat treatment [53-55]. They show that the presence of only θ-Fe_3C precipitates in the ferrite is expected because the tempering was done below the secondary hardening temperature (~400°C) when alloy carbides precipitate.

A characteristic of the primary carbides was that the interface with the matrix was smooth. It will be shown later that ion implantation induced changes to the nature of that interface (§ 4.5.4.1).

4.5 TRANSMISSION ELECTRON MICROSCOPY OF PIII TREATED XW10 TOOL STEEL.

(See Appendix 1 for details of the ion implantation treatment)

As has been described in § 2.2 and § 3.4.1, the PIII process itself induces specimen heating which, in turn, may bring about microstructural changes. As the depth of the modified surface layer resulting from the implantation process was some 100 μm, to determine the separate influence of specimen heating, an area at a depth of some 400 μm was inspected. This material constitutes what might be described as a Reference Substrate, above which the microstructure was further modified by ion implantation. For convenience, the material from the reference substrate up to the implanted surface has been divided into four separate zones, IV, III, II and I, as the surface is approached (cf. § 4.3).

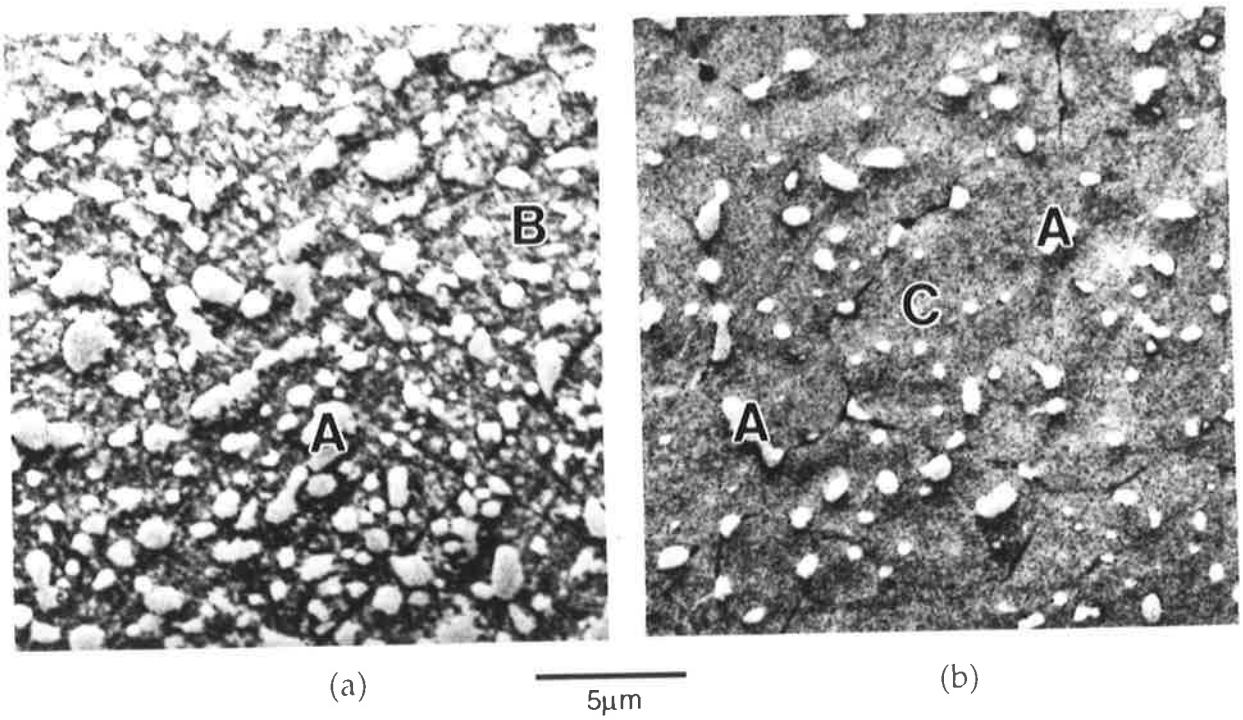

Figure 4.3(a): XW10 Steel in (a), the annealed condition, and (b), the quenched condition: - (SEI of 2% nital etched surface): A, primary carbides, B. ferritic matrix, and C, martensitic matrix.

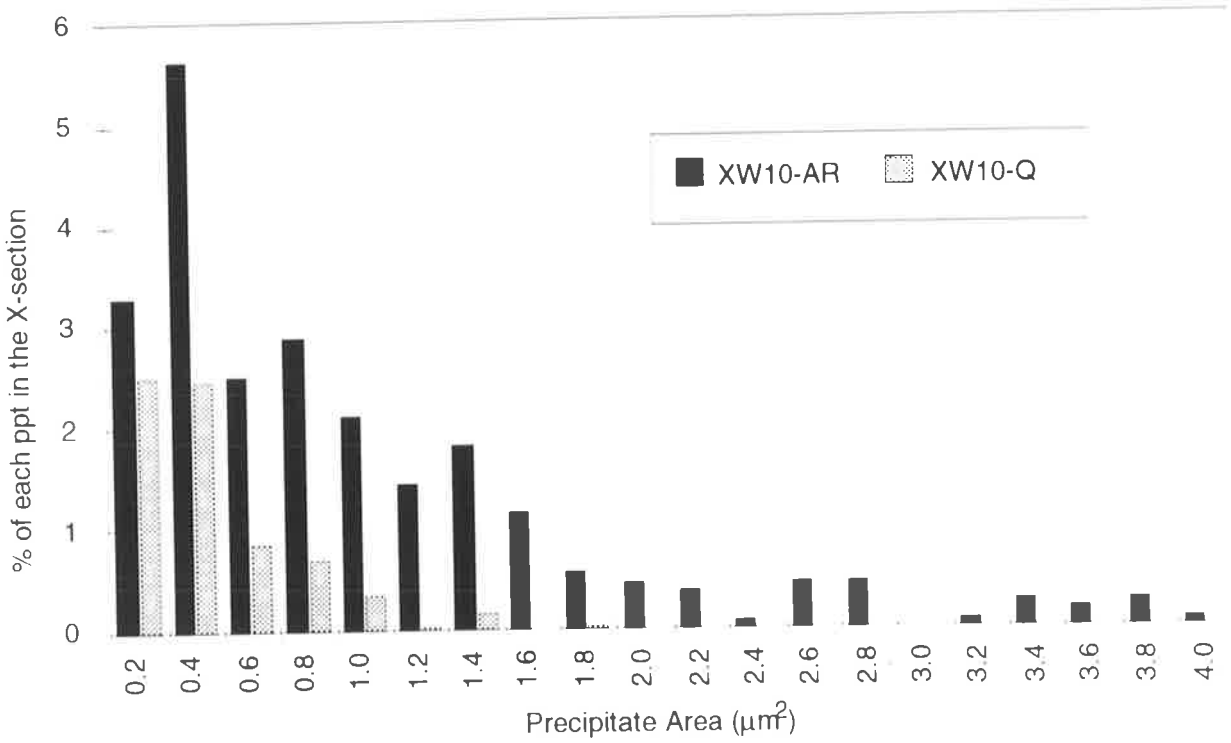

Figure 4.4: XW10 Primary carbide size distribution in the as received (fully annealed) and quenched conditions: quantitative image analysis of secondary electron images (Figures 4.3). The reduction in primary carbide volume fraction occurs during solution treatment

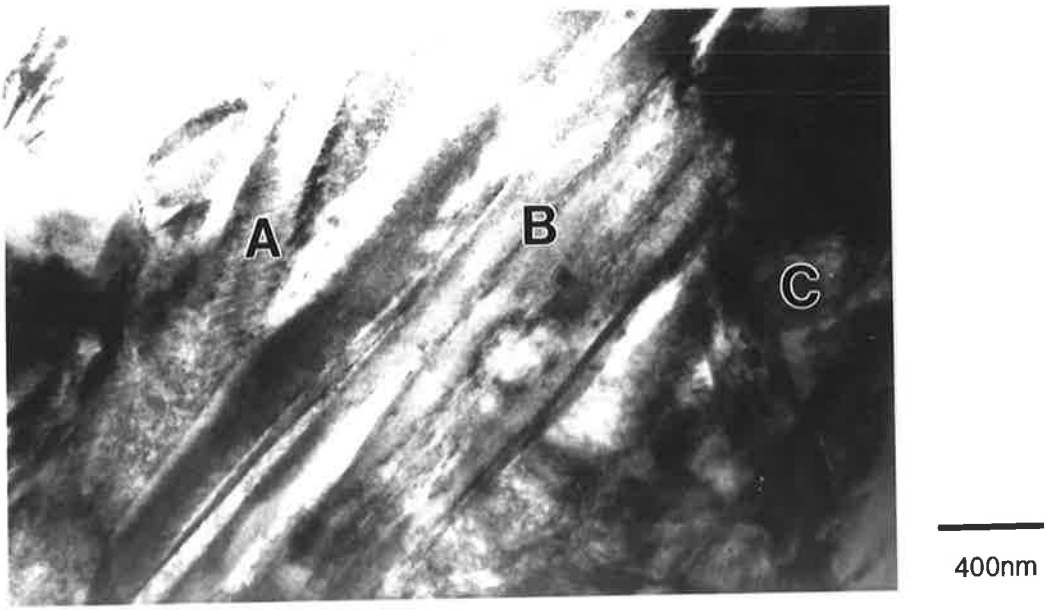

Figure 4.5: XW10 in the quenched condition: (BF) A. twinned plate martensite; B. lath martensite; and C. primary carbide.

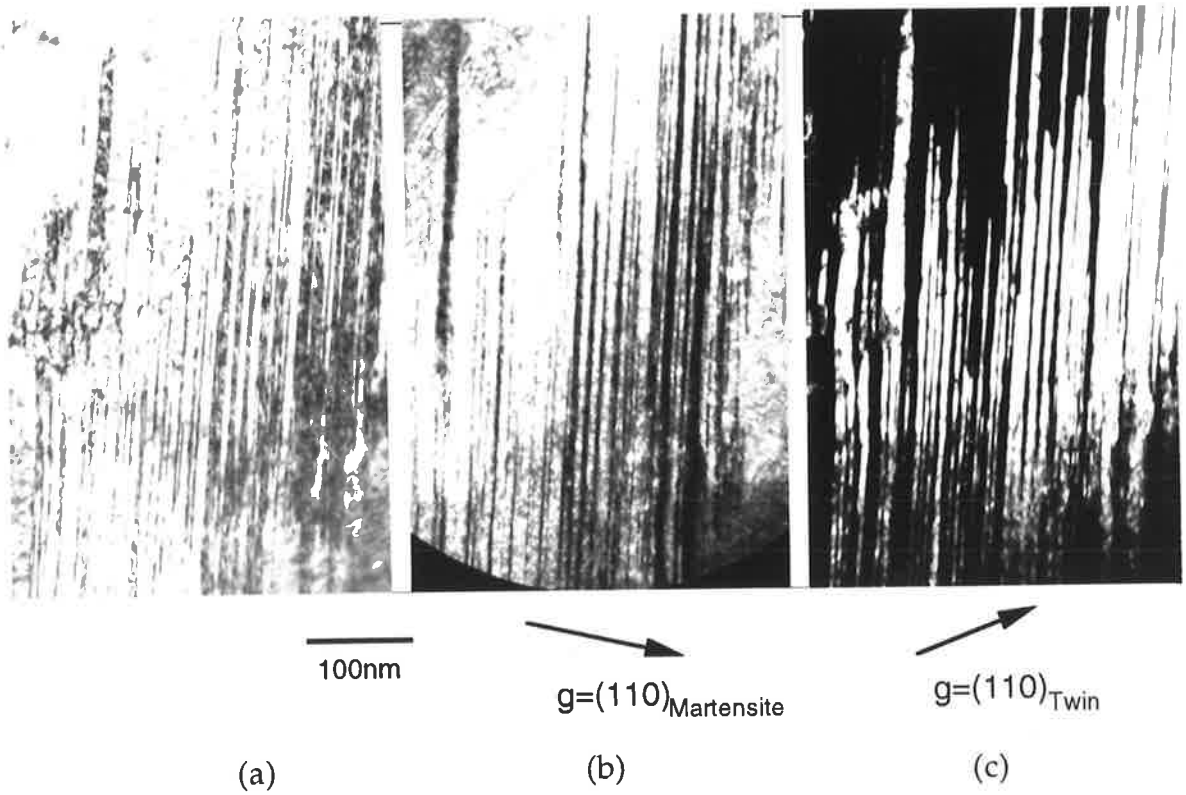

Figure 4.6: Twinned plate martensite: (a) B.F.; (b) D.F. of Martensite Plate; (c) D.F. of Twin; (d) S.A.D.P; and (e) S.A.D.P. analysis (overleaf).

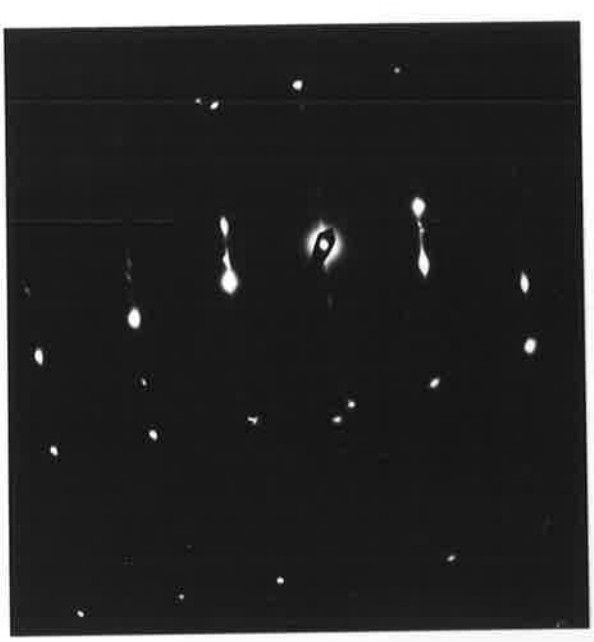

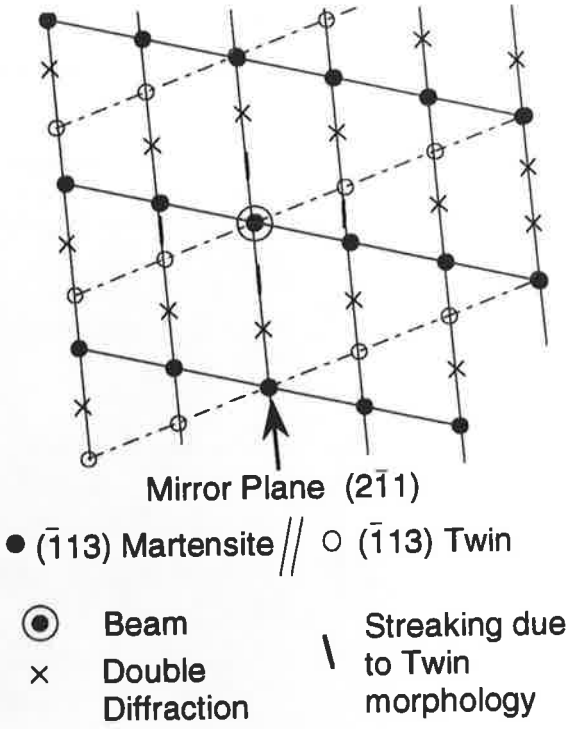

(d) (e)

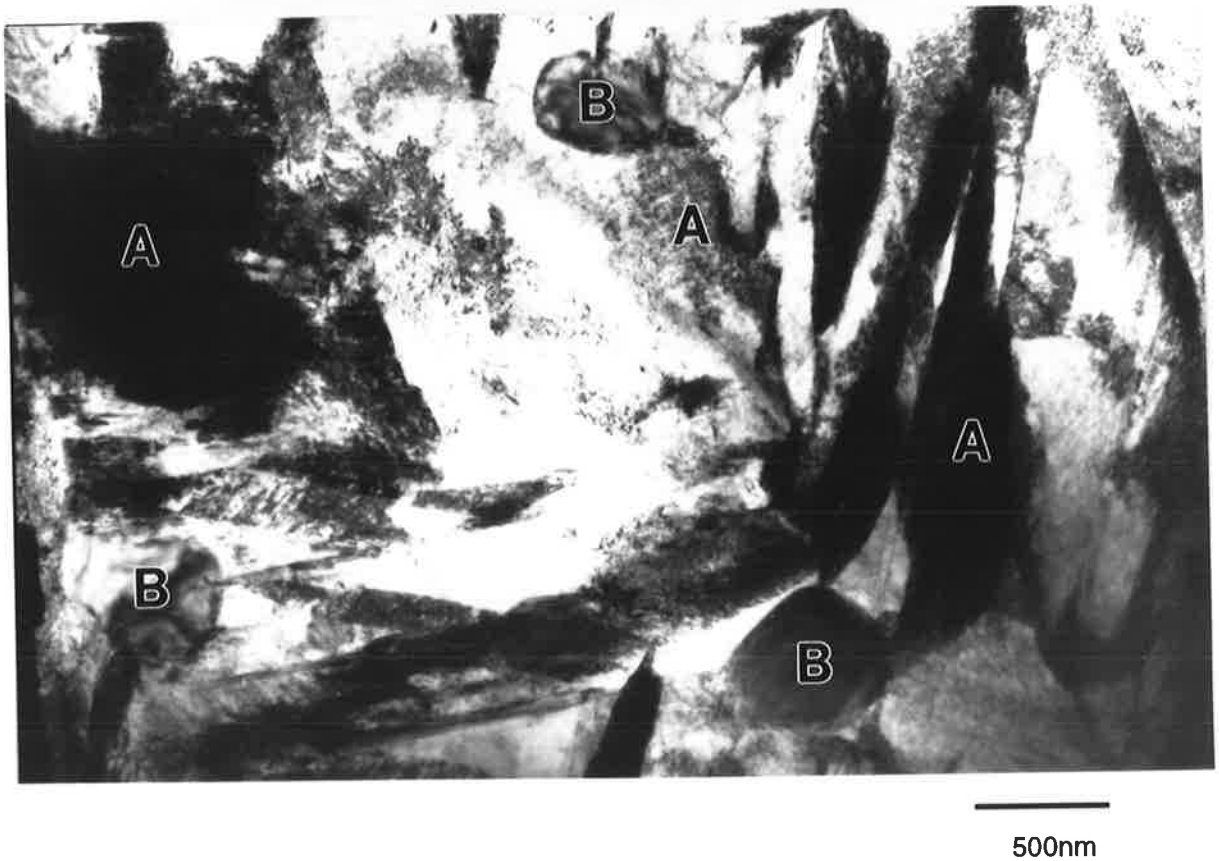

Figure 4.7: BF of XW10 in the quenched and tempered condition (350°C: 2x1hr): A, tempered martensite; and B, primary carbides.

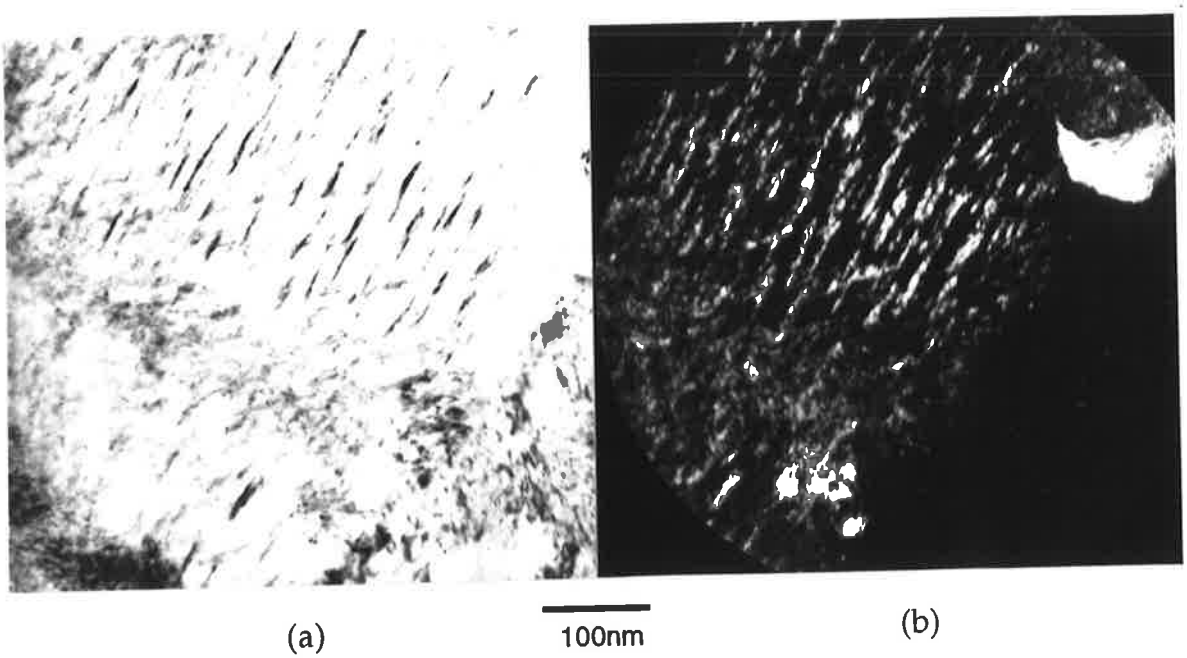

Figure 4.8: XW10 tempered martensitic matrix: (a) BF; (b) DF of Fe_3C platelets.

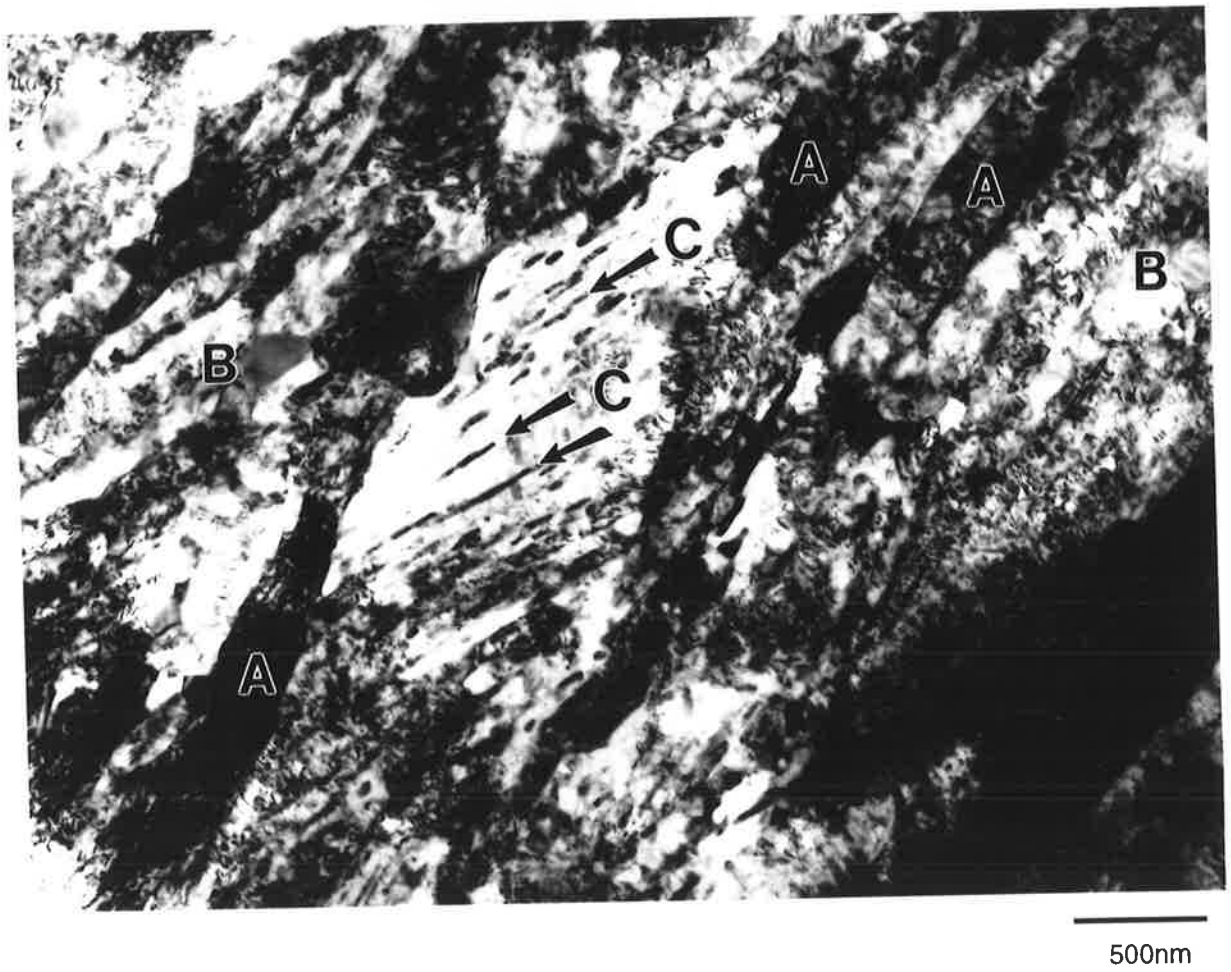

Figure 4.9: XW10 350°C PIII condition - BF of the Reference Substrate (450μm depth): A, tempered martensite laths; B, primary Cr-carbides; and C, secondary Fe_3C lamellae.

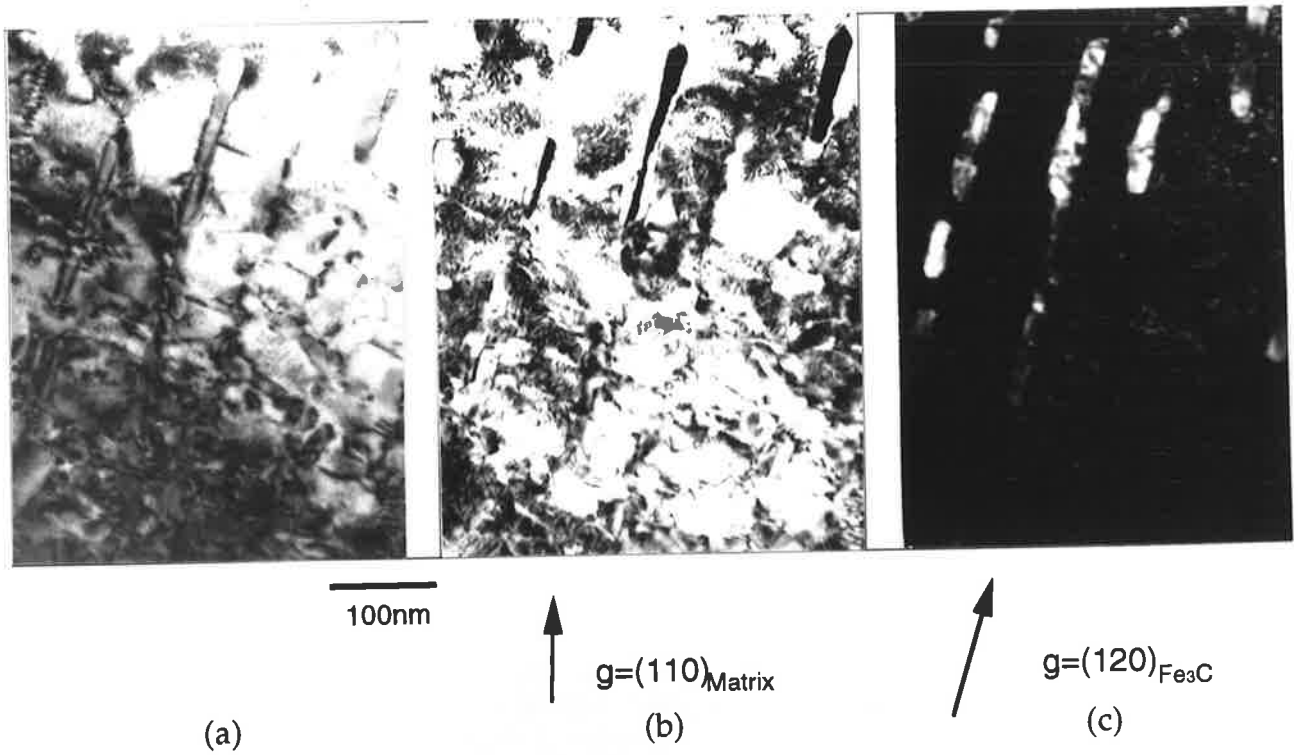

(d)

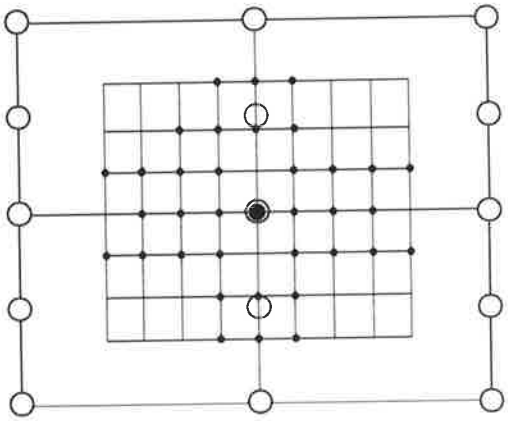

(e)

Figure 4.10: XW10 350°C PIII condition - BF of the Reference Substrate (>450 μm depth): (a) tempered martensite laths; (b) primary Cr-carbides; (c) secondary Fe_3C lamellae; (d) SADP; and (e) SADP analysis showing the Bagaryatskiy relationship between Fe_3C and the α-Fe matrix.

An examination of the microstructures in the modified layer suggested that a bimodal distribution of precipitates could be detected, e.g., (a) coarse, 100 - 500 nm, and (b) fine, 5 - 50 nm.

4.5.1 The Reference Substrate (> 450 μm).

This microstructure was found to be similar to the quenched and tempered material, Figs. 4.9. The most pronounced difference was the coarsening the fine θ-Fe_3C carbide dispersion into ~ 20 nm thick plates at the internal twin boundaries of the plate martensite and within the laths, Figs. 4.10(a-c). A well defined crystallographic orientation relationship was now observed between the θ-Fe_3C and the α-Fe matrix which followed the Bagaryatskiy relationship, Figs. 4.10(d-e). This microstructural change is consistent with that expected from an extension of the tempering process at 350°C, and is accompanied by a reduction in the core hardness of the rod from 672 to 664 HV_{25kg}.

4.5.2 Zone I (0 - 10 μm).

4.5.2.1 *Coarse Structure:*

In the first 10 μm, the microstructure had three unexpected features. First, there was a notable absence of primary carbides (Fig. 4.11) which were readily observed both before implantation and in the Reference Substrate afterwards. Second, the ferrite laths were substantially larger than those found in the bulk material, suggesting that the grain growth had occurred as a result of ion implantation: cf. Figs. 4.11(a-b). Third, no twinned plate type matrix structures were found which could still be seen in the Reference Substrate. All of these features would contribute to the lighter etching characteristic of this first 10 μm layer observed in the light microscope (§ 4.3), e.g., through an increase in the Cr content and decrease in the grain boundary area.

The only coarse precipitate found in this zone was γ'-Fe_4N which existed in the form of sheets in-between the ferrite laths (Fig. 4.12), e.g., the light grey lamellae observed in § 4.3. Closer inspection revealed that these sheets were composed of many

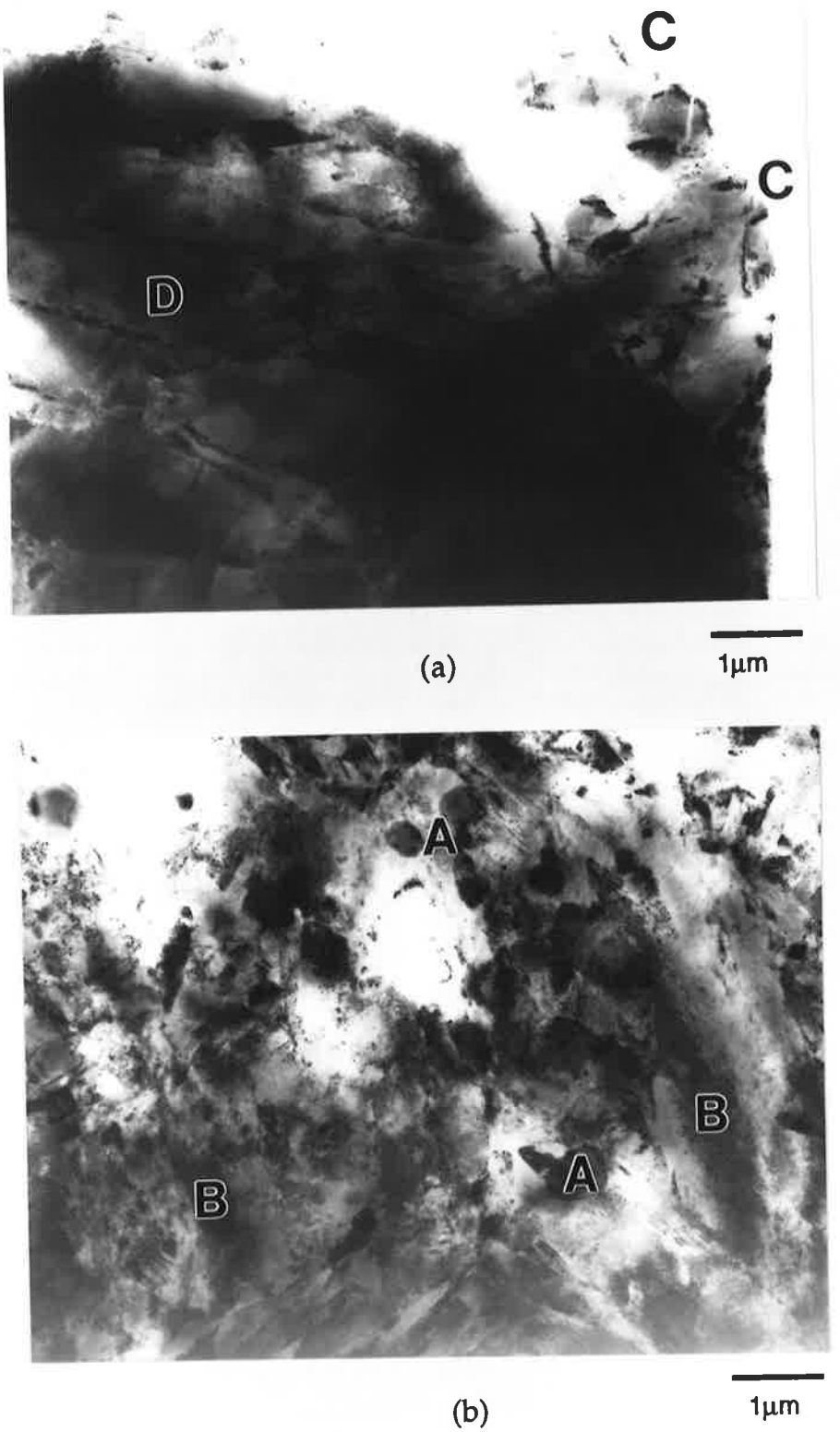

Figure 4.11: The comparison between the microstructures of (a) the near-surface region (5 μm) and (b) a region well below the surface (100 μm): A, primary carbides (100 μm only); B, standard ferrite laths; C, implanted surface of the specimen; and D, enlarged ferrite laths.

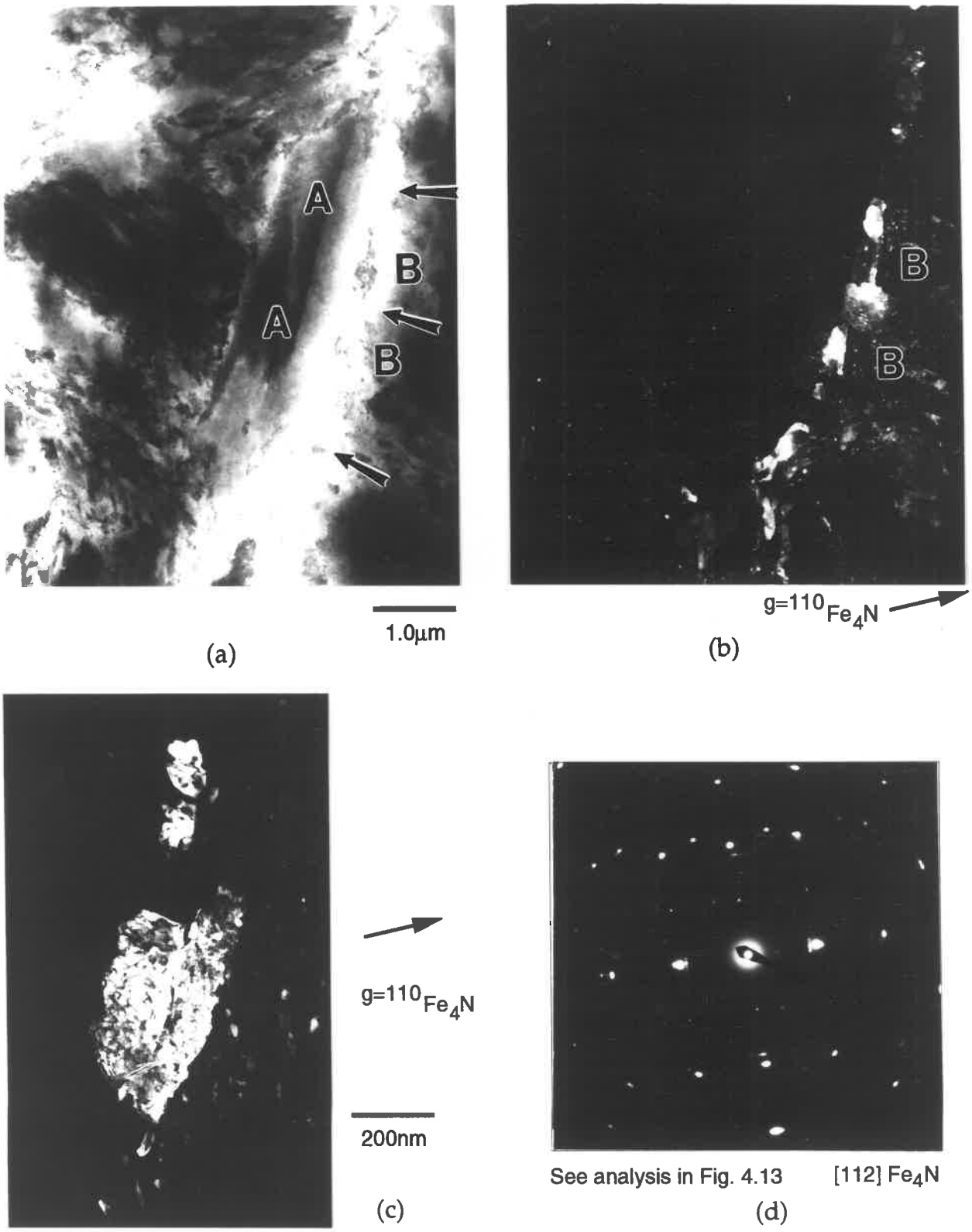

Figure 4.12: 0-25 μm depth: Inter-lath precipitates of Fe_4N at a depth of 10 μm: (a) BF; (b) DF of Fe_4N crystals; (c) enlarged DF of Fe_4N crystal; and (d) SADP of crystal in (c): A, large ferrite lath; B, location of Fe_4N.

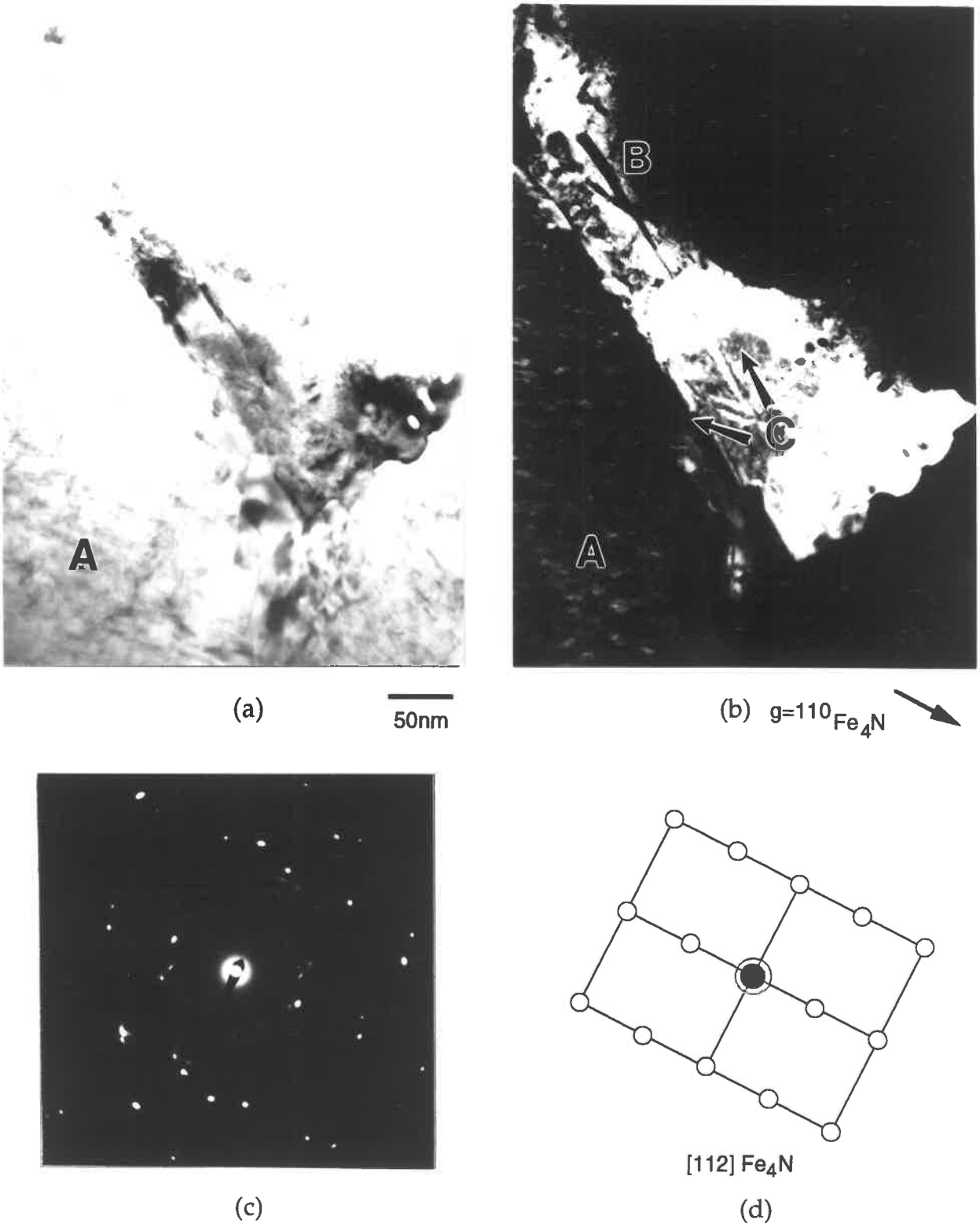

Figure 4.13: 0-25 μm depth: Inter-lath precipitates of Fe_4N at a depth of 5 μm revealing characteristic wedge and butterfly features: (a) BF; (b) DF; (c) SADP; and (d) SADP analysis: A, ferrite; B, Fe_4N wedge morphology; C, butterfly morphology with ~42° included angle (see text).

γ'-grains. The identification of Fe_4N was confirmed not only by dark field imaging techniques, which revealed the characteristic wedge and butterfly morphologies found by Dahmen *et al.* [56], Figs. 4.13, but also by EDAX and EELS microanalysis, which gave an approximate stoichiometry of $Fe_{3.6}Cr_{0.4}N$ (Appendix 4).

4.5.2.2 ***Fine Structure:***

Significant fine precipitation in the 0 - 10 μm band had occurred both within the ferrite matrix and in the Fe_4N sheets, being uncharacteristic of processing at 350°C.

In the matrix, neither the fine θ-Fe_3C plates observed before implantation (Fig. 4.8), nor the coarse θ-Fe_3C lamellae observed in the Reference Substrate after implantation (Fig. 4.10) were found. Instead, two types of finely dispersed alloy precipitates had formed, *i.e.*, no Fe_3C was found in this zone. The most conspicuous of these were MX type plates, Figs. 4.14(a-d), with {001}α-Fe habit planes and the Baker-Nutting orientation relationship with the matrix, Figs. 4.14(e-f) (NB. the matrix at 15 μm depth has been used to illustrate this form of precipitation). The crystallography of this type of precipitation has been well documented by Edington [57] and is characteristic of the secondary hardening process in this class of steel, occurring above 400°C. Despite the low concentration of V in the steel (0.25%), the MX diffraction pattern indexed as cubic V_4X_3, where X=(C and/or N). These plates were easily imaged edge-on from the $(002)_{MX}$ reflection which also revealed their existence along some of the low angle grain boundaries of the ferrite.

The second alloy precipitate dispersion, M_2X type, was identified by the presence of streaking in the [001]α-Fe diffraction pattern. The characteristic Pitsch-Schrader relationship was seen between the M_2X and α-Fe, Figs. 4.14(e-f), as observed by Stiller *et al.* [58]. Moreover, by tilting the matrix slightly off the [001] zone, double diffraction spots appeared, Figs. 4.14(g-h), indicating partial coherency of this phase with the matrix. These precipitates were too small to be imaged in dark field.

Other fine precipitates were seen in the interlath Fe_4N sheets: fine spheroidal CrN precipitates, often no bigger than 10 nm, were found to have the same (111)MX

parallel to the (001)α-Fe relationship with the adjacent ferrite lath, Fig. 4.15. No coherency with the Fe_4N could be detected. Thus, it appears that the fine precipitates existed before the surrounding Fe_4N sheet formed. Often, several orientations of CrN precipitates were observed, Fig. 4.16.

The C/N composition of these fine MX and M_2X precipitates could not be determined by analysis of the electron diffraction patterns because of the close similarity in the lattice parameters between the possible carbides and nitrides, and the continuous mutual solubility of these compounds [59]. High resolution XEDS and EELS were employed in an attempt to overcome this problem, but no conclusive information could be obtained (Appendix 4). The same techniques were used to determine the Mo and V composition of the precipitates, but, due to shadowing from stronger peaks, and the low concentration of these elements, no information was found. Thus, the exact composition of these precipitates remains undetermined.

4.5.3 Zone II (10 - 20 μm).

4.5.3.1 *Coarse Structure:*

In Zone II, the ferrite laths were in the same size range as those in the Reference Substrate: cf. Figs. 4.14(a) and 4.9, showing that the coarser laths which developed in the first 10 μm were the result of a "skin effect". However, still no primary carbides or twinned plate matrix structures were observed.

The Fe_4N precipitate sheets were clearly visible between some of the ferrite laths, except along low angle ferrite grain boundaries where heavy MX precipitation was present, Fig. 4.14(c).

A further precipitate phase was observed between 10 and 20 μm which had a 200 - 500 nm spheroidal morphology, Figs. 4.17, and a volume fraction less than 5%. Although the boundaries of these particles appeared smooth, the internal structure was irregular, composed of many different subgrains with a variety of orientations, making identification by SAD analysis extremely difficult. Possible identifications were $Fe_{16}N_2$ and CrN. Micro-analysis of these regions by EDAX and EELS found that their

stoichiometry was close to $Cr_{0.6}Fe_{0.4}N$ and contained above average levels of Mo. Thus, this phase contained the highest concentrations of Cr, Mo and N in the microstructure. These high levels of Cr and Mo, along with the boundary shape and size, strongly suggest that their origin was from the M_7C_3 primary carbides. Furthermore, analysis of the surrounding matrix indicated that the Cr and Mo did not appreciably diffuse out of the prior carbide grain boundaries, showing the stability of this phase against microstructural change.

4.5.3.2 ***Fine Structure:***

In addition to MX and M_2X (§ 4.5.2.2), a third type of finely dispersed precipitate phase was identified that fitted in-between the MX precipitates, Fig. 4.18(a-b). Indexing of the diffraction pattern giving rise to these precipitates, Fig. 4.18(c), yielded the CrN structure. The CrN precipitates were oriented with the [111]CrN zone parallel to the [023]α-Fe zone, and the (220)CrN plane coinciding with the (002)α-Fe plane: note that the mismatch between these planes is only 2.2%. However, the barely perceptible change in the Cr concentration within these precipitate containing ferrite grains, and the difficulty in obtaining images of these precipitates both suggest that this CrN phase has a small volume fraction in the microstructure. Nevertheless, as once again, coherency of these precipitates was detected with the matrix, Fig. 4.18(d), their influence on the strengthening mechanisms of the matrix cannot be neglected.

4.5.4 Zone III (20 - 40 μm).

4.5.4.1 ***Coarse Structure:***

Although Fe_4N was not seen, some 200 - 500 nm Cr_2N precipitates were still found in this zone, but no deeper.

The most significant feature of Zone III was the observation of the first primary carbides in the modified layer since traversing from the implanted surface. However, these carbides were somewhat smaller, and with misshapen interfaces with the matrix, 4.19(a), compared to the carbides in both the quenched and tempered condition, Fig.

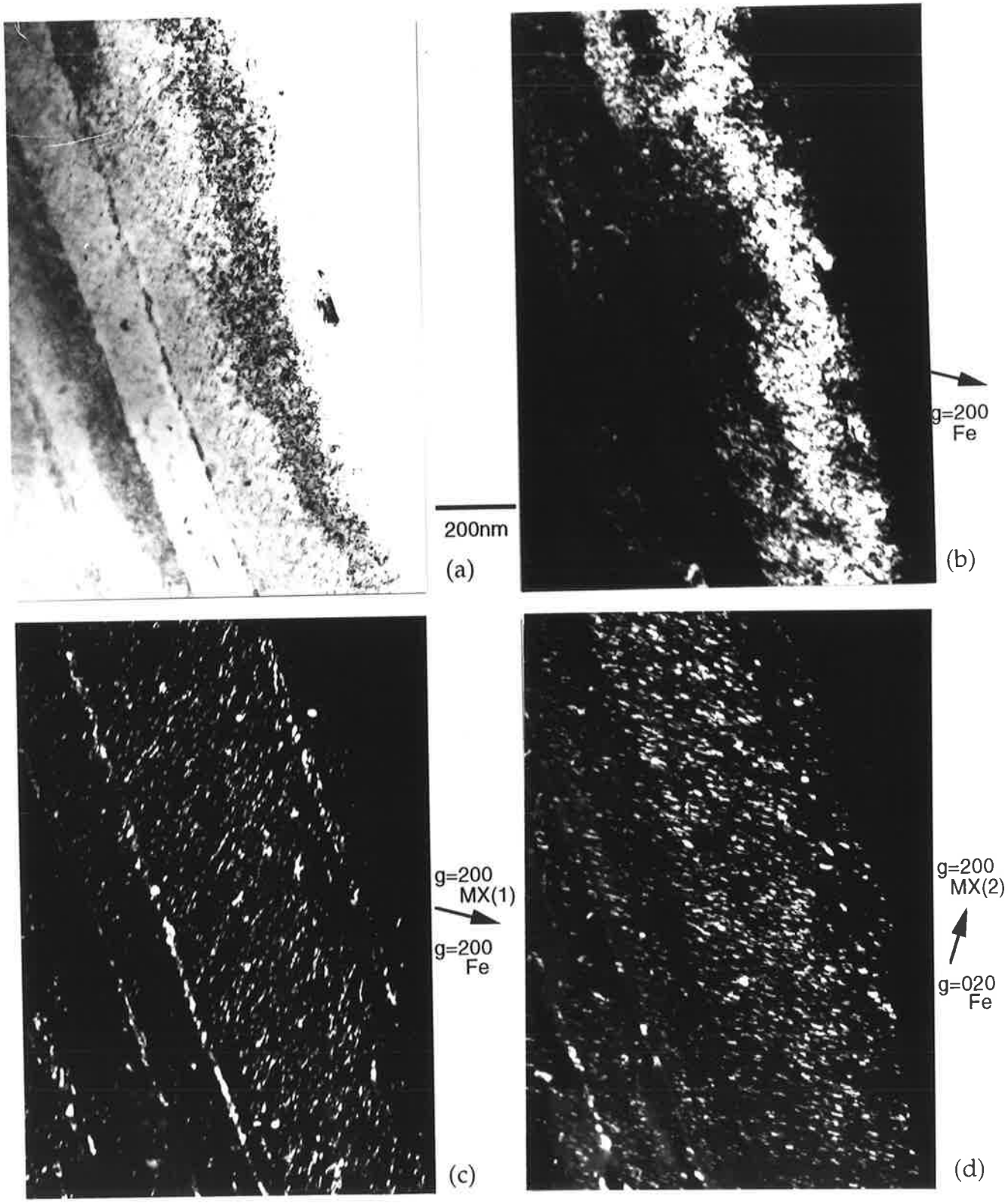

Figure 4.14: 0-100 μm depth: Fine alloy precipitate plates on the {100} α-Fe matrix planes and along some α-Fe grain boundaries (at 15 μm depth): (a) BF; (b) matrix DF; (c) DF of MX plates (set 1); (d) DF of MX plates (set 2), note the 90° angle between set 1 and set 2; (e) SADP from (a); (f) SADP analysis showing both MX and M_2X patterns superimposed on the α-Fe; (g) SADP of (a) tilted slightly off-zone revealing M_2X double diffraction; (h) simulated M_2X double diffraction pattern.

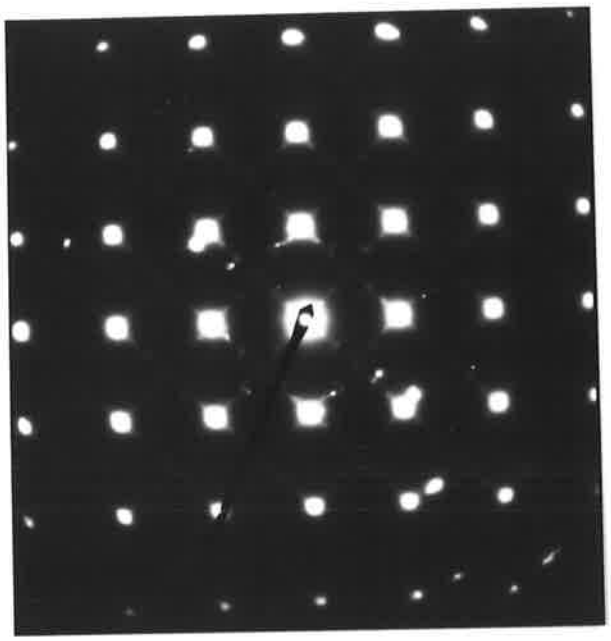

(e)

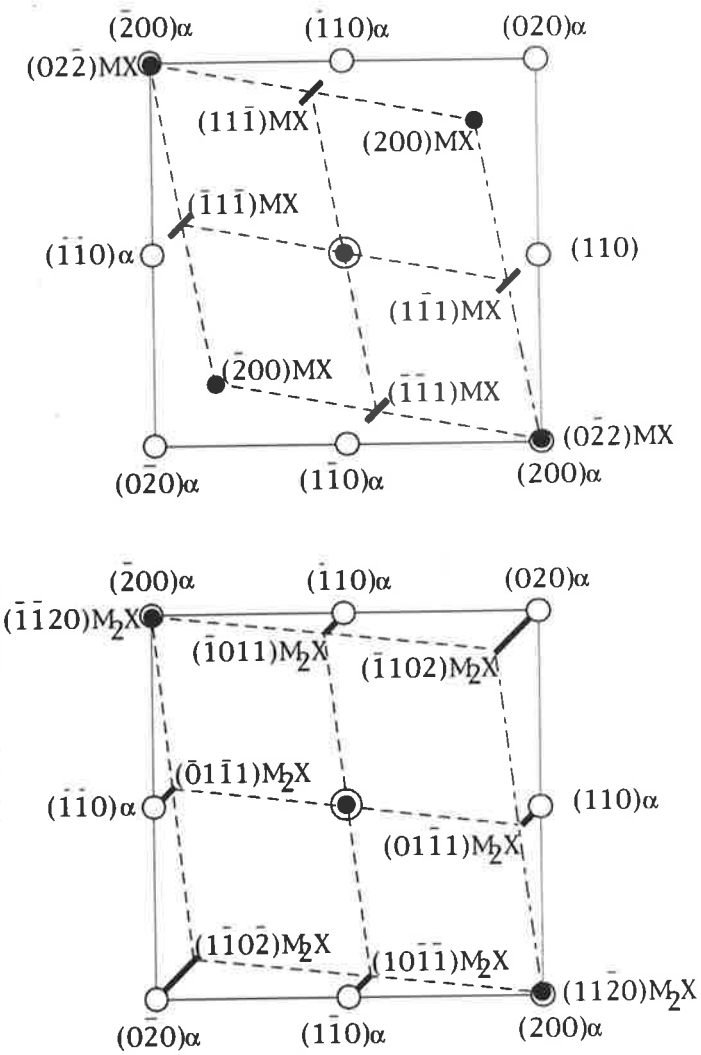
$(\bar{2}00)\alpha$
$(\bar{1}10)\alpha$
$(020)\alpha$
$(02\bar{2})MX$
$(11\bar{1})MX$
$(200)MX$
$(\bar{1}1\bar{1})MX$
$(\bar{1}\bar{1}0)\alpha$
(110)
$(1\bar{1}1)MX$
$(\bar{2}00)MX$
$(\bar{1}\bar{1}1)MX$
$(0\bar{2}2)MX$
$(0\bar{2}0)\alpha$
$(1\bar{1}0)\alpha$
$(200)\alpha$
$(\bar{2}00)\alpha$
$(\bar{1}10)\alpha$
$(020)\alpha$
$(\bar{1}\bar{1}20)M_2X$
$(\bar{1}011)M_2X$
$(\bar{1}102)M_2X$
$(\bar{0}1\bar{1}1)M_2X$
$(\bar{1}\bar{1}0)\alpha$
$(110)\alpha$
$(01\bar{1}1)M_2X$
$(1\bar{1}0\bar{2})M_2X$
$(10\bar{1}\bar{1})M_2X$
$(11\bar{2}0)M_2X$
$(0\bar{2}0)\alpha$
$(1\bar{1}0)\alpha$
$(200)\alpha$

(f)

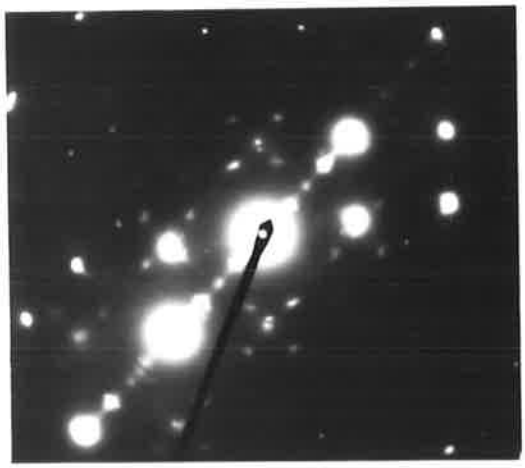

(g)

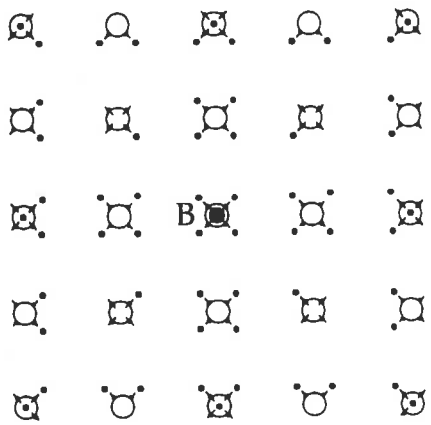
B

(h)

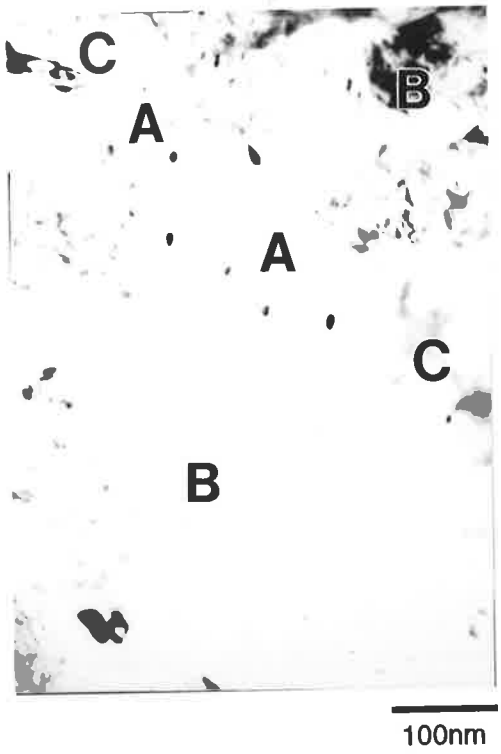

(a)

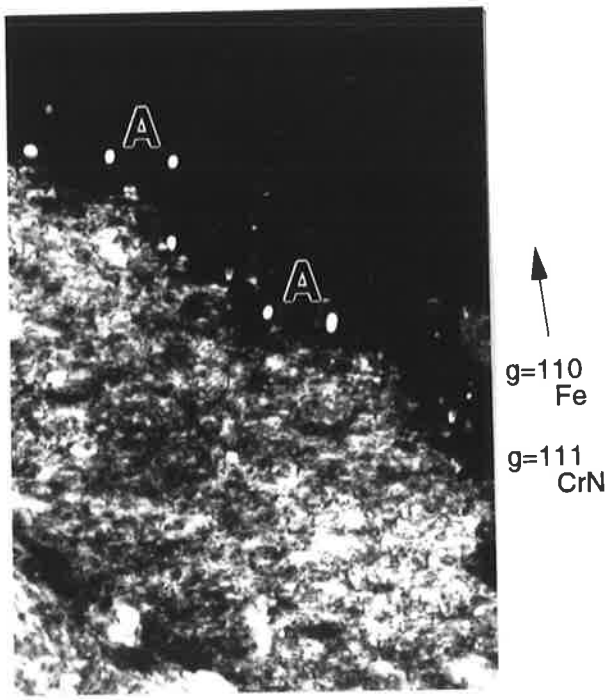

(b)

(c)

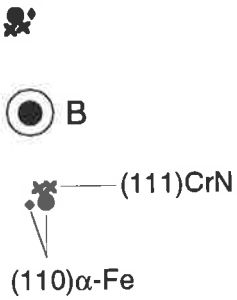

(d)

Figure 4.15: 0-25 μm depth: fine CrN precipitates within the Fe_4N structure. The crystallography of the fine CrN spheroids are consistent with having formed in the adjcent ferrite lath before the matrix transformed to Fe_4N: (a) BF; (b) DF showing both CrN and α-Fe reflections; (c) SADP; and (d) analysis of SADP. A, CrN precipitates; B, adjcent α-Fe matrix; and C, Fe_4N.

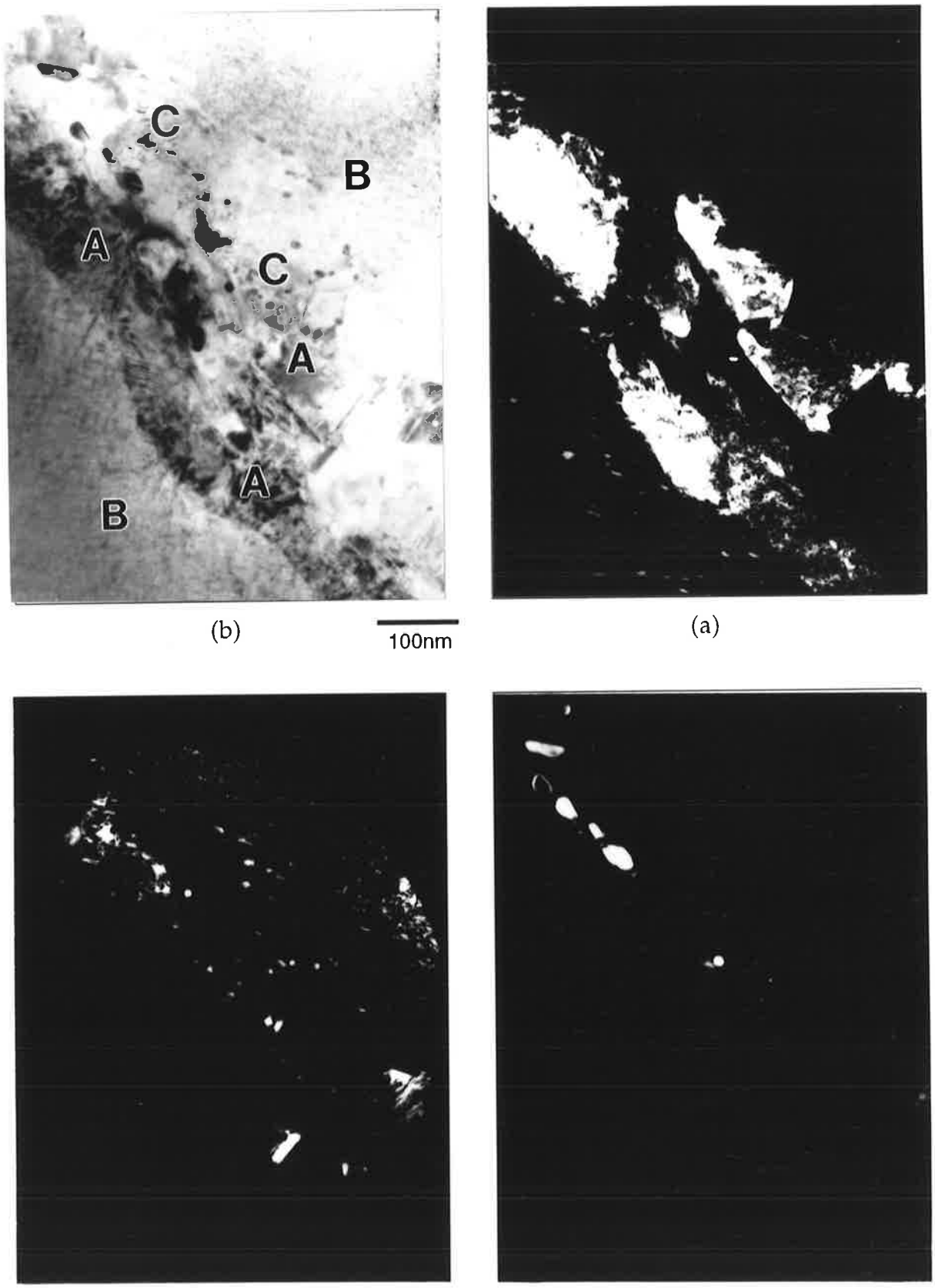

Figure 4.16: 0-25 μm depth: CrN precipitates at 10 μm depth inbetween Fe_4N precipitates: (a) BF; (b) DF of some Fe_4N; (c) DF of a set of fine CrN speroids; and (d) DF of some coarser CrN precipitates: A, Fe_4N; B, ferrite laths; and C, CrN.

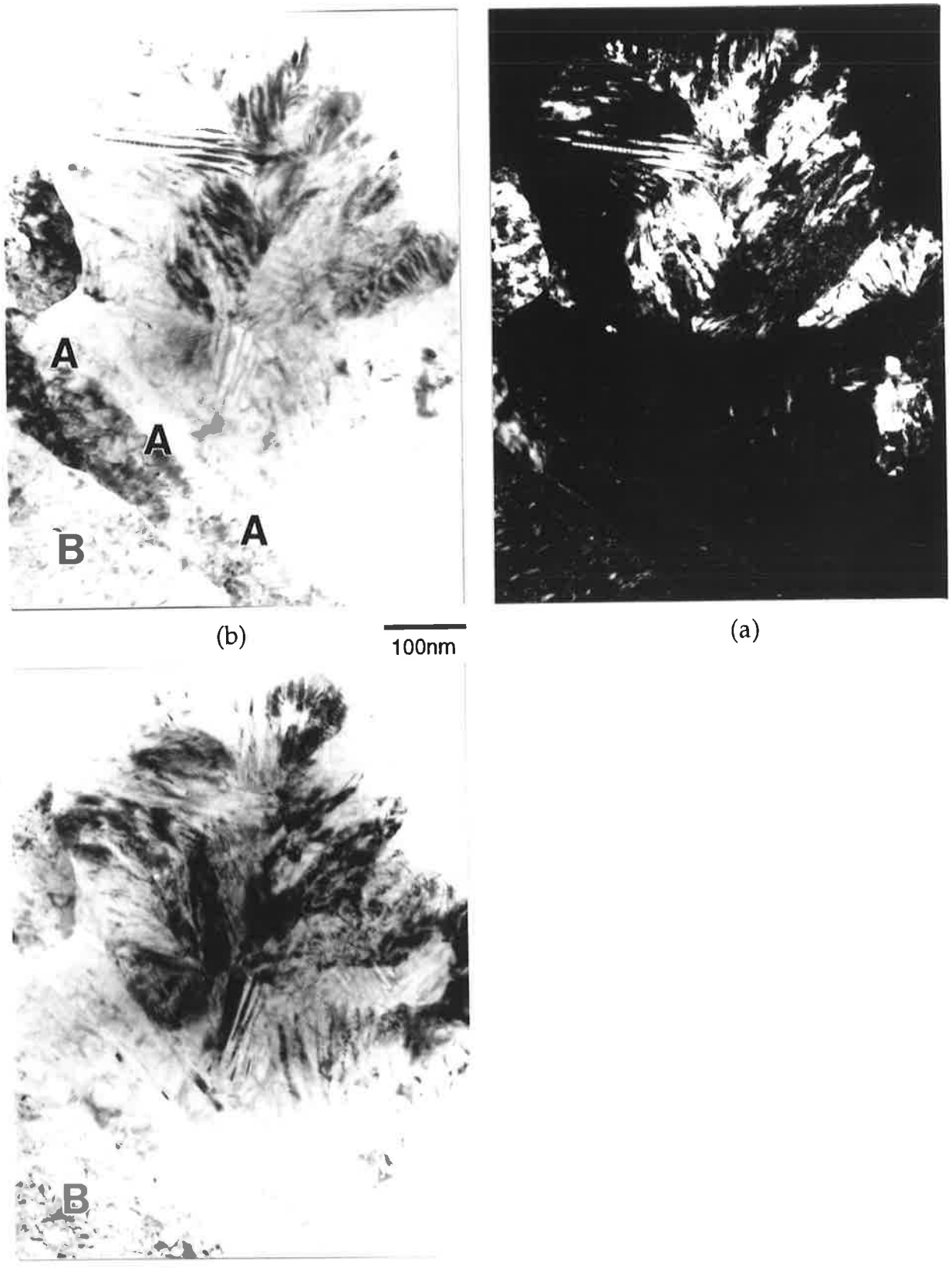

Figure 4.17: 10-40 μm depth: (Cr,Fe)N precipitate at 20 μm depth adjcent to α-Fe laths. Note the complexity in the structure and the similarity of the size and boundary shape to the original primary carbides: (a) BF; (b) DF; and (c) BF with the foil tilted from the orientation in (a): A, precipitate boundary; and B, α-Fe laths.

4.7, and the Reference Substrate Fig. 4.9. The pitted and sometimes perforated shape of these carbides was consistent with chemical attack of the interface which had partly dissolved the carbides.

4.5.4.2 ***Fine Structure:***

Both MX and M_2X precipitates were observed in the matrix (§ 4.5.2.2), but the third precipitate phase, CrN, was not found beyond 20 μm depth.

4.5.5 Zone IV (40 - 100 μm).

4.5.5.1 ***Coarse Structure:***

The size of the primary carbides increased across Zone III towards the reference substrate, Figs. 4.19(b-c), with a corresponding decrease in the level of surface attack, as evidenced by the nature of the carbide/matrix interfaces. Thus, at 120 μm the primary carbides resembled those in the Reference Substrate, *i.e.*, smooth ellipsoidal shapes.

The main feature of this zone was the presence of angular single crystals of θ-Fe_3C, some 200 - 500 nm in size. Sometimes well defined crystallographic relationships could be found in-between the Fe_3C and the adjacent ferrite, Fig. 4.20, e.g., $[110]\alpha_1//[113]\alpha_2//[001]\theta$, confirming that they had formed after the quenching process in the initial heat treatment. At 50 μm depth, Fe_3C was observed as discrete grains mixed with partly dissolved primary carbides, Fig. 4.21(a), both in a loosely spaced groups and in agglomerated sheets, Fig. 4.21(b). These sheets were still found at 100 μm below the implanted layer, but not beyond, and correspond to the coarse bands observed in the light microscope (§ 4.3).

4.5.5.2 ***Fine Structure:***

The MX and M_2X precipitation was observed throughout this Zone, but with a diminishing precipitate density towards the Reference Substrate. Evidence to support this is that deeper into the modified layer, the MX plates became thinner, and the MX patterns superimposed on the [001]α-Fe diffraction pattern became less distinct:

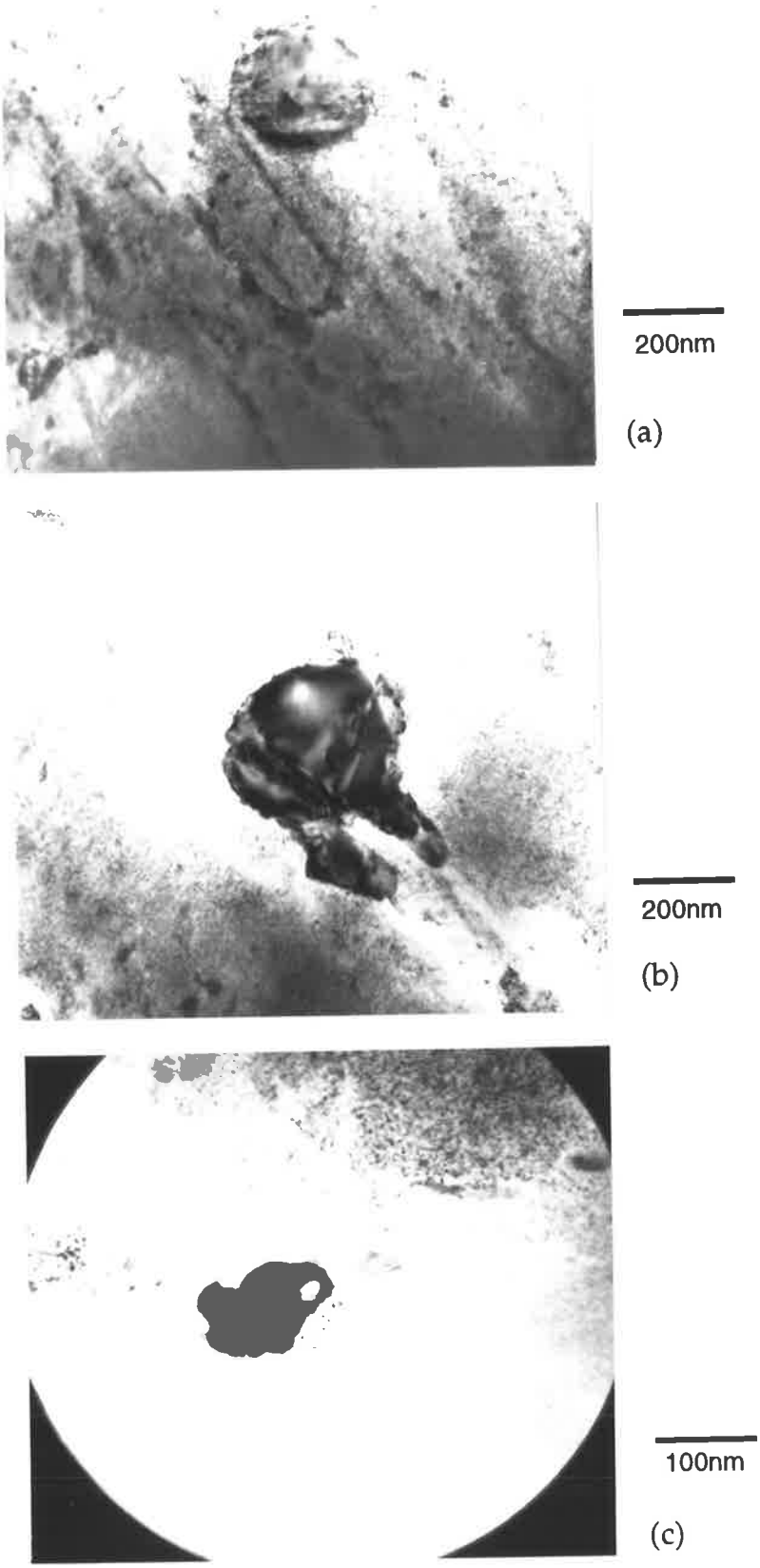

Figure 4.19: $M_{23}C_6$ Primary carbides in the PIII modified layer illustrating their level of dissolution as a function of depth: (a) 100 μm showing slight dimpling of the surface; (b) 50 μm; and (c) 40 μm showing severe pitting.

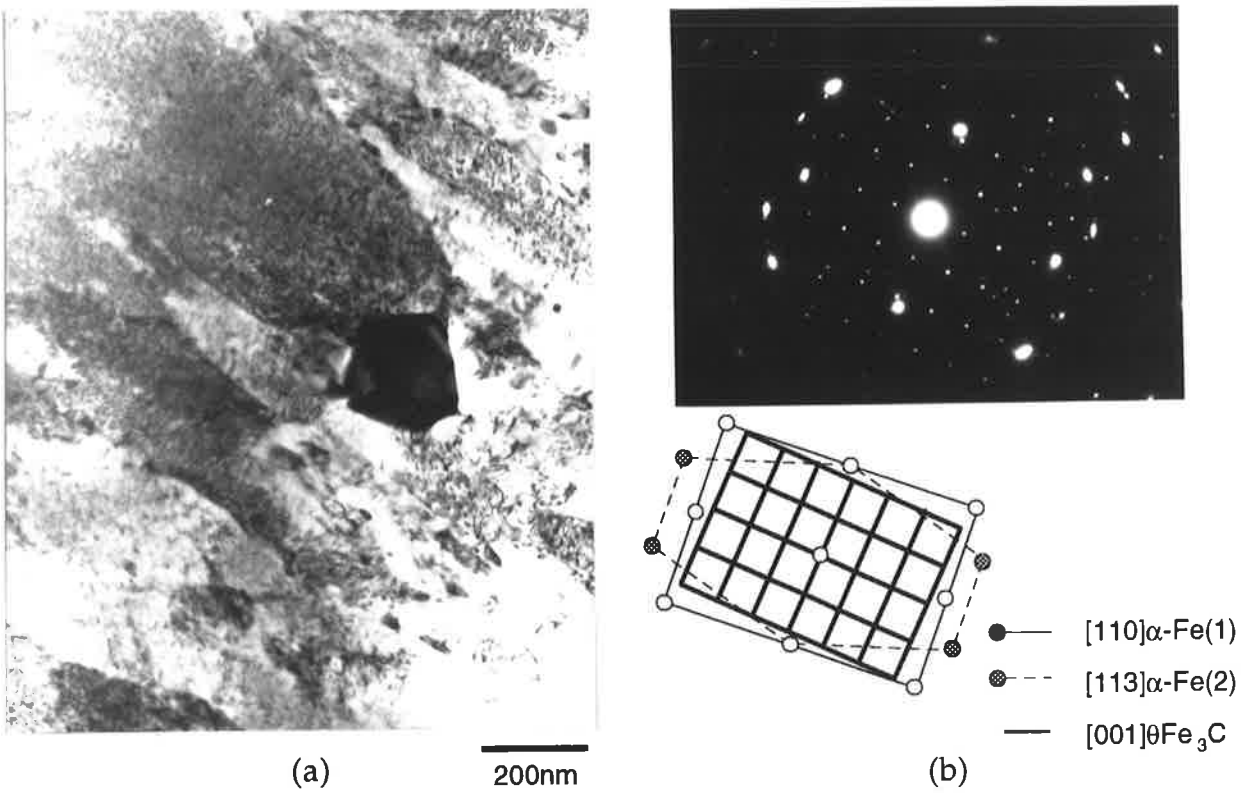

Figure 4.20: Fe_3C crystal at 40 μm depth at a triple-point ferrite grain boundary: (a) BF; and (b) SADP with analysis: two ferrite zones parallel with the carbide zone: A, Fe_3C

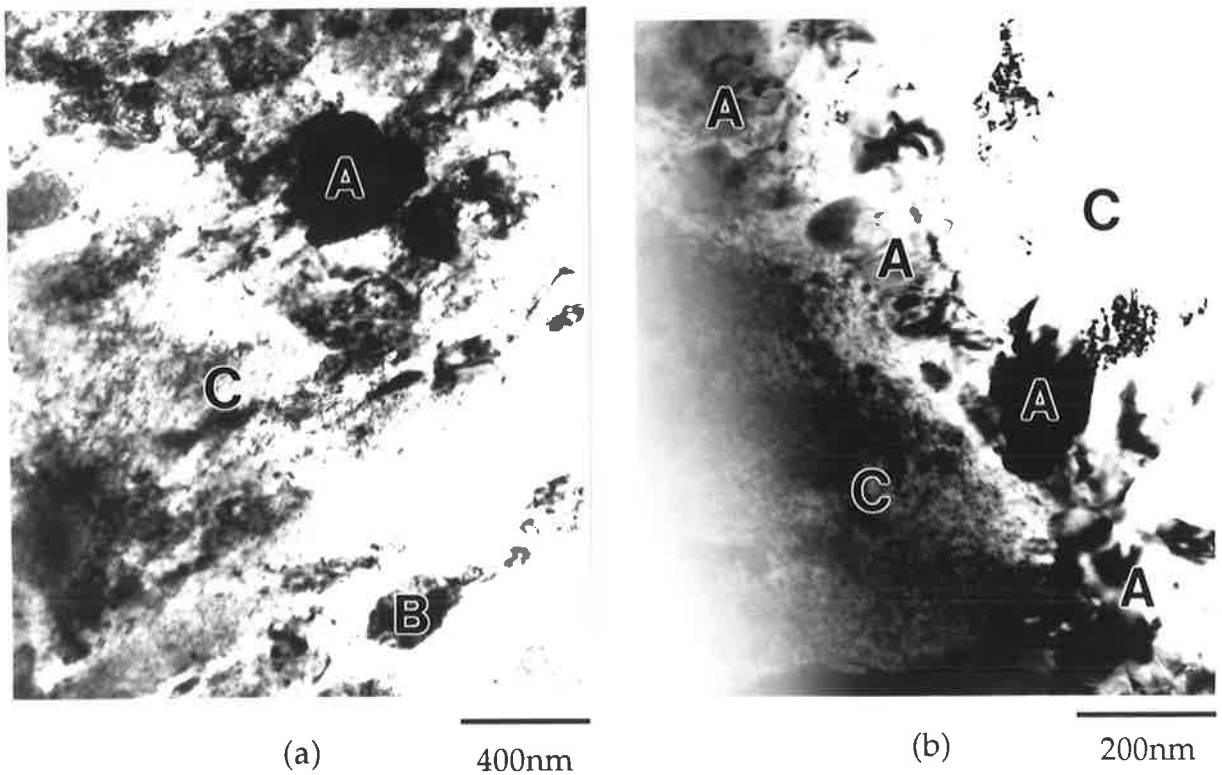

Figure 4.21: Coarse (200-500 nm) Fe_3C precipitation at ferrite grain boundaries: (a) at 50 μm depth showing a mixture of dissolving $M_{23}C_6$ and growing Fe_3C; and (b) at 100 μm depth showing a continuous band of Fe_3C composed of many individual grains: A, Fe_3C; B, $M_{23}C_6$; and C, α-Fe.

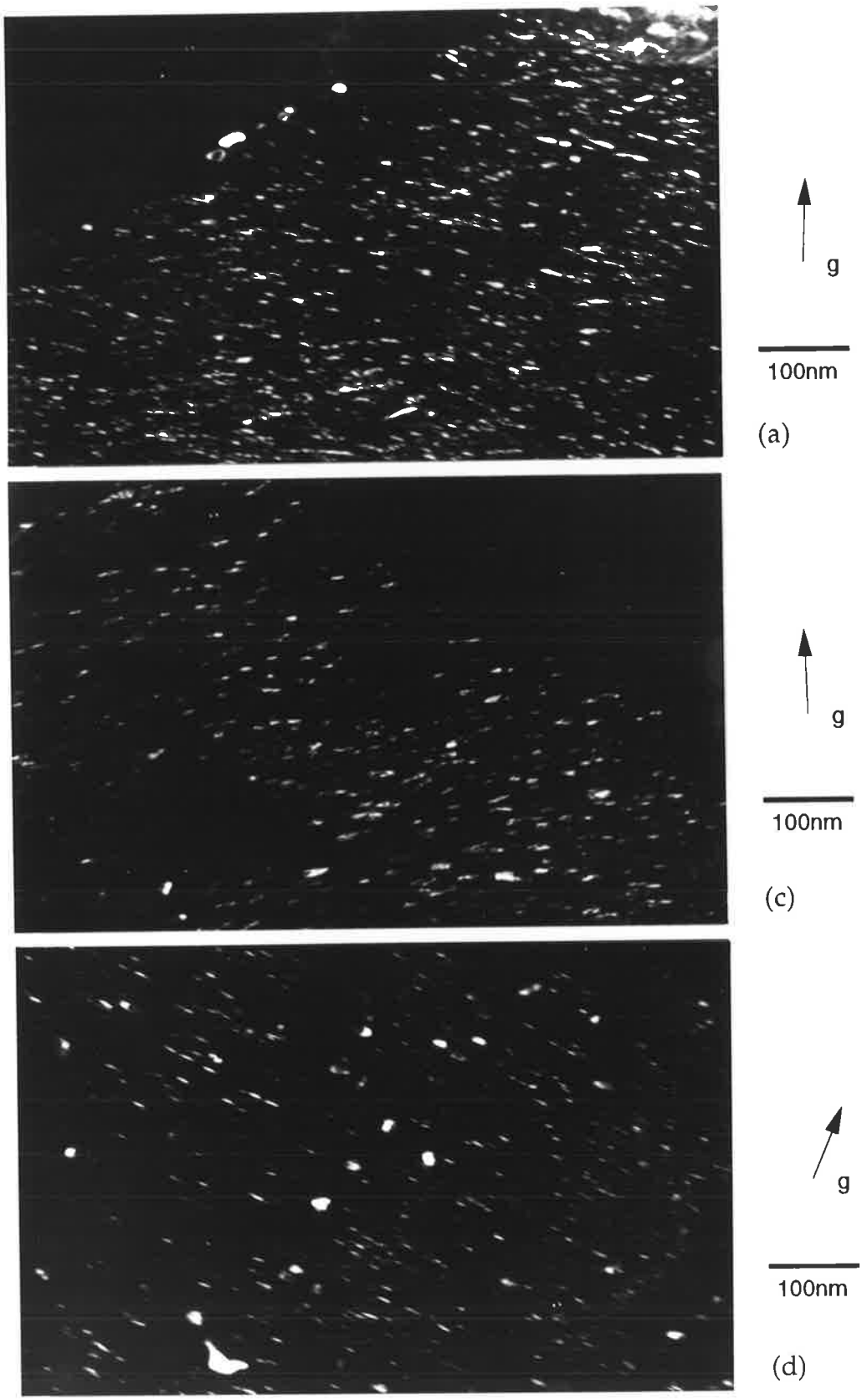

Figure 4.22: Sequence of g=(200)MX dark field images showing the reducing density of the MX precipitates in the α-Fe matrix with increasing depth (recorded under 2 beam conditions with (020)α-Fe and (200)MX diffraction spots): (a) 5 μm; (b) 15 μm (Fig. 4.15 c & d); (c) 35 μm; and (d) 60 μm.

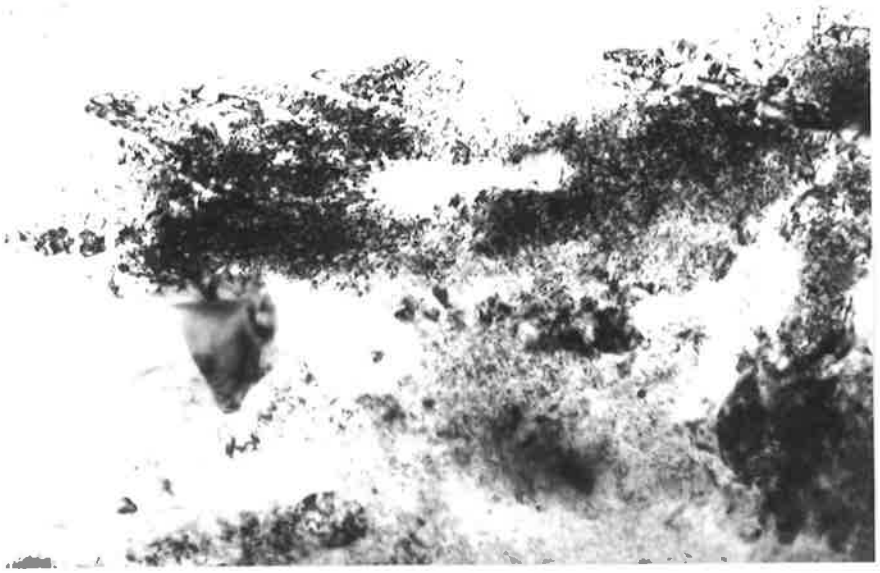

(a)

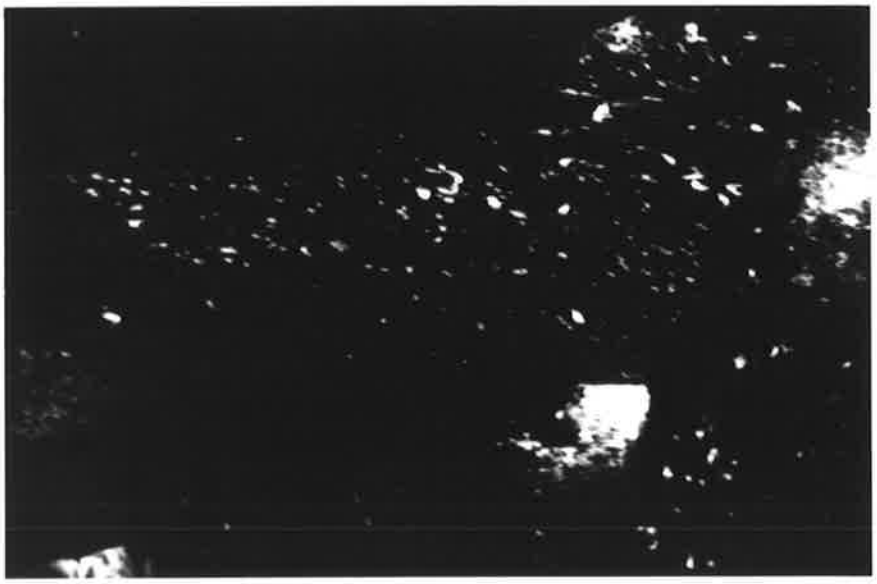

(b)

Figure 4.23: Microstructure at 100 μm depth: primary carbides in an α-Fe matrix containing a mixture of fine alloy plates and Fe_3C lamellae: (a) BF; (b) DF of fine MX precipitates; (c) DF of tempered martensite plate; (d) DF of martensite twin (diffraction conditions were the same as Fig. 4.6); and (e) DF of Fe_3C lamellae at the twin boundaries of the martensite.

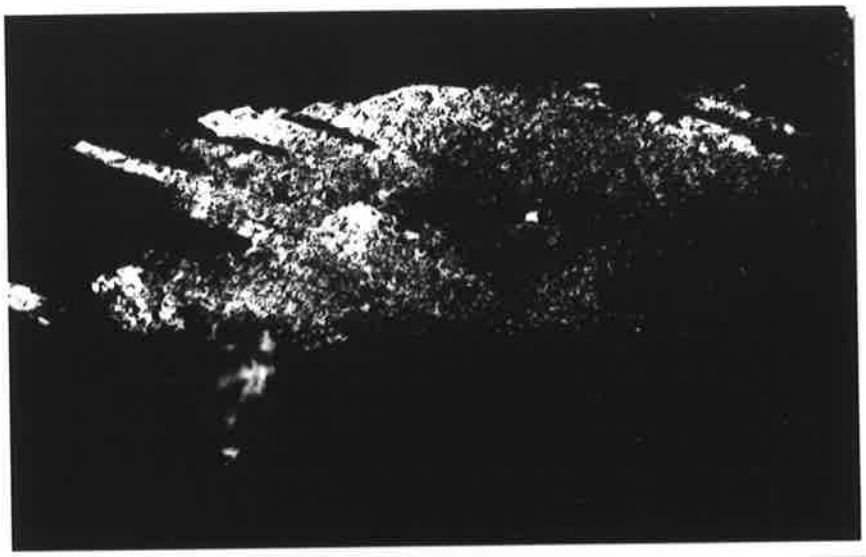

g=(110)MARTENSITE

100nm

(c)

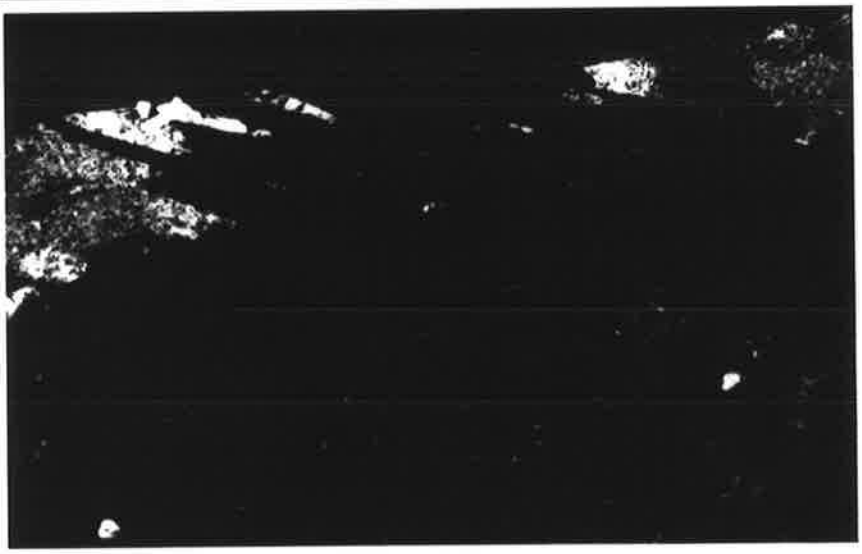

g=(110)TWIN

(d)

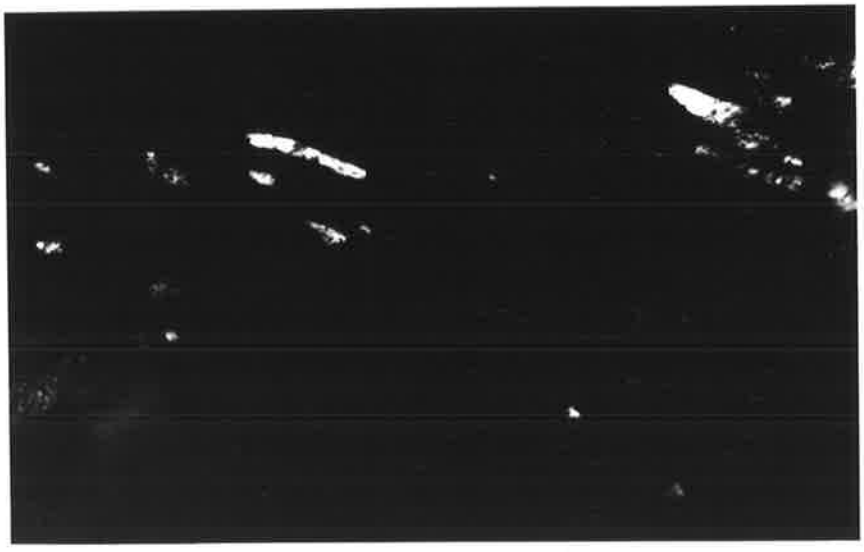

g=(211)Fe_3C

(e)

compare the sequence of plates in Figure 4.22. Double diffraction of the M_2X phase with matrix was still observed.

At 100 μm some 20 nm Fe_3C lamellae, e.g., Fig. 4.9&4.10, were first observed at the internal twin boundaries of the tempered plate martensite, as found in the Reference Substrate, coexisting with some fine alloy carbides in the matrix, Figs. 4.23.

At 120 μm, the 20 nm Fe_3C plates dominated the fine precipitates: no alloy carbides were found, and the microstructure closely resembled the Reference Substrate: Fig. 4.9.

4.6 DISCUSSION.

Four distinct bands were observed in the microstructure of the 353°C PIII treated XW10 steel rod which related to both the density and types of fine precipitates in the matrix as well as the presence and types of larger precipitates between the matrix grains. These bands roughly corresponded to regions in the microhardness-depth profile as summarized in Figure 4.24.

The development of the PIII modified layer is discussed in the following sections in relation to the present TEM observations.

4.6.1 Phase Transformations.

Precipitation, dissolution and matrix transformations occurred across the modified layer involving the long range diffusion of C and N (> 10 μm), and the short range diffusion (< 1 μm) of some metallic elements (Fe and Cr). The level of microstructural change was a maximum nearest the surface (0 - 20 μm), and diminished with increasing depth.

4.6.1.1 *Ferrite Grains/Temperature Effects:*

The apparent grain growth of the lath ferrite (0 - 10 μm) indicates diffusion of Fe atoms substantially greater than expected at 350°C: see Chapter 5. The first impression is that the near surface temperature has been elevated, on average, above the nominal treatment temperature by the energy transfer between the ions and the target lattice.

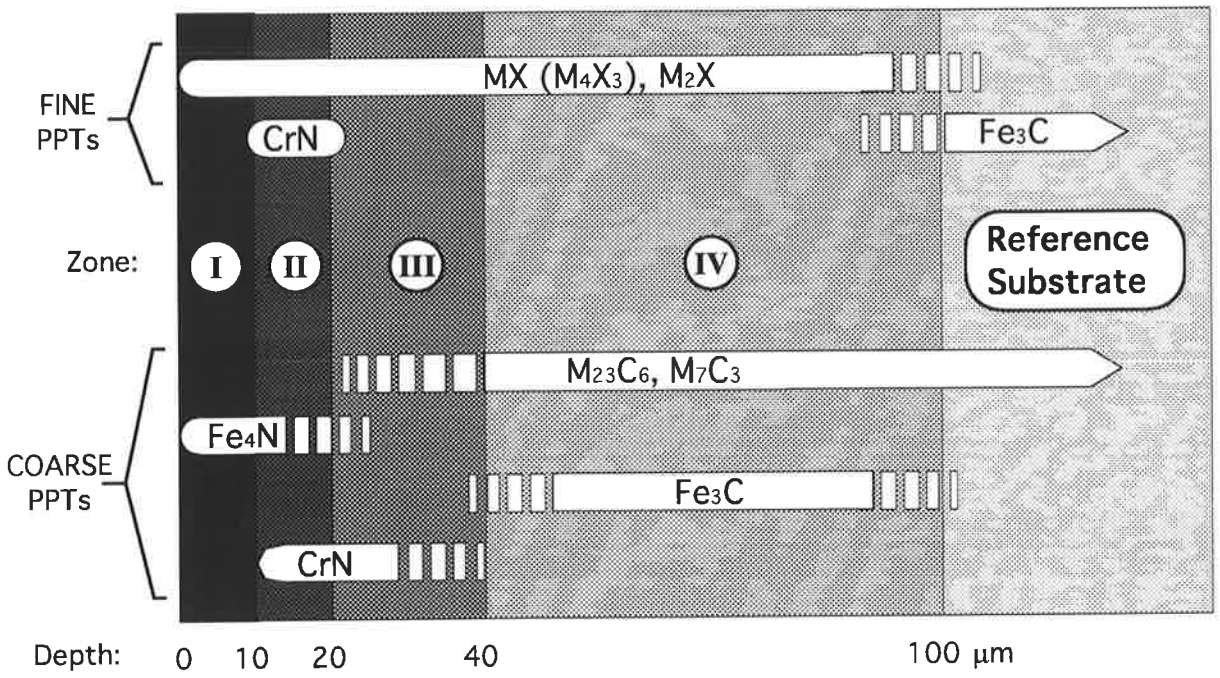

(a)

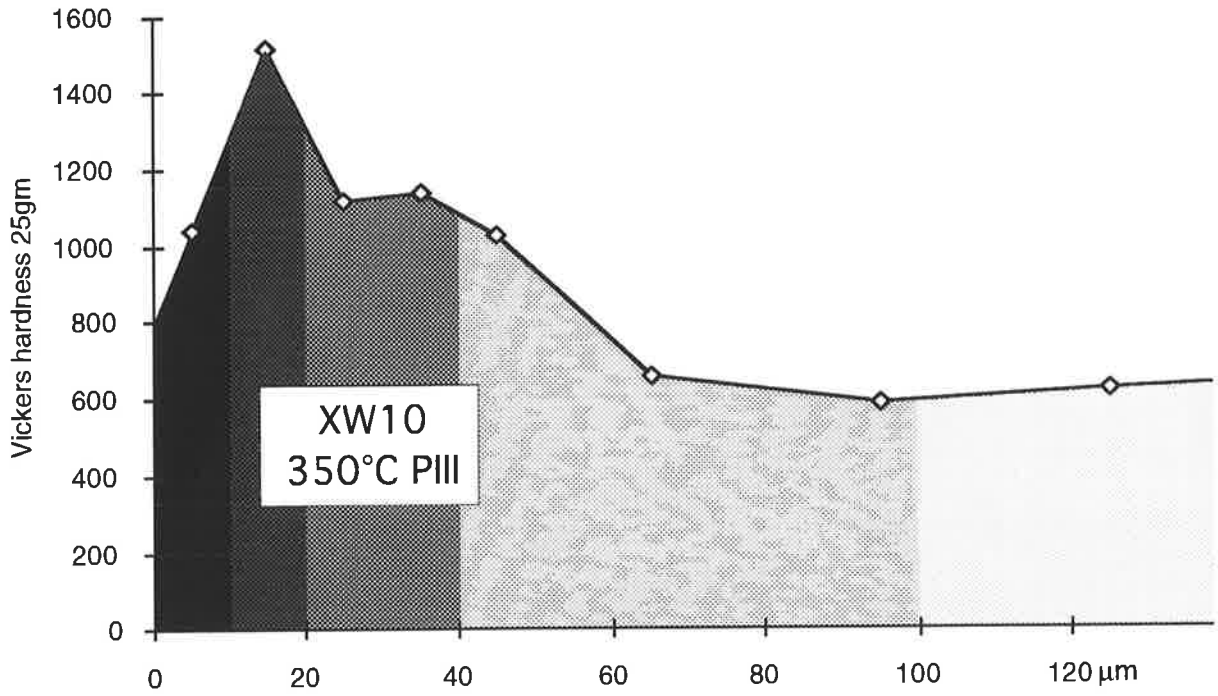

(b)

Figure 4.24: Summary of the microstructural changes with depth beneath the implanted surface of 350°C PIII treated XW10 steel: (a) the precipitate distribution; (b) the microhardness/depth profile.

Analysis of the microstructures across the modified layer provides some evidence of the likely maximum temperatures within the layer, as follows.

Under normal circumstances, the ferrite grain size is determined by the austenite grain size and the distribution of primary carbides prior to quenching in the steel's heat treatment. However, in this PIII treatment, austenite is unlikely to have formed because of two features in the microstructure. First, the {100} α-Fe habit planes of the MX and M_2X platelets (0 - 100 μm) are consistent with precipitation in ferrite. As these precipitates are unlikely to form upon rapid cooling in the near surface layer (0 - 10 μm), e.g., in-between ion pulses or at the end of the PIII treatment, the matrix phase was most likely always ferrite. Note that these platelets will usually coarsen at T>625°C. Second, the orientation relationship of the fine MX precipitates in the Fe_4N (0 - 20 μm) with the adjacent ferrite lath indicates that the Fe_4N gradually consumed the ferrite from its nucleation sites in the lath boundaries: this precludes austenite formation as Fe_4N decomposes upon the formation of nitrogen-austenite at 590°C. This evidence strongly suggests a mechanism causing ferrite grain growth other than austenite formation at elevated temperature.

The microstructure of the Reference Substrate (> 100 μm) is consistent with a 350°C treatment, e.g., the fine Fe_3C plates coarsened instead of being replaced by alloy carbides, which is normally expected at T > 425°C.

Higher near surface concentrations of interstitial elements than found in conventional gas nitriding were deduced from the phase analyses. The role of greater than equilibrium C and N concentrations on the ferrite matrix cannot be disregarded. A possible mechanism for recrystallization is the increase in the defect concentration in the ferrite lattice induced by supersaturation of N and C. This effect is not possible under the equilibrium conditions of gas nitriding, but is clearly possible when nitrogen is continuously and massively injected into the surface with high energy.

4.6.1.2 ***Primary Carbides:***

Two phenomena were observed in connection with the primary carbides: first, dissolution of $M_{23}C_6$ (0 - 100 μm), and second, the apparent transformation of M_7C_3 into Cr-rich nitrides (10 - 40 μm). Since no M_7C_3 carbides were found with the characteristic surface attack observed on the $M_{23}C_6$ carbides, these results suggest that the two original primary carbides responded differently to the ion implantation treatment. This analysis is supported by the higher thermal stability of M_7C_3 during austenitizing treatments. In addition, the final distribution of the metallic elements which dissolved into the ferrite matrix showed that these elements did not appreciably diffuse into the adjacent laths, but diffused along the lath boundaries instead. The fact that metallic elements diffused at all is unusual. Studies on gas nitriding of tool steels (§ 4.2) have reported transformation of the primary carbides to coarse nitrides across a shallow surface band. Therefore, the dissolution of $M_{23}C_6$ is evidently a characteristic of the PIII treatment of this steel which differs from conventional nitriding treatments.

The extent to which $M_{23}C_6$ dissolved was observed to be a decreasing function of depth beneath the implanted surface. This correlates to the form of the concentration-depth profile of the interstitial elements in the modified layer: clearly higher near the implanted surface than found near the gas nitrided surface. Therefore, the most likely cause for primary carbide dissolution was the presence of high concentrations of interstitial elements, cf. § 4.6.1.1.

4.6.1.3 ***Coarse Precipitation:***

Two forms of coarse precipitation resulting from ion implantation were found: large Fe_3C sheets which formed in some of the prior austenite grain boundaries (40 - 100 μm); and small Fe_4N sheets which formed in-between some ferrite laths (0 - 20 μm). Both types of iron-based precipitate sheet was composed of many individual grains suggesting limited nuclei that is a characteristic of grain boundary precipitation for misfitting crystal structures formed by diffusional transformations [60].

The Fe_3C sheets evidently formed because the carbon, initially present in the microstructure, diffused ahead of the introduced nitrogen as a consequence of the high nitrogen concentrations near the rod's surface (§ 4.6.2). Therefore, beyond the diffusion depth of nitrogen, carbon supersaturated in the α-Fe matrix enough to form substantial amounts of Fe_3C. Precipitation in the prior austenite grain boundaries is expected when the ferrite matrix already contains fine alloy precipitates.

On the other hand, the formation of Fe_4N sheets show that there was enough atomic mobility near the surface to avoid the formation of a compound layer (§ 4.2). As such layers often form during considerably longer gas nitriding treatments [34], it is clear that different mechanisms control the microstructural development in the first 20 μm beneath the surface in the 350°C PIII treatment compared to in the 500°C gas nitriding treatment. In the PIII treatment of type H13 tool steel, Hutchings *et al.* [3] reported the formation of a ε-Fe_2N_{1-x} compound layer at 350°C, although over a very shallow depth (~1.5 μm). Note that during gas nitriding treatments, the formation of a compound layer can be suppressed completely by reducing the surface nitrogen activity in the latter part of the treatment, *i.e.*, decreasing the partial pressure of NH_3 in the NH_3/H_2 mixture. No such precautions were taken during the PIII treatment. So, the mechanism responsible for this unusual characteristic of the PIII process is evidently related to the mechanism that caused the grain growth in the 0 - 10 μm layer.

In the present studies, relatively large Fe_4N precipitates were found that had surrounded fine alloy (Cr, Mo, V) precipitates. The γ′-Fe_4N phase has been identified in various nitrogen implantations into pure iron. Using CEMS (Chapter 2), Kopcewicz *et al.* [46] showed that for pure α-Fe implantated in the 350 - 400°C temperature range with high doses (> $6x10^{17}$ at/cm^2), γ′-Fe_4N is a stable precipitate. The present results confirm this observation. The fact that γ′-Fe_4N surrounded the fine alloy precipitates that were actually coherent with the adjacent α-Fe matrix, shows that the γ′-Fe_4N precipitated only after the more thermodynamically stable nitrides has precipitated first. This is the reverse of the situation found at 100 μm depth where θ-Fe_3C had precipitated in

preference to the alloy carbides and shows that ion implantation has unusual effects in the modified layer nearest to the surface.

4.6.2 Interstitial Diffusion.

The formation of coarse nitrides near the implanted surface and coarse carbides away from that surface indicate that carbon diffuses ahead of the high near-surface concentrations of nitrogen. This effect is consistent with previous reports [7,61] who reported inverse carbon concentration gradients ahead of nitrogen diffusion profiles. In this sense, PIII treatment, under these conditions, causes similar effects to gas nitriding treatments done at much higher temperatures. These observations suggest that the fine alloy precipitates will have a higher nitrogen than carbon concentration close to the surface, and the reverse towards the Reference Substrate.

A consequence of the Fe_3C-sheet precipitation is that the path for nitrogen diffusion would have been gradually blocked since the diffusion rates through carbides and nitrides is generally low [34]. This could possibly explain the formation of Fe_4N in the 0 - 20 μm layer, *i.e.*, nitrogen concentrations would have continued to increase in that layer after Fe_3C sheets "insulated" the 20 μm boundary, leading to N-rich precipitate formation.

The homogeneous precipitation of alloy nitrides or carbonitrides in the ferrite laths would also have the effect of "choking" the diffusion path for implanted nitrogen. This could also explain why Fe_4N formed in the lath grain boundaries, e.g. from nitrogen supersaturation, and suggests that extending the implantation treatment time could make the steel's surface susceptible to compound layer formation.

4.6.3 Explanation of the Peak Hardness.

The preceding section described the effects of higher than equilibrium N-concentrations and near surface effects on the quenched and tempered microstructure during PIII treatment.

As with 500 - 550°C conventional nitriding (§ 4.2), the primary hardening mechanism of the 350°C PIII treatment is precipitation hardening by fine platelets of MX (M_4X_3) and M_2X within the ferrite laths. This can produce a maximum hardness of 1000 - 1200 HV under optimal conventional nitriding conditions. The extra hardening observed in the PIII modified layer (10 - 20 μm) seems to be associated with two additional mechanisms: the precipitation of a third finely dispersed precipitate (CrN) in-between the MX (M_4X_3) and M_2X platelets in the ferrite laths, and the inter-lath precipitation of Fe_4N. The microhardness of γ'-Fe_4N with varying carbon content has been found by Levy *et al.* [62] to be in the range 485 - 565 HV_{50g}, corresponding to 2.8 - 0.01 at% C substituted for the N. However, the presence of 10 at% Cr, the small γ' grain size and the finely dispersed MX (M_4X_3) precipitates in the γ' grain boundaries would significantly harden these Fe_4N sheets.

The reduced hardness in the near-surface region (0 - 10 μm) seems to be a result of grain growth of the ferrite laths.

4.7 CONCLUSIONS.

From the surface to depths of up to 20 μm, the microstructural changes in the PIII modified layer are in excess of those occurring in conventional nitriding treatments at 500°C, while at depths greater than 20 μm, the changes are comparable to nitriding treatments at 500°C. The features of the surface of the PIII treated steel can be characterized by five microstructural changes:

1. A redistribution of the alloying elements within the ferrite grain boundaries from coarse $M_{23}C_6$ primary carbides to coarse inter-lath Fe_4N (0 - 10 μm);
2. The transformation of M_7C_3 primary carbides into coarse (Cr,Fe)N (10 - 40 μm);
3. Coarse precipitation of Fe_3C in the prior austenite grain boundaries (40 - 100 μm);
4. Increases in the of C and N contents to a depth of 100 μm;
5. The gradual dissolution of fine Fe_3C precipitates within the ferrite matrix that were replaced by fine MX (M_4X_3) and M_2X precipitates (0 - 100 μm) and later fine CrN precipitates (0 - 100 μm) that were all partly coherent with the matrix.

These changes appear to have been principally caused by high nitrogen concentrations not achievable in conventional nitriding treatments. Strong microstructural evidence indicates that the conventional mechanism, e.g., elevated temperature, likely to have caused the dramatic changes found in the 0 - 20 μm layer, could not have occurred.

It is clear that in the PIII treatment, the mobility of nitrogen near the surface is high enough to avoid compound layer formation, although Fe_4N forms in-between the tempered martensite laths close to the surface (0 - 10 μm).

Chapter 5

MATHEMATICAL MODELLING OF THE PIII PROCESS

5.1 INTRODUCTION.

In the previous chapter, the microstructural features of the PIII modified surface layer of a rod implanted at 350°C have been described. It would seem difficult to explain a number of these features solely in terms of the nitrogen addition to the Fe lattice and grain boundaries, particularly the matrix grain growth and dissolution of primary carbides found in the first 10 μm beneath the implanted surface. Both of these effects indicate an elevated atomic diffusion coefficient of metallic atoms in the near surface region. Previous studies have suggested two possible mechanisms which can elevate the local diffusion coefficient of metallic atoms in a metal lattice during ion bombardment: vacancy production, and target heating [15].

The injection of N_2^+ ions into a metallic surface during PIII occurs in discrete 50 μs pulses, during which time one N_2^+ ion will deposit into each 66 nm^2 of the specimen surface and will penetrate to a maximum depth of 80 nm. Under the implantation conditions used in the present experiment, the pulses are separated by a time interval of 28521 μs (1/35 s) during which no N_2^+ enters the surface. This cycle is repeated ~200,000 times during a typical surface treatment (3.2 hours).

The physical processes that occur within the implanted layer resulting from the impact of energetic ions with the target material are generally well understood (Chapter. 2). This has lead to the development of reliable mathematical models which predict the changes in the near surface region caused by low temperature/low dose ion

implantation into homogeneous materials, e.g., TRIM [63]. Due to the inability of such models to account for the effects found in high temperature/high dose implantation such as precipitation, radiation and diffusion effects, other models have been formulated to simulate these effects, e.g., IMPL [44]. Naturally, these models are much more computationally demanding and require specialized computer hardware to simulate long treatment times and large diffusion depths. Furthermore, the degree of microstructural complexity in the original target material, and the thermodynamics required to describe precipitation in such an alloy once again increase the computational requirements. Thus, the large diffusion depths achieved by nitrogen in the present PIII treatment, the discontinuous nature of the implantation, and the complexity of the initial microstructure and subsequent microstructural changes in the steel prevent the holistic approach permitted by these models to be undertaken here.

Nevertheless, the likely conditions under which the PIII modified layer formed in this treated XW10 steel rod can be approximated by separating the mechanisms of thermal diffusion and atomic diffusion. Thus, as a first approximation, separate studies were made of the transient heating of the rod's surface, the pseudo-steady-state temperature variations along the rod, the likely accumulated damage to the target lattice caused by vacancy production, and the depth of nitrogen diffusion expected by conventional (Fick's) diffusion at the nominal treatment temperature of 350°C. To predict the instantaneous near-surface distributions of energy, nitrogen atoms and vacancies produced in the target lattice as inputs for further modelling, TRIM '90 simulations were made. To account for variations in the chemical composition in the implanted surface, the extreme compositions observed in the TEM studies were simulated.

A mathematical model of transient diffusion of heat or interstitial atoms was developed to simulate the instantaneous changes in the temperature and nitrogen concentration within the implanted rod during cyclic ion pulsing. The model was based on linear one dimensional Fick's diffusion, with the spread of ion energy release or nitrogen with depth treated as an internal source (described by TRIM [63]

calculations). In order to include this heat or atom source in a efficient numerical technique, a Boundary Element Method (BEM) [64] was adapted and a Fortran program written. Using this model, not only were the temperature variations estimated, but also, the limits of conventional diffusion of nitrogen were explored. The overall temperature distribution within the rod was simulated by a standard numerical solution to steady-state heat transfer problems. The significance of the vacancy concentration on the diffusion coefficient of metallic atoms was estimated from the accumulated concentration of vacancies within the target lattice.

5.2 EXISTING MODELS.

A number of mathematical models have been formulated to describe the ion implantation process into solid surfaces. Without exception, these models are solved numerically. Because there are additional physical processes which occur during high temperature and high dose implantation, low dose and temperature implantation is discussed separately. Some empirical surface treatment models are also included in a later section for comparison.

5.2.1 Low-Temperature/Low-dose Ion Implantation Models.

Various models deal with low temperature, low dose implantation into amorphous targets of fixed composition, e.g., MARLOWE [65], TRIM [63] and TRYDIN [66], while others consider the consequences of crystallinity on ion chanelling, e.g., Koponen *et al.* [67], and treat layered targets, Webb *et al.* [68]. Of these models, TRIM is perhaps the best known, and is frequently used to generate input data for more complicated implantation models [63]. TRIM models the implantation process by simulating individual ions as they collide with the target atoms and through "Monte-Carlo" calculations finds the distributions with the depth below the target surface of, ion range and lateral spread, ion energy loss, vacancy production, and ionized target atoms. Other parameters found are the sputtered target atoms and back-scattered ions as percentages of the total ions implanted.

5.2.2 High-Temperature/High-dose Ion Implantation Models.

As the current implantation is performed at temperatures above which significant diffusion of N occurs, of all the mathematical model describing the ion implantation process, TAMIX [33] and IMPL [44] are the most closely related to the current problem.

TAMIX incorporates RED and RIS by following the production, diffusion and removal of vacancies and interstitials, in addition to calculating the diffusion and segregation of solute atoms. The vacancies and interstitials are produced in the implanted zone, diffuse away from the high concentrations and are lost at dislocations or combine with each other to form defect clusters and eventually voids. Interstitials are also lost when they segregate with matrix atoms. The target is considered to contain a fixed dislocation density but no metallurgical information is included, such as matrix and precipitate grain sizes, shapes and orientations. Furthermore, no precipitation effects are accounted for.

IMPL [44] on the other hand, includes the equilibrium thermodynamics of precipitation, e.g., the solubility product and stoichiometry of one nitride, Fe_2N. The researchers also include RED, RIS, radiolytic decomposition of precipitates and the removal of defects at dislocations. Thermal diffusion is also included, although from what heat source is unclear.

Rangswamy *et al.* [69] have also developed an algorithm to include defect production and mobility.

5.2.3 Models of Conventional Case Hardening Processes.

A number of models have been proposed to describe the traditional case hardening processes of carburising and nitriding of metallic substrates [70]. These have been based on Fick's diffusion of the interstitial elements and, in some cases, the metallic alloying elements. In more recent models, precipitation effects have been incorporated to account for the reduction in concentration of the interstitials. In these traditional surface treatments, mass diffusion and precipitation occur in an

equilibrium fashion at constant temperature, e.g., there is a relatively small surface flux of C or N and their diffusivity is high enough not to create large concentration gradients near the surface. Furthermore, the precipitation kinetics are much faster than the diffusion process, so that precipitate formation is essentially in equilibrium and hence can be modelled by thermodynamics, e.g., Bongartz *et al.* [71].

In addition to these numerical simulations, several empirical models [7] have been constructed for particular materials and treatments over ranges of time, temperature and surface concentration of nitrogen.

5.2.3.1 ***Case Depth Calculations:***

Some researchers have recently developed empirical equations to predict the case depth and surface hardness achieved after ion nitriding of several commercial tool steels, from the treatment time, the temperature and the surface nitrogen volume fraction. Ozbaysal *et al.* [7] have done this for H13 steel, amongst others, and their equations are repeated below:

$$(\text{case depth})^2 = 3212.47 P_{N_2} t - 20613.68 t + 28.54 Tt + 72.03 T - 48759.48 \qquad 3.1$$

$$\text{surface hardness} = -0.86 t^2 + 93.86 t - 0.11 Tt - 3.51 T P_{N_2} + 2579.5 P_{N_2} + 1162.06 \qquad 3.2$$

where the temperature, T, is in degrees K; the time, t, in hours; the case depth in mm; the surface hardness in Vickers units, kg/mm^2; and P_{N_2} denotes the volume fraction of N at the surface.

For some form of comparison between conventional nitriding processes and the PIII treatment, the two equations above have been extrapolated below 440°C to estimate the surface volume fraction of nitrogen in the 350°C PIII H13 specimen, assuming that the temperature of implantation is the unknown. The measured case depth and surface hardness were used to predict the nitrogen V.F. as the temperature was varied, producing the curves shown in Fig. 5.1: the dotted lines represent a 10% tolerance on the measured hardness and case depth. It is interesting to note that the curves intersect at a volume fraction of precisely 1.0, with a corresponding temperature of 382°C. These values are within reasonable limits knowing that the PIII process

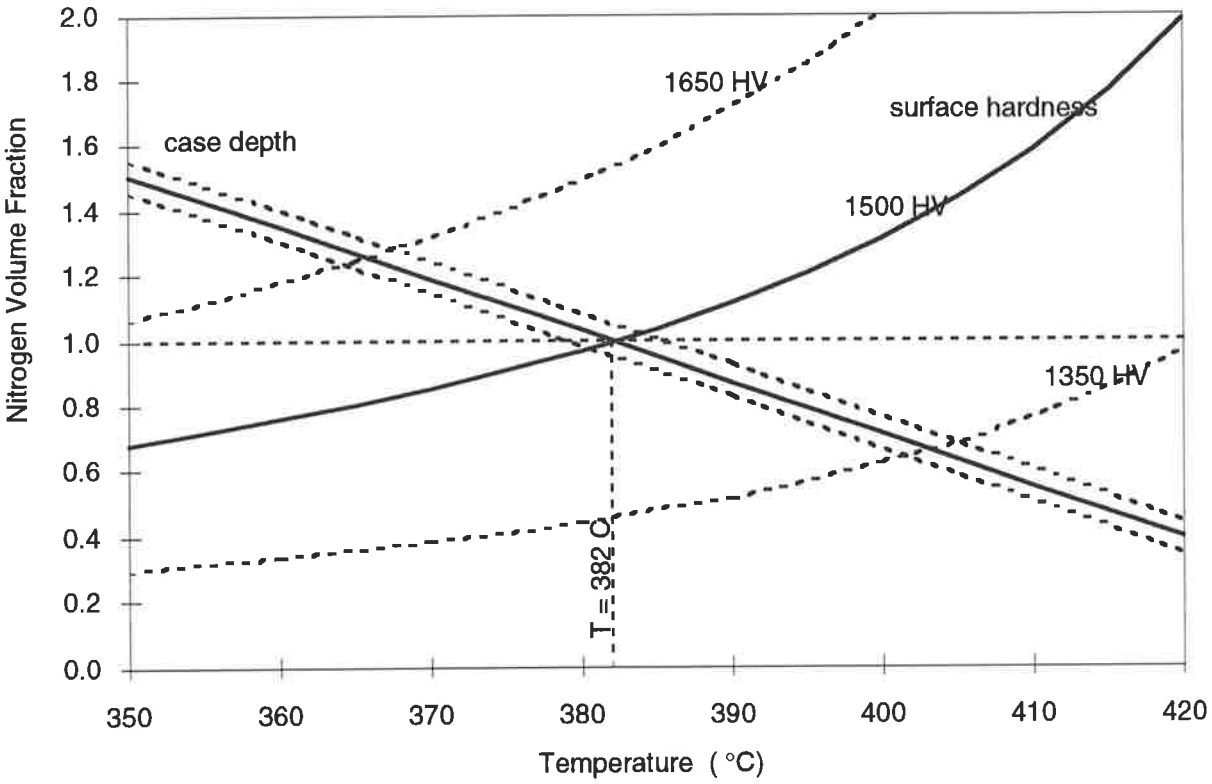

Figure 5.1: Prediction of the process temperature in the PIII of H13 steel from empirical equations derived from ion nitriding of the same steel. Dotted lines represent ±10% tolerance on the case depth and the peak hardness. Note that a volume fraction on the surface of the steel that is >1.0 is meaningless.

involves the direct injection of nitrogen into the surface, rather than letting equilibrium occur between the gas mixture and the inward diffusion of N in the metal as in ion nitriding. Furthermore, the predicted temperature is within 32°C of the nominal value.

5.2.4 Limitations of Existing Models in Describing the PIII Process.

The low-temperature/low-dose models take no account of accumulated implantation effects, such as alterations in the material properties as the target composition changes, or precipitation and radiation effects. When some or all of these effects are included, high-temperature/high-dose simulations can be made, but several important factors are still missing to model the current PIII treatment. None of the existing models can deal with either the temperature gradients induced by pulsed atom fluxes or the large diffusion depths achieved in PIII. Moreover, they cannot adequately describe precipitate growth and atomic diffusion through the fields of fine precipitates which exist in precipitation hardening steels. Lastly, grain boundary diffusion is not allowed for. The present TEM observations of the 350°C PIII treated XW10 steel indicate that diffusion path of the nitrogen and carbon is likely to have been mainly along the ferrite grain boundaries where the highest concentrations of C and N were found, *i.e.*, in carbides and nitrides. This is consistent with the low solubility of these elements in ferrite at this temperature. If this is the main diffusion mechanism, then the assumption that all of the above models make about the implanted material being isotropic with no metallurgical structure, is not valid for this PIII treatment.

Thus, none of the existing models can account for all of the significant mechanisms which cause the development of the current PIII treatment of XW10 steel.

5.3 TEMPERATURE VARIATIONS WITHIN THE SPECIMEN ROD.

As the energetic ion pulses are the main form of heating of the target and as the diffusivity of nitrogen in ferrite is strongly dependent on the local temperature, it is important to calculate the target temperature variations in space and time. Persisting surface temperatures above the temperature of the core of an implanted object which

occur as a result of pulsed surface treatment have been suggested by Worzala *et al.* [15] in PSII experiments.

The physical situation to model is cyclic surface heating/equilibrating of a 2 mm diameter rod from ion pulses, Fig. 5.2, with the geometry of the specimen given in Fig. 5.3. The heating is due to the release of energy as 50 kV N_2^+ ions slow down during collisions with target atoms. As such, the energy given to the target is spread over a shallow depth beneath the surface: TRIM calculations [72] predict that the maximum penetration of the ion energy will be ~80 nm (Appendix 5). Nevertheless, the relatively slow pulse frequency compared to the rapid ion pulses (35 Hz vs. 50 μs pulses) implies that most of the time the temperature will be equilibrating.

During the PIII treatment, the mean target temperature is set by modulating the pulse frequency, while maintaining constant pulse energy and duration. Under these circumstances, the energy input to the rod's surface by the ion pulses is balanced by the radiative heat loss from the blocks at the rod ends through conduction within the whole assembly. This thermal equilibrium is typically reached within 10 minutes of commencing the implantation [14] as measured by infra-red pyrometry of the blocks (Chapter 2). However, the temperature profile within the rod has not been measured due to the uncertainties in estimating the radiative parameters of a low emmissivity polished metal surface.

For the ion implantation of semiconductor wafers, Albaugh *et al.* [73] were able to model the target temperature exclusively by radiative heat transfer (necessarily with emmissive parameter estimates). However, conduction is likely to be a major form of heat transfer in the current problem.

Modelling of the time dependent temperature profile within the rod was undertaken. By superposition, transient conduction across a thin layer on the rod's surface were separated from steady state conduction through the whole assembly: § 5.3.1 and § 5.3.2 respectively.

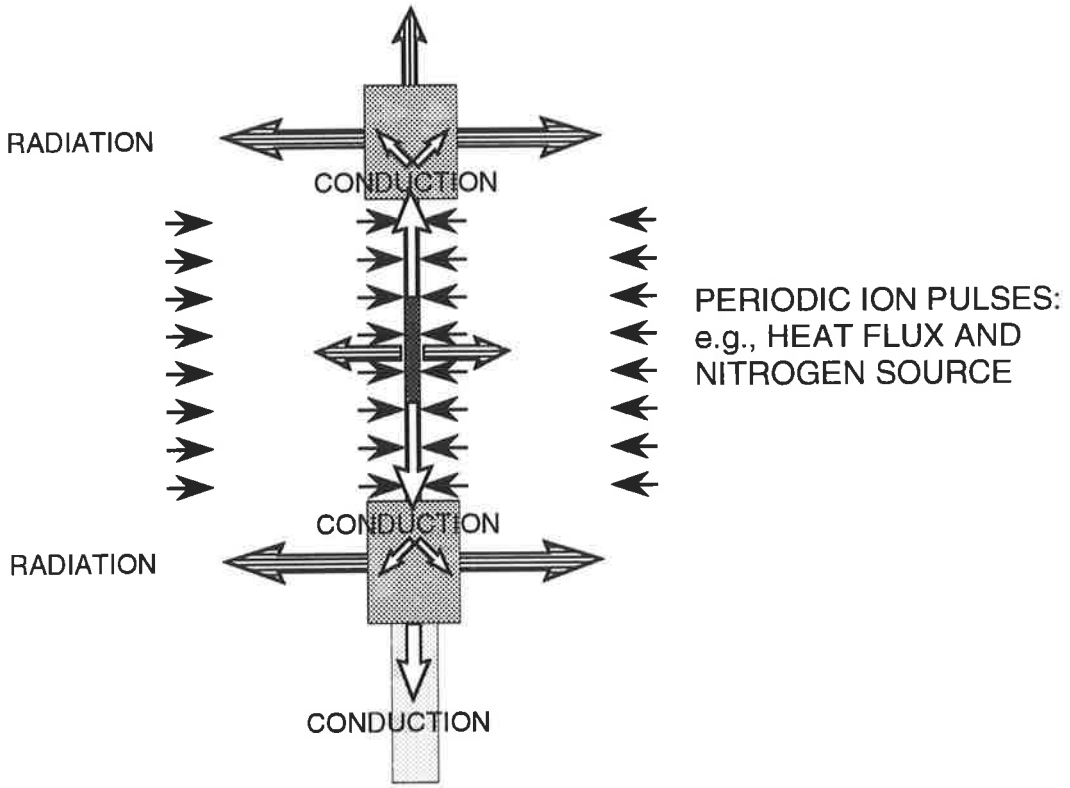

Figure 5.2: Model of heat transfer processes in the specimen rod and specimen stage during PIII treatment.

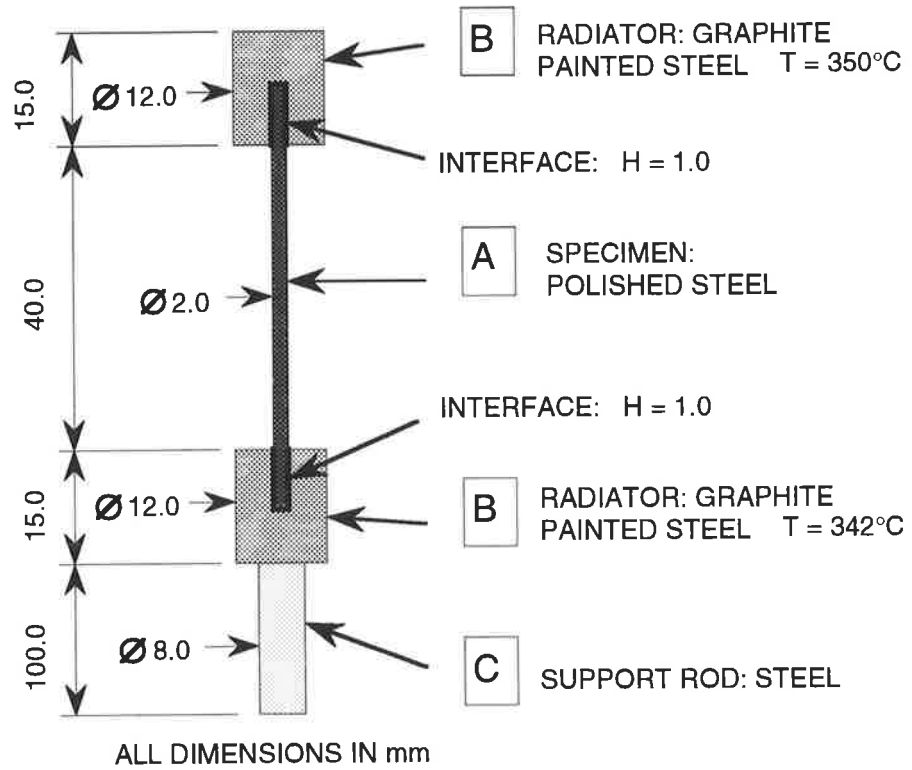

Figure 5.3: Model of conduction path used in numerical modelling

5.3.1 Transient Heating of the Rod's Surface.

Due to the large number of ion pulses, characteristic of PIII (e.g., 2 x10^5, the solution of a transient numerical model of an entire PIII treatment would be impractical in a computational sense. Therefore, it was decided to model one pulse/dwell cycle, once the target had reached working temperature, to see how much the surface temperature increased and how long the temperature took to equilibrate at the end of each ion pulse. Note that the thermal conductivity, and hence thermal diffusivity, of the steel does not vary strongly with temperature, e.g., 26.0 W/m.K at 20°C and 28.5 W/m.K at 400°C [52]. For this reason, modelling a single pulse at room temperature, 20°C, will constitute the "worst case", *i.e.*, the maximum temperature rise, to be superimposed on the equilibrium temperature of 350°C.

The use of a numerical method to calculate the transient thermal fluctuations, is essential, as analytical solutions to transient diffusion problems can only deal with constant initial conditions, such as a constant initial temperature profile, *i.e.*, finding the equilibration in the temperature at the end of a pulse would be impossible analytically.

TRIM was used to find the input distribution of energy as a function of depth beneath the rod's surface. The main limitation of TRIM (see § 5.2.4) was overcome by simulating ion implantation at the extremes of the compositions found in the TEM studies, *i.e.*, α-Fe and Fe_4N. As no major differences were observed, the penetration of the ion energy was assumed to be into an isotropic material.

The following assumptions were made, reducing the problem to solving the one dimensional transient linear conduction equation with an internal heat generation function, *i.e.*

$$\frac{\partial T}{\partial t} = \alpha \frac{\partial^2 T}{\partial x^2} + S(x,t)$$

where T is the temperature at point **x** and time **t**, **α** is the thermal diffusivity, and **S(x,t)** is the heat generation term.

5.3.1.1 ***Assumptions:***

Assumption 1: there is no convective heat transfer between the specimen and the plasma and no radiative heat loss from the specimen surface, leaving the dominant heat transfer mechanism as conduction within the rod, A, followed by radiative heat loss from the blocks, B, and conduction down the support rod, C. NB. the surface area and emmisivity of the graphite painted radiator blocks are much greater than the polished metal specimen.

Assumption 2: there is perfect heat transfer between the rod ends and the cooling blocks, e.g., H=1.0. NB. high thermal conductivity paint was used to join the specimen ends to the blocks.

Assumption 3: the steel rod has homogeneous properties on all scales.

Assumption 4: the ion pulses are applied as continuous square waves of uniform intensity in time, and a fixed axisymmetric distribution in space, allowing axisymmetric calculations.

Assumption 5: due to the shallow depth of heating, the axisymmetry can, as a first approximation, be neglected.

Assumption 6: excess vacancies which may accumulate in the main lattice from ion implantation will have no effect on the local thermal diffusion coefficient in the rod's surface layer. NB. Klemens [74] has noted that the thermal diffusivity of metals and alloys is determined by the sum of the electronic and lattice components. Point defects, such as vacancies, have been found to have little effect on the lattice component.

Thus the problem treated was treated as an infinite slab with finite thickness, *i.e.*, the model should be able to represent one point on the rod's surface during rapid heating, and approximate the thermal diffusion into the core of the rod during the entire pulse/dwell cycle.

5.3.1.2 ***Numerical Modelling:***

The Boundary Element Method (BEM) [64,75] was selected in preference to other techniques, such as Finite Difference or Finite Element methods. This technique has two advantages: first, it has an intrinsic ability to capture steep thermal gradients with a minimum number of time steps; and second, it reduces the dimensionality of the problem by one as it is only necessary to treat the surface of the object rather than the entire volume. These features are particularly useful when dealing with more complicated geometries than are modelled here. The major disadvantage of this technique is that more involved formulation and programming is required. (Nevertheless, recently available commercial packages which model 3 dimensional objects eliminate this problem.)

The problem to solve was posed as a one dimensional solution of the linear heat equation with the boundary conditions shown in Fig. 5.4(a), e.g., insulating boundaries and an initial temperature-depth profile. This figure also illustrates the algorithm for solving the BEM for the unknown final temperature-depth profile, *i.e.*, solve one time block and use the final temperature profile as input for the next time block, and so on. During an ion pulse, the release of energy with depth was modelled as an internal heat source of 80 nm depth (Appendix 5), Fig. 5.4(b). This was included into the model by re-formulating the BEM solution to the heat equation to include an internal heat source (Appendix 6). During the dwell at the end of a pulse, the source function was excluded from the calculations, leaving only insulating boundaries. Due to the discontinuities at the beginning and end of the pulse, the time period was broken up into a number of intervals, each of which was treated as a separate calculation; the temperature at the end of each interval formed the input to the next interval. In Figure 5.4(c), the discretization of the space-time grid during an ion pulse is shown: this allows sharp temperature gradients to be captured which are readily treated by the BEM due to its integration over position. The time discretization for the dwell period between ion pulses is a similar geometric progression of time blocks. Thus, the large changes in time and distance scales were efficiently dealt with.

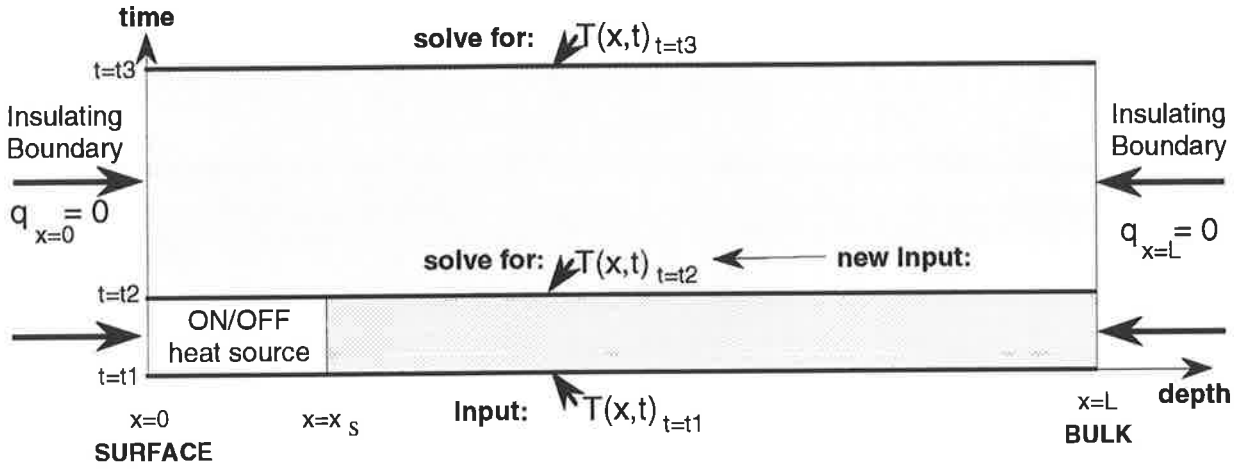

(a)

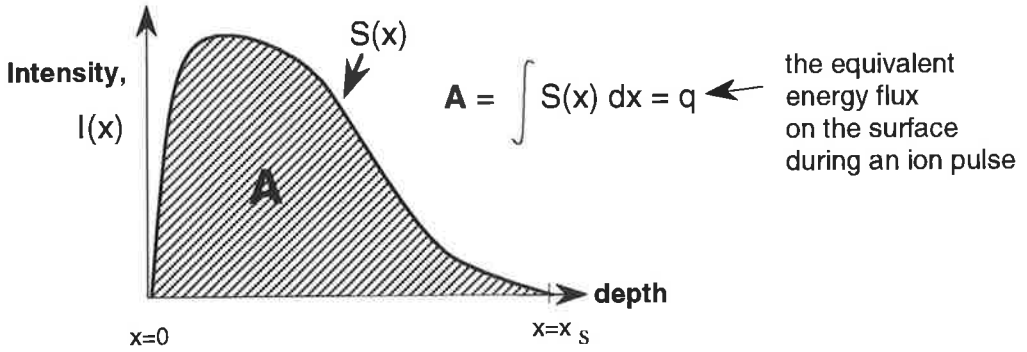

(b)

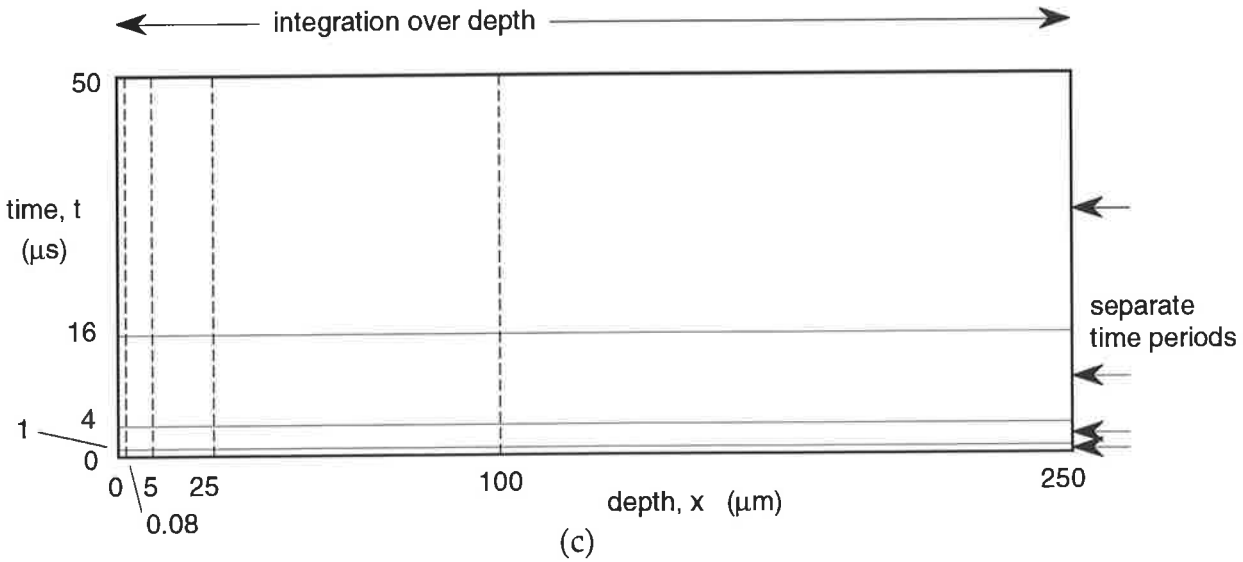

(c)

Figure 5.4: Boundary conditions for Boundary Element Method (BEM) solution to the one dimensional heat equation with internal heat source, S(x). (a) space-time boundary conditions for pulsed source (one pulse/ dwell cycle shown); (b) shape of internal heat source (from TRIM simulations: see Appendix 5); and (c) BEM space-time discretization during one ion pulse, designed to capture sharp temperature gradients.

5.3.1.3 ***Validation of model:***

The first step was to validate the model with a simple trial problem: a single 50 μs pulse into XW10 steel, Figs. 5.5. The model was checked by two simpler methods, both assuming that the internal heat source could be replaced by a surface flux (see Appendix 6). These were, first, an analytical solution with a constant surface flux on an infinite body, and second, the conventional BEM with a constant flux on the surface and an insulating boundary deep within the body. The material properties of XW10 steel were taken from the ASSAB technical data sheet [52] and the pulse power was calculated in Appendix 5. The analytical method was also checked by recalculating a standard textbook problem.

5.3.1.4 ***Results from One Pulse/Dwell Simulation:***

The temperature profile at the end of the pulse is shown in Fig. 5.6(a), with a close-up of the surface region in Fig. 5.6(b). It was found that the three solution methods gave practically identical answers. This indicates first, that there was a trivial effect due to the spread of energy with depth, *i.e.*, a constant surface flux is valid; and second, that the code written maintained numerical accuracy.

The results from one pulse/dwell period are shown in Figs. 5.6, which show that the temperature equilibrates within the length of the dwell, even in the absence of an axial gradient in the rod. So it is not only apparent that the near-surface temperature fluctuations are small (~ 2°C), but also the raised temperature rapidly equilibrates in between pulses (This temperature rise causes a change in nitrogen diffusivity of some 5% at 350°C).

A final consideration should be made regarding the above model treating the centre of the rod as an insulating boundary. If this is the case, then the temperature in the rod will increase *ad infinitum*. This could be overcome by replacing the internal boundary with a "leakage" flux equal to the average power input over the pulse/dwell period. In this case there will be no net temperature increase over a large number of

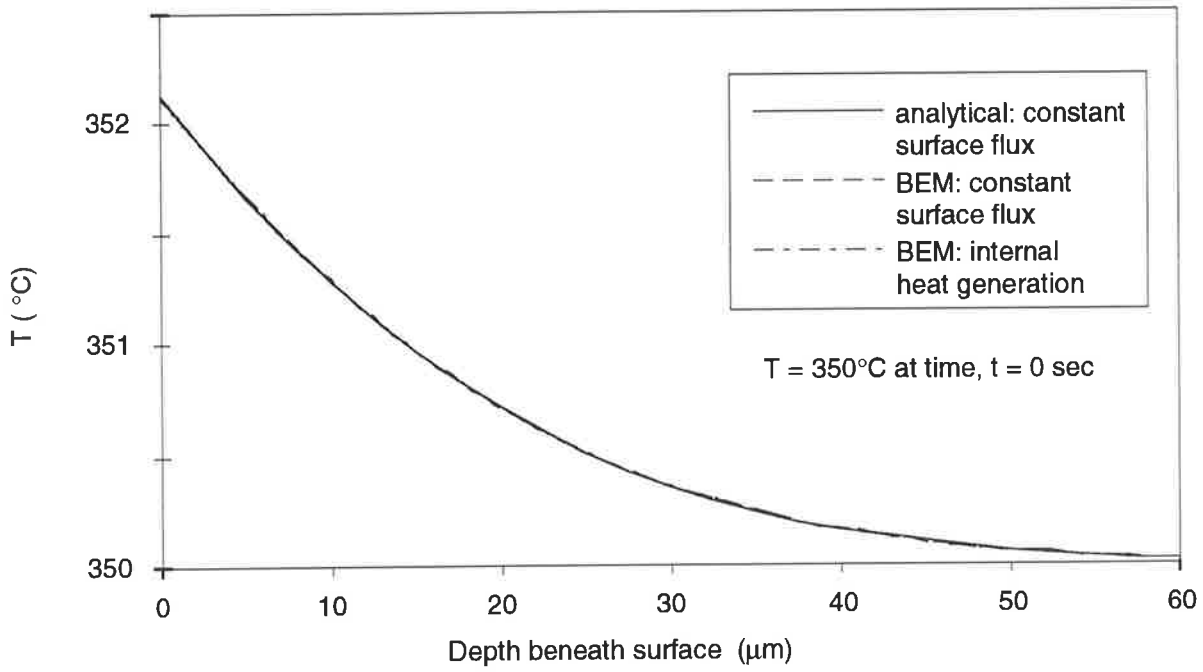

(a)

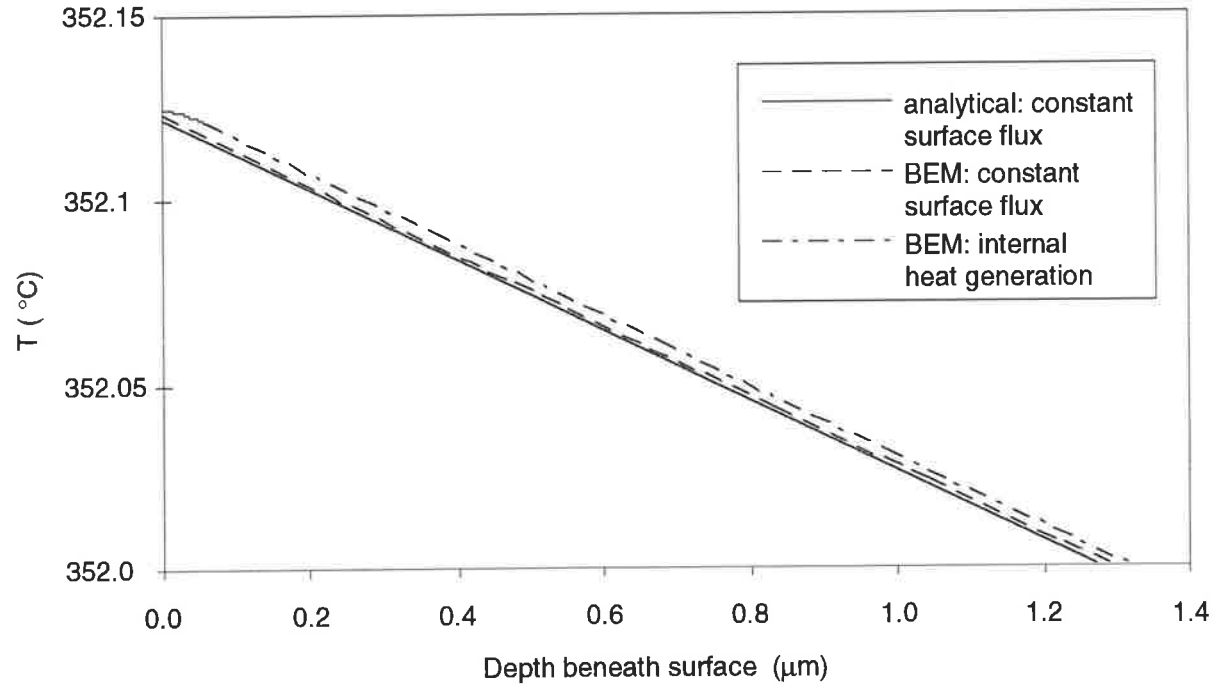

(b)

Figure 5.5: Temperature-depth profile after a 50 μs pulse of nitrogen ions: shows the solutions from three numerical heat transfer models that almost coincide: (a) overall profile up to 60μm depth; and (b) magnification of the surface region to show the differences in the three simulations. The analytical equation is given in Appendix 6.1, while the Boundary Element Method (BEM) numerical solution including an internal heat generation is derived in Appendix 6.2 (based on the "constant surface flux" derivation in Hill and Dewynne (1987).

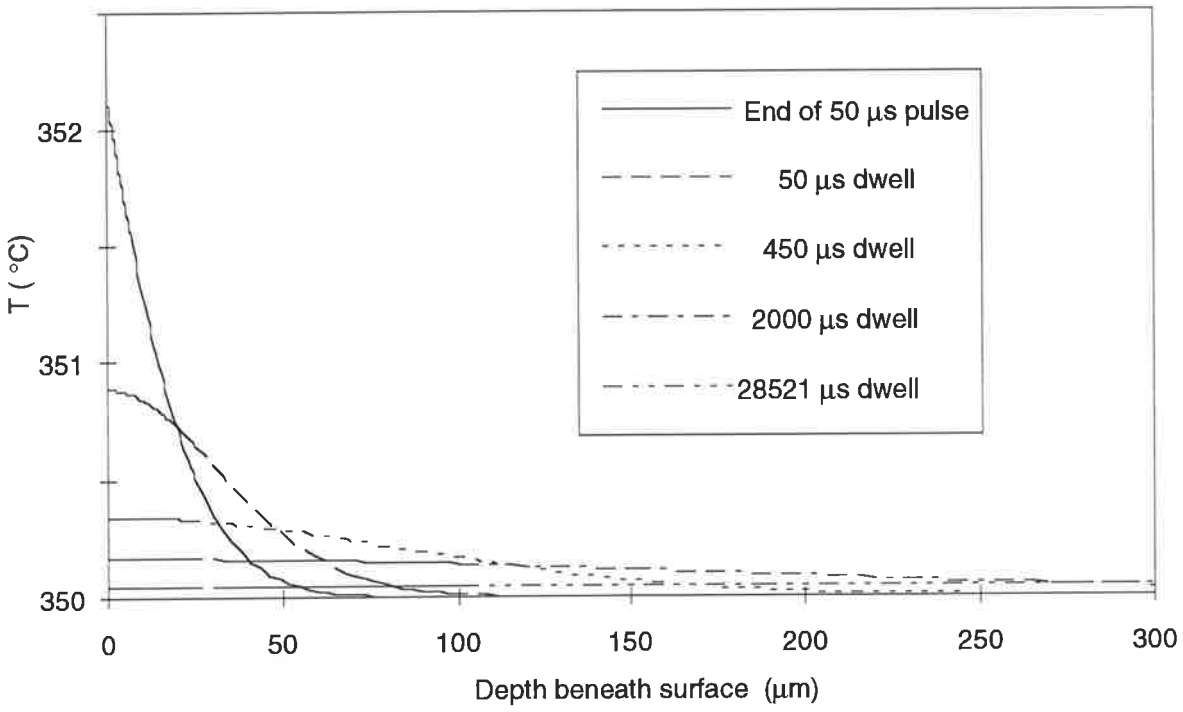

(a)

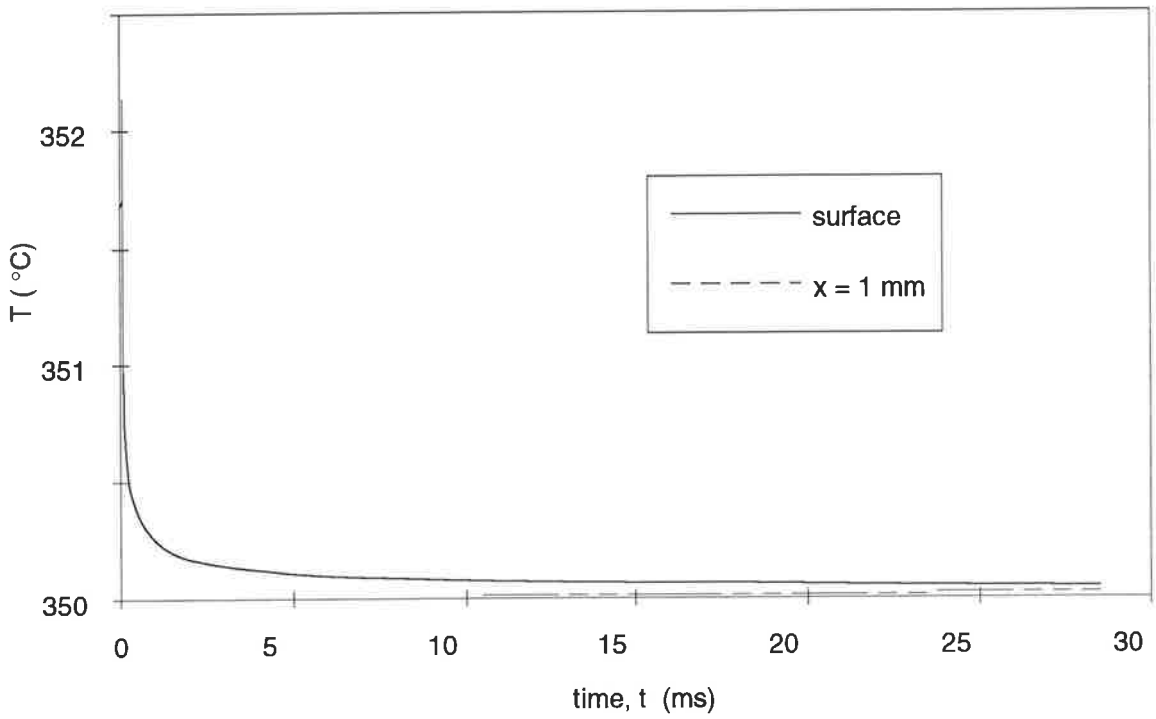

(b)

Figure 5.6: Temperature profiles during and after a 50 µs pulse of nitrogen ions: shows numerical solutions to the one dimensional heat equation with an internal heat source from a Boundary Element Method (BEM) solution: (a) overall Temperature-Depth profiles (b) overall Temperature-Time profiles of the surface and bulk (x=1 mm) up to 1/35th of a second; and (c) magnification of the time scale to show the surface temperatures during and after an ion pulse.

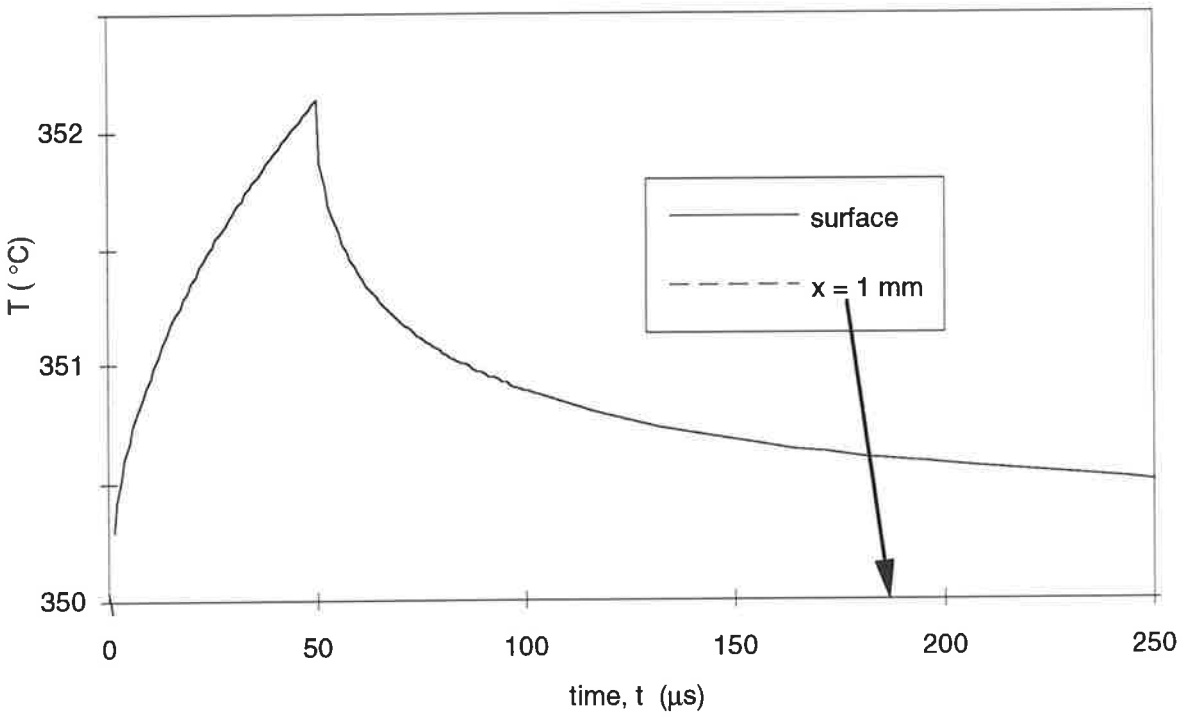

(c)

pulses. Note that this leakage flux is equivalent to the axial conduction which will occur along the rod towards the radiating blocks at the rod ends.

Thus, it is clear that the thermal diffusivity in XW10 steel at 350°C is high enough so that significant transient temperature increases in the surface of implanted rod do not occur with ion pulses of this duration and frequency. However, the long term temperature profile within the entire rod must still be simulated to find if there are any significant variations along the specimen.

5.3.2 Steady-State Temperature Distribution within the Rod.

The steady state temperature distribution within the specimen rod from the average heat surface heat flux can be calculated from standard finite element calculations if the following assumptions are made:

5.3.2.1 *Assumptions:*

Assumption 1: The specimen rod achieves a steady state temperature distribution if viewed on a sufficiently large time scale, e.g., 50 ion pulses.

Assumption 2: no radiation occurs from the surface of the rod since it is polished metal; the only path of heat transfer is conduction through the rod and radiator blocks (Figure 5.2).

Assumption 3: no heating of the blocks occurs.

Assumption 4: the blocks have the same temperature.

Assumption 6: see Assumptions 1, 2 and 3 from § 5.3.1.

5.3.2.2 *Modelling:*

Using the above conditions, the problem reduces to both axisymmetry along the rod's axis and mirror symmetry through the central cross-section of the rod. The prescribed boundary conditions used were as follows, insulating boundaries ($q = 0$) along the rod's axis and mirror plane; constant heat flux on the rod's surface exposed to the ions ($q_{av} = 0.177$ W/cm^2 from Appendix 5); the temperature of the block is 350°C; and the surfaces of the block are radiative of the form:

Heat loss, $q_c = \varepsilon(T^4 - T_o^4)$ W/m^2

A two dimensional axisymmetric finite element analysis package, ("Elcut": public domain software) was used to solve the posed problem. To facilitate the meshing process, a small fillet radius was included at the rod/block interface, *i.e.*, to overcome the discontinuity in boundary conditions. A 470 node mesh was automatically generated by the package to fill the shape, but the mesh was refined around the fillet radius and the mirror plane, Figure 5.7(a). The material properties used are given in Appendix 5.

5.3.2.3 ***Results:***

The isotherms within the specimen rod/radiating blocks calculated from the axisymmetric finite element heat transfer model, are shown in Figure 5.7(b). As seen in Figure 5.8, a maximum temperature rise of 3°C occurred at the mirror plane, *i.e.*, the centre of the rod, with reducing steady state increases along the rod towards the radiating blocks. No significant variations were found across the diameter of the rod. To check the calculations, the heat flux within the rod was also examined: a linear increase along the rod was found, as expected.

5.3.3 Combined Temperature Effects.

The largest temperature increase in the rod from the measured reference temperature of the radiating blocks, from the combined transient and steady state models is calculated to be 2.5 + 3°C = 5.5°C. This temperature increase will occur on the surface of the rod at the mid-point of the rod, and due to the pulsed nature of the implanted ions, will only occur momentarily at the end of an ion pulse. Moreover, the transient temperature component is negligible for ~ 99% of the time, as discussed in § 5.3.1, leaving a steady state increase of 3°C around the centre portion of the rod. Therefore, changes in the atomic diffusivity of the atoms through heating of the specimen rod from the ions can be neglected for these implantation conditions.

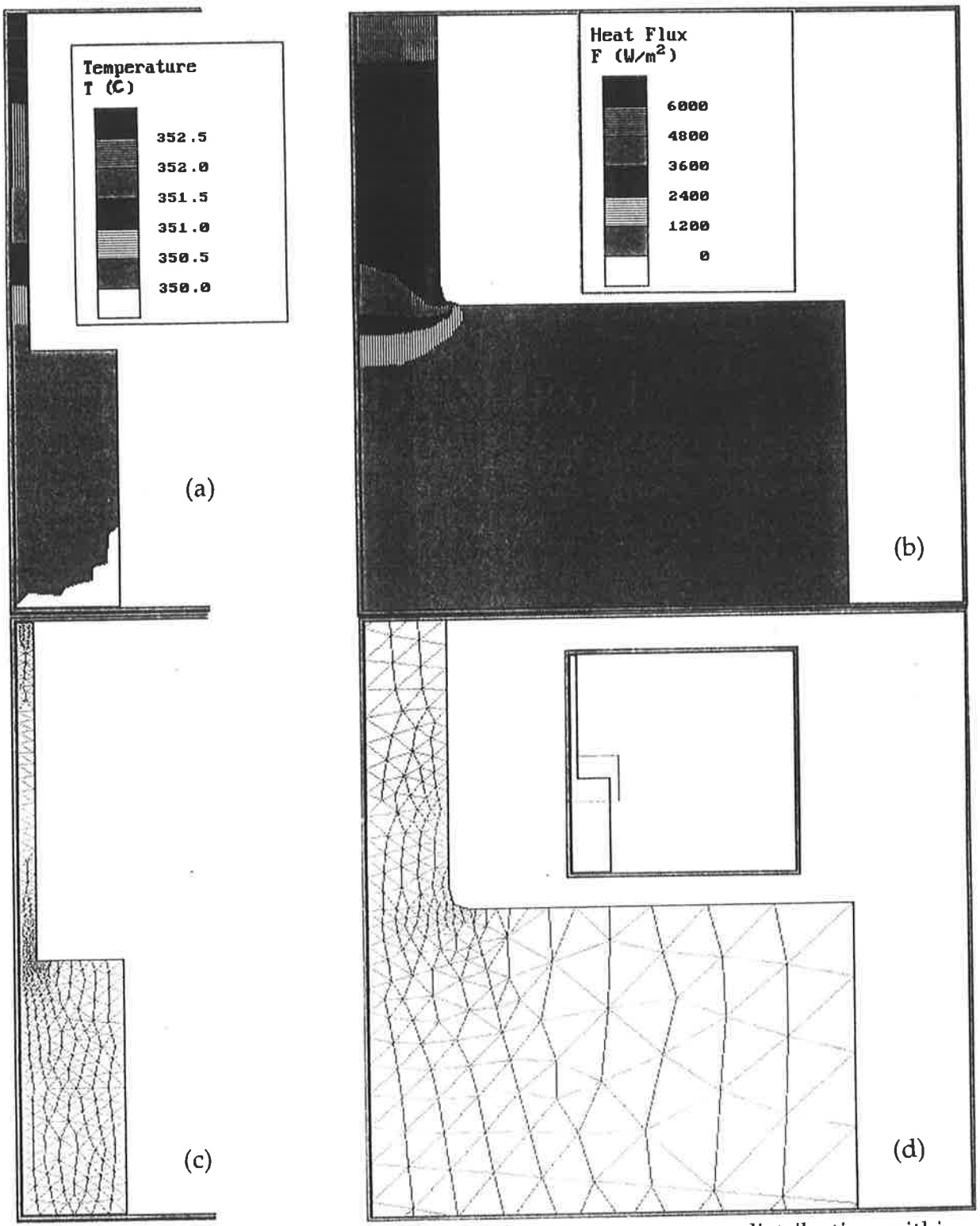

Figure 5.7: Numerical simulations of the steady state temperature distribution within a specimen-rod/radiator-block assembly during 350 °C PIII treatment of XW10 steel (see Fig. 5.3): (a) temperature distribution within assembly; (b) heat flux distribution around rod/block interface; (c) the 470 node mesh used; and (d) detail of the mesh (inset) showing mesh refinement and the small fillet radius used to overcome the mesh discontinuity at the rod/block interface: axisymmetric Finite Element Method (FEM) ("Elcut" public domain software) with radiation boundary conditions on the block surface ($T_{amb.}$=350 °C) and constant heat flux on the rod's surface.

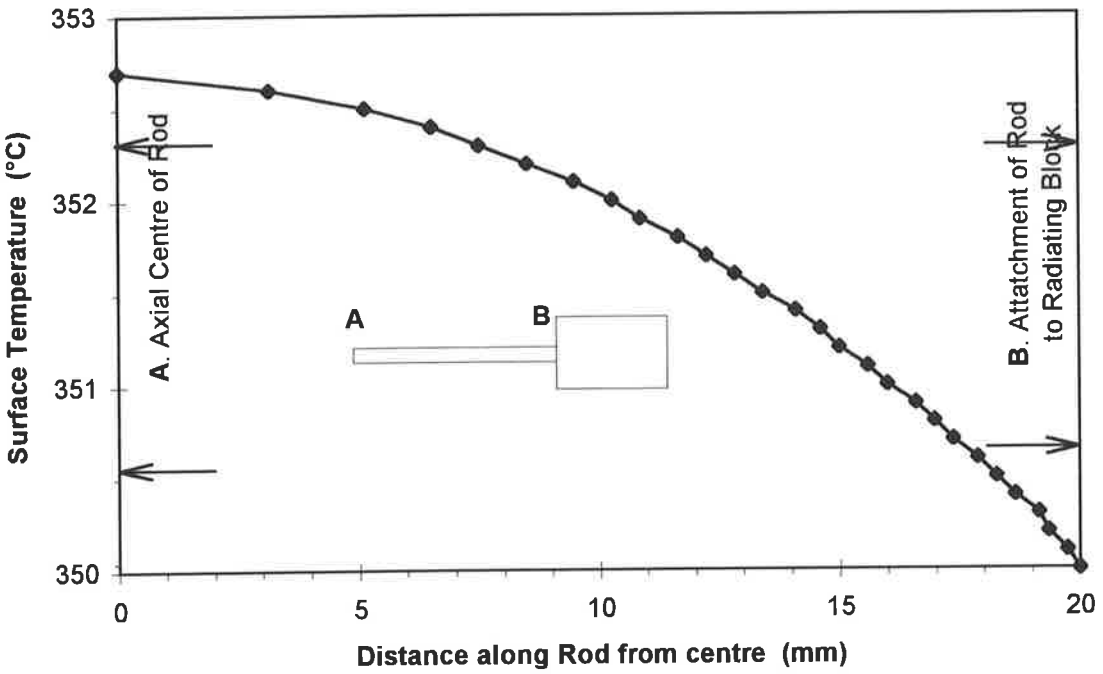

Figure 5.8: Average temperature increase along the surface of the XW10 rod due to heating from pulsed ion implantation (350°C PIII treatment). Finite Element Method (FEM) solution to the one dimensional axisymmetric heat equation ("Elcut" public domain software). This simulation of the current PIII treatment shows that the maximum steady state temperature increase is only the order of 3°C. When the maximum transient temperature increase is superimposed on this steady state temperature increase, the ~ 5°C temperature rise is not large enough to significantly change the atomic diffusivities of implanted nitrogen or the constituent elements in the steel.

5.4 MASS DIFFUSION AND PRECIPITATION.

The development of the nitrogen enriched modified layer during the 350°C PIII treatment of XW10 steel is much more rapid than that of 500°C conventional nitriding processes. This may only be due to the improved method of infusing nitrogen into the steel's surface. Modelling of the diffusion processes in both treatments could answer this issue, but because of the limited solubility of nitrogen in α-ferrite and carbides, precipitation effects are clearly important in the development of the nitride case.

Under ideal conditions, the diffusion of atoms within a metal will be analogous to the diffusion of heat in that material, and Fick's standard diffusion equations could be used to model that process. Fick's equations assume that the diffusing atoms do not interact with the metal, e.g., form a second phase, or decompose an existing one. They also assume that the diffusion is a continuous process where the concentration of diffusing atoms is averaged over a volume much greater than the atomic dimensions of the metal. By examining the microstructures in the 100 μm surface layer of the 350°C PIII treated XW10 steel, clearly neither assumption is strictly valid in this case. However, if a reaction term is added to the diffusion equation to account for the loss or gain of atoms by precipitation or dissolution, resp., then the first assumption would be valid. On the simplest level, this reaction term can be found by modelling the thermodynamics of precipitation, *i.e.*, use the equilibrium equations base on concentrations of the reactants and the equilibrium constant. This approach has been taken by Bongartz *et al.* [71] in modelling the carburization of Cr-Fe high temperature materials. That method appeared to be able to simulate the diffusion/reaction processes occurring over 1000 hours duration and the order of millimeters diffusion depth. However, the duration (3.2 hours) and diffusion depth (100 μm) in the current study are both substantially shorter than that previous simulation. The treatment duration is a particular problem because of the inhomogeneity of the steel on the microstructural scale, which implies that the local nitrogen concentrations across a slice parallel to the surface of the rod may fluctuate significantly about the average. A further issue related to this rapid processing is that the reaction kinetics may be

controlling the precipitation processes rather than equilibrium thermodynamics. Under these circumstances, much more information must be included in the model, such as the rate constants for the reactions which are influenced by local concentrations of reactants, precipitate stability and surface area of each precipitate type. To obtain this level of information would require many more experiments to determine the progression of detailed microstructures during PIII treatment, which defeats the purpose of modelling.

Precipitation of nitrides in iron is also affected by radiation damage caused by ion implantation [76]. Additional nucleation sites for nitride precipitation are generated by neutron irradiation at temperatures around 400°C. The heavier nitrogen ions used in the present experiments would produce stronger effects.

One further problem in modelling the PIII diffusion of nitrogen in XW10 steel is the discontinuous nature of the implantation process, as described in the introduction to this chapter. Hence, to model discrete pulses by Fick's diffusion from a source function, is clearly not justified. However, if the time interval is expanded considerably to cover thousands of pulses, the model will adopt an approximately continuum nature, *i.e.*, if diffusion from an average flux of atoms injected into the steel is assumed, as described by the TRIM profile.

5.4.1 Modelling of Nitrogen Diffusion.

First, to illustrate the assertion of discontinuous nitrogen injection (see the last paragraph), a simulation was made of the nitrogen diffusion during one ion-pulse/dwell period using the same model developed for thermal diffusion, *i.e.*, the BEM solution to the one-dimensional transient heat equation with internal atom generation. The input parameters to the model are given in Appendix 5, while the results of the simulation are shown in Figure 5.9. The slow spread of the nitrogen atoms from their points of injection into the steel lattice is not realistic because the shape of the injected profile describes the average profile over many square micrometers, over which the nitrogen atoms would not interact with each other

laterally in such a shallow layer. Thus, a pulse by pulse treatment of N diffusion from a source function during the implantation process is invalid.

Next, a surface nitrogen flux was simulated over the entire PIII treatment using the analytical solution to the heat equation for an infinitely deep planar body (Appendix 6), Figure 5.10. The magnitude of the surface flux was set at the average injection rate of nitrogen into the surface during the PIII treatment while the substrate temperature was set at 350°C (from Appendix 5). As a check, the retained dose was calculated from the simulated diffusion profile by numeric integration of the concentration over depth, and compared to the nominal ion dose: the figures agreed within 1%. This 11,420 second simulation predicts that the surface nitrogen concentration will built up to ~ 0.09 wt% and a diffusion depth of ~ 20 μm.

In understanding the interstitial diffusion processes during the ion implantation process, it is important to consider the initial presence of carbon in the microstructure. From purely the view point of diffusion, e.g., no precipitation, the carbon will act as an initial concentration, above which the calculated nitrogen profile will be a transient. Interstitial diffusion in this PIII treatment is considered in more detail in § 4.6.2.

The observed level of microstructural change in the present TEM studies (Fig. 4.24) sugest that the concentrations of carbon and nitrogen are of the same order of magnitude in this treatment, *i.e.*, nitrogen has a substantial effect on the carbon diffusion. However, the present diffusion simulations suggest that the nitrogen concentrations are much less than carbon concentrations. This suggests that the surface flux of nitrogen was higher than the nominal rate of implanted ions, *i.e.*, there was a higher retained ion dose. This could be possibly be explained by nitrogen infusing into the steel surface inbetween ion pulses, e.g., in a similar manner to gas nitriding. However, it is clear that the distribution of the nitrogen atoms injected over an 80 nm depth (Appendix 5) has little effect on the diffusion process over the treatment duration.

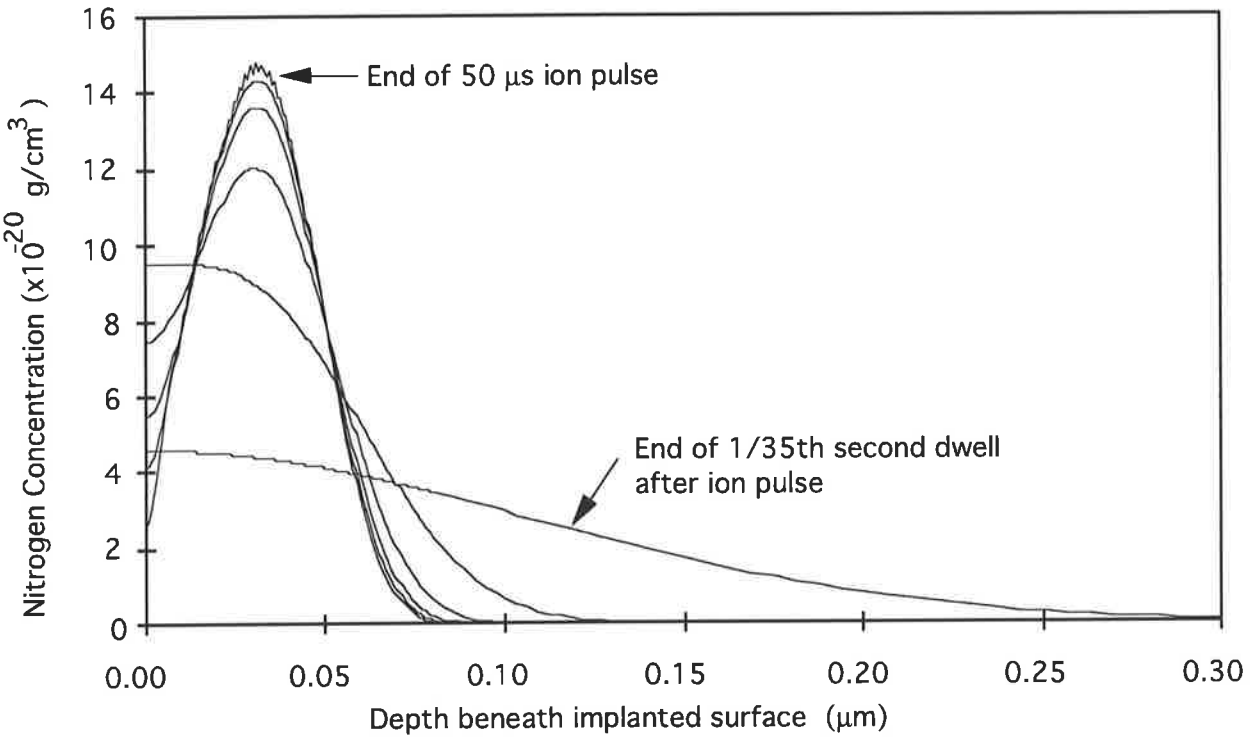

Figure 5.9: Nitrogen concentration profiles during and after a 50 μs pulse of nitrogen ions: shows numerical solutions to the one dimensional heat equation with an internal atom source from a Boundary Element Method (BEM) solution.

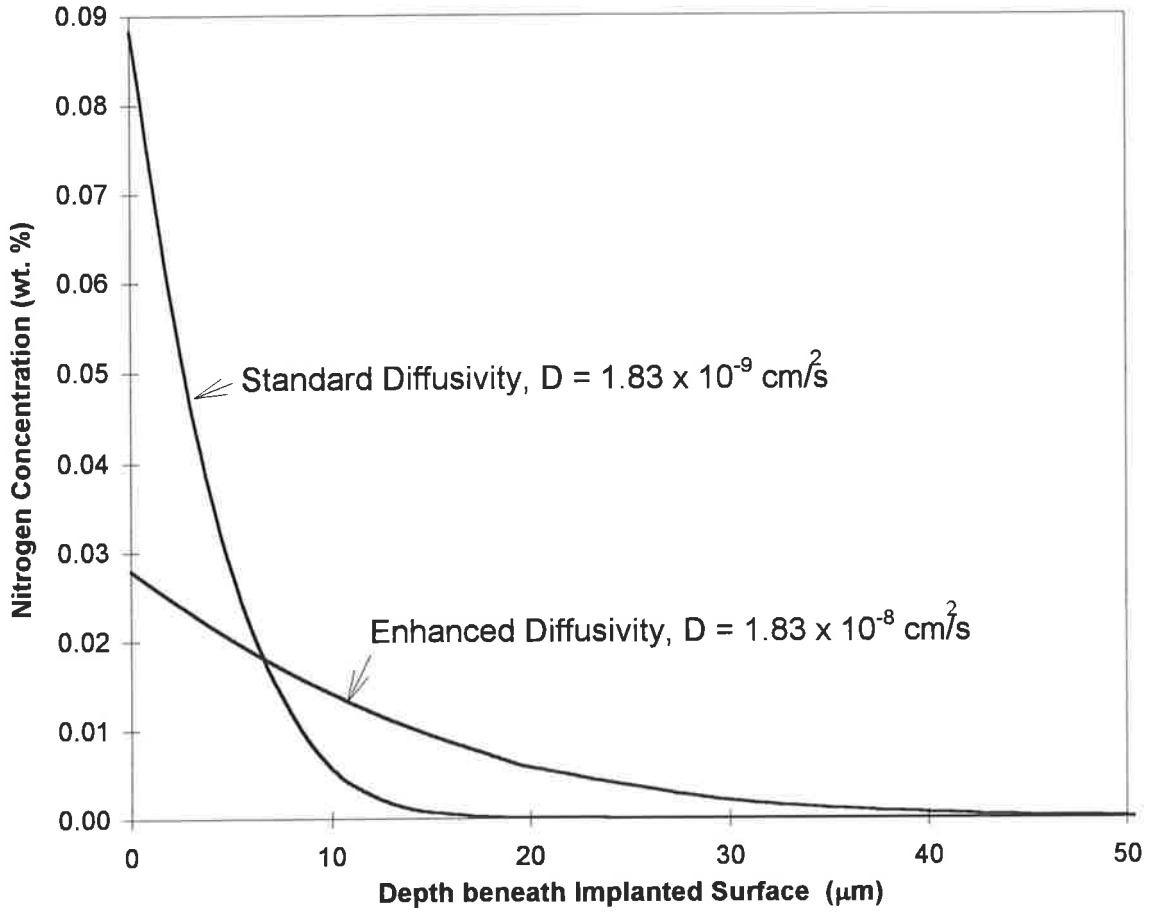

Figure 5.10: The diffusion behavior of nitrogen during a 350°C PIII treatment of a pure ferrite substrate as predicted by conventional linear diffusion (analytical solution to Fick's equation, Appendix 6) with no reaction (precipitation or dissolution) terms. The duration simulated corresponds to the entire PIII treatment: 11,420 s (Appendix 5). In comparison to the level of microstructural change observed in the present TEM studies (Fig. 4.24), higher nitrogen concentrations are suggested and to greated diffusion depths: see text for explantation. The solubility limit of N in α-Fe at 350°C is <0.02 wt. %, suggesting that nitrides should precipitate, as observed. As an experiment, a diffusion profile was simulated with the diffusivity of nitrogen increased by an order of magnitude, resulting in a lower surface concentration and an effective maximum diffusion depth of 50 μm.

5.5 ATOMIC DIFFUSION COEFFICIENTS IN ION IMPLANTED MATERIALS.

The metallic diffusion rates observed in the steel ion implanted at 350°C is 2 orders of magnitude higher than what is expected from the nominal diffusion coefficient at that temperature. For example, in the first 25 μm beneath the surface, the Cr-redistribution along the grain boundaries and the precipitation of Cr-nitrides within the α-Fe grains both require a diffusion range the order of 1 μm. This implies that there are additional physical effects which occur during the PIII process that are not present in the conventional surface treatments.

The mechanisms of conventional atomic diffusion in metals have long been understood and numerous clear accounts can be found, e.g., Cottrell [77]. In metals, two mechanisms dominate: vacancy diffusion and interstitial diffusion. Hence in steels, these take place on effectively two lattices: the main lattice, e.g., (Fe, Cr, Mn, Mo, V), and the sub-lattice: (C,N...), respectively. The rate controlling parameters in diffusion are the probability of a vibrating atom jumping to an adjacent site and the vibrational frequency of the atoms. In vacancy diffusion, because of the increasing concentration of vacancies, C_{Va}, with increasing temperature, the probability of an atom making the jump becomes greater. So the solute diffusion rate is directly proportional to $C_{Va,}$ which in turn, depends on the temperature. Interstitial diffusion is usually a much more rapid process because of the lower activation energies, e.g., in XW10 steel at 350°C, interstitial C and N diffusion in the sub-lattice is ~10^8 times faster than self diffusion in the main lattice. The local diffusion rate at grain boundaries is also increased because they are sites for weaker bonding of atoms and, at lower temperatures, tend to dominate the diffusion process [78,79].

In ion implantation, there is an increased concentration of vacancies due to radiation damage from the impinging ions (Appendix 5). Therefore, the effective temperature of the main lattice can be increased, even though the vibrational frequency of the atoms remains the same. In principle, this means that the substitutional atoms near the surface will have a higher diffusivity than those in the bulk material. Thus, from the local vacancy concentration, the effective temperature, and hence the local

diffusivity can be estimated as follows. For binary alloys of mole fraction, X_b, the vacancy mole fraction is given by:

$$X_{va} \_ EXP[-g_{va}/kT]\{1 - zX_b[1 - EXP[-\Delta g_{va}/kT]\}$$

where z is the coordination number, g_{va} is the free energy of formation of vacancies and Δg_{va} is the additional free energy arising from interaction of vacancies with solute atoms. For weakly interacting, dilute solutions this expression reduces to that of pure metals, e.g.,

$$X_{va} = EXP[-g_{va}/kT]$$

Since a typical value of g_{va} is 1.5 ± 0.5 eV [80], it follows that the effective absolute temperature for solute diffusion with excess vacancies is given by

$$T_{eq} = - 17.4x10^3/ln[X_{va}]$$

The vacancy diffusion rate, D_{va}, in the metal lattice will equal the self-diffusion rate of Fe atoms in α-Fe. Hence, D_{va} and X_{va} are interdependent. The above derivation describes radiation enhanced diffusion (RED) which is a common feature of high temperature ion implantation.

The effects of excess main-lattice vacancies on the interstitial sub-lattice is uncertain, but increased diffusivity of interstitial carbon and nitrogen is expected. In the 20 μm surface layer, potential examples of these effects were found, *i.e.*, the decomposition of Fe_3C and Cr-Fe-based primary carbides, and the large diffusion depths of C and N.

5.5.1 Discussion.

In the 350°C PIII treatment of XW10 steel, the assumptions of being able to model nitrogen diffusion by Fick's equations and precipitation by thermodynamics (e.g., phase diagrams), are not valid as these processes occur principally between the ferrite laths, and are therefore heterogeneous on the scale of the microstructural modifications. The near surface concentrations of nitrogen the PIII process are expected to be significantly higher than those observed in conventional treatments. Rather the reaction kinetics, nucleation processes, and heterogenous diffusion are more likely to

explain the development of the observed microstructures. Furthermore, the diffusivity of N in the modified layer will vary with time and depth due to the accumulating radiation damage and changes in target composition during the treatment.

To satisfactorily model the diffusion and precipitation processes within the complex microstructure of this steel is beyond the scope of this thesis.

5.6 CONCLUSIONS.

Numerical simulations of the 350°C PIII treatment of XW10 steel were performed, *i.e.*, the microstructure that was examined in the TEM (Chapter 4) and the treatment used for shearing comb manufacture (Chapter 6). From the estimated ion dose, the following conclusions were made about the thermal and atomic diffusion from energetic nitrogen ions pulses ("internal source functions") into an XW10 steel rod.

1. The predicted near-surface temperatures in the specimen rod were not large enough to significantly increase the diffusivities of nitrogen, carbon or metallic elements in the surface region.
2. In this case, the limited penetration depth of the medium energy ion source into steel was equivalent to applying a surface flux. However, the model developed could be used to simulating pulsed ion implantation into specimens with a low thermal diffusivity at the implantation temperature, or when high energy ion pulses are used.
3. Fick's theory of diffusion could not be used to predict the instantaneous near-surface nitrogen concentrations from individual ion pulses because the ions were too dispersed on the surface.
4. The penetration depths of the ions are unlikely to effect the nitrogen concentration profiles over the time scale of the PIII treatment.
5. Radiation enhanced diffusion is strongly suggested in the diffusional development of the 350°C PIII treated XW10 steel microstructure.

5.6.1 Suggestions for Future Work.

The ultimate aim of a model would be to predict the PIII process parameters that would develop an optimum hardened layer of maximum depth when the component geometry and material are given. This model would most likely be an extension of the TAMIX [33] code, with enhanced ability to model the evolution of the microstructures observed in the implanted tool steel.

An extension of the present boundary element methods for heat and mass transfer could be to examine three dimensional problems, or even, to involve non-linear diffusion with reaction techniques [81].

Chapter 6

THE APPLICATION OF PIII TO SHEARING COMBS

6.1 INTRODUCTION.

While sheep shearing is primarily a manual task at the present time, the emergence of automated sheep shearing has prompted renewed efforts into extending the wool severing life of shearing tools. The standard tools used in manual shearing can be used for a maximum of two hours before re-sharpening is necessary, but a more typical tool life is one hour. While this is tolerable in manual shearing, the tools used for automated shearing must operate continuously and reliably for eight hours because of economic constraints.

Shearing tools consist of a thirteen toothed "comb" and a four toothed "cutter" [4], Figs. 6.1. The comb is fastened into a hand held body, a "handpiece", which drives the cutter to oscillate over the comb. The scissoring action of the cutter teeth over the comb teeth severs wool fibers as the handpiece is pushed through the sheep's fleece.

The aim of the present study was to help use PIII technology to extend the operational life of manual shearing tools. The strategy chosen to apply PIII was: only treat combs as cutters normally wear sacrificially; only treat the edge faces of combs as the top face will be removed progressively by sharpening; change the steel used in comb manufacture to allow surface hardening to useful depths; and change the sharpening process to protect and maintain hardened surface layers in the area critical for wool severance. The justifications for these choices are explained in § 6.4.

In order to evaluate the effects of the above strategy, controlled shearing trials of modified combs were undertaken: see § 6.4. Combs were manufactured from XW10 tool steel (great thanks to Sunbeam, Australia) in a condition suitable for PIII treatment at 350°C (Chapter 3), then metallurgically polished on the rake faces and PIII treated at 350°C. This PIII treatment temperature was chosen since it was found experimentally to produce the hardest modified layer in XW10 rod specimens (Chapter 3).

Since changes were anticipated in the wear processes of implanted combs in the shearing environment compared to conventional combs, detailed examination of the wear damage of conventional combs was conducted (Chapter 7) to provide reference data.

The following sections describe conventional shearing tools, the shearing technology relevant to this project, previous attempts to improve tool life, and progress made by the current research program towards applying PIII treatment to shearing combs.

6.2 CONVENTIONAL SHEARING TOOLS.

6.2.1 Tool Design and Operation.

Figures 6.1 show the geometries of the combs and cutters widely used for manual shearing of Merino sheep, the most common sheep in Australia. These designs have evolved empirically since the introduction of reciprocating handpieces in Australia in 1938 [82].

Combs are a high-carbon, low-alloy steel form with 13 cantilevered teeth, Figures 6.1(a) and 6.2(a), made from a 75 x50 x3 mm plate. The teeth are evenly spaced across the comb plate, but the tips of the edge teeth are flared out laterally to collect more wool for severance. To minimize the fleece penetration force, the teeth are tapered from the comb plate forwards, to end in rounded tips. The groove in the planar face comb is included to help clear debris from the wool severing process, while the holes and slots are to assist sharpening and allow fastening of the comb into the handpiece,

respectively. Cutters are a forged high-carbon, low-alloy steel form 60 x30 x6 mm with 4 hollow tapered teeth, Fig. 6.1(b). Both the comb and the cutter are heat treated after final machining. Before the tools are sharpened, the edge teeth on the comb are tempered to gain toughness to guard against accidental fracture, and the comb's back face is electropolished to minimize drag of the comb through the fleece. The sharpening process, termed "hollow grind" [4,83], puts a concave curvature in the comb of some 20 - 50 μm across the width of the comb and from the heel of the comb to the teeth tips: see § 6.2.2. A similar curvature is ground into the cutter by the same process.

During operation in the shearing handpiece, the cutter is loaded onto the comb and oscillates over the comb at a frequency of 50 Hz and a radius of ~ 75 mm, Figure 6.2(b). The cutter tooth tips pass approximately 5 mm from the tips of the comb's centre tooth. The nature of the comb and cutter geometries and the load applied to force these tools together as they operate put the cutting edges into close contact. Figure 6.3 shows three views of the cutting edge interactions during shearing. The closure angle, scissor angle and the normal force between the tools creates a small contact patch which continually moves along the comb tooth. This localized contact of the comb and cutter cutting edges allows the tools to locally wear to conform to each other and therefore maintain the close tolerances necessary for severing wool fibers (Chapter 7).

The steel used in comb manufacture must be hard enough to provide wear resistance from abrasion and adhesion while retaining acceptable fracture toughness to prevent tooth tip fracture (as discovered later in this chapter). Low material and manufacturing costs are also desirable. Since the tools are designed to be re-sharpened successively down to half their thickness, low alloy steels have been considered more suitable for conventional sharpening than high alloy steels because they do not leave a residue on the abrasive paper. "Silver" steel, e.g., Bohler K510, is the conventional comb material: see Table 3.1.

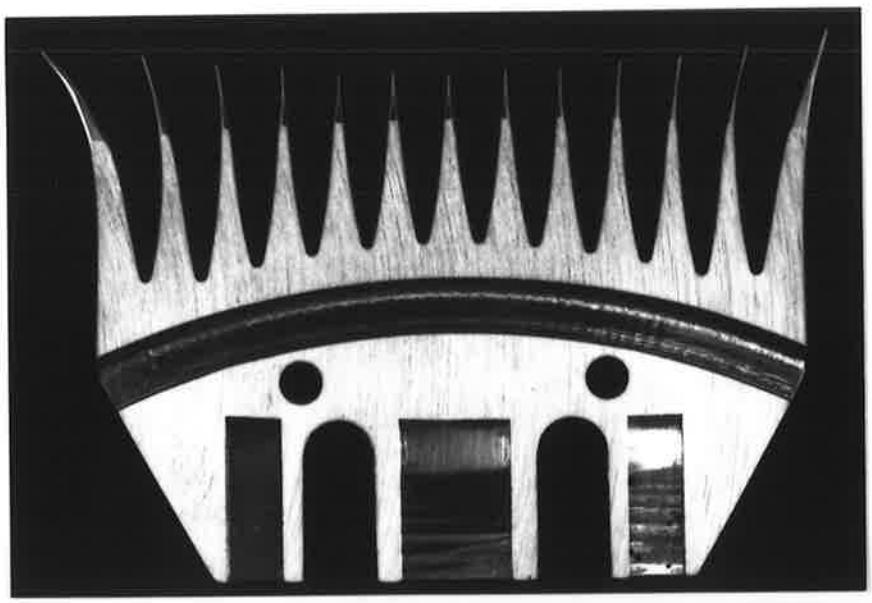

(a) 10 mm

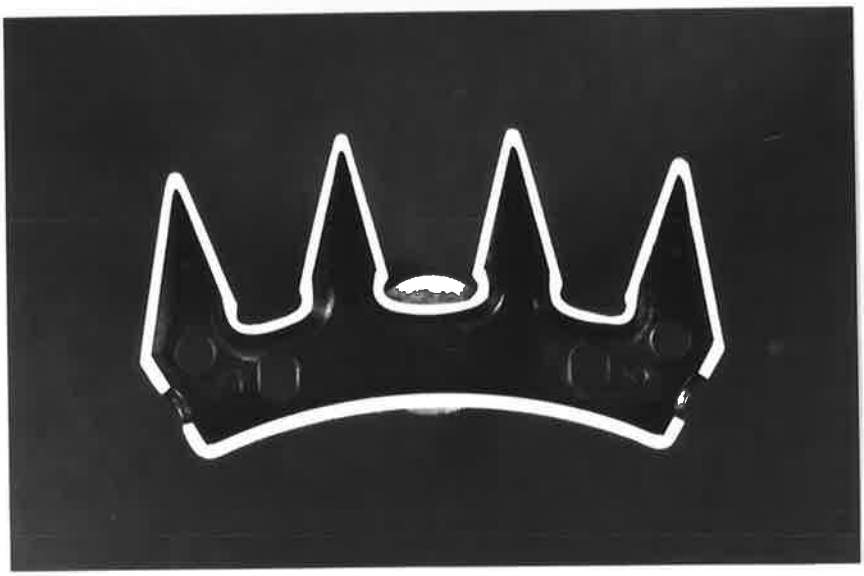

(b) 10 mm

Figure 6.1: Sheep shearing tools: (a) comb and (b) cutter. See Fig. 6.2 and 6.3 for details of the interaction of the tools during wool fibre severance.

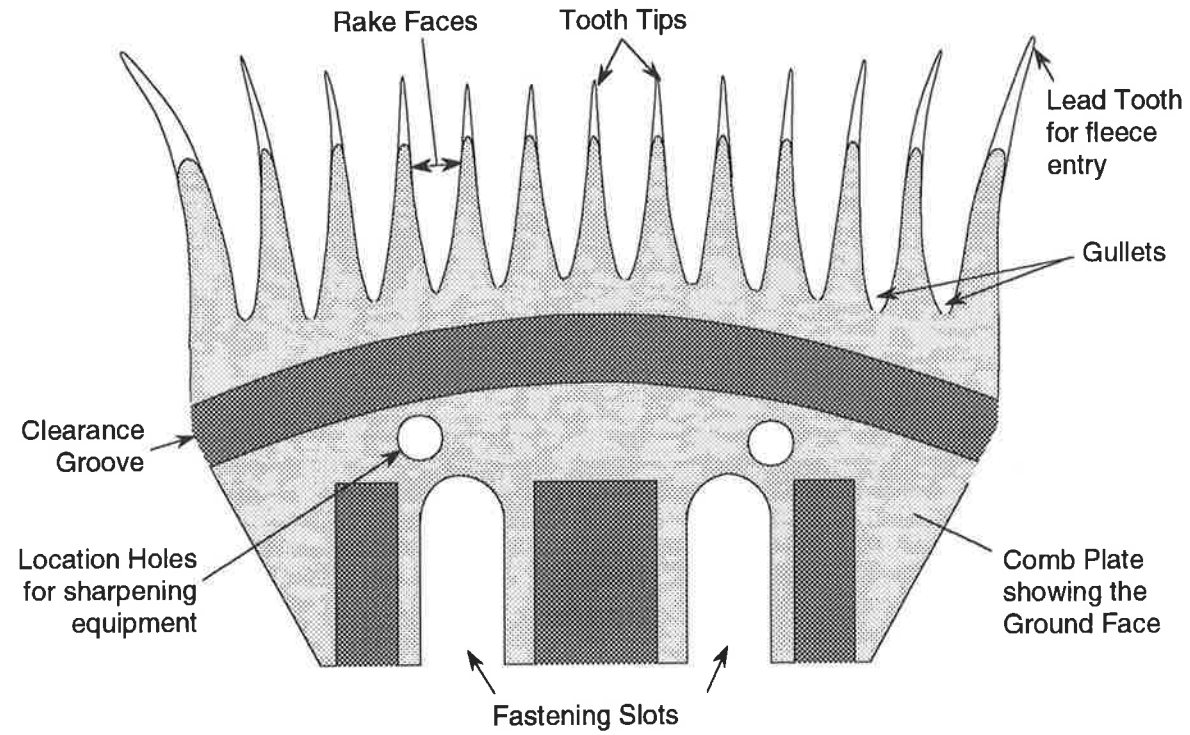

(a)

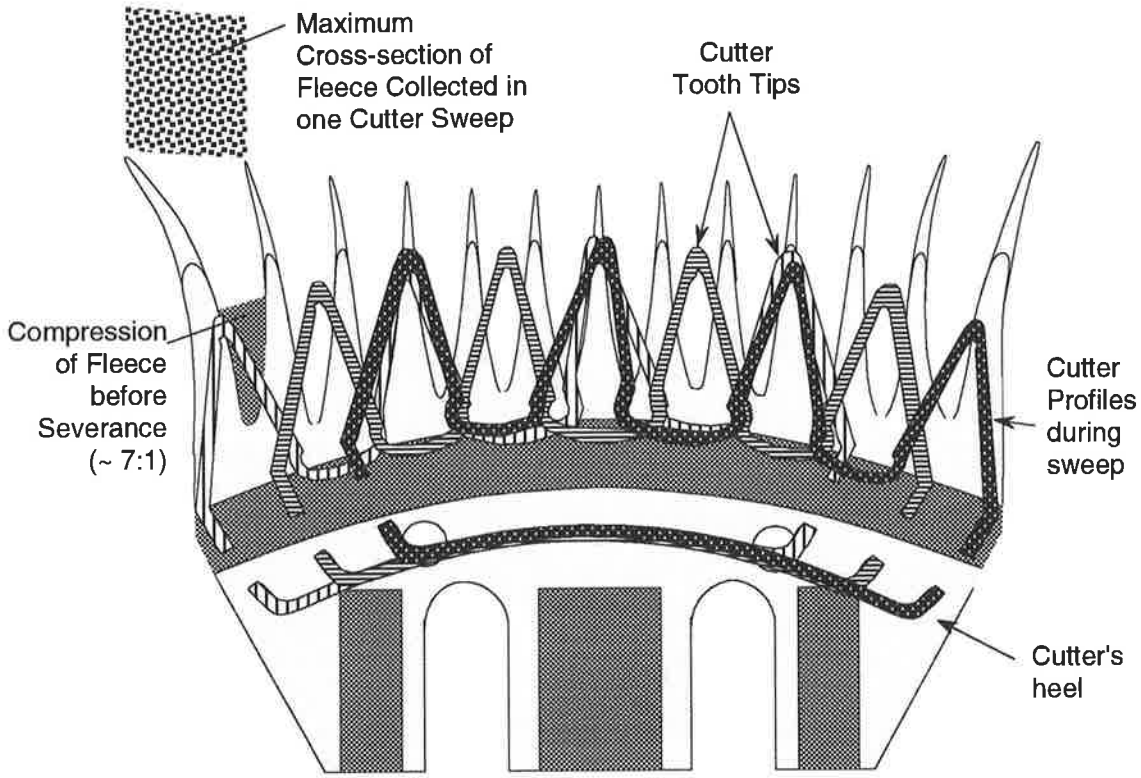

(b)

Figure 6.2: (a) features of shearing comb; (b) comb with cutter's range of motion and maximum cross-section of fleece collected in one cutter sweep.

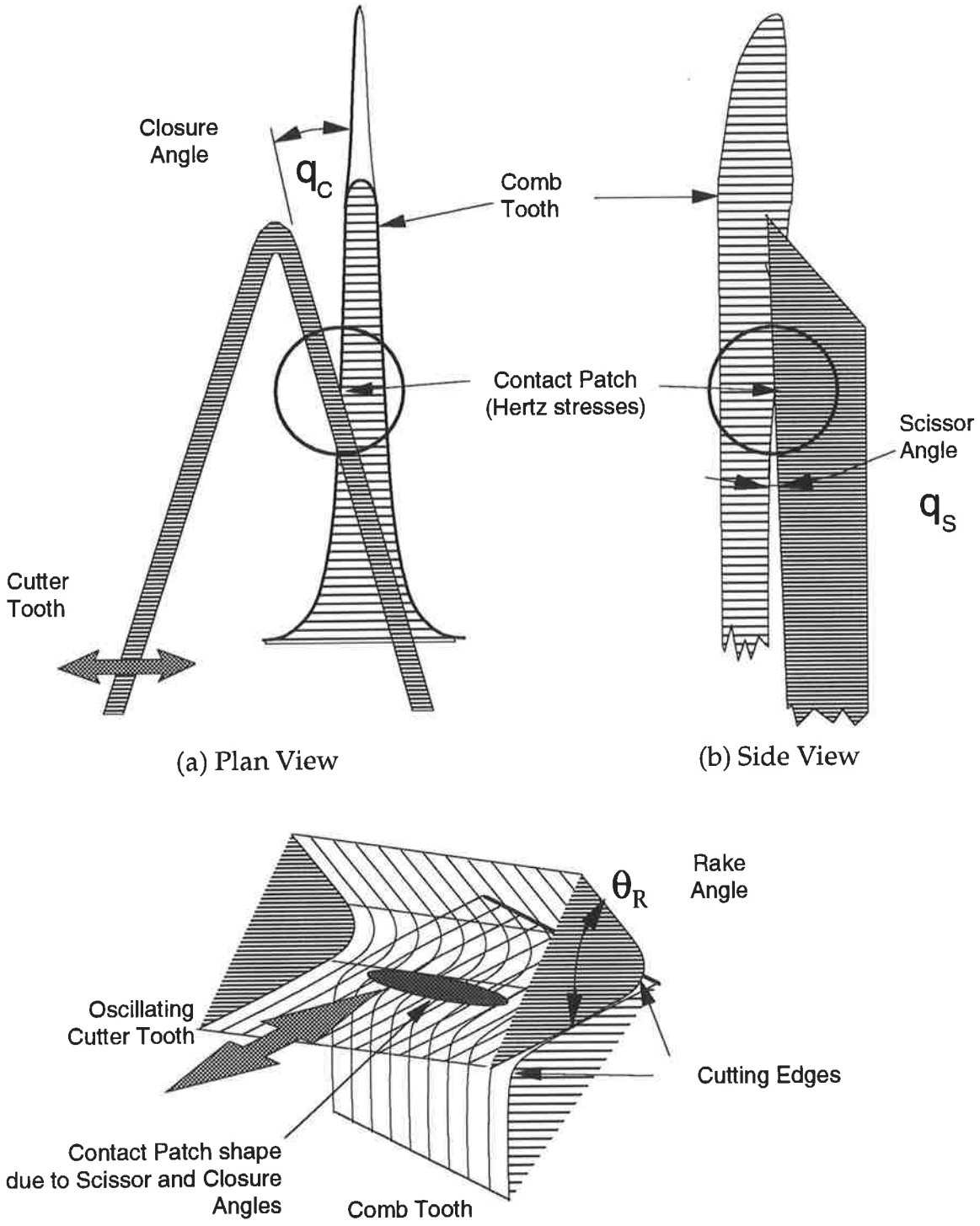

(a) Plan View

(b) Side View

(c) Close up

Figure 6.3: Cutting edge interaction

6.2.2 Conventional Sharpening of Tools.

The sharpening process used for shearing tools, termed "Hollow Grinding" [4,83], uses a coarse, unlubricated abrasive sheet bonded to a high speed rotating disc to remove the worn surfaces on the mating surfaces of the tools. The comb or cutter is pressed against the disc and moved radially across the disc for 10 - 20 seconds during which ~ 20 μm of the top face is removed; the resulting shower of sparks is used to gauge the success of the process. Hollow grinding also produces a concave profile in the face of the comb. In the shearing handpiece, this profile causes the comb teeth to deflect against the cutter teeth as the cutter oscillates, maintaining the desired small vertical separations of the cutting edges (§ 7.3), even after some wear has occurred. However, this ground profile is sensitive to technique and is the cause of many problems in comb sharpening. In particular, conventional sharpening can generate too much, too little or uneven concave curvature in the tools.

While this technique is rapid, the final surface of combs sharpened by this technique must have inferior metallurgical structure to the original steel because of the heat and deformation inherent in this process. First, the sparks generated by the abrasion process indicates that the carefully controlled heat treatment of the steel is destroyed in at least a shallow surface layer in the comb's surface. Second, the coarse abrasive leaves behind folded lips of metal on the surface and thin protrusions at the cutting edges [84]. This softened and deformed surface must be quickly worn away in the vicinity of the cutting edges at the beginning of the shearing process. Ironically, this rapid wear must be countered by grinding a deeper concavity in the tools and greater loading between the tools for the tools to continue severing. Protrusions over the cutting edges can be roughly removed before the comb is used by rubbing a knife blade along the side faces of the comb teeth. However, if they are left, then they curl downwards during shearing, blunting the cutting edge temporarily. The occurrence of the protrusions on the cutting edges can be minimised by careful technique, but the metallurgical damage remains.

The 20 - 50 μm concave curvature is formed in the ground face of combs by two mechanisms. First, the rotating disc is not planar, but conical (~ 1.5° convex), which forms a concave profile along the length of the comb teeth. Second, the rapid heating of the ground face causes differential expansion across the thickness of the comb plate, which causes the comb plate to bow outwards towards the abrasive. When this convex surface is ground and allowed to cool, a concave profile remains [85]. The magnitude of this second effect is sensitive to the following variables: the thickness of the comb, the pressure distribution of the comb on the abrasive, the duration of the pressure, and the radial temperature distribution of the abrasive. The pressure distribution is affected by the shape of the comb's surface before grinding, and the magnitude and direction of the loads on the back surface of the comb. The abrasive temperature distribution is affected by the pattern of radial movement of the comb across the abrasive and the pressure distribution during abrasion. Thus, the concave profile, retained in the comb by the temperature gradient mechanism, suffers great variability across the width of the comb plate, and even between adjacent teeth.

6.2.3 The Severance Life of Shearing Tools.

For the purposes of this study, the "severance life" of shearing tools is defined as the number of sheep that can be de-fleeced before sharpening is required, while the "total life" is the accumulated number de-fleeced after all sharpenings. The mechanisms which cause the of loss fiber severance are considered in § 7.4.

The severance life of combs is determined by four factors: the wear rate of the comb, the shearing technique, the quality of the sharpening, and the size of the sheep. A comb is rejected by a shearer when the force required to push the comb through the fleece becomes too great, or when the torque required to drive the handpiece is excessive. At this point, the comb is considered to be worn to the end of its severance life. Another reason to reject a comb is when scoring (adhesive wear) occurs between the comb and cutter. Usually the severance life of a comb is extended by using several cutters with the same comb, but not if scoring occurs.

The total life of a comb is determined when it is too thin to resist excessive deflection during use, or if catastrophic fracture of one of the teeth occurs. The total life is reduced if poor sharpening practices are used, e.g., if the comb tapers to one edge.

6.3 PREVIOUS MODIFICATIONS TO SHEARING COMBS.

6.3.1 Alternative Materials used for Comb and Cutter Manufacture.

While "Silver" steel remains the standard material used for both comb and cutter manufacture, several alternatives have been used in experimental programs. These materials range from alternative tool steels to cemented tungsten carbide. None of these alternatives have increased the service life of combs on a consistent and affordable basis.

6.3.1.1 *Steels:*

High carbon, high chromium steels (Uddenholm Sverker types S3 and S21) have been used in the manufacture of solid section cutters [86]. That project also examined a sintered tool steel (PX10) and two conventional tool steels (razor blade steel, SF67, and 1.3 wt% C).

6.3.1.2 *Other Materials:*

Solid-section cemented tungsten carbide cutters were made for use with conventional combs [86]. They reported that combs could not be made from solid WC since this material did not have enough fracture resistance for thin sections of comb teeth.

6.3.1.3 *Summary of Limitations:*

In conclusion, the performance of many of these alternative steels have not been evaluated in isolation from other processing, nor have sufficient precautions been taken to avoid damage in the re-sharpening procedures.

6.3.2 Surface Treatments Applied to Conventional Combs and Cutters.

Many types of coatings and surface modification techniques have been applied experimentally to improve the performance of combs and cutters both on silver steel and alternative substrate materials. Mair *et al.* [87], and Hudson, Berndt and McPherson (Monash University, Victoria) have also examined wear resistant coatings.

6.3.2.1 *Case Hardening Treatments:*

Carburized cutters have been tested [86].

6.3.2.2 *Ceramic Spraying:*

Thermally sprayed coatings have been used. The most experiments have been made on detonation gun (D-Gun) composite tungsten carbide/cobalt coatings which have shown some promise, but poor repeatability and the need to condition the comb after coating [88]. Chromium oxide and composite molybdenum/iron coatings have been deposited on steel cutters by plasma spraying techniques [86].

6.3.2.3 *Other Coatings:*

Thin diamond coatings (5 μm) composed of 3 - 5 μm particles embedded in electroless Ni plating were used by Smith [86].

6.3.2.4 *Summary of Limitations:*

Invariably, the cause of failure of coatings is delamination of the coating in the vicinity of the cutting edges. In view of the high contact stresses in the comb and cutter edges during shearing, two possible mechanisms have been suggested in the delamination process:

1) tensile overload at the external surface of the coating caused by incompatible material properties (e.g., elastic modulus) of the coating and substrate;
2) fatigue crack propagation through the interface or weakest phase of the coating through flexure of the comb and cutter teeth during shearing (See Appendix 7).

Further problems with ceramic spraying is that coating thickness must be controlled and uniform to avoid rounded cutting edges; general observations from

these previous studies are that the coating should be thinner than the maximum allowable cutting edge radius, e.g., 15 μm. Another problem is that the steel substrate chosen for case hardening or ceramic coatings would have softened in many cases, through the poor thermal resistance of conventional silver steel: most of these processes involve heating of the substrate, at least locally.

6.4 EXPERIMENTS ON PIII TREATMENT OF SHEARING COMBS.

6.4.1 Strategies to Help Apply PIII to Shearing Tools.

First, maintaining the practice that cutters can wear sacrificially to extend the life of combs, combs were selected as the tool to surface treat by PIII. This practice originates from the higher cost of combs and the slower wear rate of combs, because combs have more cutting edges to distribute damage, *i.e.*, 24 cutting edges (comb) compared to eight (cutter). Therefore, this 3:1 ratio of cutting edges translates into a distinct advantage of surface treating combs over cutters. The next choice was to treat the whole comb, but remove the modified surface layer on the sharpened face before shearing, *i.e.*, use only the rake faces of combs as the top face will be removed progressively anyway by repeated sharpening. The PIII process is well suited to harden the side faces of the comb teeth because of its ability to implant recessed surfaces (Chapter 2). In fact, to prevent ion implantation into potentially damaged surfaces (possible through coarse grinding during manufacture), we decided to give the rake faces of test combs a metallurgical polish before implantation.

However, before PIII processing could be realistically applied, the steel used to manufacture combs needed to be changed to allow surface hardening to useful depths, e.g., greater than 100 nm, without softening at elevated temperatures. The steel chosen was ASSAB XW10, the same steel investigated in Chapters 3 and 4. Finally, the sharpening process used to refurbish worn combs needed to be changed to protect and maintain hardened surface layers in the area critical for wool severance, the cutting edges: the conventional method was thought to be too harsh for PIII treated surfaces. A

"cold-grinding" process using a diamond plated profiled disc was developed by Miller and Young (Chapter 1), but was not used in these trials.

6.4.2 Shearing Trials of Modified Combs.

Initial shearing trials used low temperature implanted conventional shearing combs (Ovina, Heiniger, Austria) that could be used in the robotic shearing equipment of Merino Wool Harvesting, Inc. (Salisbury, Australia; closed in 1990), as robotic shearing trials were planned. However, due to the closure of this company, trials were carried out by manual shearers. Further shearing tests of PIII treated combs were conducted after selecting a suitable alternative steel and finding the best experimentally determined PIII treatment for that steel (Chapter 3). Combs of ASSAB XW10 steel, in a pattern more acceptable for manual shearing (Supersonic, Sunbeam Pty Ltd., Sydney, Australia), were kindly manufactured by Sunbeam, Australia, using their standard production facilities (except for solution treatment and quenching of this steel).

In order to separately evaluate the effects of (a) polishing the side faces of combs and (b) PIII treatment, two groups of control combs of each steel were used: one completely unmodified, and the other polished on the rake faces only. The third group of combs was both polished on the rake faces and ion implanted. For both the silver steel "Ovina" combs and the XW10 "Supersonic" combs, each group consisted of two combs.

Trials were conducted by manual shearers (gratefully organized by Mr. Greg Germain of the AWC) in South Australia. Each professional shearer who participated in these trials was asked to shear a single group (flock) of sheep, in an attempt to control the grit content of the fleece, using one comb from each group, *i.e.*, unmodified, polished only, and polished on rake faces then ion implanted. To minimize bias, shearers were instructed not to shear with a comb once they determined that the comb had passed its "severance life" (combs can still be used, but with increasing difficulty).

6.4.3 Preparation of Modified Combs for Shearing Trials.

Before implantation, all PIII treated combs were given a metallurgical polish (to 6 μm diamond on cloth) on the rake faces of the comb teeth to obtain the maximum benefit from the PIII treatment. The effects of polishing of the rake faces can be seen in Figure 6.4. One group of control combs for each steel was also polished on the combs' rake faces, but not implanted. Precautions were taken to avoid rounding the cutting edges. In the XW10 comb trials, the right hand most tooth of each comb was re-shaped at the recommendation of a professional shearing instructor (Mr. Greg Germain of the AWC): this tooth tip was thinned and given a 0.5 mm radius at the top of the tooth tip in the thin direction of the tooth. This is standard practice for preparing combs because this tooth is used to guide the comb during passes of the comb through dense sections of the fleece. The bulk Vickers hardness of each comb was measured in three places to later determine changes in hardness of the comb resulting from ion implantation. Groups of three measurements were taken on the ground face of the centre tooth, and on the front and rear of the comb plate.

PIII treatment of experimental combs was kindly performed by the staff at the ANSTO Lucas Heights laboratory. The PIII treatment conditions for conventional silver steel combs were chosen to minimize softening of the substrate (See Chapter 3), *i.e.*, a temperature of 180°C and a dose of $5x10^{17}$ cm^{-2}. However, since XW10 steel has secondary hardening characteristics, the PIII treatment of XW10 combs could be chosen to substantially harden the combs' surfaces, *i.e.*, at a temperature of 350°C and dose of $12x10^{17}$ cm^{-2} (the "high dose" treatment in Chapter 3). During implantation of XW10 combs, copper conducting plates, approximately 6 mm thick, were used on the front and rear of the comb "plate" (Fig. 6.1(a)) to assist the heat transfer away from the comb teeth and increase the thermal mass of the implanted object for temperature stability during treatment. As estimated in Chapter 5, no significant heating of the protruding comb teeth was expected, *i.e.*, the geometry of the comb teeth was similar in cross section to the rod specimens investigated in Chapters 3, 4 and 5.

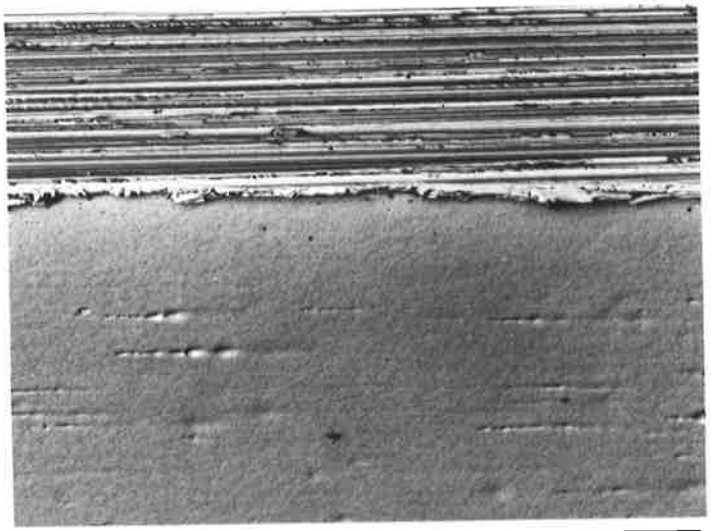

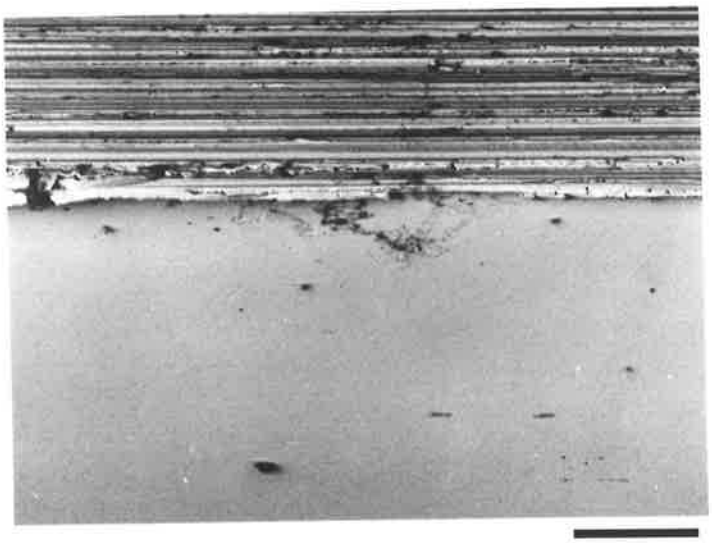

Figure 6.4: Effect of metallurgically polishing the rake faces of shearing combs before PIII treatment: (a) typical rake face of "Supersonic" comb as received from the manufacturer; and (b) rake face after polishing, PIII treatment and sharpening. SEM back-scattered electron images recorded with the beam 45° to both the ground and polished faces.

The final preparation of combs before shearing trials consisted of sharpening combs and duplicating earlier hardness measurements. Hardness values were also recorded after shearing, whenever possible.

6.4.4 Results of Shearing Trials of Modified Combs.

6.4.4.1 *Effects of PIII Treatment and Shearing on Bulk Hardness:*

Table 6.1 illustrates the effect of low temperature PIII treatment of silver steel shearing combs. Comparing the hardness of the ground face of combs' centre teeth, no significant change ($p>0.05$) was found between implanted and unimplanted combs before shearing. However, once an implanted silver steel comb had been used for shearing, significantly lower hardness ($p<0.05$) was found compared to unimplanted silver steel combs before or after shearing. Note in the table that the hardness of the comb plate (front or back) was significantly lower ($p<0.05$) than that of the centre tooth before shearing in both the implanted and unimplanted combs. However, no significant hardness differences ($p<0.05$) between these areas were found after shearing. The comb plate average hardness was significantly lower ($p<0.05$) after ion implantation, but no significant differences ($p>0.05$) were observed between comb hardness before and after shearing for both the implanted or unimplanted silver steel combs. Judging by the comb plate, significant softening of the silver steel substrate was induced by ion implantation. However, apparently a thin hardened surface layer existed on the centre teeth of combs that was not influenced by ion implantation. Nevertheless, wear induced by shearing caused this layer to be removed during the shearing process, exposing the softened substrate.

Table 6.1. Hardness changes in silver steel "Ovina" shearing combs resulting from low temperature PIII treatment and shearing use: Vickers hardness measurements using a 20 kg load (mean ± standard deviation).

Sampling Position	Before PIII and Shearing	After PIII	After Shearing	
			PIII	Un-imp.
# Front	741 ± 61	649 ± 60	673 ± 27	751 ± 17
# Rear	749 ± 27	678 ± 9	675 ± 5	741 ± 4
Centre tooth	789 ± 34[b]	754 ± 40[b]	680 ± 9[a]	739 ± 0[a,b]
* Comb Plate	745 ± 47[b]	663 ± 43[a]	674 ± 18[a]	746 ± 12[b]
No. Samples	n=18	n=6	n=6	n=3

Front and rear of the comb plate: *i.e.*, ground face and polished back.
* average from the front and rear of the comb plate.
Letter superscripts represent no significant difference ($p>0.05$) between horizontal groups for the centre tooth and comb plate average.
Vertical bars represent no significant difference ($p>0.05$) between hardness values at the three sampling positions (ANOVA and Scheffe's test).

On the other hand, high or low temperature ion implantation did not significantly ($p>0.05$) affect the hardness of shearing combs made from XW10 steel, Table 6.2, nor were there any significant differences ($p>0.05$) between hardnesses at the front and rear of the comb plate and centre tooth. Nevertheless, a small decrease in hardness due to high temperature implantation, some 20 - 40 Vickers points, was suggested by the mean values, which is consistent with the hardness changes expected from the results of Chapter 3. No post-shearing hardness data could be collected as described in the next section.

Table 6.2. Hardness changes in XW10 steel "Supersonic" shearing combs resulting from low and high temperature PIII treatment (LT and HT, resp.): Vickers hardness (20 kg load) (mean ± standard deviation).

Sampling Position	Before PIII	After LT PIII	After HT PIII
# Front	850 ± 50	856 ± 63	824 ± 41
# Rear	779 ± 19	794 ± 15	782 ± 11
Centre tooth	862 ± 45[a]	862 ± 50[a]	812 ± 33[a]
* Average	831 ± 54[α]	837 ± 54[α]	806 ± 35[α]
No. Samples	n=12	n=6	n=6

Front & rear of comb plate, *i.e.*, ground face & polished back.
* average from the front and rear of the comb plate and the centre tooth.
Letter superscripts (horizontal groups) and Vertical bars (vertical groups) no statistical differences: See Table 6.1.

6.4.4.2 ***Trials of PIII Treated Silver Steel Combs:***

A summary of shearing trials on low temperature PIII treated silver steel "Ovina" combs and the two groups of control combs are given in Table 6.3. No clear trend could be distinguished between the implanted combs and the control combs, suggesting that neither were the benefits of the surface hardening nor the deleterious effects of substrate softening (as described in the last section) significant.

Table 6.3. Results from shearing trials on 180°C PIII treated silver steel shearing combs and two groups of control combs: polished on comb tooth rake faces only, and unmodified.

Comb		Totals			Average severance life	
		No. de-fleeced (sheep)	shearing time (min.)	regrinds	(min./ grind)	(sheep/ grind)
Polished and PIII treated	1	388	1066	5	214	78
	2	220	907	5	181	44
Polished only	1	290	962	6	160	48
	2*	63	180	2	90	32
Un-modified	1	318	790	4	197	80
	2*	176	440	2	220	88

Polished refers to the metallurgical polish given to the rake faces of selected combs (6.4.3).
* Not considered reliable data since only two regrinds were performed.

6.4.4.3 ***Trials of PIII XW10 Combs:***

Shearing trials of XW10 combs were carried out in 1991 in South Australia. Unfortunately, before any worthwhile data could be obtained, the trials were terminated because of several fractures of XW10 comb teeth during shearing. Later, using fractographic techniques in the laboratory, the fracture origins were identified as coarse carbides in the steel. These carbides can be seen in the optical micrograph of the ion implanted rod (Figure 4.1(a)). Since the fracture of one comb tooth constitutes the premature end of a comb's operation (the drag force through the fleece becomes excessive), we concluded that fracture toughness in the comb's steel is critical, and a problem that was not anticipated.

6.5 CONCLUSIONS AND SUGGESTED FUTURE WORK.

In these experiments, the application of PIII treatments to two steels used to manufacture shearing combs was unsuccessful. Silver steel, the conventional material used to manufacture combs, could not be given a PIII treatment of sufficient depth (e.g., ~ 50 μm) to change the "bulk" surface hardness to affect the wear resistance of the cutting edges because of its poor thermal stability (Chapter 3). Low temperature implantation (180°C) did not improve the severance life of these silver steel combs. On the other hand, combs manufactured from XW10, the new steel selected to offer high thermal stability during PIII treatment (Chapter 3), did not survive shearing because of premature fractures of some comb tooth tips. Surface hardening was detected on 350°C, high dose PIII treated combs showing that it is possible to efficiently ion implant shearing combs by this process. Further shearing trials should be undertaken to assess the benefits of applying the PIII process to shearing combs. From the lessons of the present trials, combs should be manufactured from an alternative tool steel which has both secondary hardening characteristics and high fracture toughness in thin plate sections, e.g., 0.5 mm.

Combs coated with a cemented tungsten carbide by the "D-gun" process (Appendix 7) are not considered suitable for shearing use because the coating was found to crack. Cantilever bending of the comb teeth, of magnitude similar to that measured during shearing use, induced stresses that cracked a brittle intermetallic phase in the coating through fatigue. This showed that this type of coating is vulnerable to fatigue and therefore the loss of coating integrity, even in the absence of fiber severance loads.

Chapter 7

WEAR OF SHEARING COMBS

7.1 INTRODUCTION.

The aim of this chapter is to improve the application of ion implantation to shearing combs by understanding the mechanisms of comb wear and loss of wool severance.

Shearing tools operate in fleeces that have a range of wool fiber diameters and lanolin contents, and that often contain contaminants such as grit, vegetable matter and water; The tools also operate out of the fleece at times, e.g., when the width of the fleece to be severed is narrower than the comb. This exposes the tools to a variety of wear environments. Previous work [84], has identified the dominant wear mechanism on the ground face of shearing tools as abrasion from grit in the wool. Adhesive wear has also been suggested on the ground face [84], but only when the shearing tools were run without lubrication or grit. Rounding and indenting of the cutting edges have been recorded [84,89], but no investigation has specifically examined wear or wear mechanisms of the cutting edges and rake faces. Rake face wear is of particular importance to the PIII surface treatment of shearing combs, *i.e.*, wear processes could damage the hardened layer.

Wear damage on conventional combs was investigated to extend the knowledge of wear mechanisms and to provide a datum for wear studies on surface modified combs. Since examination of rake face wear had not previously been made, and in view of the relevance to the proposed rake face PIII treatment (Chapter 6), particular attention was focused on rake face and cutting edge wear. A number of conventionally

ground combs that had been used for shearing were examined by both optical and scanning electron microscopy. Modelling of the cutting edge and rake face wear was undertaken to suggest the dominant wear mechanisms and to explain some unusual features observed on worn combs.

Finally, the mechanisms leading to the loss of wool severance were examined to suggest methods of prolonging severance. Another model was developed to predict the effects of cutting edge wear on the fiber severance process, and therefore to predict the conditions under which this process is likely to break down.

7.2 CHARACTERIZATION OF COMB WEAR.

Overall wear patterns on the ground face of shearing combs were first investigated by Field *et al.*,[89] who ran a hand-piece with a standard comb and cutter at low speed in a lapping compound. They were able to illustrate some features of comb wear but their methods produced patterns that were much more severe than real patterns, *i.e.*, subtle wear features were obliterated. Smith numerically modelled the abrasive wear of a cutter running on a plate in terms of the contact areas and the motion, and once again, produced wear patterns resembling those found on actual combs. Other investigators [84] ran a handpiece with tools polished on their ground faces with no lubrication and found that severe adhesive wear (scoring) occurred under the load points of the cutter after 15 seconds. They correlated polishing with the loss of lubrication and adhesive wear. There appear to be two main limitations of the previous comb wear characterization studies: their focus on the final wear damage without addressing the intermediate processes, and their inability to explain the relationship between wear of the rake faces and wear of the cutting edges.

In the present studies, for convenience, the comb's surface was divided into three regions to be examined as they have different wear mechanisms: the ground face (in contact with the cutter's ground face), the rake faces and the cutting edges.

For characterizing the complete pattern of wear at low magnification, a new optical technique was developed which used the differences in the directions of

scratches from the sharpening and wear processes to highlight the comb wear pattern, Appendix 2. For studies of the rake faces and cutting edges, combs were mounted in a holder which could reposition a comb after shearing use to record the accumulated damage. Several new combs, polished on their rake faces, were inspected by this technique both before and after shearing until the end of their first severance life. To observe the accumulated wear damage on the rake faces, other combs were inspected that were at the end of their total life.

7.2.1 Wear of the Ground Face.

In general, two forms of wear were observed on the ground faces of the combs inspected: abrasion and adhesion. Overall wear patterns on the ground faces of two combs are shown in Figure 7.1 . Although wear was clearly restricted to the areas contacted by the cutter (see Figure 6.2), the wear was not uniform. However, as highlighted by the still visible sharpening scratches, the wear depth was not great over much of the comb. Three distinct regions of wear could be observed: 1) 0 - 10 mm behind the cutter tips on the comb teeth; 2) in the vicinity of the gullets; and 3) under the heel of the cutter. The impression of Region 1 wear was that all comb teeth wear in a similar manner: most severely under the cutter tips and around the cutting edges, and least severely in-between the rear portion of the cutting edges. However, wear in the gullet depended on the mating profiles across the comb and cutter generated by the previous sharpening process. Figure 7.1(a) indicated compatible mating profiles, while 7.1(b) indicates excessive concave curvature in the comb and/or cutter profiles. Wear in-between gullets was generally less severe than behind the same gullets. This is attributed to the geometries of the comb and cutter: see Figures 6.1 and 6.2. Region 3 (under the cutter's rear) was found to be the least worn region, but exhibited more wear at the extremities of the cutter's stroke than in the centre region.

7.2.1.1 *Abrasion:*

Scanning electron microscopy of other worn combs provided more information on the wear processes of the comb teeth and gullet regions. Figure 7.2(a) shows a worn

surface midway between the comb gullet and the cutter tip path. Two wear facets are evident: one parallel to the comb ground face, and one angled down towards the cutting edge. On the first facet, abrasion seems to be the dominant wear mechanism with rounded scratches 2 - 5 μm wide, while the height of the worn surface is generally not uniform. The rounded appearance of these scratches suggests that the abrasive responsible was not large (>20 μm) or consistently sharp. While the angled facet shows signs of abrasion, smearing is also apparent; Figure 7.2(b) indicates that the smear direction was away from the cutting edge. Smearing indicates highly localized shear stresses in the plane of contact generated by a dull abrader, e.g., the mating cutting edge, and an absence of lubricant. The width and angle of these angled facets varied locally along the comb, which indicates that matching wear facets developed on the cutter "ground face". A minor feature of both wear facets is sporadic scratches which deviate from the direction of the cutter's motion.

The abrasion in the forward portion of under the cutter tooth tips was similar to the mid-tooth abrasion but the angled facet was generally not found. Towards the gullet regions, other surface topologies were found. Figure 7.3(a) shows a wide wear facet adjacent to a cutting edge with minimal wear in the centre of the comb tooth. These two types of wear can be related back to the overall wear patterns, Figs. 7.1, as the light and dark areas respectively. Figure 7.3(b) and (c) show enlargements of an interesting form of wear which was often found in low wear areas of the ground face, e.g., as just described. Figure 7.3(b) shows the original grinding scratches that mostly have been worn away by the cutter. Closer inspection of the speckled areas, Figure 7.3(c), show that the α-Fe matrix has been removed, revealing the carbides. This wear is likely to have been caused by wool fiber fragments which lodge inside the cutter teeth during the shearing process, as matted balls. Other possible explanations are offered in § 7.2.1.2.

The typical overall effects of abrasion on the profiles across the comb teeth are shown in Figure 7.4. This figure was obtained by recording serial profiles of a worn comb tooth in a depth-focus calibrated optical microscope.

7.2.1.2 ***Adhesion:***

Other features distinguished by the optical macrographs, Figure 7.1, were coarse light and dark streaks across some comb teeth in directions parallel to the motion of the cutter. These streaks were usually found on at least two adjacent comb teeth on the same cutter radius. This indicates a comb/cutter interaction dependence for this process. Scanning electron microscopy of these marks, Figure 7.5, identified that they had formed as a result of adhesive wear, e.g., comb/cutter metal transfer. Field *et al.* [89] found that this type of wear dominated the ground face wear when combs were operated out of the fleece without lubrication or grit. They concluded that friction between partly polished mating surfaces was responsible for the adhesion. In the combs inspected, this type of wear occurred predominantly in the regions of higher contact pressures, e.g., on the front half of the comb teeth, but was often found in the gullet regions.

Figure 7.3(c) shows what could be an early stage of adhesive wear through the mechanism of micro-spalling of the ferrite (or martensite) matrix, as indicated by the remaining harder carbides, followed by metal transfer to the cutter. It is likely that this micro-spalling wear begins on the foward half of the comb teeth when the closure force is still relatively light in the middle part of the comb's severance life, then gradually deteriorated into gross adhesive wear as the closure force is increased to overcome cutting edge wear.

Another probable mechanism which can initiate gross adhesive wear is large spalling sites, e.g., Figure 7.6. However, these sites were rarely found (only in two instances), and only in combs that had been used for a substantial portion of their total life. The cracks visible at the bottom of the spalled region indicate the sub-surface fatigue mechanism characteristic of spalling.

The consequence of adhesive wear is that in severe cases, adhesive deposits will cause the comb and cutter edges to separate and hence break down the severing process (see § 7.3 and § 7.4). The irreversible nature of this wear can be critical for future use of

the comb if severe adhesion (scoring) occurs, *i.e.*, because repeated sharpening will be required to remove deep score marks.

7.2.1.3 ***Overall Wear Patterns:***

The information gained from the SEM images could be used to explain features in the optical macrographs. The more intense reflections from the gullet regions compared to the foward part of the comb teeth are caused by more polishing around the gullets compared to coarser abrasion around the teeth foward halves. The reduced wear in-between the centre section of the comb teeth close to the gullets is likely due to the load transfer from the cutter cutting edges to the cutter tips and the heel of the cutter as the cutter tips pass over the comb teeth. The pattern of three patches of heavier wear under the heel of the cutter confirms this mechanism. The load transfer seems to take place because of excess concave curvature in the cutter's ground face in comparison to both the closure force and the stiffness of the comb and cutter teeth perpendicular to their contact plane.

Comparing the wear found on the gullet region, the tooth edges and under the tip of the cutter's traverse, the expected changes in contact pressure clearly contribute to the different wear types and severitys, *i.e.*, heavy abrasive wear followed by adhesive wear in regions with high contact pressures. Abrasion by both grit and metal/metal contact are indicated in these studies. Grit abrasion is likely to become more severe when the cutting edges become excessively rounded or if local clearances develop between the mating surfaces (see § 7.3).

The wear patterns on relatively thick combs with thick cutters were less even than those found on thin tools, particularly the wear observed in the gullets. In Figure 7.1, the force applied to the cutter was clearly sufficient to distort the comb and cutter teeth enough to produce contact in the gullet region.

No significant wear was recorded outside the region contacted by the cutter, *i.e.*, wear caused by the wool fibers on the remainder of the ground face was minimal.

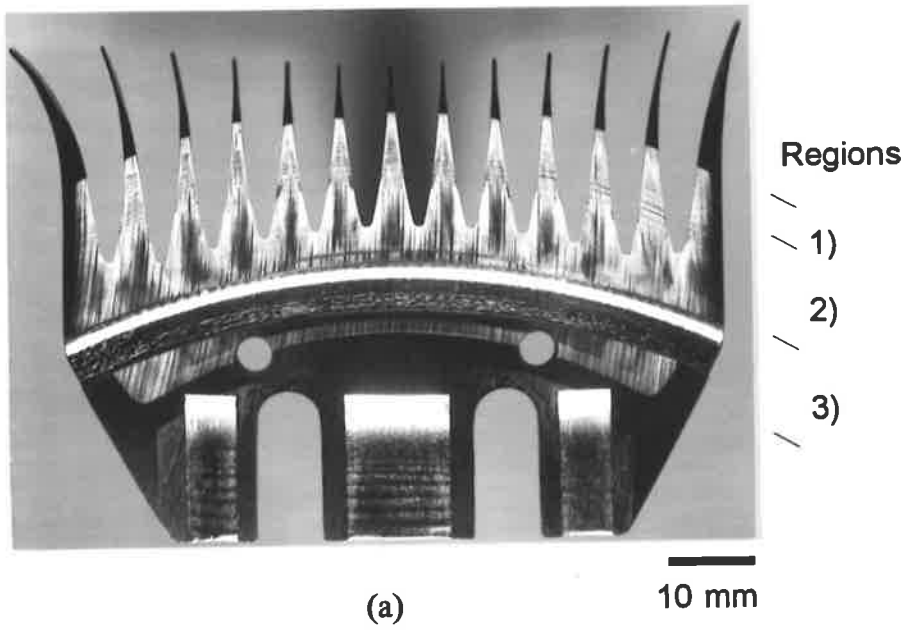

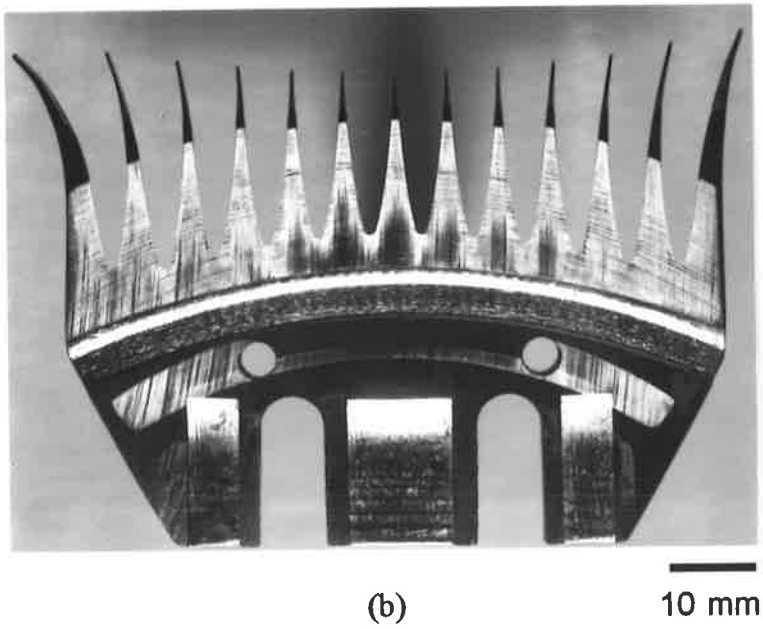

Figure 7.1: Overall patterns of wear: combs used until the end of their severance life: (a) uniform wear pattern: correct sharpening profile; and (b) uneven wear in centre of comb plate: too much concave curvature in sharpening profile. Wear characterized by 3 regions: 1) under cutter tip path; 2) around comb gullets; and 3) under cutter's heel. (refer to Figures 6.1 and 6.2)

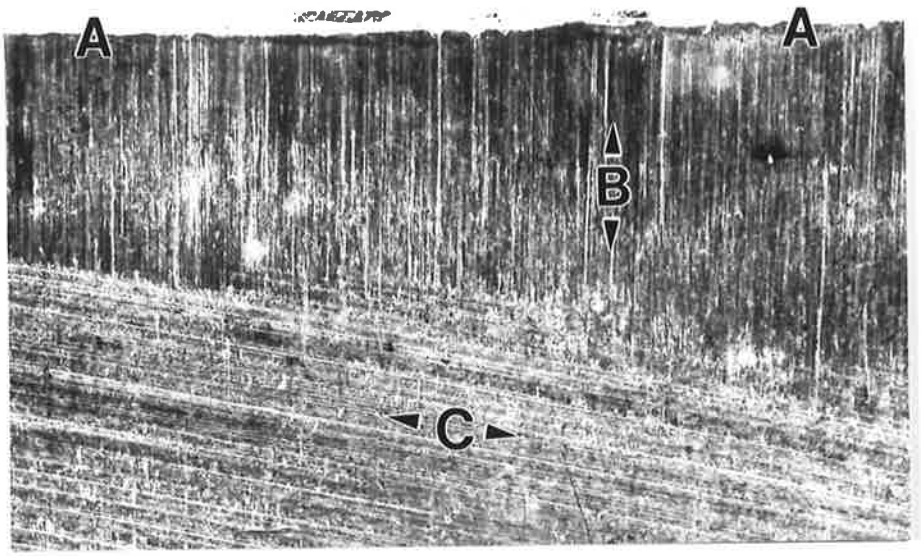

(a)

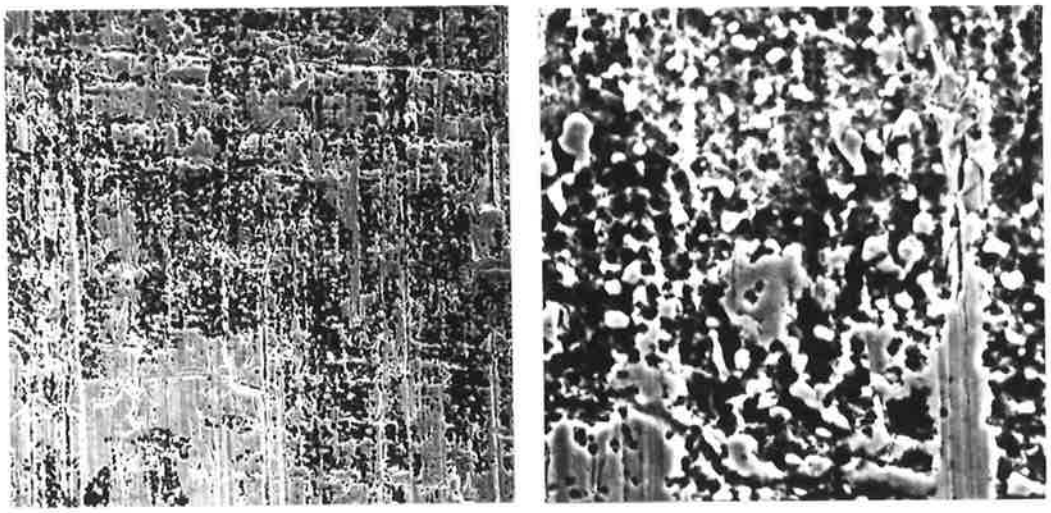

(b) (c)

Figure 7.3: Ground face wear inbetween the tip of the cutter and the gullet regions: (a) macroscopic view showing the cutting edge, A, abrasion from the; cutter, B, and the direction of the original sharpening scratches, C; (b) enlargement of the border in (a); and (c) detail enlargement showing spheroidal carbides, appearing white, and the ferrite matrix, appearing light grey when scratched, or dark grey where carbides have been removed.

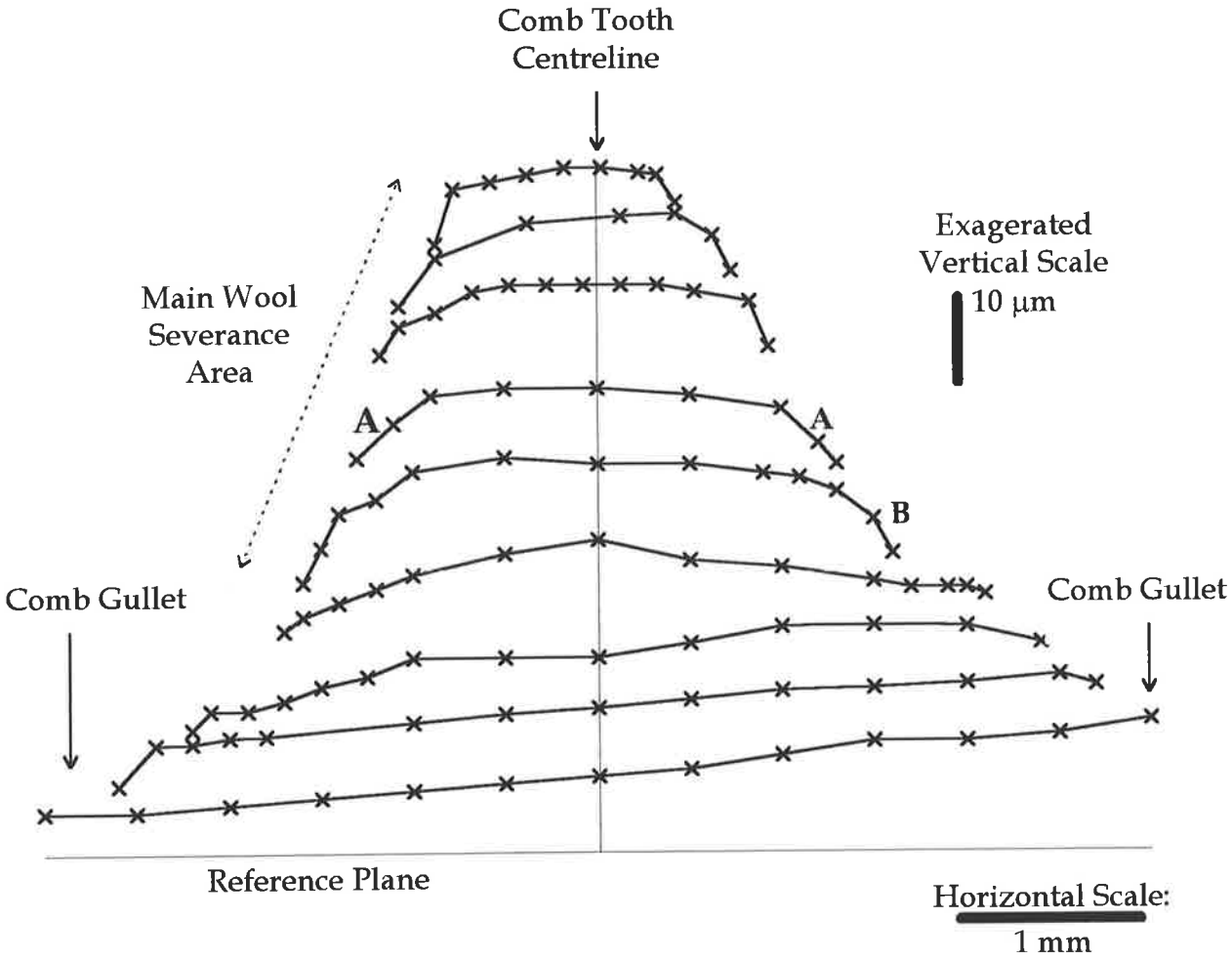

Figure 7.4: Measured surface profiles of a worn shearing comb tooth (from a depth calibrated, travelling optical microscope): 2 mm spacing of profiles. The exagerated vertical scale shows the general "ground face" wear features: the centre of the comb tooth has the least wear, the wear depth increases towards the cutting edges (the edges of each profile), and the cutting edges are both faceted (A) and rounded (B).

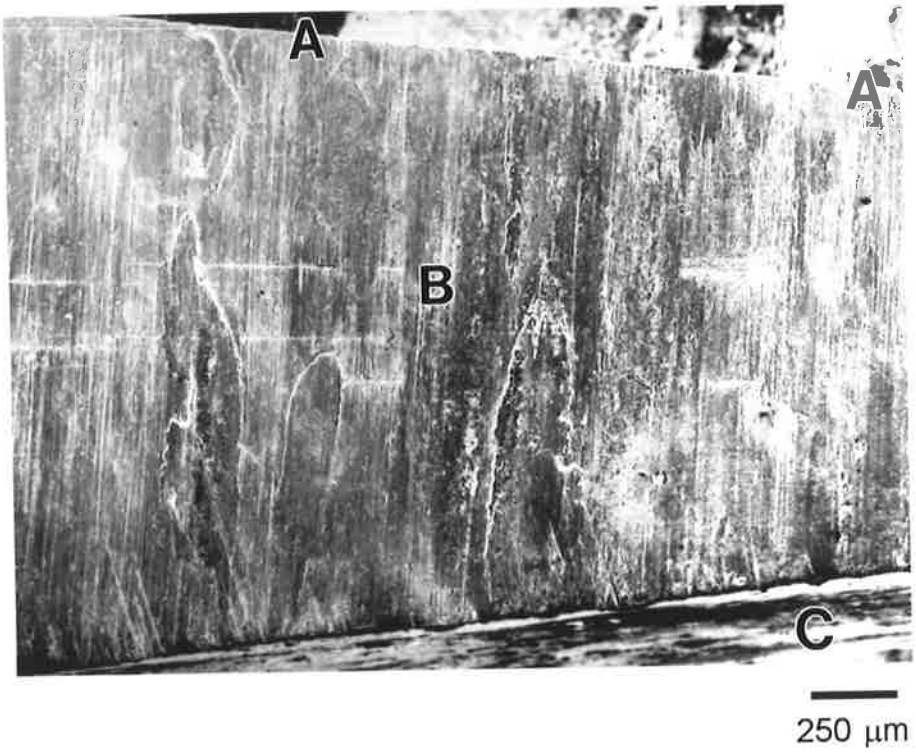

Figure 7.5: Adhesive wear damage across the ground face of a shearing comb tooth (SEM back-scattered electron image): A, cutting edges; B adhered metal; C, direction of cutter's motion.

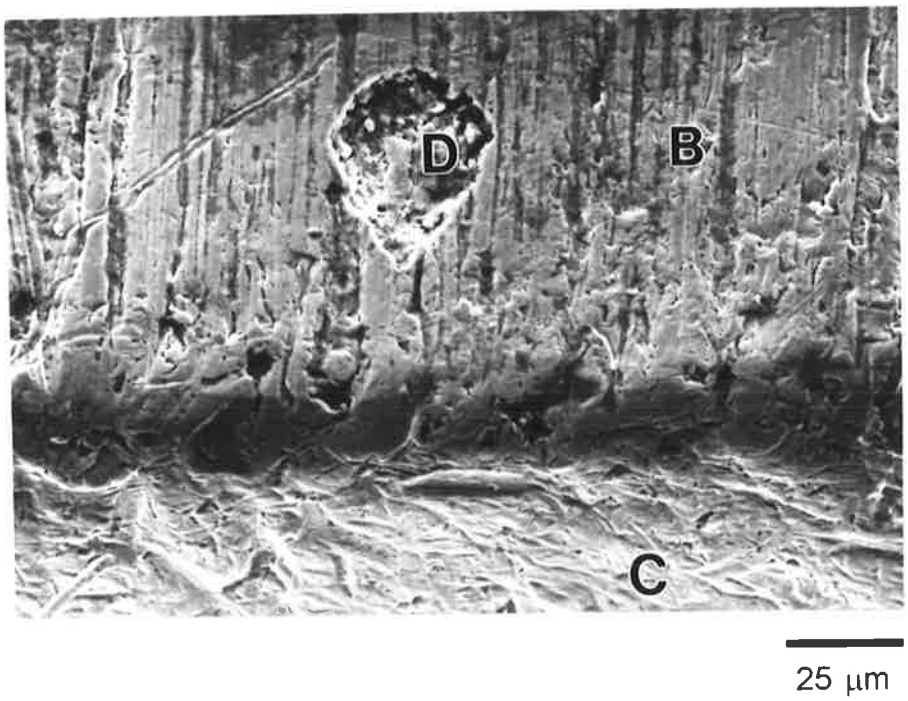

Figure 7.6: Ground face adhesive wear damage (spalling) near the cutting edge of a shearing comb (SEM back-scattered electron image): A, cutting edge; B ground face; C, rake face; D spall. Note the fine cracks in the bottom of the spall which are indicative of the sub-surface fatigue mechanism characteristic to spalling wear.

7.2.2 Wear of the Rake Faces.

In general, three forms of wear were observed on the rake faces of the combs inspected: coarse abrasion, indentation and fine polish. A newly ground, previously unused comb, e.g., Figure 6.4(b), was examined to reveal what wear damage would accumulate in just two hours of shearing. Next, a comb used until the end of its severance life was examined to show the total accumulation of wear damage.

7.2.2.1 *Abrasion:*

After the first 2 hours of shearing with the once used comb, abrasion of the rake faces was found to be concentrated in a 100 μm band starting at the cutting edges and extending down the rake faces, Figure 7.7(a). This band was found to run from under the tip of the cutter's traverse to 5 - 10 mm back towards the gullets, which corresponds to the main wool severance area. Closer inspection, Figure 7.7(b), revealed that while individual 1 - 20 μm scratches were visible, the original planar surface was still readily distinguished. Plastic deformation was apparent in many of the 5 - 20 μm scratches through protrusions along their edges. The appearance of the rake face scratches was distinctly different from the ground face scratches. The rake face scratches were shorter, sharper and deeper than ground face scratches, and had a greater range of scratch densities and directions. Nevertheless, a pattern in the directions of the coarser scratches was distinguished, the dominant direction being normal to the cutting edges. Indentations were also observed on the rake faces of this once used comb having a sparse random distribution and widths of 1 - 5 μm. Clearly the abrasive responsible for these scratches and indentations were mostly angular, while they apparently had a range of indentation force and lateral force.

Abrasion of the of the rake faces outside the distinct 100 μm deep by 5 - 10 mm long region was far less severe, *i.e.*, in the width and density of the scratches. No distinct direction of these fine scratches could be distinguished. At the tips of the comb teeth, 2 μm scratches were found on the rake faces parallel to the comb teeth. Towards the gullet regions, where the rake angle was >5°, a fine polish was sometimes found on

the rake faces which had revealed the 0.5 - 2 μm carbides found in the steel's microstructure. Pre-trial inspection of these combs showed no such scratches or surface relief. The nature of these fine scratches suggest that the abrasives were not applied with a heavy load. On that basis, wool fibers and grit particles compressed together in-between the comb teeth by the foward motion of the handpiece are suggested as the mechanism for this light abrasion (see § 7.3).

For comparison, another comb was inspected which had been used until the end of its "total" life, Figure 7.7(c). The density of scratches on this comb was much higher than on the relatively new comb described above, leaving noticeable relief from the original planar rake faces of the comb. Note the deeper indentations and sharp scratches to greater than 100 μm down the rake face. However, the dominant direction of the scratches was still away from the cutting edges.

7.2.2.2 ***Overall Wear Patterns:***

Rake face wear by abrasion is clearly associated with wool fiber severance and is a cumulative process. The accumulation of damage occurs because the depth of scratching down the rake faces is greater than the ground face thickness removed by the sharpening process, e.g., 100 μm compared to 20 - 50 μm. It is expected that wear of the rake faces will weaken the wear resistance of the cutting edges, which is the reason why hardening of these faces may improve the service life of combs (see § 7.3 and § 7.4).

7.2.3 Wear of the Cutting Edges.

In general, wear of the cutting edges appeared to be a mixture of ground face wear and rake face wear. The degree of rounding of the cutting edges corresponded with the severity of rake face wear, *i.e.*, most severe 0 - 10 mm along the cutting edge from the tips of the cutter teeth. Wear damage included abrasion, adhesion and indentation.

7.2.3.1 ***Abrasion:***

Abrasion of the cutting edges often had a smooth appearance in comparison to both ground and rake face abrasion, Figure 7.6 and Figure 7.7(b), as if the abrasives were fine, or applied with light contact pressure. However, the severity of the abrasion varied considerably as shown Figure 7.7(c).

7.2.3.2 ***Adhesion:***

Adhered metal was found periodically on the ground face side of the cutting edge rounded profile, Figure 7.7(b) and (c). The underlying comb metal of the adhered debris often had evidence of compressive deformation, as if there had been high contact pressure on the top of the adhered metal. As deformed metal from indentations can sometimes protrude above the surrounding worn surface, it is suggested that these protrusions are a possible mechanism which triggers adhesive wear on the ground face.

7.2.3.3 ***Indentation:***

Indentations into the cutting edges were mainly small in size and depth, similar to the fine indentations in the rake faces. Large indentations seemed to convert to gouges across the cutting edges in directions either towards the rake face or towards the ground face. In isolated cases, large indentations were found, Figure 7.7(c), occasionally with embedded particles, Figure 7.7(b).

7.2.3.4 ***Effect of Sharpening Scratches:***

The uneven depth of abrasion in the conventional sharpening process, *i.e.*, before wear, is highlighted in the partially worn regions on the ground face of the combs, Figure 7.1. The angle of the deeper scratches relative to a cutting edge, seems to be important to the running in wear of cutting edges. In particular, if the scratch is nearly parallel to the cutting edge and right on the edge, then this constitutes an initial edge radius, the size of which depends on the depth of the scratch. Figure 7.7(b) shows an example of wear around this type of sharpening scratch: note the apparent work hardening around the deformed zone (less worn). Such a scratch is likely to degrade the severing

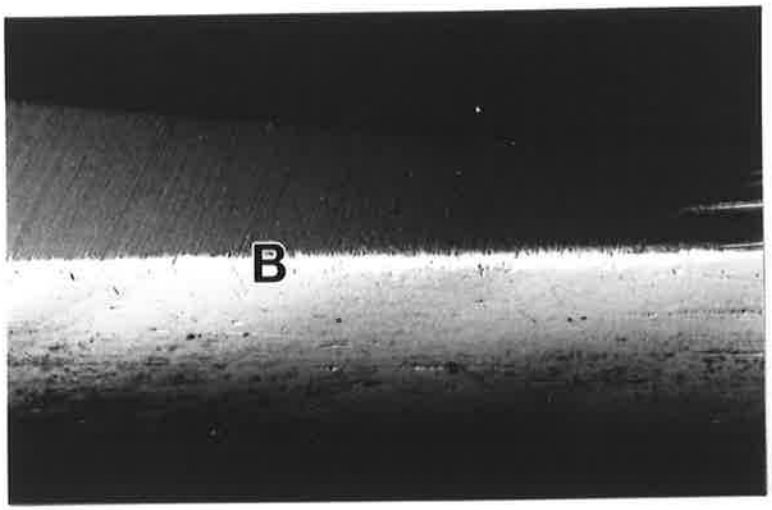

(a)

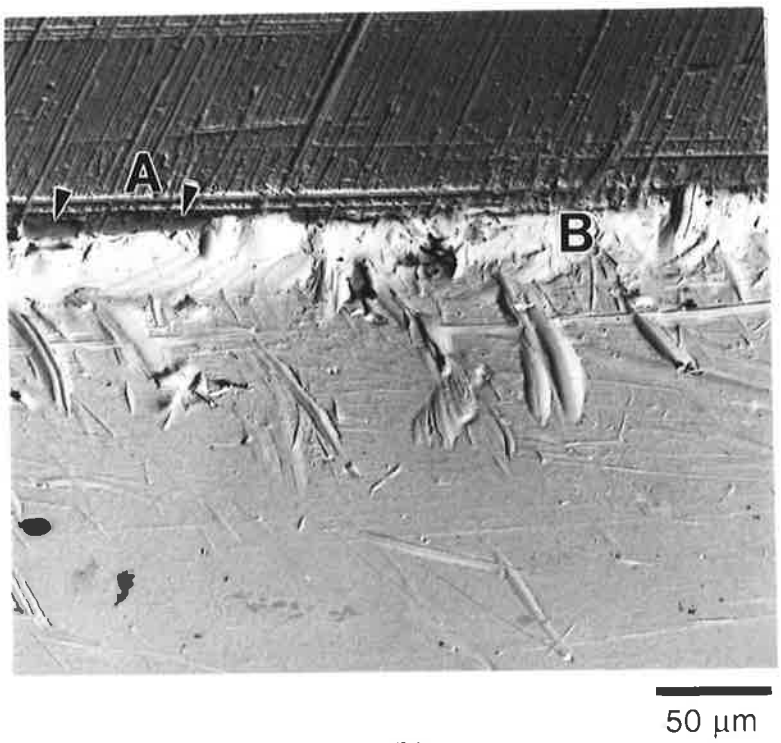

(b)

Figure 7.7: Cutting edge and rake face wear on shearing comb teeth used until the end of their severance life: (a) and (b) are from a comb used for the first time, while (c) is from a comb tooth at the end of its total life: (a) overall view of cutting edge (appears white) in the primary wool severance area (from cutter tip to 8 mm towards gullet); (b) detailed view of (a) showing abrasion marks, indented silica particles, A, adhesion, B, and rounding of the cutting edge: cf. Fig. 6.4; (c) (next page) note the accumulated wear damage to the rake face, e.g., deep indentations, C.

Figure 7.7 (c)

Figure 7.8: Comb tooth wear facet showing where cutter teeth have traversed. Upper and lover grooves were formed by the outside and inside edges of cutter teeth. These grooves apparently formed because of an obstruction, A, that was probably harder than the comb and cutter steel.

performance of that portion of the comb tooth from the beginning of the comb's operation.

7.2.3.5 *Effect of Ground Face Wear:*

The smearing of metal on the angled face, as identified in the ground face wear patterns (Figure 7.2(b)), is likely to cause rounding of the cutting edges if the metal flow occurs only in the direction away from the cutting edge. This single direction is probable through of torsional deflections of the comb teeth suggested in a previous study [84] and the present results. While the results of that study suggest that comb teeth twist to remain in contact with each other, they did not account for the initial process which forms a faceted wear profile. It is suggested that friction forces from abrasion on the ground face and perhaps the force required to sever wool fibers will influence the torsional deflections of the comb teeth. Under these circumstances, on the cutting stroke of the cutter, the comb teeth will twist in the direction of the cutter's motion, while on the reverse stroke of the cutter, the severance loads will not exist and the friction force will separate the comb and cutter faces so that the angled faces will not rub together.

7.2.3.6 *Important Observation:*

Figure 7.8 shows what are clearly indentations from the cutter outer leading edge and inner trailing edge: refer to the comb/cutter interaction shown in Figure 6.2. In-between these indentations, an embedded hard particle seems to have obstructed the wear of the comb edge by the cutter. This observation strongly suggests that the cutter directly contributes to the comb ground face wear through abrasion, without third body grit particles. Furthermore, the embedded particle suggests that uniformly hardened rake faces should improve the wear resistance of the cutting edges and increase the service life of combs.

7.3 MECHANISMS OF COMB WEAR.

Comb wear is significant because it leads to the breakdown of wool fiber severance at the cutting edges. The geometric conditions at the comb and cutter edges at the loss of severance have been estimated in a previous experimental study [84]. In that work, the cutting edges were modelled by three parameters, Figure 7.9(a): the radii of the edges, R_{comb} and R_{cutter}, and their vertical separation, Δ. Therefore, in this study, comb wear is separated into two regions: ground face wear (Δ can increase), and cutting edge rounding wear (R increases). Rake face wear is considered in conjunction with cutting edge wear.

7.3.1 Ground Face Wear Mechanisms.

Previous studies [84,89] have concluded that the dominant wear mechanism of the ground face is three body abrasion from grit ingested between the comb and cutter mating surfaces, *i.e.*, grit initially trapped in the wool fibers. Increased particle size and/or contact pressure was found to increase the wear rate. [84] demonstrated that a short period of "run-in" wear precedes steady abrasion. Adhesive wear has also been found on the ground face [89], but only when the shearing tools were run without lubrication or grit.

However, the present observations suggest that metal/metal wear can be important, without grit (§ 7.2.3.6). Further evidence to support this statement is that combs wear rapidly even when the grit content of the fleece is low, e.g., for pastoral sheep, although wear is more rapid when the grit content is high. Moreover, the present wear studies (§ 0) show that adhesive and fatigue wear can occur during normal operation of the shearing tools, at least in the latter portion of the severance life and total live, respectively. Lim and Ashby [90] have mapped the possible wear modes for 2-body wear of steels against sliding speed, v, and contact pressure, p. In the operational ranges of v and p for shearing tools, adhesive wear and delaminative wear are possible. However, with lanolin as a lubricant, adhesive wear is more likely to occur only at higher contact pressures.

These observations suggest the following progression of ground face wear beyond the above sequence.

Stage 1: "Break-in" wear offsets the high contact pressures between the comb and cutter when they start operation, as discussed by Perrot and Muller [84]. The deformed as-sharpened surface, which has many folds and grooves, can be easily worn away, so, break-in wear is likely to be rapid.

Stage 2: Abrasive wear occurs, both 3-body (comb/grit/cutter) and 2-body (comb/cutter), which will gradually widen the wear facets developed during the break-in stage. The contact pressure, hence wear rate, depends on the location on the comb, the depths of the hollow grind, the loading of the comb onto the cutter, and the instantaneous width of the wear facets (on the ground face). Wear will retard further comb wear, *i.e.*, as the wear facets widen the contact pressure reduces. Nevertheless, the loading of the comb onto the cutter is usually increased periodically during the severance life to offset rounding wear of the cutting edges. Grit will accelerate comb wear. Surface fatigue is possible since the reciprocating motion of the sliding wear generate both local shear forces under the wearing surface, and cantilever bending of the entire comb teeth (see Appendix 7).

Stage 3: Adhesive wear is favored when the mating surfaces become polished and slide under high contact load, *i.e.*, when friction heating reduces the lanolin's viscosity which can cause the hydrodynamic films to break down. Polishing can occur in the final portion of Stage 2 abrasion which can be assisted by accumulations of matted wool fibers which build up inside the hollow sections of the cutter's teeth. Increasing contact loads are usually applied towards the end of the severance life, as discussed in Stage 2.

7.3.2 Cutting Edge and Rake Face Wear Mechanisms.

The present observations of comb wear have shown that the strongest abrasion of the rake faces coincidences with the most pronounced rounding of the cutting edges in

the wool severance regions along the cutting edges. This indicates that rake face and cutting edge wear are caused by the same mechanism. Since the cutter cutting edges cannot directly contribute to comb cutting edge and rake face wear (a geometric impossibility), indirect wear by grit particles and wool fibers are the only possibilities. Previous studies on cutting edge wear [84] suggest that wear occurs by the ingestion of grit particles (borne by the fleece) in-between the edges.

Therefore, the interactions of grit particles with the cutting edges and rake faces are modelled below (§ 7.3.2.1) to explain mechanism of edge rounding wear and suggest the link between cutting edge and rake face wear. This model assumes that the wool fibers take no part in the wear processes but only act as a passive carrier for the grit.

The wear damage on the rake faces in this study extended more than 100 μm down the rake faces of comb teeth, beyond the range of unsupported grit particles. This shows that wool fibers must have an active role in rake face wear, either as a substrate to press grit against the rake faces, or as an abrasive. Sharp ends of severed fibers may even gouge the rake faces depending on their relative hardnesses. Now, wool fibers in a fleece are severed only after the fibers are collected by the tapered regions between comb teeth pairs (during the foward motion of the comb), and after the fibers are compressed by the cutter [89], Figure 7.10. Collection, compression and severance all involve the movement of wool fibers and supported grit particles relative to the comb teeth, under pressure (reaction to being compressed). During the collection and compression stages, the fibers and grit move essentially parallel to the cutting edges, while during severance, the fibers and grit move perpendicularly to the cutting edges. In the collection stage, the fibers will be lightly compressed, depending on the fiber density and foward speed of the comb, so there will be a light pressure of the fibers on the rake faces available for abrasion. From the experiments of [89,91], the pressure on the fibers during the compression stage was found to continually increase, while reaching a maximum during the severance stage. Based on this limited information, the deepest scratches are likely to be perpendicular to the cutting edges in a direction down the rake

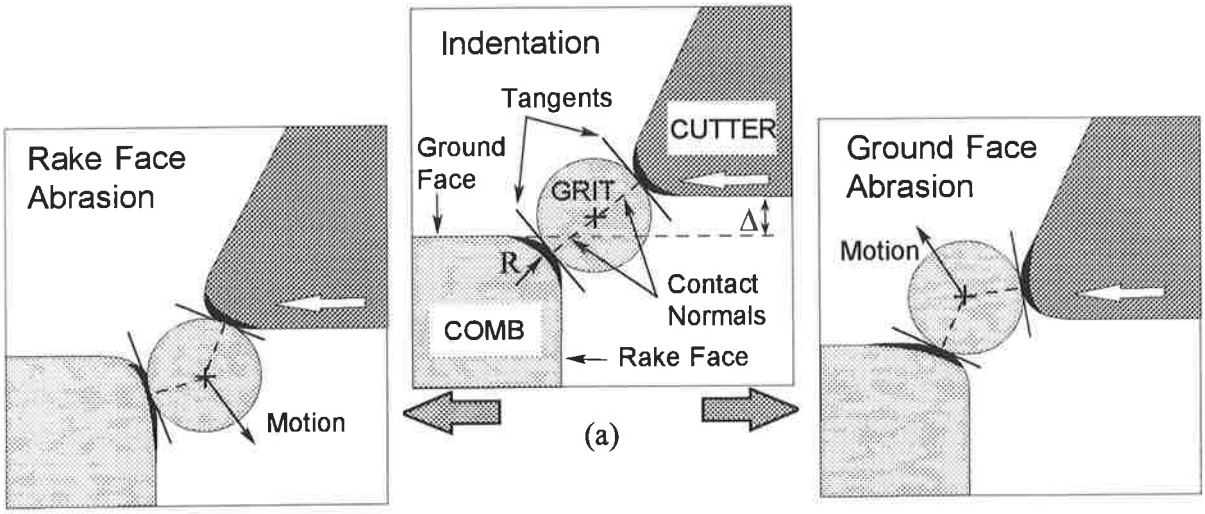

Figure 7.9: Wear processes on cutting edges and rake faces from grit indentation and abrasion, as viewed in cross-section along the cutting edges (assumes spherical grit particles). The cutting edge wear is described by the radius of each edge, R, and by the vertical separation of the edges, Δ. If a grit particle is initially directly inbetween the cutting edge pair (a), then the particle may indent either edge, or be squeezed from between the edges causing abrasion during ejection (b) or (c).

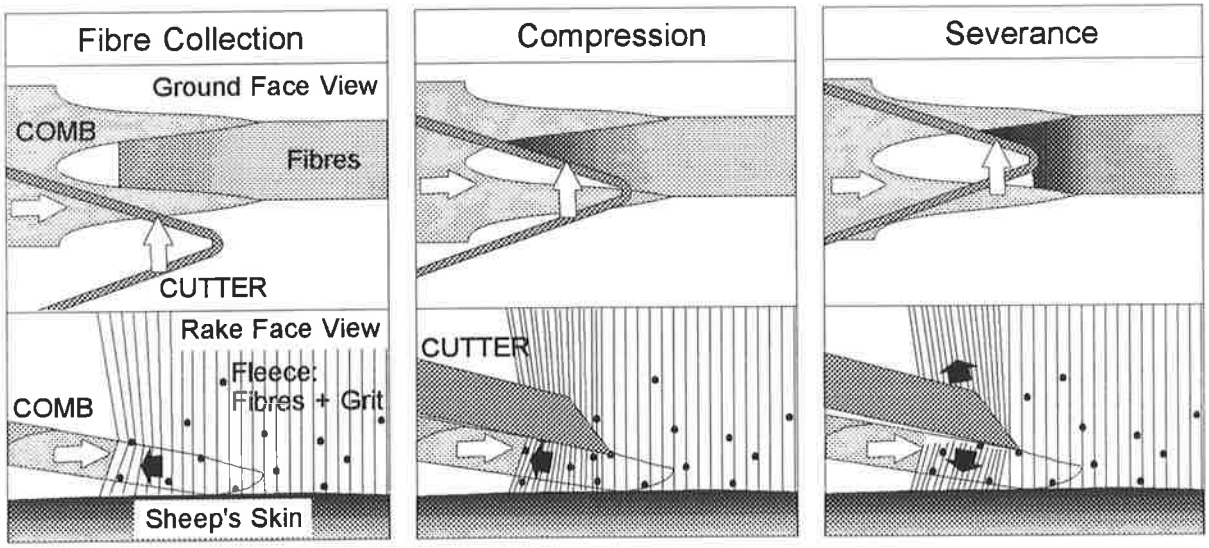

Figure 7.10: Wear processes on rake faces from grit particles and wool fibres during the three stages involved in shearing: (a) collection of the fibres, (b) compression of the fibres, and (c) fibre severance. Due to the reaction pressure, which must develop in the fibre group during each stage, and the motion during re-arrangement of the fibres, abrasion of the rake faces is probable.
➧ shows the probable abrasion direction from fibre movement, while ⇨ shows the motion of the comb and cutter.

faces, while the shallowest scratches should be parallel to the edges. Discrete scratches in these directions were observed on worn combs in § 7.2. Both grit particles and wool fibers could abrade the rake faces:

7.3.2.1 ***Model of Wear from Unsupported Grit Particles:***

Since hard grit particles are of approximately equal hardness as quenched steel, possible wear mechanisms are indention and abrasion by grit particles trapped in-between the cutting edges. Perrot and Muller [84] measured the size range of grit particles to be from 25 - 125 μm, and the cutting edge radii from 15 to 50 μm (at the loss of severance).

In modelling this form of wear, consider first the special situation of a spherical particle positioned in-between a cylindrical chamfered cutting edge pair so that the contact normals are 180° apart, Figure 7.9(a). In the worst case, as the edge pair converge, the particle will indent both edges. Since the cutter is driven by the handpiece to oscillate over the comb, indenting must be a temporary process. Examples of indented particles were found in the present study (Figure 7.7), but edge rounding was more prevalent. The probable mechanism which reduces the chance of particle indentation is cantilever deflection of the comb and cutter teeth, which instead favors ejection of the particle out of the edge pair (see § 7.4.1.3). Therefore, edge rounding must occur during the ejection process. Next, consider the events as the grit particle moves tangentially in-between the cutting edges under load. The angle in-between the contact normals will increase, and in addition to the indenting force, a force component becomes available for plowing the surface, Figure 7.9(b) and (c). Thus, the overall sequence of events which will lead to wear of the cutting edges by a centrally located grit particle is likely to be:

$$\text{Indentation} \rightarrow \text{Abrasion} \rightarrow \text{Grit Ejection}$$

In a more general situation, grit particles will be randomly positioned in relation to the cutting edges, so the first steps in the sequence will not always occur. The above

description has not considered elastic deformation of the cutting edges since the force required to cause plastic deformation around small particles is low.

Based on the above descriptions, a geometric model was constructed to predict the likelihood of particles causing damage to the cutting edges and rake faces. The grit particle size relative to both the edge radii and the edge vertical separation (R and Δ) were anticipated as the principle variables to model.

7.3.2.2 ***Geometric Model:***

The particle size, D, the position of the particle with respect to the cutting edges, y, and the angle between the contact normals, $\Delta\theta$, were the three parameters investigated, Figure 7.10. The cutting edge radii were assumed to both equal R. For the purposes of generalization, both D and y were non-dimensionalized to the cutting edge radius, R, giving D/2R and y/2R, respectively. A 30° rake angle was assigned to the cutter profile, while the comb rake angle was 0°: values typical of the cutting edges towards the tooth tips. Scissor and closure angles were both assigned zero in these calculations, *i.e.*, the ground faces of both the comb and cutter were modelled flat and parallel to the cutter's motion.

Since particles are of the size range 25 - 125 μm, while the edge radii are in the range 0 - 50 μm, two geometric cases were formulated as shown in Figure 7.11: Case 1: large abrasive ($D/2 > R+\Delta$) and particle centreline below the comb edge radius ($y < 0$); Case 2: any abrasive size with contact points on each cutting edge radius. The third case when the particle is in contact with the cutter's rake face was not considered, as the rake face and cutting edge wear damage only were of interest here. The geometric formulae used to calculate $\Delta\theta$ for each case are shown in Figure 7.11.

With reference to the sequence of Indentation/Abrasion/Ejection described above, arbitary $|\Delta\theta|$ ranges for each process were set at: 0° to 30° for indentation, 30° to 60° for abrasion, and 60° to 90° for particle ejection.

7.3.2.3 *Simulations:*

The plot of the comb/cutter contact normal angular difference, $\Delta\theta$, as functions of grit vertical position with respect to the comb, y/2R, and grit size, D/2R, is shown in Figure 7.12(a). This model shows that increasing the particle size increases the range of particle positions over which the particle can damage the cutting edges, e.g., when $\Delta\theta$ is between -90° to +90°. Next, regarding the kind of damage caused by grit particles, Figure 12(b), shows the regions where indentation and abrasion of the ground face rake face and cutting edge are likely to occur. Using the dimensional variables, Δy, R and D, this data can alternatively be presented, Figure 7.13, as the range of grit positions, Δy, over which a particle will have a $\Delta\theta$ value less than $\Delta\theta$ of +/-90°. An almost linear increase in Δy is observed for both increasing particle size and cutting edge radius, irrespective of that size. This suggests that cutting edge wear is an accelerating process: edge wear makes the edge more susceptible to wear.

A limitation of this model is that real grit particles are not spherical but have irregular surfaces and morphologies. Therefore, wear damage will be more severe than can be accounted for by ideal spherical particles. A final consideration: as the surface roughness of the rake faces and cutting edges increase, the chance of a grit particle becoming trapped in a local indentation increases because the contact planes will favor more indentation. Thus, more abrasion is likely to occur, as seen in Figure 7.7(c).

7.4 MECHANISMS OF LOOSING WOOL FIBER SEVERANCE.

The primary reason for loosing wool fiber severance while shearing must be insufficient localized shear stress developing in the fibers. Since the shearing handpiece is designed to transmit more than sufficient force to the cutter to fracture even the maximum cross-section of fibers possible (see § 7.4.1.2), unsuitable geometries of the comb and cutter edges and their local interaction must be the cause of loosing severance. In the previous section, these geometries were approximated by two variables: the radii of the cutting edges, R (assumed equal for comb and cutter), and the vertical separation of the cutting edges, Δ.

Case 1: Grit particle contacting the Rake Face: $\frac{D}{2} \geq R + \Delta$

$y \leq 0$

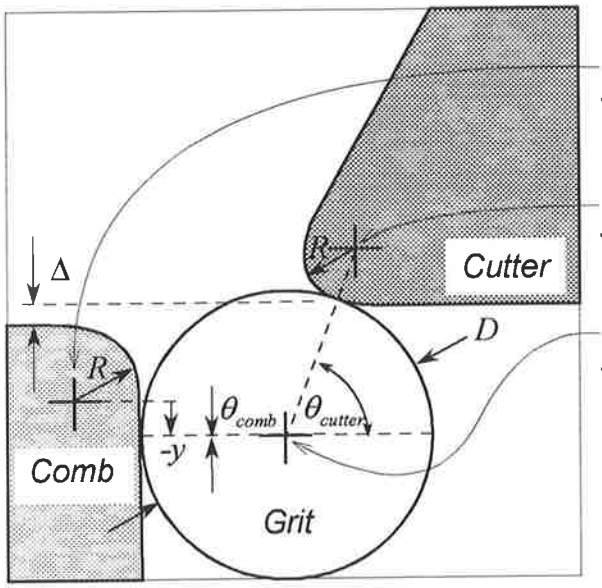

$$x_{comb} = 0$$
$$y_{comb} = 0$$
$$x_{cutter} = R + \tfrac{D}{2} + \sqrt{(R+\tfrac{D}{2})^2 - (2R + \Delta - y)^2}$$
$$y_{cutter} = 2R + \Delta$$
$$x_{grit} = R + \tfrac{D}{2}$$
$$y_{grit} = y, \ (R + \Delta - \tfrac{D}{2}) \leq y_{grit} \leq 0$$
$$\theta_{comb} = 0$$
$$\theta_{cutter} = \sin^{-1} \frac{2R + \Delta - y}{R + \frac{D}{2}}$$

Case 2: Grit particle contacting the Cutting Edge:

$0 < y \leq (2R + \Delta + R.\sin 30^o)$

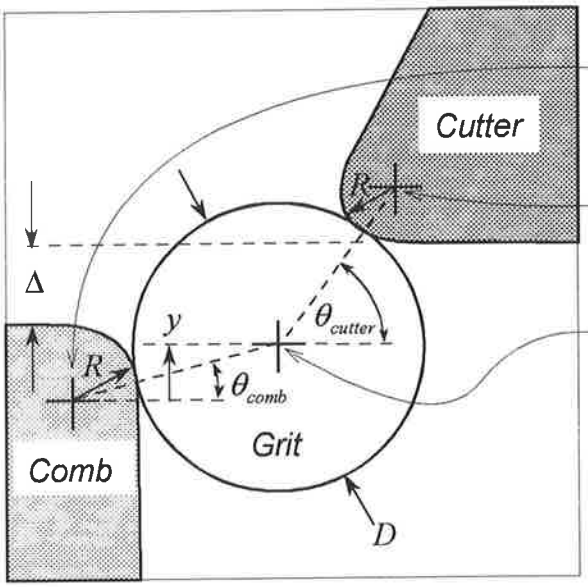

$$x_{comb} = 0$$
$$y_{comb} = 0$$
$$x_{cutter} = \sqrt{(R+\tfrac{D}{2})^2 - y^2} + \sqrt{(R+\tfrac{D}{2})^2 - (2R + \Delta - y)^2}$$
$$y_{cutter} = 2R + \Delta$$
$$x_{grit} = \sqrt{(R+\tfrac{D}{2})^2 - y^2}$$
$$y_{grit} = y, \ 0 < y_{grit} \leq (2R + \Delta + R.\sin 30^o)$$
$$\theta_{comb} = \sin^{-1} \frac{y}{R + \frac{D}{2}}$$
$$\theta_{cutter} = \sin^{-1} \frac{2R + \Delta - y}{R + \frac{D}{2}}$$

$$\Delta\theta = \theta_{cutter} - \theta_{comb}$$

Figure 7.11: Model of spherical grit particle interaction with the cutting edges of a shearing comb cutting edge and rake face. The model calculates the angular difference in the contact normals of the particle with both the comb and cutter edges to predict the type of wear damage inflicted by the grit on the comb. See text for details of model.

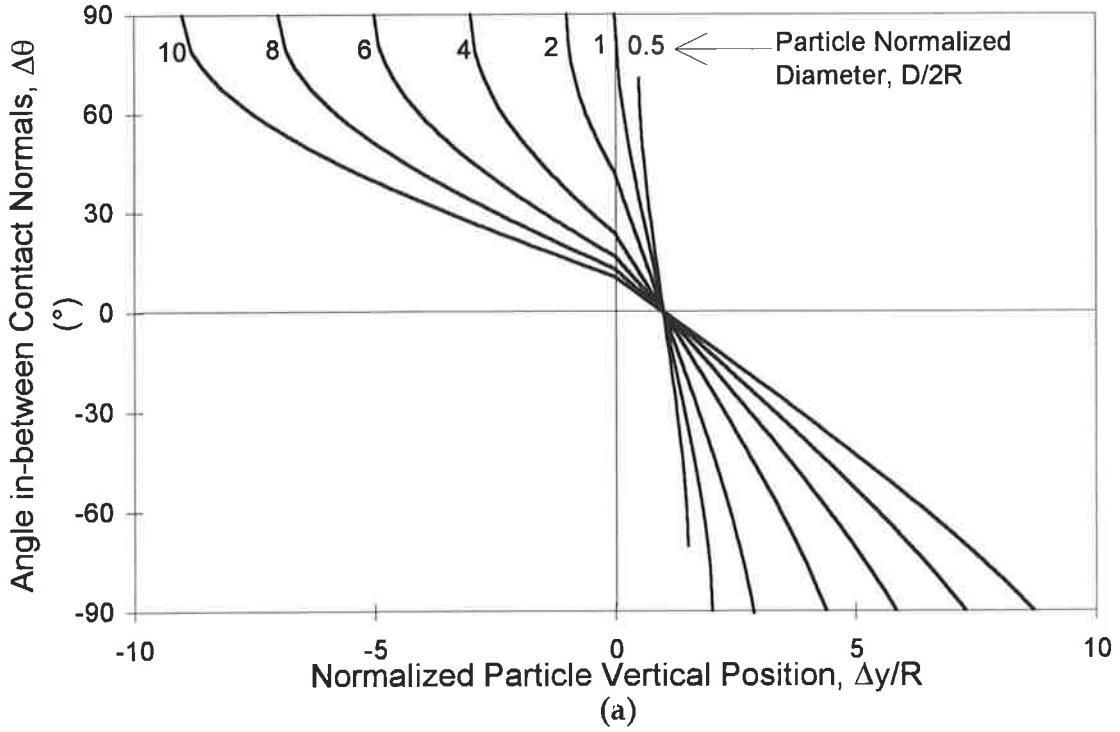

(a)

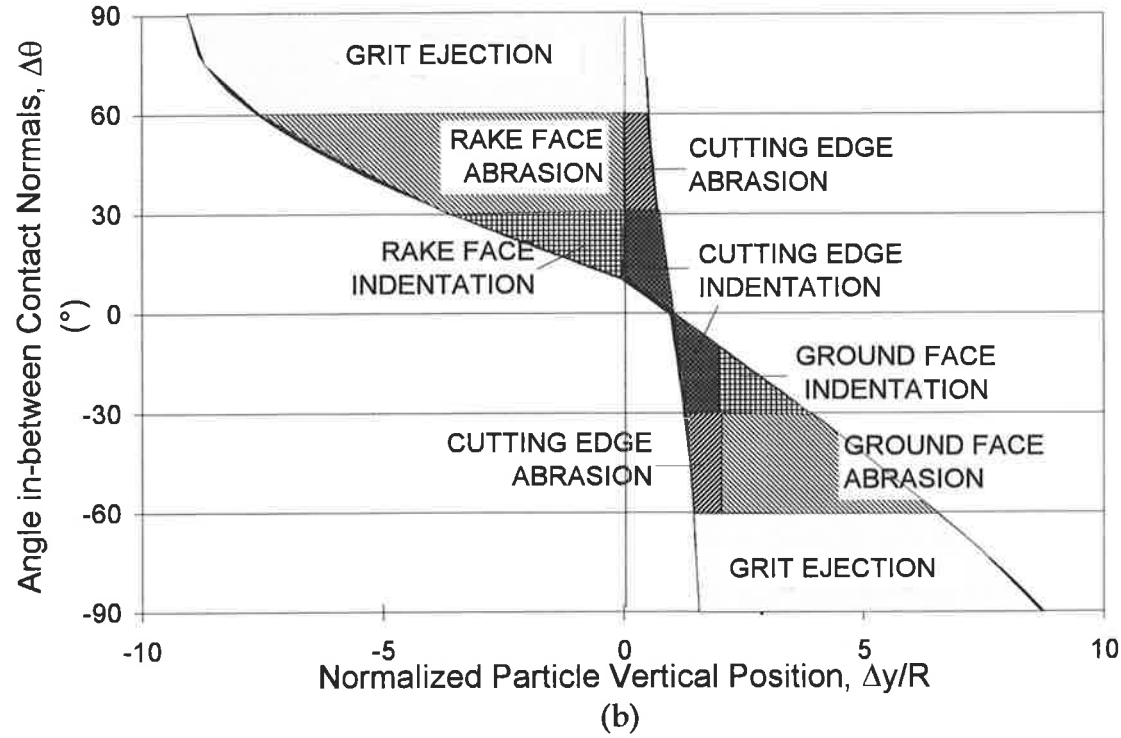

(b)

Figure 7.12: Simulation of ideal spherical grit particle movement during closing of comb and cutter cutting edges while sheep shearing. The assumption about particle movement is that it depends only on the angular difference, $\Delta\theta$, between the contact normals made between the particle and the cutting edges and rake faces (see Fig. 7.11): at low $\Delta\theta$-values, indentation; particle movement (abrasion) at intermediate $\Delta\theta$-values; and particle ejection at high $\Delta\theta$-values.

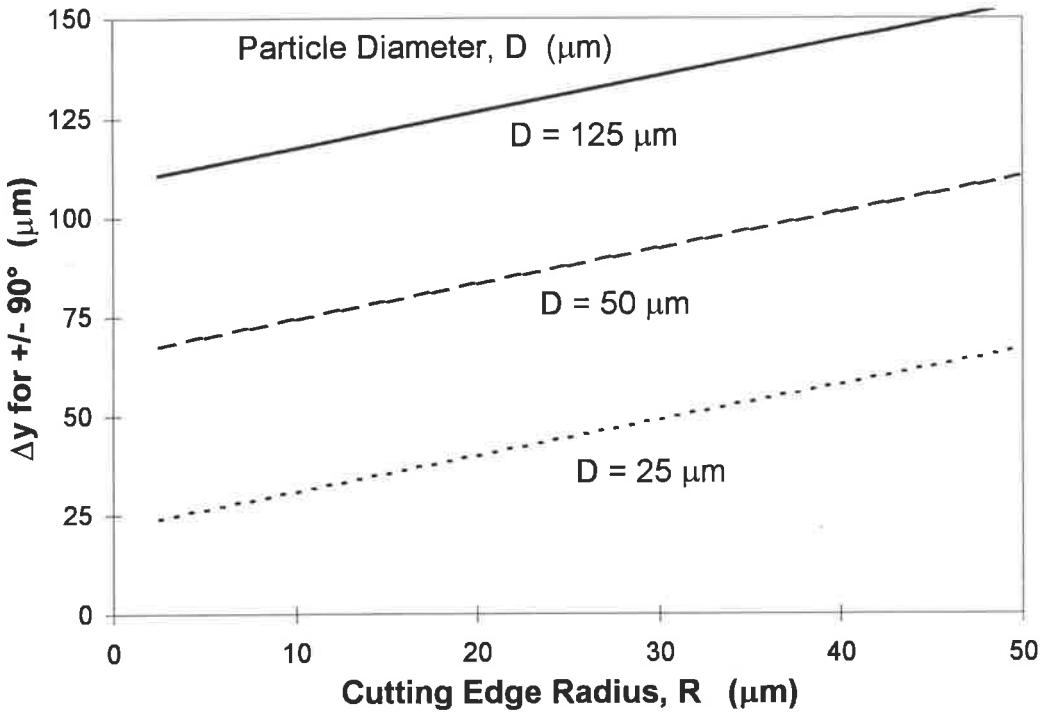

Figure 7.13 Effects of grit particle diameter, D, and cutting edge radius, R, on the likelihood of grit particles damaging the cutting edges and rake faces of a comb tooth. This graph uses the range of grit particle vertical positions, Δy, where particles could be captured by by comb and cutter cutting edges as they converge, to show that for typical values of R and D, increasing either R or D increases the chance of grit being captured. This simulation uses a zero vertical separation of the cutting edges (Δ = 0), expected to be typical of cutting edges in their intermediate stages of wear during shearing. If Δ is greater than zero, then grit particles are less likely to be captured (from other simulations).

In this section, a model is developed to predict the conditions where fiber severance breaks down through excessive wear. The model is based on the analogous process of shearing sheet metal in a guillotine. Next, the importance of ground face wear, cutting edge wear and rake face wear is discussed in terms of R and Δ.

7.4.1 Model of Fiber Severance with Worn Tools.

Since wool fiber severance relies on the local interaction of small fiber groups with the sections of the comb and cutter cutting edges, only this local situation is modelled here. The model consists of a geometric description which accounts for the alignment (rotation angle) of a bundle of wool fibers in-between the comb and cutter edges just before severance, Figure 7.14. The supposition of this model is that above a certain fiber rotation angle, fiber severance will deteriorate.

The concept of this model came from the author's experience in operating a guillotine to shear sheet metal. If the guillotine blades were excessively worn (rounded) or if the alignment of the blades was poor, then thin narrow sheets, in particular, would rotate around the cutting edges causing either poor severance (e.g., a bent edge) with increased cutting force, or no severance if the sheet became jammed between the those edges. During sheep shearing, Figure 7.10, wool fibers are compressed together by the cutter tooth onto the comb tooth before severance, which naturally tends to tilt the fibers around worn cutting edges in the direction of the cutter's motion.

However, shearing problems in the guillotine could be partly or totally alleviated when a clamping plate was used to clamp the sheet metal close to the cutting edges, *i.e.*, a rotational restraint. However, in wool severance, this kind of rotational restraint only occurs under specific circumstances. Real fibers are not rigid parallel cylindrical shapes but actually "crimped" along their length, so will therefore act like soft springs when stretched during the compression process. This property of the fibers will tend to reduce the restraints on fiber rotation around the cutting edges. In the case of high fiber density from the fiber collection process, Figure 7.10(a), e.g., when the comb is moving

foward rapidly, Figure 6.2(b), then the fibers will tend to provide their own rotational restraint by the width if the bundle.

In the guillotine problems, sheet metal accommodates rotation by shear deformation in the plane of the sheet which accelerates the problem. However, a group of wool fibers is more susceptible to internal shear deformation because the fibers are free to slide over one another. Under these conditions, fibers could wedge the cutting edges apart (through cantilever deflection of the thin comb teeth) and break down the severance process along the remainder of the comb tooth cutting edge, at least on that pass of the cutter.

If a single row of fibers is to be severed in-between a cutting edge pair, then if the fibers are restrained just below the comb edge, intuitively the greater the R and Δ values, then the greater the bending moment (torque) generated in the fibers. Increasing R and/or Δ will increase the bending stresses, while increasing R will reduce the contact stresses (necessary to locally sever the fiber). However, if the fibers are free to rotate so that they sit directly in-between the cutting edges (Figure 7.14(b)), then intuitively the angle of rotation of the fibers will change with both R and Δ, as long as Δ does not exceed the fiber diameter. Now the angle of rotation of the fibers will also depend on the number of fiber rows in the fiber bundle trapped in-between the cutting edges: the greater the number, the smaller the expected rotation.

A geometric model based on fiber rotation was constructed as follows. The model assumes that: the fiber bundle has parallel sides, the cutting edges are parallel, and the fiber bundle will rotate freely until it lies normal to both cutting edges. The fiber bundle consists of an arbitrary number of cylindrical wool fiber rows, N (parallel to the cutting edges), and is positioned in-between a parallel cutting edge pair (the scissor and closure angles (Figure 6.3) are both assumed to be zero). The fiber diameter, d=20 μm, while the pitch between fiber rows, $p=d.\sin(60°)$. The comb and cutter rake angles are 0° and 30°, respectively, while the cutting edge radii are both equal to R, and the vertical separation is Δ. The rotation angle, ϕ, of a fiber bundle consisting of N fiber rows in-between a cutting edge pair is calculated by Equation 7.1.

$$\phi = \sin^{-1}\frac{R+\Delta}{2R+\Delta F_{Real}}, \qquad (7.1)$$

where the estimated thickness of the fiber bundle, $\Delta F_{Real} = C_{compaction} \cdot \Delta F_{Ideal}$; the ideal thickness of the fiber bundle, $\Delta F_{Ideal} = (N-1).p + d$; and $C_{compaction}$ is a factor which relates the real compaction ratio of the fibers to the ideal compaction ratio. However, to use this model, typical numbers of fiber rows in the fiber cross-section must be estimated as a function of the speed of the comb through the fleece, and typical compaction ratios must be calculated, as follows.

7.4.1.1 ***Estimates of Fiber Cross-Sections During Shearing & Fiber Compaction Ratios:***
The number of fibers collected in-between a pair of comb teeth depends on the density of fibers in the fleece, the spacing of the comb tooth tips, the position of the pair of teeth across the comb, the frequency of cutter oscillation, and the speed of the comb through the fleece (the "blow speed"). The blow speed typically ranges from 0.2 - 1.2 m/s. In a standard Merino fleece, there are typically 200 - 250 fibers, 20 μm in diameter, per square millimetre of the sheep's skin: the "free fiber density". Now, as the comb has 13 teeth and is 75 mm wide, the comb will collect 0.35 - 1.6 x10^6 fibers/s in-between each pair of comb teeth based on the free fiber density and range of blow speeds. Since each cutter tooth oscillates across four comb teeth and has the slowest sweep speed at the edge comb teeth, the longest and shortest periods before severing the collected fibers will occur on the outer pair of teeth, *i.e.*, the maximum number of fibers will be severed as the cutter sweeps towards the outer tooth then, soon afterwards, the minimum number of fibers will be severed as the cutter reverses its sweep. This situation is simultaneously repeated four times across the width of the comb. Field *et al.* [89] have measured the instantaneous force required to drive the cutter over the comb while severing wool: three force peaks were observed per sweep of the cutter (*i.e.*, left-to-right, or right-to-left) which correspond to the three wool collection areas per cutter tooth. The magnitudes of the peaks were found to be: lowest (1st peak), middle (2nd) and highest (3rd), confirming the above statement. Based on these magnitudes, the ratio of the maximum to minimum collected fibers severed per oscillation of the cutter

is approximately 5:1. Therefore, at a cutter frequency of 50 Hz and the fastest blow speed (1.2 m/s), the maximum number of fibers collected per cycle will be 2.67×10^4. At the slowest blow speed (0.2 m/s), the minimum number of fibers collected will be 0.12×10^4. If these fibers are evenly spread over the length of the cutting edge where severance occurs (~15 mm), then the maximum depth of fibers severed would be 36 fiber rows, while the minimum depth would be 1.6 fiber rows. The minimum number of fiber rows is likely to be one, since there must be periods when the handpiece moves through the fleece slower than 0.2 m/s.

The fiber compaction from the free fiber density also affects the rotation angle of the fiber bundle around the cutting edges. An ideal group of wool fibers would be axially parallel, 20 μm diameter cylinders that are free of contaminants (lanolin, water or grit), Figure 7.14(a). The area percentage occupied by the uncompacted fibers in an axial cross-section is 6 - 8%. If these ideal cylinders could be ideally close packed into the minimum cross-section, then the area percentage occupied by the fibers would be 6.6 - 8.8%, or a compaction ratio of 11 - 15 from the free fiber density. To test real compaction ratios, a sample of 226 fibers was compressed between four flat surfaces into a square cross-section. This fiber bundle fitted readily into a 0.25 mm^2 area, e.g., a compaction ration of 4:1 was easily achieved. As shown in Figure 6.2(b), at the fastest blow speed, fibers collected by the advancing comb will be compacted in an approximately 7:1 ratio before they can be severed; before severance, further compaction is likely. Differences from the ideal compaction behavior could be related to the irregular surfaces of the fibers, the irregular packing of the fibers through friction, and the non-parallel fiber orientations. From the perspective of fiber rotation around the cutting edges before severance, the ideal compaction ratio will estimate a higher rotation angle than the real compaction ratio, *i.e.*, ideal compaction is the worst case.

7.4.1.2 ***Simulations using Geometric Model:***

From the estimates above, as the worst case, the minimum number of fiber rows was set at one, while the maximum was set at 10 (since more rows than this would have

difficulty in rotating). Figure 7.15 shows the angles that fiber bundles rotate around worn cutting edges before severance, as predicted from Equation 7.1. This model of fiber rotation demonstrates that the rotation of the fiber bundle reduces with increasing handpiece speed, and increases with increasing cutting edge wear (radii and cutting edge separation, R and Δ). The usual range of R where fiber severance breaks down is 15 - 50 μm [84]. Assuming that the cutting edges remain in close proximity (Δ = 0 μm), at R = 15 μm, 1 fiber will rotate ~ 35°, while at R = 50 μm, 10 fibers will rotate ~ 20°. Beyond 45°, slippage of the fibers in-between the cutting edges is probable, which could wedge the cutting edges apart (an increase in Δ) and lead to incomplete fiber severance. For thin fiber bundles, *i.e.*, low comb advance speeds, the effect of increasing Δ above zero on the fiber rotation angle has a stronger effect on the rotation angle than increasing R. For thick fiber bundles, the reverse is true, but the rotation angles are smaller than with thin bundles.

This simple model can reasonably describe the effects of wear on the break down of the fiber severance process. The significance of this model is that is predicts that fiber severance at low blow speeds will be the most difficult test of a worn comb.

7.4.1.3 ***Effects of Comb Tooth Deflections:***

Fiber severance can be lost if a comb tooth excessively deflects away from the cutter tooth as a cantilever because of a foreign body in-between the comb and cutter teeth. Apart from metal build up from adhesive wear, wool fibers, debris and grit can become ingested between the teeth if the force applied to the cutter tooth onto the comb tooth is too low. In Appendix 7, the cantilever deflection of a typical comb tooth was studied. For a new comb that has an overall thickness of ~ 3.2 mm, the spring constant of a comb tooth perpendicular to the comb plate under the tip of the cutter is ~ 670 N/mm. That is, to deflect 1 μm away from a cutter tooth, a force of 0.67 N (~ 67 grams) must be applied. However, a pre-load exists between the comb and cutter, to assist fiber severance, which already deflects the comb teeth up to 200 μm. This pre-load is evidently not sufficient to counteract the effects of worn cutting edges: comb tooth

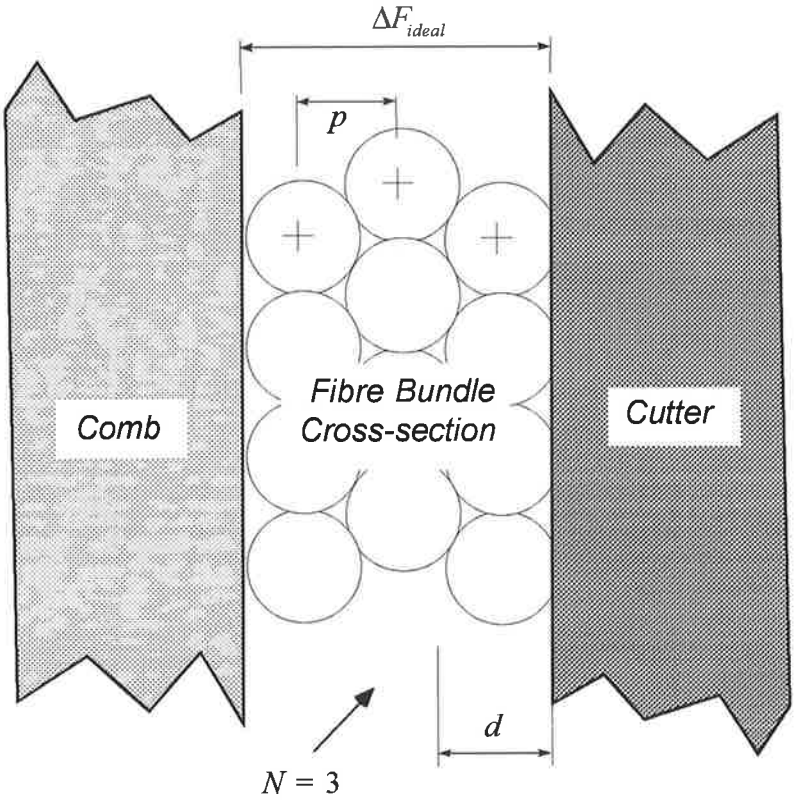

(a)

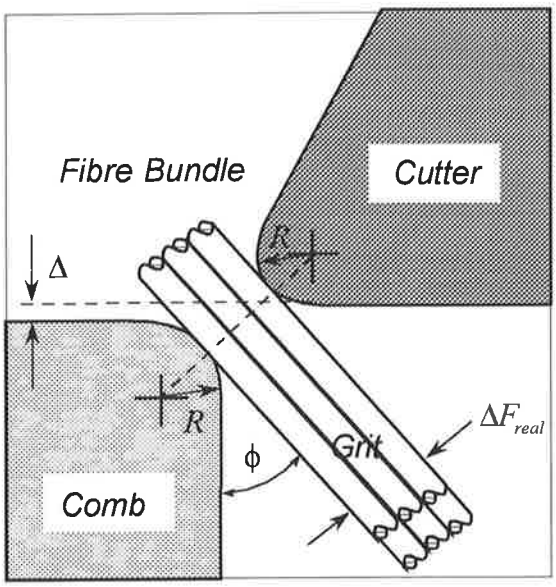

(b)

Angle of rotation of wool fibre bundle inbetween cutting edges,

$$\phi = \sin^{-1} \frac{R + \Delta}{2R + \Delta F_{real}}$$

(Equation 7.1)

Figure 7.14: Diagram of the ideal geometry of a group of fibres about to be severed by a worn comb and cutter edge: (a) geometry of fibre group in the plane of contact with the comb and cutter edges; and (b) geometry perpendicular to the contact plane [e.g., (a)]. See text for details.

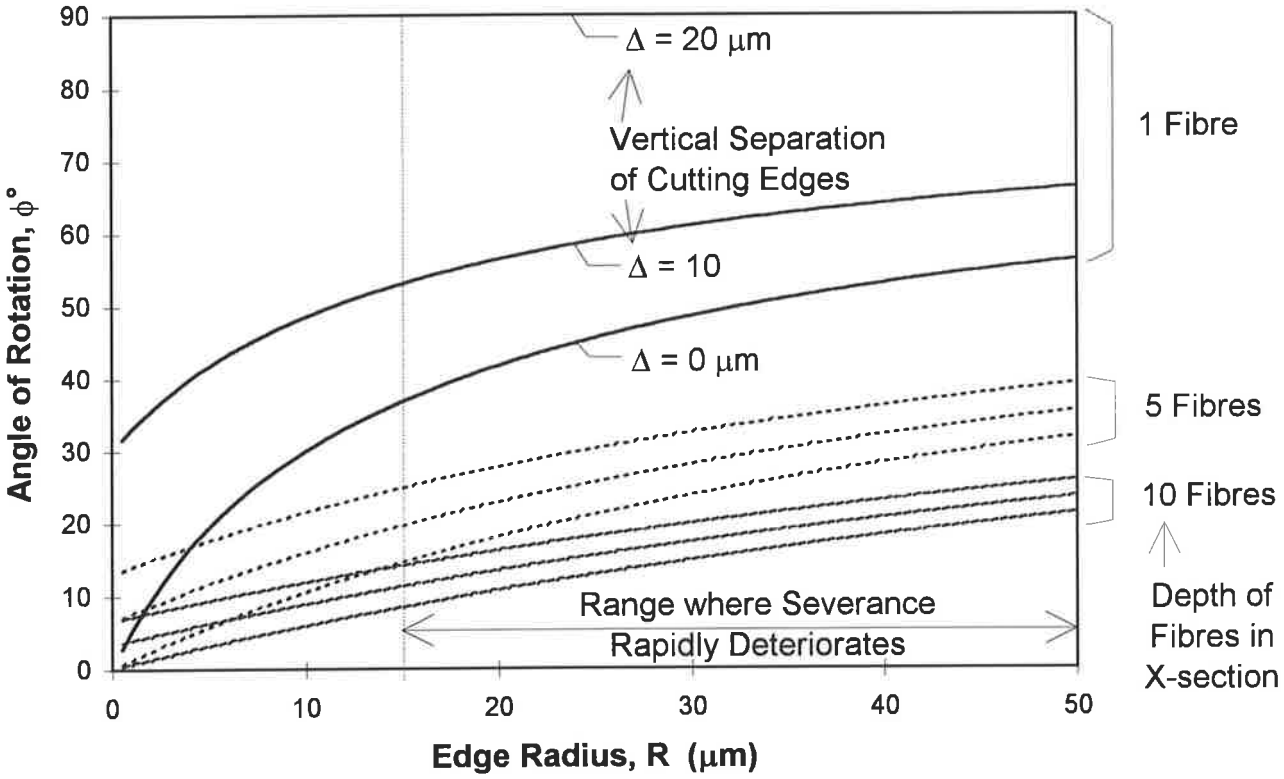

Figure 7.15: Prediction of the angle that a fibre bundle rotates around worn cutting edges, before severance (from Equation 7.1). The "bundle" refers to the depth of fibres sandwiched between converging cutting edges. Wear of the cutting edges is described by the edge radius, R, (assumed equal for comb and cutter) and the vertical separation of the cutting edges, Δ. The usual range of R where fibre severance breaks down is 15 - 50 μm. Assuming Δ = 0 μm, at R = 15 μm, 1 fibre will rotate ~ 35°, while at R = 50 μm, 10 fibres will rotate ~ 20°. Beyond 45°, slippage of the fibres inbetween the cutting edges is probable, which could wedge the cutting edges apart (increase Δ) and lead to incomplete fibre severance. The effect of increasing Δ above zero on the fibre rotation angle is more pronounced for thin fibre bundles.

deflections which cause fibers to rap around the cutting edges and hence, the loss of severance.

7.4.2 Effects of Wear on Fiber Severance.

7.4.2.1 *Ground Face Wear:*

The ground face appears to wear in three stages: "run-in" wear, stable abrasive wear, and adhesive wear (§ 7.3). The most critical stages of this wear is toward the end of the abrasive wear stage because maintaining small vertical cutting edge separations (Δ), necessary for fiber severance, across the entire comb becomes increasingly difficult and requires greater force on the cutter. During this process, some portions of the cutting edges can loose fiber severance, but the overall performance of the comb may still be acceptable.

In the final stages of the severance life of a comb, adhesive (Stage 3) wear can cause significant metal to deposit on either ground face in an accelerating manner because of local heating. This will increase Δ and will probably end fiber severance in the vicinity of the adhesion. The damage caused by adhesive wear can be reduced by carefully incrementing the force applied to the cutter ("tension") during shearing use from a low value, and by monitoring the appearance of score marks towards the end of the comb's expected life.

Ground face wear also affects severance by negating the effects of cutting edge wear, as discussed next. Nevertheless, ground face wear must ultimately be responsible for loosing severance.

7.4.2.2 *Cutting Edge Rounding Wear:*

From the present model (§ 7.4.1), the most probable mechanism which breaks down fiber severance is slippage of fibers in-between the cutting edges caused by fiber rotation around the cutting edges. This is aggravated by comb tooth deflections which allows the comb and cutter teeth to wedge apart. This mechanism is a direct result of cutting edge rounding wear.

What maintains fiber severance over most of the severance life of a comb is the ground face wear of the comb, which progressively removes the edge radius as it forms. Due to the geometries of the tools, the ground face initially wears under relatively high contact stresses, and therefore is initially a rapid process which appears to keep up with the edge rounding wear. Late in the severance life, the rate of ground face wear is too slow to remove the edge radius and the system deteriorates.

Grit indentation and abrasion around the cutting edges was proposed as the dominant mechanism of cutting edge rounding wear (§ 7.3). Wear that rounds the cutting edges by grit trapped in the wool fibers is apparently an unstable process. The results of § 7.3.2 suggest that once the cutting edges start to become rounded, the edges are more susceptible to further wear, *i.e.*, edge wear in isolation is an accelerating process. On that basis, to maximize the severance life of a comb, adjustment of the force applied to the cutter, which controls the wear rate of the ground face, should initially be set to a minimum and then continuously incremented to provide only enough load to wear away the edge radius as it forms. There is presently no method of monitoring the relevant wear parameters during operation of the shearing tools, which perhaps explains why these tools are so difficult to use and one reason why their severance life is short.

7.4.2.3 ***Rake Face Wear:***

Rake face wear is unlikely to influence the severance process in conventional combs, except with regards to the force required to push combs through the fleece if coarse surface relief develops. However, the magnitude of rake face wear damage is very important for surface hardened combs since this wear could remove part of the hardened layer. This could have consequences later in the total life of the comb since re-sharpening was not found to remove the damaged portion of the rake face (damage is cumulative) (§ 7.2.2). From the present model (§ 7.3), the rake faces apparently wear primarily by grit indentation and then by three body abrasion in a direction away from the cutting edges. Abrasion by grit (supported by wool fibers) and fractured fibers

themselves were suggested as secondary mechanisms which caused either fine scratches or a fine polish on the rake faces.

7.5 CONCLUSIONS AND SUGGESTED FUTURE WORK.

The continuing operation of combs is critically dependent on the type of wear and its severity occurring around the wool severance areas. The wear on the remainder of the comb is important in terms of distortions of the ground profiles and separation of the mating surfaces by adhesive wear deposits.

While loading of the contact of the cutter onto the comb can initially prevent separation of the mating edges, and proper sharpening practices can initially provide sharp edges, wear will eventually destroy the small geometric tolerances necessary to maintain fiber severance.

The present wear studies show that:

1. cutting edge rounding wear is the critical process in the breakdown of wool fiber severance.
2. ground face wear is beneficial in reducing the cutting edge radii as the edges wear, but is ultimately responsible for loosing fiber severance.
3. hardening of the rake faces of the comb teeth alone (not the ground face) should reduce the edge rounding wear rate.

The consequence of these conclusions is that if the edge rounding wear rate can be reduced by hardening the rake surfaces, then the wear rate of the ground face can be reduced (by reducing the contact load) without affecting the severance process, and the life of the comb should increase. However, to be effective in reducing the cutting edge rounding wear rate, the minimum depth of surface hardening on the rake faces should correspond to the maximum acceptable cutting edge radius (~ 50 μm). These observations confirm the justification for the PIII treatment chosen in Chapter 6. On the other hand, if such a surface treatment softens the substrate appreciably, then the ground face wear rate will increase compared to a standard comb and the benefits of

the treatment may be lost. This confirms the justification for selecting XW10 steel for the manufacture of combs intended for surface treatment (Chapter 6).

The anticipated consequences of PIII treating the rake faces of XW10 shearing combs are that this treatment could extend the period in-between re-sharpening the comb. However, as described in Chapter 3, there is a relatively soft surface layer (although still > 800 HV) induced by the PIII treatment of this steel. Therefore, the benefits of a 10 - 50 μm hardened layer on the rake faces of shearing combs may not appear because the cutting edges in a shearing comb have a maximum allowable radius of ~ 15 - 50 μm. On the other hand, rake face wear could remove some of this surface layer during extended shearing use, as found in normal use of conventional combs, exposing the hardest material in the latter portion of the life of the comb, so that the cutting edge wear rates may substantially reduce.

The geometric models developed in the present studies could be extended to calculate stresses in the vicinity of the cutting edges with grit or wool fibers and deflections of the comb and cutter teeth which must occur simultaneously. Such calculations could help to simulate the effect of loading the cutter onto the comb: a critical variable in extending the life of tools. Experiments on the crushing strength of wool fibers would be useful input for fiber severance models.

Heat Treatments and Surface Treatments given to Selected Tool Steels

All ion implantation was conducted by the staff at ANSTO (see Acknowlegments).

K510 Specimens: (solution treated at 800°C for 15 mins; quenched into 70°C oil)

No.	Temper	PIII Treatment	
		Dose ($x10^{17}/cm^2$)	Temp. (°C)
K510-1	2 hrs@155°C	8	220
K510-2	2 hrs@155°C	8	240
K510-3	2 hrs@155°C	8	260
K510-4	2 hrs@155°C	12	300
K510-5	2 hrs@155°C	12	350
K510-6	2 hrs@155°C	12	400

H13 Specimens: (solution treated at 1015°C for 20 mins; quenched into oil)

No.	Temper	PIII Treatment		
		Dose ($x10^{17}/cm^2$)	Temp. (°C)	Duration (mins)
H13-1		7.0	200	
H13-2		15.1	250	
H13-3		14.1	300	
H13-4		15.0	350	~ 190
H13-5		15.0	400	
H13-6		22.7	480	
H13-7		GN	500	1960

XW10 Specimens: (solution treated at 960°C for 15 mins; quenched into 70°C oil)

No.	Temper	PIII Treatment		
		Dose ($x10^{17}/cm^2$)	Temp. (°C)	Duration (mins)
XW10-1	2x1hr@250°C	12	250	
XW10-2	2x1hr@300°C	12	300	
XW10-3	2x1hr@350°C	12	350	~ 190
XW10-4	2x1hr@400°C	12	400	
XW10-5	2x1hr@480°C	12	480	
XW10-6	2x1hr@480°C	GN	500	1920

Appendix 2

Experimental Techniques

A2.1 Preparation of PIII and Gas Nitrided Rod Specimens:

Rods 2 mm in diameter, Fig. A2.1, of each steel were machined on a lathe from single blocks of standard tool steels in the as received condition (either annealed or spherodised). The rods were turned initially 0.2 mm oversize and then heat treated: see Appendix 1. Rods were then gripped by the 3 mm shank in the chuck of a drill press and spun in order to polish the 2 mm surface. A metallurgical polish was given using 320, 600 and 1200 SiC papers with water lubrication followed by 3 - 6 μm diamond paste. The hardness was tested on the 3 mm diameter end face of each rod. Nitrogen ion implantation was performed in the ANSTO laboratories with the doses, temperatures and times listed in Appendix 1.

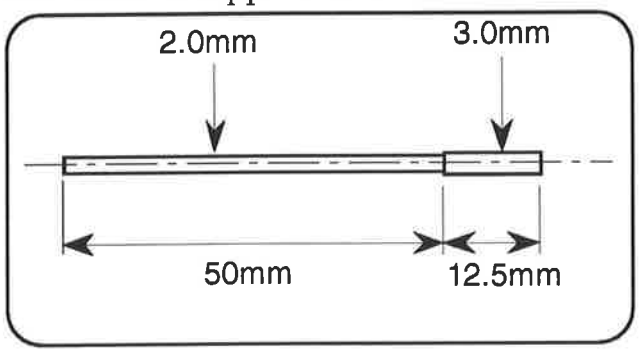

Figure A2.1: Specimen rod for hardness and wear tests and microscopy

A2.2 Conventional Metallography and Hardness measurements:

Cross-sectional specimens of the treated rods were prepared by mounting a segment of each rod in bakelite with a stainless steel tube to protect the rod surface during polishing. These specimens were then given a standard metallographic polish using SiC bonded papers (320, 600 and 1200 grades) followed by diamond paste on polishing laps (4 - 6, 0 - 1 and 0.1 μm particles).

A Leitz Durimet microhardness tester was used to make 25 g Vickers impressions on these specimens along a radial line from the surface to 450 μm depth. As the impressions in the hardened layer were of the order of 10 μm, measurements were done on a scanning electron microscope. The bulk hardness was tested with a standard Vickers tester using a 20 - 30 kg load.

These hardness specimens were used for metallography by lightly etching them in 2% Nital. Micrographs were recorded on a Zeiss Ultraphot II optical microscope, and a Phillip's 505 scanning electron microscope in secondary electron mode.

A2.3 Transmission Electron Metallography:

TEM specimens were prepared by dimple grinding and ion milling mechanically polished wafers some 100 μm thick and 3.05 μm diameter, which were sectioned from the same rod specimens. A Gatan model 656 dimple grinder was used to polish the specimens to a thickness of 5 - 10 μm using 4 μm CBN paste, followed by ion milling on a Gatan model 600 ion mill, to perforation.

The special technique that was developed for preparing XTEM samples of the PIII modified layer is discussed separately in Appendix 4.

The techniques of Bright Field (BF) and Dark Field (DF) imaging and Selected Area Diffraction (SAD) were employed to determine the size, shape, distribution and crystallography of each phase in the microstructures. A JEOL 2000 FX analytical electron microscope (AEM) was used at 200 kV accelerating voltage.

The TEM specimen prepared in §4.4 was inspected on the AEM at 200 kV using the above techniques, while additional micrographs, XEDS, EELS and micro-diffraction patterns were recorded on a Philips CM30 operated at 300 kV.

A2.4 XEDS and EELS Microanalysis in the A.E.M.:

The standard techniques of high resolution X-ray Energy Dispersive Spectroscopy (XEDS) and Electron Energy Loss Spectroscopy (EELS) were performed in a Philips CM30 operated at 300kV by Dr. Peter Miller at CSIRO (Clayton, Victoria, Aust.). These facilities were kindly made availible by the staff at CSIRO, but could not be used on a routine basis. Dr. Miller also performed the data analysis to quantify both the XEDS and EELS data.

EEL spectra were acquired using a Gatan model 607 electron spectrometer and Gatan model 666 parallel electron detector. Spectra were acquired with the microscope in diffraction mode (image coupled) with a camera length of 105 mm and a 3 mm electron spectrometer entrance aperture. The convergence angle was 1.47 mR and the spectrometer acceptance angle was 11.0 mR.

A gain reference spectrum of 100 x1 s acquisitions with the parallel detector evenly illuminated, a corresponding zero reference spectrum (no beam), a readout noise spectrum, a dark current noise spectrum, and a ramp spectrum were acquired to characterise the detector performance.

For each analysis spot, three electron energy-loss spectra were acquired: 1) the zero-loss region with 100 x0.05 s acquisitions and the attenuator on; 2) the low-loss region with 100 x0.05 s and attenuator off; and 3. the high-loss region with 10 x2 s and attenuator off and 100 V shift applied.

XED spectra were acquired concurrently with the EEL spectra, using an EDAX PV 9900 multi channel analyser and super ultra-thin ((SUTW) Si(Li) X-ray spectrometer with 20° take-off angle. The sample loaded in a low X-ray background (Be) double-tilt holder was tilted 15° towards the detector.

Data Processing: EELS - the standard background subtraction fitting technique was used to find the presence of EELS edges. The edge energy, Table A2.1, was used as the end point to fit an exponential relationship (Intensity = $A.E^{-r}$, where A and r are constants, and E is the energy) to the spectrum. This fitted curve was then subtracted

from the spectrum over the portion of the edge. The spectra were calibrated using the Fe-L3 edge position giving 0.996 eV/channel. Each spectrum was corrected for variations in gain and offset in the channels. No calibration was performed using standard materials.

To quantify the spectra, partial ionisation cross-sections were used to find the ratio of the N, Fe and Cr peak intensities. The accuracy of this analysis was the order of 10 - 20%. Partial ionisation cross-sections were calculated using two procedures "SIGMAK2" and "SIGMAL2" developed by R.F. Egerton. Electron energy-loss spectra were processed using a program EELSA (Electron Energy Loss Analysis) developed by Dr. P.R.Miller.

XEDS - spectra were analysed using a program called PVSUPQ provided with the EDAX analyser which employed standard X-ray quantitative techniques: e.g., correcting for atomic number variations and determining the ratio of corrected peak cross-sections. No corrections were made for specimen thickness and no calibration was performed using standards. The accuracy of the present compositional analysis is the order of 10 - 20%.

The composition of each area analysed was determined using a combination of the EELS and XEDS spectrum analyses based on element ratios.

A2.5 Optical Technique for Inspecting the Wear Patterns on Shearing Combs.

A halogen light source and an adjustable bellows camera were used. Since the scratches from the sharpening process were essentially parallel to the comb's teeth while the scratches from the comb/cutter related wear were perpendicular to the teeth, the worn regions could be distinguished from the as sharpened regions by tilting the illumination behind the comb and positioning the camera in front of the comb. To avoid distortion of the recorded image, the lens plane and the film plane were kept parallel to the comb plane, but the centres of the three planes were skewed at the opposite angle to the illumination. The contrast mechanism was as follows:

scratches perpendicular to the incident light rays reflected more light in the direction of the lens because their topology was much finer than grinding scratches and their rounded morphology provided wider reflective faces irrespective of the angle of illumination. Thus, sharpening scratches appeared dark while the wear scratches appeared bright. Despite the curvature of both sets of scratches on the comb's top face, the entire wear pattern could be revealed and recorded by careful manipulation of the light source. The severity of wear in different locations within the pattern could be approximated by the intensity of the reflected light. This was possible because depth of the scratches formed during the sharpening process were of the same order of magnitude as the depth of metal removed by wear. Thus, the more intense the reflected light, the more the original sharpening marks had been worn away, hence the greater the wear depth.

Appendix 3

Cross-Sectional TEM Specimen Preparation of Surface Hardened Rods

A3.1 Introduction:

Conventional T.E.M. specimen preparation techniques have difficulties in achieving areas of electron transparency near the surface of of an implanted specimen, especially where significant hardening has occurred to some depth and where the specimen is not planar.

The following reviews the current techniques and their limitations, then outlines the method used to successfully prepare a T.E.M. specimen from a rod of type XW-10 steel, treated by the PIII process.

A3.2 Review of T.E.M. Specimen Preparation Techniques for Ion Implanted Layers:

There are two general techniques for producing areas of electron transperancy for TEM specimens. Firstly, electropolishing, which suffers from two problems, *i.e.*, it can fragment samples which have microstructural components with different etching rates, and can selectively attack interfaces such as electroplated surfaces and crack faces. Secondly, dimple grinding to several microns and ion milling to electron transperancy. With this method, caution must be taken to avoid plastic deformation which is manifest as long dislocations in the plane of the foil. Furthermore, if a composite specimen is to be made, care must be taken to minimize the thickness of glue lines to avoid increased sputter loss in these regions.

Next, there is a choice of preparing a plan view specimen or a cross sectional one. Note that the former is restricted to observing changes in planar surfaces, where only the first 100 nm is of interest, *i.e.*, for most room temperature, low energy ion implantation. Researchers have prepared plan view specimens by using the following two methods:

method 1: Deposit a 100 nm film of target metal onto cleaved NaCl then implant ions and dissolve the NaCl.

method 2: Mechanically polished a 0.1 mm thick wafer, then implant the surface, protect it with a lacquer and back-thin the wafer with an etchant [24-26].

The limitation of the first method is that only single components of microstructures can be investigated, thus cannot be used for multicomponent materials used in engineering applications. The second method is impractical for materials which etch selectively, but this could be overcome by dimple grinding and ion milling prior to implantation.

However, the effects of surface stress sometimes induced by implantation cannot be determined with either of these methods as there is no buckling resistance in the plane of the specimen.

Modified layers greater than 100 nm deep must be viewed in cross-section, i.e. by XTEM, which invariably requires the manufacture of a composite specimen, in some way, to protect the implanted edge during preparation. The simplest specimen to make is one in which no significant hardening has occurred. The next two techniques have been used as the steps prior to cross sectioning wafers:

method 3: Implant a large target, electroplate a thick layer of similar hardness material, e.g. Cu [25-27].

method 4: Repeat Method 3 but replace the electroplating with a solid body glued to the surface, e.g. a mating planar surface (not reported for GN or ion implanted steels).

The limitation of the 3rd method is that very hard layers cannot have a suficiently hard electroplated layer applied to avoid polishing problems, and with the

4th method there are usually difficulties in minimizing the glue thickness for plate or rod specimens, hence ion milling problems.

The techniques used to prepare gas nitrided specimen cross-sections have included twin-jet electropolishing [7,47]. However, with the current specimen, electropolishing was found to be unsuitable, perhaps because of the sharp transition in the hardness/depth profile between the peak and the bulk, not found in gas nitriding procedures.

A3.3 A Modified Method for Preparing Cross-sectional T.E.M. specimens of Surface Hardened Rods:

The method developed uses the principle of Method 4 above, with care to avoid thick glue lines in the composite cross section. Other steps were taken to ensure a robust final product and a minimimum of astigmatism problems by centring the implanted surface in the 3.05 mm wafer. The method is as follows (see Fig. A3.1 for the composite specimen geometry):

Step 1: Section a short length of the implanted rod (~ 5 mm);

Step 2: Grind the rod into a prism of the shape shown in Fig. A3.1 by mounting it on a small thin block and using a diamond plated lap;

Step 3: Similarly, grind the two sets of hardened steel wedges shown in Fig. A3.1;

Step 4: Fit the rod and the wedges into a 3.05 mm O.D., 2.0 mm I.D. stainless steel tube, 5mm long;

Step 5: Reassemble and with an appropriate epoxy, e.g. super strength araldite or Gatan G1 epoxy, and lock the implanted specimen with the wedges, then cure it;

Step 6: Cross-section the composite rod and polish it to a metallographic finish on one side with a final thickness of ~ 80 μm;

Step 7: Dimple grind with water-based 4 μm CBN paste to a shallow depth (~ 5 μm) on the polished side, centred on the contact point of the implanted

surface with the wedge. Repeat the shallow dimple to the same depth at several places across the interface then polish briefly with a felt wheel and 0.05 μm aluminia paste. Turn the specimen over and repeat the dimples but so the remaining metal thickness is 5 μm, then polish as before.

Step 8: Ion mill to electron transperancy with 4 kV Ar ions.

The results from specimens prepared by this method from an XW10 rod surface hardened at 350°C by the PIII process, are shown in Chapter 4. In general, high quality electron transparent areas were found in individual specimens from ~ 5 to 120 μm depth beneath the implanted surface (in cross-section, *i.e.*,, the plane of the specimen disc). The central location of the dimple enabled large specimen tilt angles possible in the TEM while permitting the exacting magnetic and astigmatism corrections required for imaging at up to 200,000 X magnification. Such experiments were found to be impossible with specimens made by other (earlier) preparation methods (of the author).

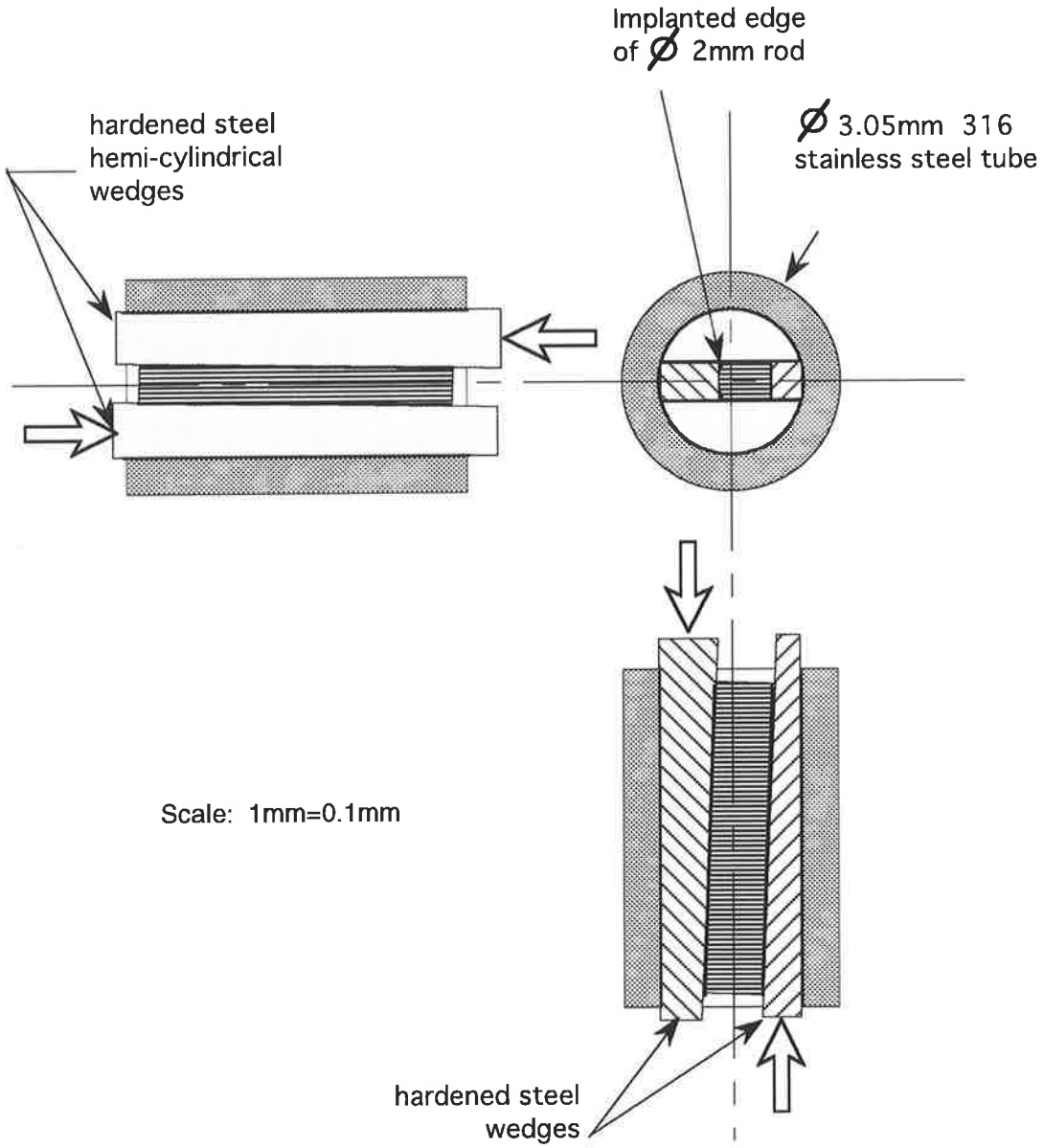

Figure A3.1: A modified technique to prepare a cross-sectional TEM specimen of a surface hardened rod (from PIII treatment) for dimple grinding and ion milling.

Appendix 4

EELS and EDAX Microanalysis

As electron diffraction alone could not distinguish some carbides and nitrides, high resolution XEDS and EELS were employed to in attempts to obtain compositional information from the 350°C PIII- and Q&T XW10 specimens. This data was recorded and analysed by Dr. Peter Miller at CSIRO (Clayton, Victoria, Aust.).

A4.1 Limitations:

Determination of the relative amounts of the metallic elements Fe, Cr and Mo was possible by XEDS. However, despite having a thin polycarbonate window on the X-ray detector, carbon and nitrogen were not detectable because of Fe and Cr subsidiary peaks.

Nevertheless, EELS could record C and N as well as Fe and Cr, but the Mo and V edges were overshadowed by other elements. The quantitative information from EELS was considered to be more approximate than the nominal 20% as carbon contamination on the surface of the specimen prevented long acquisition times, resulting in imprecise background subtractions. The carbon contamination made the detection of carbon unreliable.

A4.2 Results:

The quantitative information (in the absence of standards) from the XW10 steel in the quenched and tempered condition (just before PIII treatment) and from across the PIII modefied layer is summarised in Table A4.1 and Figure A4.1. This analysis uses complementary data from the EELS and matching XEDS spectra to find the ratios of the five elements listed. Representative EELS spectra are shown in Figures A4.2.

	at%					wt%				
Description	**Fe**	**Cr**	**Mo**	**V**	**N**	**Fe**	**Cr**	**Mo**	**V**	**N**
Matrix										
PIII 5um	77.7	4.4	0.6	0.2	17.1	89 1	4.7	1.1	0.2	4.9
PIII 15um	88.2	5.6	0.5	0.4	5.3	91.9	5.4	0.8	0.4	1.4
PIII 50um	81.4	4.7	0.5	0.3	13.0	90.2	4.9	1.0	0.3	3.6
PIII 100um	93.3	5.4	0.9	0.4	0.0	93.1	5.0	1.5	0.4	0.0
PIII 120um	94.3	4.5	0.9	0.3	0.0	94.0	4.2	1.6	0.3	0.0
QTT	94.0	4.9	0.7	0.5	0.0	93.8	4.5	1.2	0.4	0.0
Precipitates										
100um M23C6	49.6	24.8	3.7	1.3	20.7	58.1	27.0	7.5	1.3	6.1
15um Fe4N	73.0	8.0	0.0	0.0	19.0	85.6	8.8	0.0	0.0	5.6
20um CrN	23.7	28.8	0.8	1.2	45.5	36.8	41.7	2.2	1.7	17.7

Table A4.1: Compositions of coarse precipitates and the matrix at different depths beneath the surface. From high resolution XEDS and EELS.

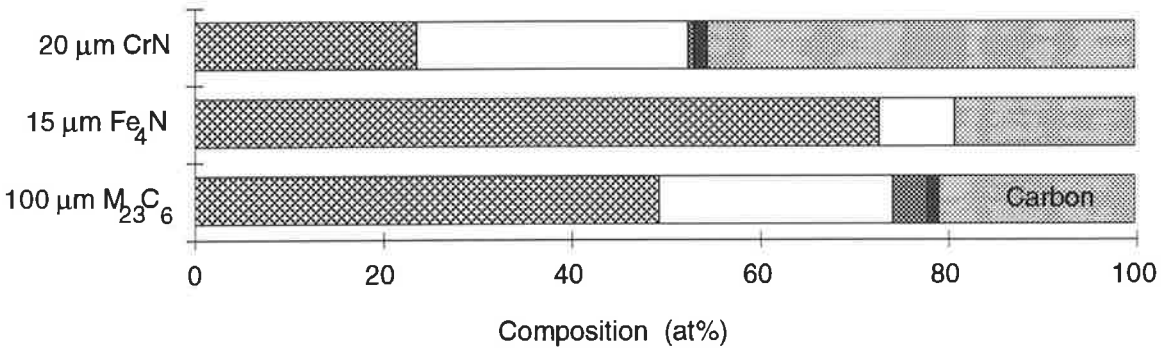

(a)

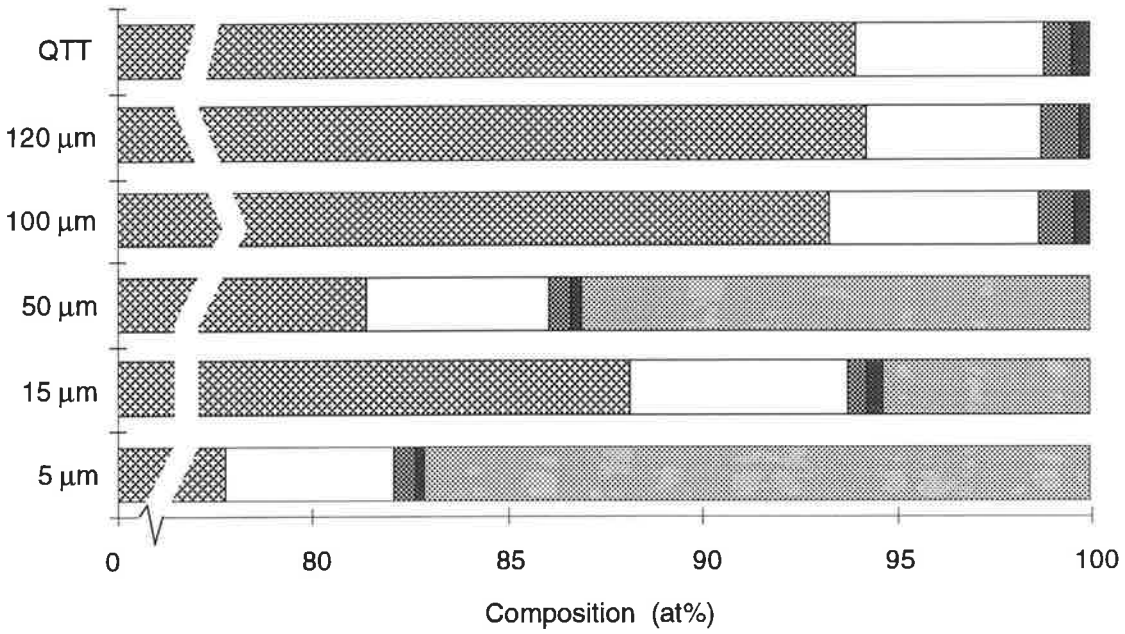

(b)

Figure A4.1: Compositions of (a) coarse precipitates; and (b) the matrix at different depths beneath the surface: from high resolution XEDS and EELS.

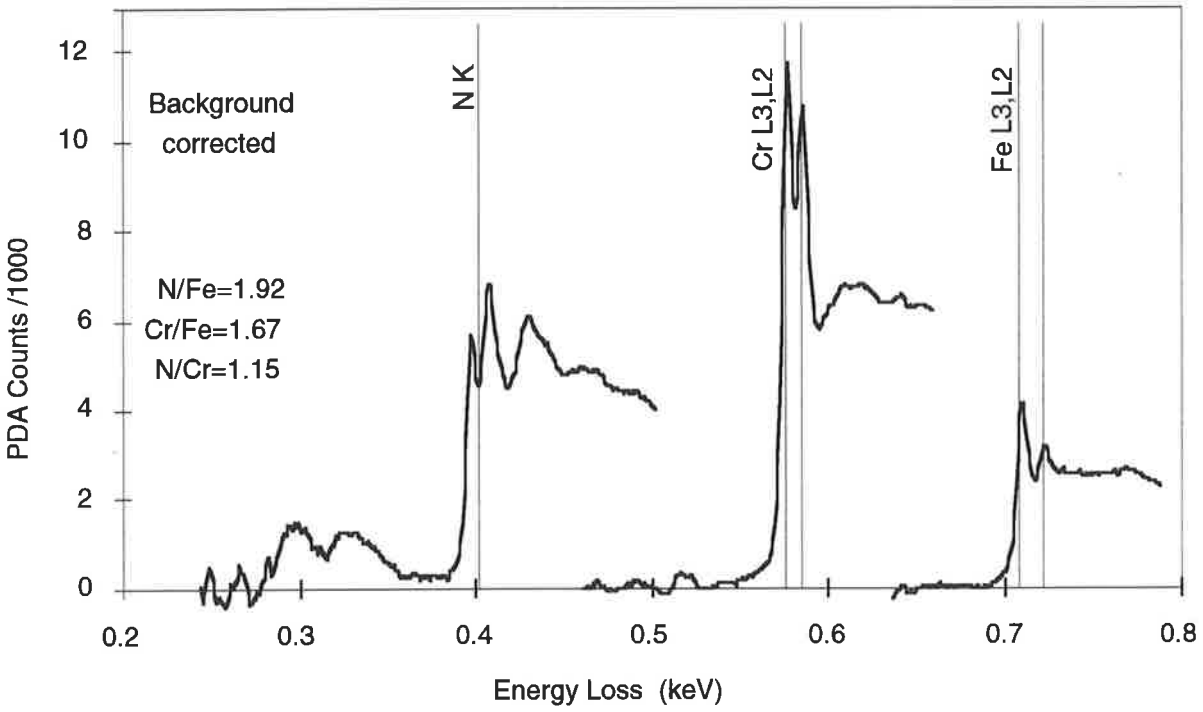

(a)

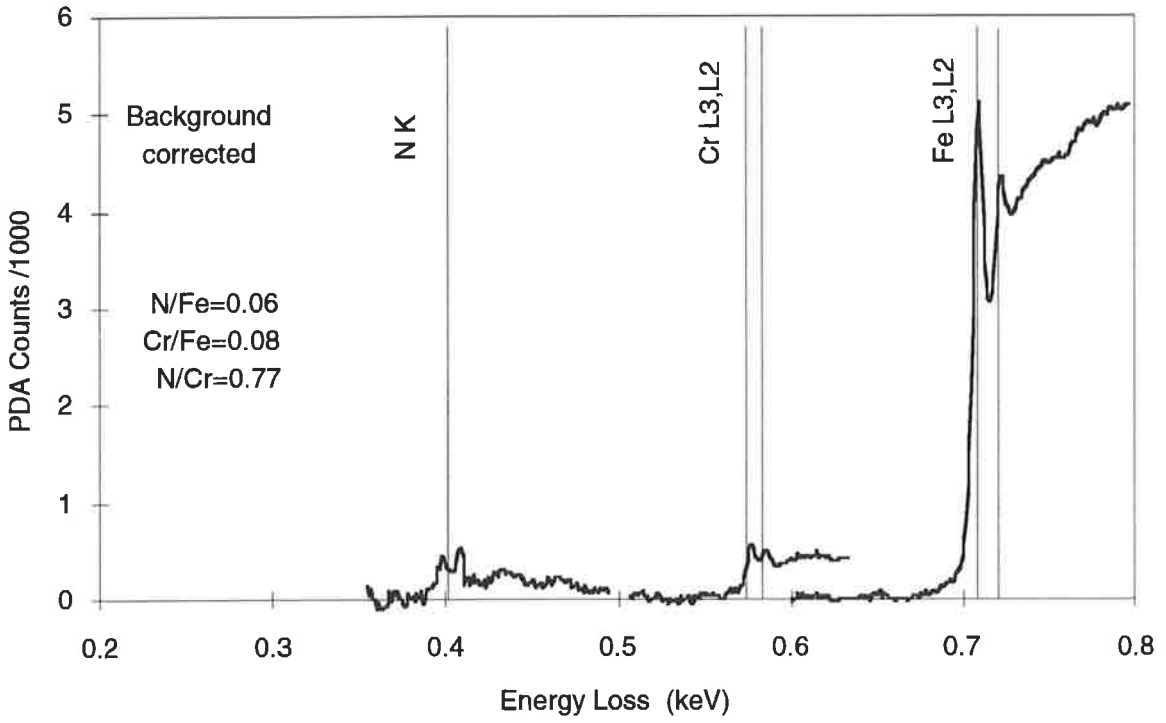

(b)

Figure A4.2: EELS spectra of (a) (Cr,Fe)N at 20μm; and (b) matrix at 15μm

Appendix 5

Input Variables for Mathematical Modelling of PIII

A5.1 TRIM Calculations of Ion Energy, Range and Vacancy production Distributions with Depth in XW10 Steel:

The "TRIM '90" code [63] was used to find some input parameters to the mathematical simulations developed in this thesis. A standard of 20,000 N_2^+ ions were simulated with 50 kV energy, i.e. 25 kV Nitrogen, into targets of the average XW10 composition and Fe_4N, see Table A5.1.

The TRIM results of the percentage of the ion energy converted into lattice vibrations and the vacancy production rate per ion are given below in Table A5.2.

Seventh order polynomials of the form given below, were fitted to the statistical data obtained for the ion range, energy release and vacancy production distributions intensities with depth by using the "Mathematica" software on an Apple IIcx computer.

$$\text{Intensity, } I(x) = -a_0 + a_1x - a_2x^2 + a_3x^3 - a_4x^4 + a_5x^5 - a_6x^6 + a_7x^7$$

The polynomial coefficients are tabulated in Table A5.3. A sample fit is shown in figure A5.4, while the polynomial functions are shown in Figs. A5.1.

Table A5.1: TRIM Input Parameters:

Material	Density (g/cm^3)	Binding Energy (eV)
XW10 avg	7.75	1.5
Fe_4N	6.57	1.5

Table A5.2: Ion Energy Loss and Vacancy Production:

	XW10 avg.		Fe_4N	
Energy Loss (%)	ions	recoils	ions	recoils
ionization	44.51	10.1	44.2	10.5
vacancies	0.18	0.75	0.19	0.73
phonons	**1.95**	**42.5**	**1.98**	**42.4**
Vacancies/Ion	176.9		174.8	

Table A5.3: Polynomial Curve-fitting Coefficients for TRIM Depth Distributions:

	Ion Range		Ion Energy Release		Vacancy Production	
	XW10 avg	Fe_4N	XW10 avg	Fe_4N	XW10 avg	Fe_4N
a_0	1.76897e-4	2.63886e-5	9.51742e-3	7.74805e-3	1.76897e-4	2.63886e-5
a_1	2.72728e-3	2.33733e-3	3.67250e-3	3.31710e-3	2.72728e-3	2.33733e-3
a_2	2.50967e-4	2.38571e-4	3.17283e-4	2.98352e-4	2.50967e-4	2.38571e-4
a_3	1.53604e-4	1.48871e-5	1.56180e-5	1.54729e-5	1.53604e-4	1.48871e-5
a_4	4.91495e-7	4.66799e-7	4.78257e-7	4.75089e-7	4.91495e-7	4.66799e-7
a_5	7.97141e-9	7.47013e-9	8.22763e-9	8.00261e-9	7.97141e-9	7.47013e-9
a_6	6.3254e-11	5.9447e-11	7.1917e-11	6.8236e-11	6.3254e-11	5.9447e-11
a_7	1.9627e-13	1.8806e-13	2.4858e-13	2.3074e-13	1.9627e-13	1.8806e-13

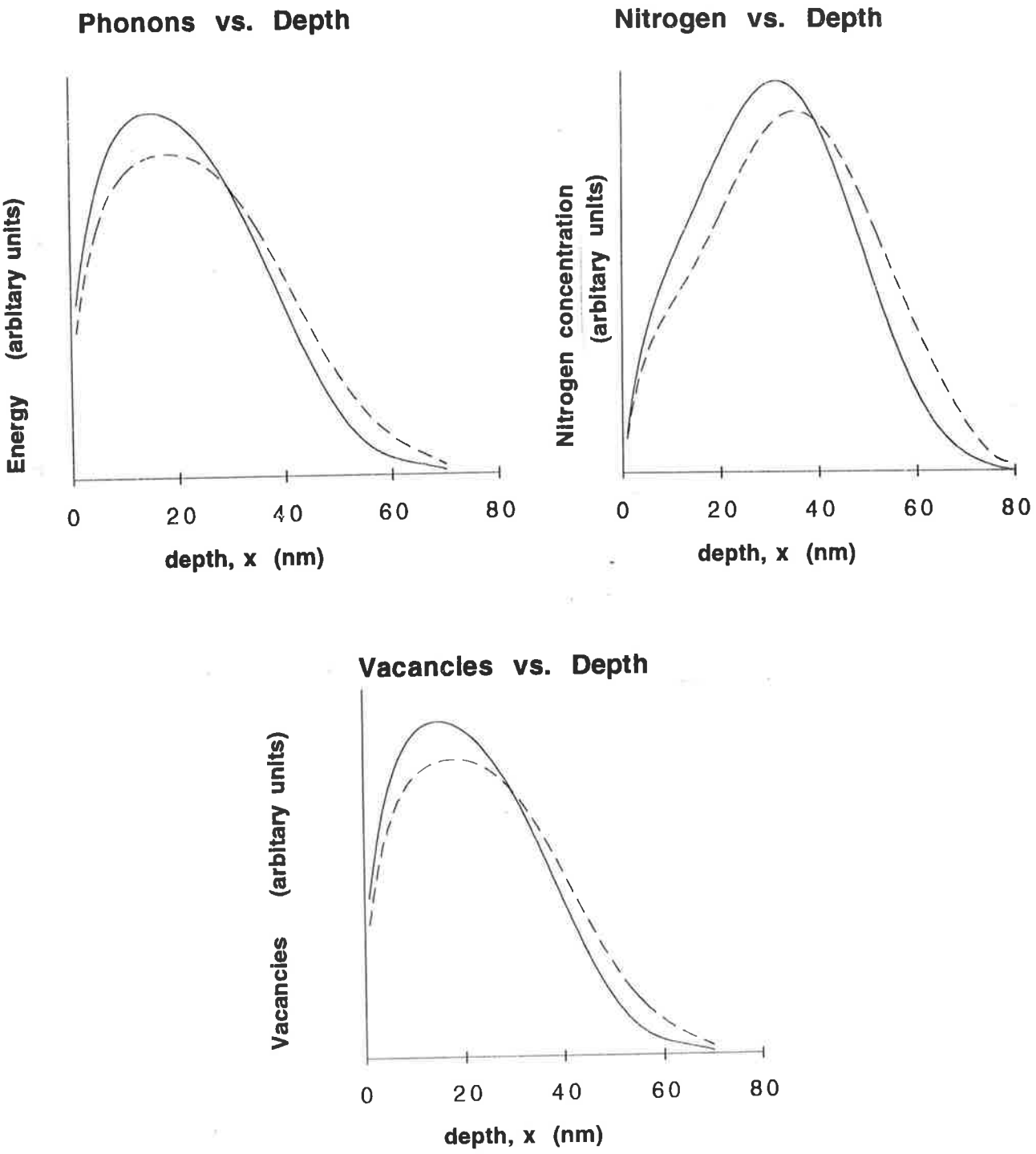

Figure A5.1: TRIM simulations of 50 keV N_2^+ ions into α-Fe matrix of XW10 steel (——) and Fe_4N precipitate (- - - -), being the two constituents found in the surface of the 350 °C PIII treated XW10 steel (Chapter 4). The matrix composition was set at the average atomic percentages specified in the steel (ASSAB) (assumed that allof the Cr, Mo and V carbides dissolved into the matrix (Chapter 4)). Energy (phonons imparted to the crystal lattice), nitrogen concentration and vacancy production are estimated as functions of depth beneath the implanted surface.

A5.2 PIII Process Parameters:

The setup of the operating parameters of the PIII equipment determines the target temperature, nitrogen concentration profile, etc, which control the final microstructural changes to the specimen. As the implantation was done outside of these laboratories by another research team, and their techniques reported elsewhere, only a summary of the relevant parameters will be given here.

$$\text{Impl. temperature, } T_{imp} = 350^{\circ}C$$
$$\text{Dose, } D = 1.2 \times 10^{18} N / cm^2$$
$$\text{Ion energy, } E = 25keV$$
$$\text{Pulse frequency, } f = 35Hz$$
$$\text{Pulse duration, } \tau_p = 50\mu s$$
$$\text{Dwell duration, } \tau_d = \left(1/35 - \tau_p\right)$$
$$= 28521\mu s$$
$$\text{Total time of Pulses, } \tau_{imp} = 20s$$
$$\text{Total treatment time, } \tau_{tot} = \tau_{imp} \times \left(\frac{1/35 - \tau_p}{\tau_p} \right)$$
$$= 3.17 hours$$

Heat Transfer parameters:

$$\text{Pulse power, } P_p = \frac{E.D.\Omega}{\tau_{imp}}$$
$$= 100.8 W / cm^2$$
$$\text{Average power, } P_{avg} = P_p \times \frac{\tau_{imp}}{\tau_p}$$
$$= 0.177 W / cm^2$$

From the ASSAB technical data sheet on XW10 steel:

$$\text{Density, } \rho = 7750 kg / m^3$$
$$\text{Thermal conductivity, } k_{20^{\circ}C} = 26.0 W / m.^{\circ}K$$
$$k_{350^{\circ}C} = 27.0 W / m.^{\circ}K$$
$$\text{Specific heat, } C_p = 460 J / kg.^{\circ}K$$
$$\text{Hence, the Thermal diffusivity, } \alpha = 0.0729 cm^2 / s$$

Nitrogen diffusion parameters:

$$\text{N atom flux during a pulse, } J_P = \frac{D}{\tau_{imp}}$$
$$= 60\times10^{15}\,N/s.cm^2$$
$$\equiv 1.395\times10^{-6}\,g/s.cm^2$$
$$\text{Average N flux, } J_{avg} = \frac{D}{\tau_{tot}}$$
$$= 0.1052\times10^{15}\,N/s.cm^2$$
$$\equiv 2.445\times10^{-9}\,g/s.cm^2$$

According to Morral [70] the equivalent to the thermal conductivity in mass diffusion equations equals the atomic diffusivity, hence:

$$\text{Diffusivity of N in } \alpha\text{-Fe, } D_N = D_o.e^{\left(\frac{-Q}{R.T}\right)},\ (T \text{ in } {}^oK)$$
$$D_o = 7.8\times10^{-3}\,cm^2/s$$
$$\text{and } Q = 18.9\times10^3\,cal/mol$$
$$\text{N atomic} \left\{\begin{matrix}\text{diffusivity}, D_{350^oC} \\ \text{"conductivity"}, k_{350^oC}\end{matrix}\right\} = 1.832\text{x}10^{-9}\ cm^2/s$$

Appendix 6

Numerical Diffusion Methods

A6.1 Standard Solution Techniques for Transient Diffusion Problems:

1. Analytical Solution for an Infinite Body with a Constant Surface Heat Flux [93]:

$$T - T_i = \frac{2q\sqrt{\alpha t/\pi}}{k}\exp\left(\frac{-x^2}{4\alpha t}\right) - \frac{qx}{k}\left(1 - \text{erf}\frac{x}{2\sqrt{\alpha t}}\right) \qquad (3.1)$$

This model assumes the following:

A1. Infinite slab geometry with a uniform surface flux.

A2. Constant material properties with temperature: i.e. k, ρ and C_p.

A3. An infinitessimally thin surface layer over which the heat transfer occurs.

A4. No internal heat generation.

A5. Constant initial temperature.

2. Boundary Element Method (BEM) or Finite Element (FE) or Finite Difference (FD) Solution to the 1D Linear Heat Equation [64]:

$$\frac{\partial T}{\partial t} = \alpha\frac{\partial^2 T}{\partial x^2}$$

3. BEM or FE or FD Solution to the 1D Diffusion Equation with a Variable Diffusion Coefficient:

$$\frac{\partial c}{\partial t} = \frac{\partial}{\partial x}\left(D_{AB}\frac{\partial c}{\partial x}\right)$$

4. BEM or FE or FD Solution to the 1D Transient Reaction-Diffusion Equation [81]:

$$\frac{\partial c}{\partial t} = \alpha\frac{\partial^2 c}{\partial x^2} - Kf(c)$$

A6.2 The Derivation of the Boundary Integral Solution to the One Dimensional Linear Heat Equation with Internal Heat Generation:

This solution follows the method given by Hill and Dewynne [64], the only difference being the treatment of one additional term in the heat equation, the source term. The same fundamental solution, the Green's function, is assumed valid in this case.

Consider the 1D linear heat equation with internal heat generation:

$$\frac{\partial T}{\partial t} = \alpha \frac{\partial^2 T}{\partial x^2} + S(x,t) \tag{1.1}$$

with the prescribed boundary conditions in the given problem being

$$\frac{\partial T}{\partial x}(a,t) = v_1(t) = q_1 \,, \quad \frac{\partial T}{\partial x}(b,t) = v_2(t) = q_2 \quad \text{for} \quad 0 \le t \le \text{time} \tag{1.2}$$

and initial condition

$$T(x,0) = f(x) \quad \text{for} \quad a \le x \le b \tag{1.3}$$

with the internal heat source term only dependent on position, e.g.

$$S(x) \equiv S(x,t) \tag{1.4}$$

At this point, the unknown to determine is the temperature as a function of position and time. Usual solution techniques involve finding the temperature over the entire space-time grid in order to calculate the final temperature profile with position. However, with the BEM, it is only necessary to find the boundary temperatures over the time interval, i.e. T(a,t) and T(b,t), in order to obtain the final temperature profile.

The derivation proceeds as follows:

Using a Green's function as a fundamental solution to the standard heat equation, the adjoint equation can be written as

$$\frac{\partial G}{\partial \tau} + \alpha \frac{\partial^2 G}{\partial \xi^2} = -\delta(t-\tau)\delta(x-\xi) \tag{1.5}$$

Now, multiplying (1.5) by the temperature at point (ξ,τ) and integrating w.r.t. position and time, we obtain

$$\int_0^t \int_a^b T(\xi,\tau)\left(\frac{\partial G}{\partial \tau} + \alpha \frac{\partial^2 G}{\partial \xi^2}\right) d\xi d\tau = -T(x,t) \tag{1.6}$$

Similarly, multiplying (1.1) by Green's fn. and integrating:

$$\int_0^t \int_a^b G(x,\xi,t,\tau)\left(\frac{\partial T}{\partial \tau} - \alpha \frac{\partial^2 T}{\partial \xi^2} - S(\xi)\right) d\xi d\tau = 0 \tag{1.7}$$

When (1.6) and (1.7) are summed and simplified, the integral equation for the temperature at a point can be written:

$$\begin{aligned} T(x,t) = {} & \int_a^b f(\xi) G(x,\xi,t,0) d\xi \; - \; \int_a^b S(\xi) \int_0^t G(x,\xi,t,\tau) d\tau d\xi \\ & + \alpha \int_0^t u_1(\tau) \frac{\partial G}{\partial \xi}(x,a,t,\tau) d\tau \; - \; \alpha \int_0^t u_2(\tau) \frac{\partial G}{\partial \xi}(x,b,t,\tau) d\tau \\ & - \alpha \int_0^t v_1(\tau) G(x,a,t,\tau) d\tau \; + \; \alpha \int_0^t v_2(\tau) G(x,b,t,\tau) d\tau \end{aligned} \tag{1.8}$$

Using, now, the set of non-dimensional variables:

$$\bar{T}=\frac{T}{T_0},\quad \bar{x}=\frac{x}{L},\quad \bar{t}=\frac{t\alpha}{L^2},\quad \bar{q}=\frac{qL}{kT_0}$$

equation (1.8) can be written over the interval $0 \le \bar{x} \le 1$ as

$$\begin{aligned}-\lambda\bar{T}(\bar{x},\bar{t}) &= \int_0^1 f(\xi)\bar{G}(\bar{x},\xi,\bar{t},0)d\xi - \int_0^1 S(\xi)\int_0^{\bar{t}}\bar{G}(\bar{x},\xi,\bar{t},\tau)d\tau d\xi \\ &+ \int_0^{\bar{t}} u_1(\tau)\frac{\partial\bar{G}}{\partial\xi}(\bar{x},0,\bar{t},\tau)d\tau - \int_0^{\bar{t}} u_2(\tau)\frac{\partial\bar{G}}{\partial\xi}(\bar{x},1,\bar{t},\tau)d\tau \\ &- \int_0^{\bar{t}} v_1(\tau)\bar{G}(\bar{x},0,\bar{t},\tau)d\tau + \int_0^{\bar{t}} v_2(\tau)\bar{G}(\bar{x},1,\bar{t},\tau)d\tau\end{aligned} \tag{1.9}$$

where

$$\lambda=\begin{cases}1, & \text{for } 0<\bar{x}<1\\ \dfrac{1}{2}, & \text{for } \bar{x}=0 \text{ or } \bar{x}=1\end{cases} \tag{1.10}$$

and the non dimensional Green's function is

$$\bar{G}(\bar{x},\xi,\bar{t},\tau)=\frac{H(\bar{t}-\tau)}{2\sqrt{\pi(\bar{t}-\tau)}}\exp\frac{-(\bar{x}-\xi)^2}{4(\bar{t}-\tau)},\quad \bar{t}-\tau>0$$

where the Heaveside unit step function,

$$H(\bar{t}-\tau)=\begin{cases}0, & \text{for } (\bar{t}-\tau)<0\\ 1, & \text{for } (\bar{t}-\tau)\ge 0\end{cases} \tag{1.11}$$

Now, substituting $\bar{x}=0$ and $\bar{x}=1$, B.C.s (1.2) and I.C. (1.3) we obtain the following integral equations:

$$\begin{aligned}&\frac{1}{2}u_1(\bar{t})+\int_0^{\bar{t}} u_2(\tau)\frac{\partial\bar{G}}{\partial\xi}(0,1,\bar{t},\tau)d\tau \\ &= \int_0^1 f(\xi)\bar{G}(0,\xi,\bar{t},0)d\xi - \int_0^1 S(\xi)\int_0^{\bar{t}}\bar{G}(0,\xi,\bar{t},\tau)d\tau d\xi \\ &- \int_0^{\bar{t}} q_1\bar{G}(0,0,\bar{t},\tau)d\tau + \int_0^{\bar{t}} q_2\bar{G}(0,1,\bar{t},\tau)d\tau\end{aligned}$$

$$\begin{aligned}&\frac{1}{2}u_2(\bar{t})-\int_0^{\bar{t}} u_1(\tau)\frac{\partial\bar{G}}{\partial\xi}(1,0,\bar{t},\tau)d\tau \\ &= \int_0^1 f(\xi)\bar{G}(1,\xi,\bar{t},0)d\xi - \int_0^1 S(\xi)\int_0^{\bar{t}}\bar{G}(1,\xi,\bar{t},\tau)d\tau d\xi \\ &- \int_0^{\bar{t}} q_1\bar{G}(1,0,\bar{t},\tau)d\tau + \int_0^{\bar{t}} q_2\bar{G}(1,1,\bar{t},\tau)d\tau\end{aligned} \tag{1.12}$$

Note that the all of the known terms are on the r.h.s. of these equations.

Making a numerical approximation that the boundary temperatures are piecewise constant over time step, i, (1.12) becomes a set of 2N equations:

$$\frac{1}{2}u_1(\bar{t}_i)+\sum_{j=1}^{N}u_2(\bar{t}_j)A_{ij}(0,1)$$
$$= \int_0^1 f(\xi)\bar{G}(0,\xi,\bar{t},0)d\xi - \int_0^1 S(\xi)B_{ij}(0,\xi)d\xi - \sum_{j=1}^{N}\left\{q_1B_{ij}(0,0) - q_2B_{ij}(0,1)\right\}$$

$$\frac{1}{2}u_2(\bar{t}_i)-\sum_{j=1}^{N}u_1(\bar{t}_j)A_{ij}(1,0) \qquad (1.13)$$
$$= \int_0^1 f(\xi)\bar{G}(1,\xi,\bar{t},0)d\xi - \int_0^1 S(\xi)B_{ij}(1,\xi)d\xi - \sum_{j=1}^{N}\left\{q_1B_{ij}(1,0) - q_2B_{ij}(1,1)\right\}$$
$$\text{for } 1 \le i \le N$$

where

$$A_{ij} = \int_{(j-1)\Delta\bar{t}}^{j\Delta\bar{t}} \frac{\partial\bar{G}}{\partial\xi}(\bar{x},\xi,\bar{t}_i,\tau)d\tau$$
$$B_{ij} = \int_{(j-1)\Delta\bar{t}}^{j\Delta\bar{t}} \bar{G}(\bar{x},\xi,\bar{t}_i,\tau)d\tau \qquad (1.14)$$

Similarly (1.9) becomes

$$\lambda\bar{T}(\bar{x},\bar{t}_i) = \int_0^1 f(\xi)\bar{G}(\bar{x},\xi,\bar{t}_i,0)d\xi - \int_0^1 S(\xi)B_{ij}(\bar{x},\xi)d\xi$$
$$+\sum_{j=1}^{N}\left\{u_1(\bar{t}_j)A_{ij}(\bar{x},0) - u_2(\bar{t}_j)A_{ij}(\bar{x},1) - q_1B_{ij}(\bar{x},0) + q_2B_{ij}(\bar{x},1)\right\} \qquad (1.15)$$

The integrals (1.14) can be performed analytically, e.g.,

$$A_{ij}(\bar{x},\xi) = \begin{cases} \frac{1}{2}\operatorname{erf}\left(\frac{\bar{x}-\xi}{2\sqrt{\Delta\bar{t}(i-j)}}\right) - \frac{1}{2}\operatorname{erf}\left(\frac{\bar{x}-\xi}{2\sqrt{\Delta\bar{t}(i+1-j)}}\right), & i > j \\ \frac{1}{2}\operatorname{sgn}(\bar{x}-\xi) - \frac{1}{2}\operatorname{erf}\left(\frac{\bar{x}-\xi}{2\sqrt{\Delta\bar{t}}}\right), & i = j \\ 0\ , & i < j \end{cases} \qquad (1.16)$$

$$B_{ij}(\bar{x},\xi)=\begin{cases}\left\{\sqrt{\frac{\Delta\bar{t}}{\pi}(i+1-j)}\exp\left(\frac{-(\bar{x}-\xi)^2}{4\Delta\bar{t}(i+1-j)}\right)-\frac{|\bar{x}-\xi|}{2}\operatorname{erfc}\left(\frac{|\bar{x}-\xi|}{2\sqrt{\Delta\bar{t}(i+1-j)}}\right)\right\}, & \\ \left\{-\sqrt{\frac{\Delta\bar{t}}{\pi}(i-j)}\exp\left(\frac{-(\bar{x}-\xi)^2}{4\Delta\bar{t}(i-j)}\right)+\frac{|\bar{x}-\xi|}{2}\operatorname{erfc}\left(\frac{|\bar{x}-\xi|}{2\sqrt{\Delta\bar{t}(i-j)}}\right)\right\} & i>j\\ \sqrt{\frac{\Delta\bar{t}}{\pi}}\exp\left(\frac{-(\bar{x}-\xi)^2}{4\Delta\bar{t}}\right)-\frac{|\bar{x}-\xi|}{2}\operatorname{erfc}\left(\frac{|\bar{x}-\xi|}{2\sqrt{\Delta\bar{t}}}\right), & i=j\\ 0\ , & i<j\end{cases} \tag{1.17}$$

Equation (1.13) can now be written in matrix form as 2N equations with 2N unknowns:

$$\left.\begin{aligned}\mathbf{C}\tilde{u}_1+\mathbf{D}\tilde{u}_2&=\tilde{b}_1\\ \mathbf{D}\tilde{u}_1+\mathbf{C}\tilde{u}_2&=\tilde{b}_1\end{aligned}\right\} \tag{1.18}$$

where matrices **C** and **D** are given by:

$$\mathbf{C}=\frac{1}{2}\mathbf{I},\quad \text{where } \mathbf{I} \text{ is the NxN identity matrix}$$

and through the symetry of A_{ij}

$$\mathbf{D}=\begin{pmatrix}A_{11}(1,0) & 0 & 0 & .. & .. & 0\\ A_{21}(1,0) & A_{11}(1,0) & 0 & 0 & .. & 0\\ A_{31}(1,0) & A_{21}(1,0) & A_{11}(1,0) & 0 & . & :\\ : & : & : & . & . & :\\ : & : & : & : & . & 0\\ A_{N1}(1,0) & .. & .. & .. & .. & A_{11}(1,0)\end{pmatrix}$$

and the vectors $\tilde{u}_1$ and $\tilde{u}_2$ by

$$\tilde{u}_1=\begin{Bmatrix}u_1(\bar{t}_1)\\ :\\ :\\ u_1(\bar{t}_N)\end{Bmatrix},\quad \tilde{u}_2=\begin{Bmatrix}u_2(\bar{t}_1)\\ :\\ :\\ u_2(\bar{t}_N)\end{Bmatrix}$$

and the ith component of vectors $\tilde{b}_1$ and $\tilde{b}_2$ are

$$\tilde{b}_1(i) = \int_0^1 f(\xi)\overline{G}(0,\xi,\bar{t}_i,0)d\xi - \int_0^1 S(\xi)B_{ij}(0,\xi)d\xi - \sum_{j=1}^{N}\left\{q_1 B_{ij}(0,0) - q_2 B_{ij}(0,1)\right\}$$

$$\tilde{b}_2(i) = \int_0^1 f(\xi)\overline{G}(1,\xi,\bar{t}_i,0)d\xi - \int_0^1 S(\xi)B_{ij}(1,\xi)d\xi - \sum_{j=1}^{N}\left\{q_1 B_{ij}(1,0) - q_2 B_{ij}(1,1)\right\}$$

This system of equations can be solved by the method of foward substitution, yielding the following algorithm:

1. Calculate $b_1(i)$ and $b_2(i)$ for $1 \le i \le N$
2. Find $u_1(1)$ and $u_2(1)$ e.g.

$$u_1(1) = \left[\frac{1}{2}b_1(1) - A_{11}(1,0)b_2(1)\right] \Big/ \left[\frac{1}{4} - [A_{11}(1,0)]^2\right]$$

$$u_2(1) = \left[\frac{1}{2}b_2(1) - A_{11}(1,0)b_1(1)\right] \Big/ \left[\frac{1}{4} - [A_{11}(1,0)]^2\right]$$

3. Then iterate the following while $2 \le i \le N$:
   3.1 modify the $b_1(i)$ and $b_2(i)$ so that

$$b_1(i) = b_1(i) - \sum_{j=1}^{i-1} u_2(j)A_{i+1-j,1}(1,0)$$

$$b_2(i) = b_2(i) - \sum_{j=1}^{i-1} u_1(j)A_{i+1-j,1}(1,0)$$

   3.2 calculate $u_1(i)$ and $u_2(i)$ using the equations in point 2 above but replacing the $b_1(1)$ and $b_2(1)$ for the i^{th} component of $\tilde{b}_1$ and $\tilde{b}_2$ respectively.

Once the time boundary temperatures, $\tilde{u}_1$ and $\tilde{u}_2$ have been found, the final temperature-depth profile may be calculated by the use of equation (1.15).

Treatment of Numerical Integrals:

Some of the above space integrals cannot be evaluated analytically, e.g., those involving $S(\xi)$ and $f(\xi)$. For $S(\xi)$ (Appendix 5), the space domain was discretized into equally spaced elements only over the width of $S(\xi)$ and integrated using Simpson's rule (n=4). Similar treatment was given to $f(\xi)$ integrals, with the additional feature of breaking the space domain into blocks of elements which were organised to capture steep gradients in the temperature-depth profile, *i.e.,,* the block lengths followed a geometric progression, increasing the element length away from the surface, Fig. 5.4.

FATIGUE FAILURE OF CEMENTED WC-Co DETONATION-GUN COATINGS

D.R. Miller and J.H. Watkins
Department of Chemical Engineering,
University of Adelaide,
P.O. Box 498,
Adelaide 5001,
Australia.

Abstract

The microstructure and fatigue performance of WC-Co coatings produced by the patented Union Carbide Detonation-Gun (D-Gun) process have not been widely reported in the literature. The purpose of this paper is to establish that fatigue failure of WC-Co D-Gun coatings applied to sheep shearing combs can occur under alternating stresses of a magnitude comparable to those to which the combs are subjected to in practice.

Cantilever bending fatigue tests were conducted on single undamaged coated comb teeth. After 1.44×10^6 cycles with a surface strain amplitude of 0.4% a network of interconnecting cracks was detected. Further fatigue cycling resulted in partial coating disintegration accompanied by crack propagation into the steel substrate.

Examination of the microstructure of the coating indicated that during deposition, substantial alloying of WC with Co had occurred and the presence of the η phase (Co_3W_3C) of the W,Co,C system was established. Crack propagation in the coating due to fatigue cycling occurred largely in and around the η phase.

The damage sustained in coated combs used in sheep shearing service was consistent with fatigue damage of the kind induced in the laboratory.

1.0 INTRODUCTION

Wool harvesting has long been a major industry throughout the world, and yet the problem of short cutting tool-life in shearing equipment persists. The advent of robotic sheep shearing has further stimulated the search for more durable combs and cutters. Research conducted during the last decade has greatly enhanced understanding of the mechanisms of wool severance and the factors determining the performance of shearing handpieces. This work has resulted in a number of new developments. Of these, the application of a cemented tungsten carbide coating on the wear face of the comb [1], applied via the UNION CARBIDE "Detonation Gun" (D-Gun) process [2], has shown considerable promise. However, field trials* of combs coated by Union Carbide in Japan have shown a considerable variation in performance, with the tool life ranging from 1 to 10 times

---

* Conducted by Merino Wool Harvesting Pty. Ltd. of Technology Park. Pooraka, South Australia 5095 (Private communication).

that of the uncoated combs when shearing normal wool, and a maximum life 50 times greater when shearing "clean" wool** .

A typical material used in the manufacture of commercially available combs is a 1.2%C, 0.7%Cr, 0.3%Mn steel, quenched and tempered to a hardness of 750-850HV_{30}. These uncoated combs generally have a mean service life of 1-2 hours or 20-40 sheep; the breakdown of the shearing action occurs when the fine tolerances at the cutting edges, essential in severing wool fibres, are destroyed by sliding wear between the comb and the oscillating cutter. Both combs and cutters may be resharpened, (combs up to 50 times), giving them a life of ~1000 sheep.

When the standard comb is coated using the D-Gun process the hardness of the wearing surface is increased to ~1400HV_{30}, and hence wear is considerably reduced. Furthermore, this coating can promote a self-sharpening effect to rounded cutter edges through beneficial wear. In this situation, the cutter life is increased by a factor of 6 to 8, so that it may last for as much as 2 hours (40 sheep).

However, the D-Gun coated combs cannot be resharpened. Hence, for this comb to be economically viable, its single service life must not only be equal to the accumulated use of a resharpenable standard comb but also be capable of recovering the cost incurred by applying the coating.

Extensive field trials have shown that the performance of coated combs is improved by a factor of 1 to 10, giving them a life of 20 to 200 sheep. This variation in life is considerably greater than that found with the uncoated combs and suggests that the structure and properties of the WC-Co coating produced by the D-Gun process may not be consistent.

1.1 Shearing

The shearing action is achieved by the 50Hz oscillation of the cutter over the fixed comb, Fig. 1(a) and (b), which causes sliding contact between the many cutting edge pairs, which trap and sever a large number of wool fibres, only ~20μm in diameter, each cycle. Restrictive tolerances are required in order to maintain wool fibre severance, such as a maximum clearance of 20μm between the comb and cutter edges which must have a maximum edge radius of 2μm. To achieve this close proximity, both tools are "hollow ground" [3], a procedure which dishes the contact faces by 20-50μm for a comb width of 75mm. The cutter is then maintained in contact with the hollow ground surface of the comb by applying a normal force via a loaded radius arm which acts on the cutter. Not only does this technique put the edges into near point contact, which improves the edge proximity, but also considerably increases the edge contact stresses. When silica grit from the wool or wear debris from the surface of the tools is introduced between the tools under high normal force, the result is a 3-body abrasive environment which quickly wears the cutting edges*** and requires higher normal force to maintain wool severance. A limit is eventually reached when the comb and cutter cannot be adequately forced together, at which time they must be removed from service and replaced by a fresh comb and cutter. The worn tools may be resharpened at a later time. The process of replacing and resharpening worn tools may involve as much as 30 minutes of unproductive labour in 8 hours of shearing: a figure which is tolerated in manual shearing but is unacceptable in the more highly capital intensive automated shearing procedure.

** The bulk of wool growing areas in Australia are in drier climates and hence normal wool contains silica grit which accumulates next to the sheeps skin where wool severance takes place. Clean wool is found in regions with high rainfall.

*** The comb life is marginally longer when shearing clean wool due to the smaller quantity of hard particles available to abrade the surface

1.2 The D-Gun Process

This process involves the application of a hard ceramic composite coating to a substrate by spray deposition. A gun barrel-like tube some 100cm long is aimed at the surface to be coated. Into the closed end of this tube is injected oxygen, acetylene and in the present case, milled WC-Co powder. The gaseous mixture is then ignited and the resulting explosion accelerates particles of powder towards the substrate at speeds of up to 800m/sec. When the particles impact the substrate they form a layer ~2μm thick and 25mm in diameter. The overall coating is realized by building up the layer with successive overlapping applications, so that any relatively flat area may be covered by a ceramic layer of a nominated uniform thickness.

The impinging particles in D-Gun deposited coatings have sufficient momentum to plastically deform the substrate and to cause localized liquefaction around the impact zones. Thus good adhesion is achieved through a mechanical keying, not only between the WC-Co particles and the substrate, but also between successive depositions of WC-Co. The impinging particles can experience rapid cooling rates(up to $10^5{}^{o}$C/sec) and therefore can contain non-equilibrium and sometimes amorphous phases.

An advantage of WC-Co coatings applied by the D-Gun process is that the temperature increase of the substrate is small, so that the benefits obtained from having a comparatively hard surface layer can be obtained without adversly affecting the properties of the substrate.

2.0 EXPERIMENTAL

2.1 Fatigue Testing

In the shearing action, when a cutter tooth passes over a comb tooth with a normal force between them, the comb tooth deflects in a cantilever fashion. This is a cyclic action with the peak comb tooth deflection occurring at the instant when the cutter tooth tip is in contact with the comb tooth tip, due to the hollow ground surfaces of comb and cutter. This effect was investigated by Perrott and Muller [4] who determined the nature and magnitude of dynamic comb tooth deflections using high speed cinematography, and who indicated that conditions for surface fatigue existed.

The current work has isolated the comb tooth cantilever bending (in the major direction of bending) from abrasive processes by conducting bending fatigue tests on single comb teeth in a servo-hydraulic testing machine. As illustrated in Fig. 2, the comb tooth was clamped in the region formerly part of the comb plate, with a point load applied to the tooth via a punch positioned at the point of action of the cutter tooth tip. The punch was driven onto the tooth under computer position control, putting the D-Gun coating into tension, with a frequency of 50Hz, an amplitude of 0.05 to 0.25mm and a cantilever length of 16mm. The peak surface stress developed was ~700MPa which occurred ~2mm in front of the clamp. These conditions are in close parallel with those found during the shearing action.

Three single teeth were tested: two for $1.44\text{x}10^6$ cycles and the third for $4.32\text{x}10^6$ cycles. $1.44\text{x}10^6$ test cycles is equivalent to the bending fatigue cycling induced by the operation of a shearing handpiece for 8 hours.

2.2 Tooth Preparation

Single teeth were sectioned from both used and unused D-Gun coated combs to conduct fatigue tests and for microscopy. The three teeth used for fatigue testing were polished to determine the microstructure of the cemented carbide layer and to help in the location of defects. However, due to the hollow ground curvature in each tooth, the coating thickness was reduced towards the tooth tip,

but was virtually unchanged in the region of maximum bending stress: towards the comb plate. Mechanical polishing was carried out using 600 and 1200 grades SiC papers, and then on 6μm and 0.1μm diamond laps.

2.3 Microscopy

The microstructure of the polished D-Gun layer was examined using back-scattered electron (B.S.E.) imaging on a scanning electron microscope (S.E.M.). The composition of each phase was determined by quantitative wavelength dispersive spectra (W.D.S.) analysis on an electron microprobe.

Surface relief of the D-Gun coating used in shearing trials was revealed by the use of secondary electron (S.E.) stereo pairs on an S.E.M.

3.0 RESULTS

3.1 The D-Gun Coating Microstructure

A 7^{o} taper section was taken to determine the coating thickness which was found to be 30 +/- 2.5μm, the variation being due to the surface roughness of the substrate and the slight unevenness of deposition.

The deposited material was heterogeneous both in terms of the phases present and their distribution. In no portion of the layer was there the conventional WC-Co type structure [5], indicating that the total volume of the starting powder had been subjected to temperatures in excess of $1400^{o}C$, as expected of the D-Gun process. The integrity of the coated layer was high with a void content of approximately 2%.

The bulk of the coating was composed of grains of WC surrounded by a matrix of Co,W,C alloy. From W.D.S. analysis, this matrix contained between 1 and 10% Co but constituted a small volume fraction compared to WC. However, as shown in the B.S.E. images in Fig. 3(a) and (b), and the S.E. images in Fig. 4(a) and (b), there were portions of the coating (~10%) with Co,W,C alloys much higher in Co. Fig. 3(a) shows the three major phases present in the matrix with compositions identified by W.D.S. analysis being, A: WC, B: Co_2W_4C (θ), and C: Co_3W_3C (η). Small quantities of CoW_3C and Co_2W_3C were also detected.

The WC particles in contact with these mixed carbide phases generally had rounded edges and were often coral-like in appearance: Fig. 4(a). The η-phase usually appeared in large homogeneous volumes (10-20μm across) as illustrated in Fig. 3(a) and Fig 4(b). In contrast, the θ-phase seldom occurred more than 2μm from the boundary of a WC grain.

There is evidence in Fig. 3(b) (point E) which indicates that the mixed carbide phases were molten at some point in the formation of the layer. Further S.E.M. images showed that some of the larger WC particles had fractured on impact with the substrate and had been subsequently infiltrated by liquid Co,W,C alloys.

3.2 Hardness Measurements Of The D-Gun Layer

The bulk coating hardness, measured using a 500g load, ranged between 800 to 1400 $HV_{0.5}$

3.3 The Used D-Gun Coating

Four D-Gun coated combs which had been used in field trials were inspected to obtain S.E. stereo pairs and B.S.E. images of the surfaces. Each comb had been used for 3-5 hours to shear sandy merino wool.

The most noticeable difference between the initial and used condition of the comb was that the coating had delaminated to a width of 10-20μm along most of the cutting edges of the comb teeth. At the edges where the steel substrate was exposed there was extensive intergranular fatigue cracking and the remaining areas in which the D-Gun layer was still attached showed signs of abrasive wear.

In the main body of the deposited layer, there was abrasive wear of the high points in the coating, leaving them polished flat, and many of the remaining areas having extensive fatigue damage. As illustrated in Fig 4., cracks were predominantly found in regions of η phase, both in the mixed WC/η regions, (a), and in homogeneous volumes, (b).

3.4 The Laboratory Fatigued D-Gun Coating

The surface of the comb tooth subjected to 1.44×10^6 fatigue cycles exhibited cracking of a fatigue nature where bending stresses had been induced during testing, although there was no disintegration of the coating. The fatigue cracks were less than 50μm in length and not usually interlinked. They were aligned laterally across the comb tooth, a direction which is consistent with the direction of maximum bending stress.

Cracks appeared in all mixed carbide phases and occasionally in grains of WC, but were principally found in areas of η phase and the regions immediately surrounding it. Figure 3(a) shows a fatigue crack in a large area of η phase which contains a region of θ phase and small WC grains. The crack appears to have initiated from point D and then propagated upwards. The crack path through the η phase is substantially linear indicating a large grain structure. Figure 3(b) illustrates another crack which has selectively propagated through the η phase.

Away from the η phase regions, in the bulk of the coating, the only damage found was a few scattered hairline cracks through the (Co,W,C) matrix between the WC grains.

In the 24 hour fatigued comb tooth, the surface damage induced was much more severe and had all of the features found in the in service comb tooth, except for edge delamination.

4.0 DISCUSSION

4.1 The D-Gun Coating Microstructure

It is clear from observations of the microstructure that high temperatures and pressures are involved in the formation of the D-Gun layer. The initial temperature rise occurs in the starting powder as a result of the heat transfer from the combustion gases during their passage down the firing tube. It is suggested that a further temperature increase takes place when the kinetic energy of the supersonic particles is converted to thermal energy as they impact the substrate through the mechanism of plastic deformation. Furthermore, there are large instantaneous pressure gradients generated around the impact zones which reduce the likelihood of voids and assist in the infiltration of liquid phases.

As all of the cobalt metal present in the starting powder is converted to Co,W,C alloys in the coating within a very short space of time, the temperature rise must be sufficient to form molten cobalt. This liquid Co is then able to flow under the high pressures and to alloy with WC.

Generally there was a complete cementing of the WC particles by a low percentage Co alloy into a non-porous structure, indicating a sufficient volume fraction of cobalt. However, at discrete regions in the coating there were large volumes of the η phase, suggesting that the distribution of Co in the starting powder was not uniform. The formation of the η phase was studied by Park et al. [6] who used the infiltration of a sintered WC 3 wt.%Co surface by eutectic Co rich liquid at 1440^{o}C. They state that the η phase has a high nucleation energy which favours the formation of large near perfect crystals. In the current investigation, the WC particles present in these Co-rich regions appeared to have undergone severe chemical attack leaving coral-like structures and in some cases complete dissolution.

The microstructure of D-Gun deposited WC-Co coatings has been reported elsewhere by Alfintseva et al [7] and Shmyreva [8] who used a starting powder with a higher Co content. They found that the coatings had significant decarburization, leaving only 40-50% of the original WC, the remainder being W_2C, W, Co, Co_7W_6 and Co_3W, with small amounts of mixed carbides Co_3W_3C and $Co_3W_9C_4$. Furthermore, they state that an important factor in the extent of decarburization is the shock impact forces which act on the particles striking the substrate.

4.2 Fatigue Performance

It is clear from laboratory tested comb teeth that fatigue cracks had initiated and propagated in the coating as the consequence of cyclic tensile surface stresses alone. In addition areas of complete layer delamination and crack propagation into the steel substrate were observed.

Cracks were generally found in regions containing significant volume fractions of (Co,W,C) alloys, especially the η phase indicating its low relative toughness. The predominance of linear cracks in this phase is consistent with a large grain size which will permit relatively easy crack propagation.

The major difference between the in-service coating and the laboratory fatigued coating was the rate of fatigue damage: 5 hours use in a shearing handpiece was roughly equivalent to 24 hours of fatigue cycling in the laboratory. However, this is attributable to the harsher in-service stresses acting on the D-Gun layer during shearing, such as caused by abrasion and high local normal forces.

The coating on the cutting edges is subjected to a variety of cyclic stresses in addition to cantilever bending, namely: Hertzian stresses and torsional stress from eccentric loading of the comb teeth. It is worth noting that there is a torsional stresses concentration at the cutting edges due to the acute angles and small radii there. Therefore this is a fatigue weakness and indeed a likely cause of coating delamination at the cutting edges of the comb teeth.

Vibrating contact fatigue tests on D-Gun WC-Co coated compressor blades have been conducted by Shmyreva [8] who reported that the presence of the brittle low strength intermetallic compounds, pores and blowholes, as well as structural heterogeneity were the cause of initiating fatigue cracks and general destruction of the layer.

Although the phases present and methods of testing of the D-Gun coating in the current investigation are different to those of Refs. 7 and 8, similar observations have been made about the structures and fatigue performances.

5.0 CONCLUSIONS

In this paper it was demonstrated that fatigue of the (Co,W,C) matrix surrounding the WC grains in the D-Gun deposited coatings as applied to shearing combs, occurred as a result of either the normal operation of the comb in a shearing handpiece or from cyclic cantilever bending stresses alone as applied in laboratory tests. The particular fatigue weaknesses in the microstructure of this coating are (a) large volumes of brittle matrix, especially η phase, which provide low energy crack paths, and (b) residual stresses resulting from the method of deposition.

The advanced state of surface fatigue was characterized by particles of the coating falling out of the surface and cracks propagating into the steel substrate. These effects led to coating delamination and in the case of the in-service comb, ultimately the loss of shearing performance.

Surface damage occured at a higher rate in the in-service comb teeth compared with the laboratory tested comb teeth. This was attributed to the more complex cyclic loading system acting on the in-service comb teeth compared with applying the single load of greatest amplitude to the laboratory tested comb teeth. Torsional stresses in the in-service comb teeth were considered important in the delamination of the cutting edges.

Fatigue crack development is seen as a major primary mechanism in the breakdown of the D-Gun cemented carbide coating as applied to shearing combs. Improvements in the above aspects of the coating structure appear essential if a positive improvement in the performance of this spray coating on shearing combs is to be obtained.

Acknowledgements

The authors would like to thank the Australian Wool Corporation for their support and Mr H. Rosser of the University of Adelaide E.O.C. for his assistance with the E.M. work.

References

(1) Field, B.W., Mackenzie, A.J. and Amery, M.I., Proc. 2nd Nat. Conf. on Wool Harvesting R. & D., Sydney, pp 276-283, 10-13 August, 1981.

(2) Chagnon, P. and Fauchais, P., *Cer. Int., 10,* pp.119-131, 1984.

(3) White, A.P., "A Guide for the preparation of Combs and Cutters for Shearing Merino Sheep", Univ. W.A. and the Aust. Wool Corp., 1987.

(4) Perrott, C.M. and Muller, J.P., Proc. 2nd Nat. Conf. on Wool Harvesting R. & D., Sydney, pp. 255-263, 10-13 August, 1981.

(5) A.S.M. Metals Handbook, Vol. 9, 9th edit., pp.273-278, 1985.

(6) Park, J.K., Eun, K.Y.and Yoon, D.N., *Mat. Sci. & Eng. A,* A105/106, pp.233-236, 1988.

(7) Alfintseva, R.A., Kadyrov, V.Kh., Fedorenko, V.K. and Sharypov, A.Z., *Sov. Powder Metall. and Met. Ceram.,* 10, pp.24-29, 1982.

(8) Shmyreva, T.P., *Sov. Powder Metall. and Met. Ceram.,* 12, pp.30-39, 1982.

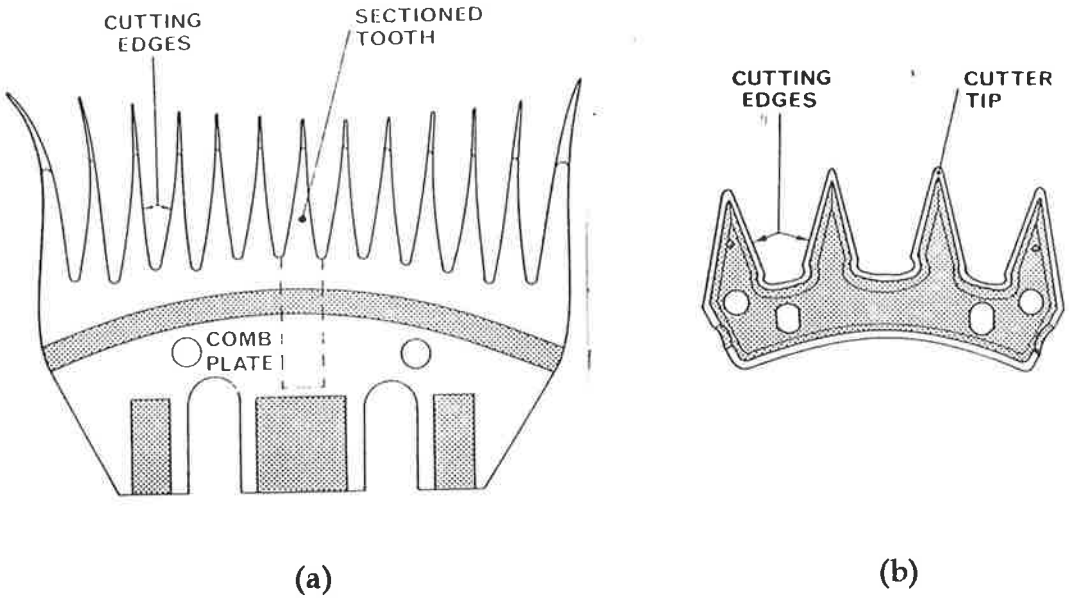

Fig. 1: Sheep shearing comb, (a), and cutter, (b), viewed from their ground faces. Several comb teeth were sectioned from a WC/Co D-gun coated comb for fatigue tests.

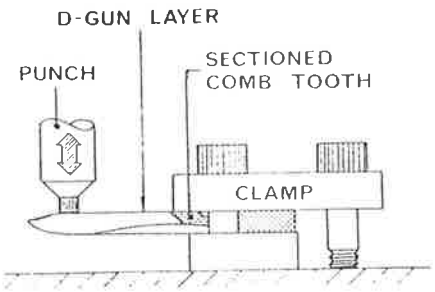

Fig. 2: Experimental arrangement for Instron fatigue tests. A punch was clamped in the upper hydraulic grip of the machine while a plate supporting the comb tooth clamping assembly was bolted to the lower grip (attatched to the hydraulic ram).

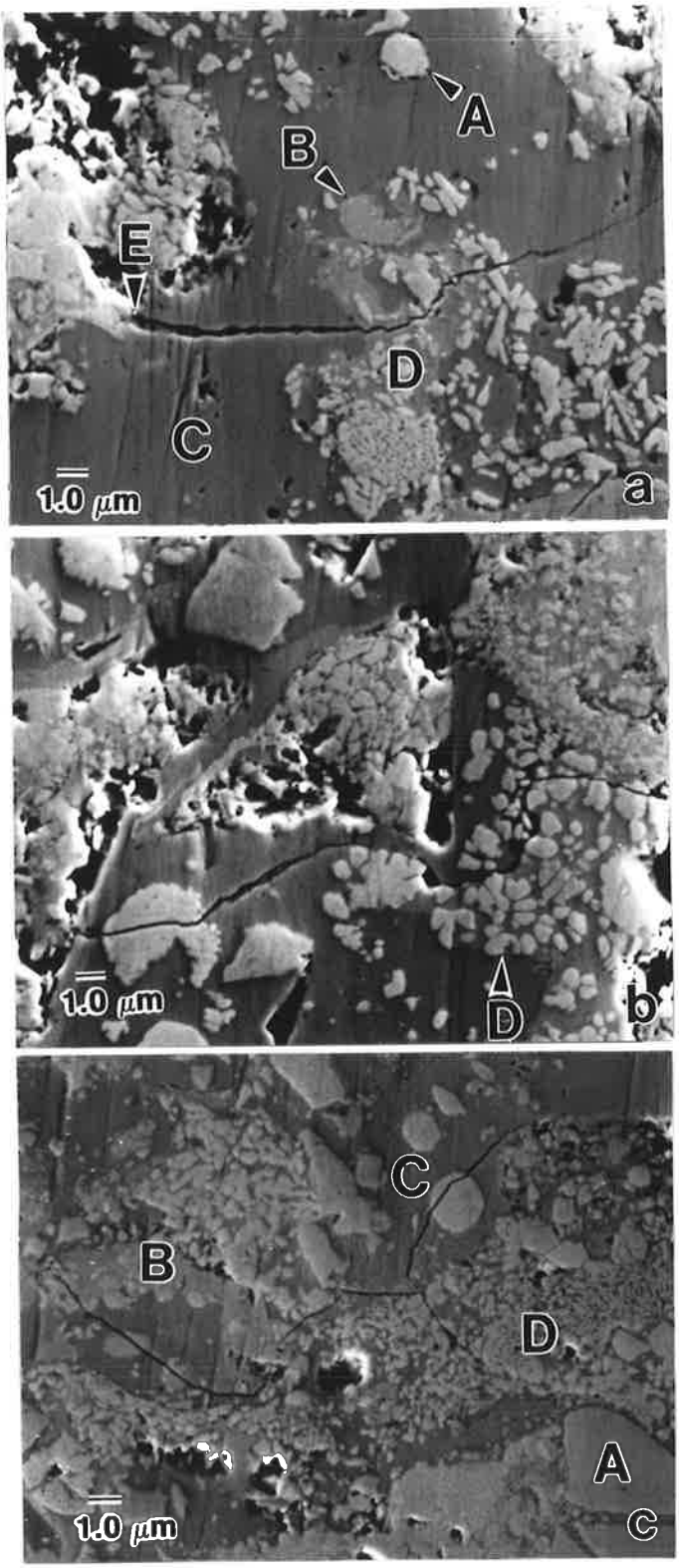

Fig. 3: Fatigue cracks in polished WC/Co D-gun coating on shearing comb tooth (1.44×10^6 laboratory cycles): (a) and (b), η phase cracks; (c) crack branching in a dual phase area.
A, WC; B, Co_2W_4C; C, η-Co_3W_3C; D, mixed phase region; and E, crack initiation site. (B.S.E. images).

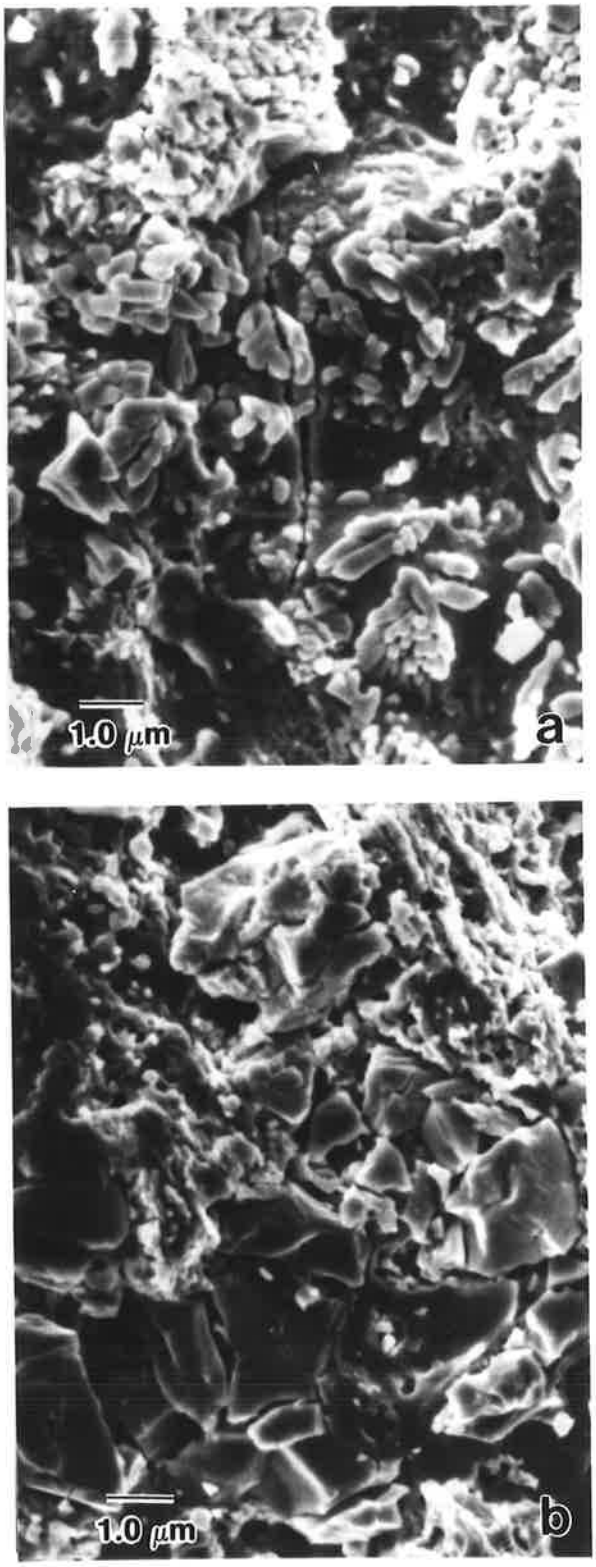

Fig. 4: Fracture surface of fatigued WC/Co D-gun coating on shearing comb (laboratory): (a) crack branch in a direction parallel to applied stress through coral-like WC particles; and (b) crack network through a homogeneous volume of η phase.

BIBLIOGRAPHY

1. Tendys, J., Donnelly, I.J., Kenny, M.J., and Pollock, J.T.A. *Plasma Immersion Ion Implantation using Plasmas generated by Radiofrequency Techniques.* 1989, presented at the Surface Engineering Conf. - SAIT.
2. Conrad, J.R., Radtke, J.L., Dodd, R.A., Worzala, F.J., and N.C., T., *Plasma Source Ion-implantation Technique for Surface Modification of Materials.* J. Appl. Phys. 1987, v. **62**((11)): p. 4591-4596.
3. Hutchings, R., Collins, G.A., and Tendys, J. *Plasma Immersion Ion Implantation: Duplex Layers from a Single Process.* in the Proceedings of the *7th Int. Conf on the Surface Modification of Metals by Ion Beams.* 15-19 July, 1991. Washington D.C.
4. White, A.P., *A Guide for the Preparation of Combs and Cutters.*, Australian Wool Corporation.
5. Dressler, S., *Plasma nitriding gives improved extrusion die performance.* Light Metal Age. 1991, v. **Feb.**: p. 6-12.
6. ASM. *Heat Treating.* in *Metals Handbook.* 1981. Metals Park, Ohio, USA: ASM.
7. Ozbaysal, K., Inal, O.T., and Romig, A.D., *Ion-nitriding Behavior of Several Tool Steels.* Mat. Sci. Eng. 1986, v. **78**: p. 179-191.
8. Hutchings, R., Kenny, M.J., Miller, D.R., and Yeung, W.Y. *Plasma Immersion Ion Implantation at Elevated Temperatures.* in *Surface Engineering.* SAIT:
9. Fujihana, T., Okabe, Y., and Iwaki, M., *Effect of Implantation Temperature on the Hardness of Iron Nitrides Formed with High Nitrogen Dose.* Nucl. Instrum. Meth. 1989, v. **B39**: p. 548-551.
10. Jagielski, J., Gawlik, G., Podgorski, A., Turos, A., Dygo, A., and Madi, N., *Thermal Effects on Depth Distribution of Nitrogen Atoms Implanted in Ferrous Alloys.* Phys. Stat. Sol. 1989, v. **112**: p. 343-346.
11. Terwagne, G., Piette, M., Bodart, F., and Möller, W., *Temperature and Dose Dependence of Nitrogen Implantation into Iron: Experimental Results and Numerical Modelling.* Mat. Sci. Eng. 1989, v. **A115**: p. 25-30.
12. Terwagne, G., Piette, M., Bertrand, P., and Bodart, F., *Temperature and Dose Dependences of Nitrogen Implantation into Iron.* Mat. Sci. Eng. 1989, v. **B2**: p. 195-201.
13. Collins, G.A., Hutchings, R., and Tendys, J. *Plasma Immersion Ion Implantation of Steels.* in *Second International Conference on Plasma Surface Engineering.* 1990. Garmisch-Partenkirchen, FRG.
14. Tendys, J., Personal Communication on: *PIII Experiments with XW10 Steel.* 1991.

15. Worzala, F.J., Conrad, J.R., Dodd, R.A., and Sridharan, K., *Influence of Temperature on Nitrogen Ion Implantation of Incoloy Alloys 908 and 909.* Mat. Sci. Eng. 1991, v. **A139**: p. 179-184.

16. Rehn, L.E., Averback, R.S., and Okamoto, P.R., *Fundamental Aspects of Ion Beam Surface Modification: Defect Production and Migration Processes.* Mat. Sci. Eng. 1985, v. **69**: p. 1-11.

17. Wiedersich, H., *Kinetic Processes during Ion Bombardment.* Nucl. Instr. Meth. 1985, v. **B7/8**: p. 1-10.

18. Bourcier, R.J., Follstaedt, D.M., Dugger, M.T., and Myers, S.M., *Mechanical Characterization of Several Ion-implanted Alloys: Nanoindentation Testing, Wear Testing and Finite Element Modeling.* Nucl. Inst. Meth. Phys. Res. 1991, v. **B59/B60**: p. 905-908.

19. Meyers, M.A. and Chawla, K.K., *Mechanical Metallurgy principles and practice.* 1984, New Jersey: Prentice-Hall, Inc. 761.

20. McHargue, C.J., *Ion Implantation in Metals and Ceramics.* Int. Met. Rev. 1986, v. **31**(2): p. 49-76.

21. Bodart, F., Terwagne, G., and Piette, M., *Migration Studies of Nitrogen Implanted Iron by Improved Depth Profiling.* Mat. Sci. Eng. 1987, v. **90**: p. 111-117.

22. Hashiguchi, Y., Ohtsubo, T., and Sugiyama, K., *Depth Profile of Nitrogen Implanted in Steel.* Nucl. Instr. Meth. 1989, v. **B39**: p. 578-582.

23. Moncoffre, N., *Nitrogen Implantation into Steels.* Mat. Sci. Eng. 1987, v. **90**: p. 99-109.

24. Fayeulle, S., Treheux, D., and Esnouf, C., *TEM Study of the Structural Changes of Nitrogen Implanted Iron Alloys.* Nucl. Instrum. Meth. 1985, v. **B7/8**: p. 171-176.

25. Arnold, A., Ramlau, R., and te-Kaat, E.H., *Cross-sectional TEM investigations of Iron after High-Dose Nitrogen Ion Implantation.* Nucl. Inst. Meth. 1991, v. **B59/60**: p. 726-730.

26. Kozubowski, A., *et al.*, *TEM Studies of Nitrides in Surface-treated and Implanted 12% Chrome.* Mat. Sci. Eng. 1988, v. **100**: p. 161-167.

27. Gerritsen, E., Keetels, H.A.A., and Ligthart, H.J., *Depth Selective Microstructural Analysis of Ion Implanted Metals by Cross-section Transmission Electron Microscopy and Computer Model.* Nucl. Instrum. Meth. 1989, v. **B39**: p. 614-618.

28. Tendys, J., Collins, G.A., and Hutchings, R. *RF Plasmas for Surface Treatment by Ion Implantation and Diffusion.* in *Plasma Technology Conference.* 1991. School of Electrical Engineering, University of Sydney.

29. Tendys, J., Internal Report on: *Secondary Electron Emission from Carbon for Nitrogen Ion Collisions.* 1990, ANSTO.

30. Conrad, J.R., *Sheath Thickness and Potential Profiles of Ion-matrix Sheaths for Cylindrical and Spherical Electrodes.* J. Appl. Phys. 1987, v. **62**((3)): p. 777-779.

31. Conrad, J.R., *Plasma Source Ion Implantation: A New Approach to Ion Beam Modification of Materials.* Mat. Sci. Eng. 1989, v. **A116**: p. 197-203.

32. Conrad, J.R., Baumann, S., Fleming, R., and Meeker, G.P., *Plasma Source Ion Implantation Dose Uniformity of a 2x2 Array of Spherical Targets.* J. Appl. Phys. 1989, v. **65**((4)): p. 1707-1712.

33. Han, S.H., Klucinski, G.L., and Conrad, J.R., *Computer Simulation of Ion Beam Mixing.* Nucl. Instr. Meth. 1990, v. **B45**: p. 701-706.

34. Somers, M.A.J. and Mittemeijer, E.J., *Layer growth kinetics on gaseous nitriding of pure iron: evaluation of diffusion coefficients for nitrogen in iron nitrides.* Metall. Mater. Trans. 1995, v. **26A**: p. 57-74.

35. Pickering, F.B., in *Physical Metallurgy and the design of Steels,* A. Kelly, Editor. 1978, Applied Science Publishers Ltd.: London.

36. Ustinovshchikov, Y.I., *Secondary Hardening Mechanisms of Alloy Steels.* Metal Science. 1984, v. **18**: p. 337-344.

37. Marest, G., Skoutarides, C., Barnavon, T., Tousset, J., Fayeulle, S., and Robelet, M., *Conversion Electron Mössbauer Spectroscopy and (ρ, $\alpha\gamma$) Nuclear Reaction Studies of ^{15}N Implanted Steels.* Nucl. Instr. Meth. 1983, v. **209/210**: p. 259-265.

38. Dos Santos, C.A., Behar, M., De Souza, J.P., and Baumvol, I.J.R., *Composition and Thermal Evolution of Nitrogen Implanted Steels: A Systematic Study.* Nucl. Instrum. Meth. 1983, v. **209/210**: p. 907-912.

39. Rauschenbach, B. and Kolitsch, A., *Formation of Compounds by Nitrogen Ion Implantation in Iron.* Phys. Stat. Sol. 1983, v. **80**: p. 211-222.

40. Rauschenbach, B., Kolitsch, A., and Hohmuth, K., *Iron Nitride Phases Formed by Nitrogen Ion Implantation and Thermal Treatment.* Phys. Stat. Sol. 1983, v. **80**: p. 471-482.

41. Moncoffre, N., Hollinger, G., Jaffrezic, H., Marest, G., and Tousset, J., *Temperature Influence during Nitrogen Implantation into Steel.* Nucl. Instr. Meth. 1985, v. **B7/8**: p. 177-183.

42. Barnavon, T., Jaffrezic, H., Marest, G., Moncoffre, N., Tousset, J., and Fayeulle, S., *Influence of Temperature on Nitrogen Implanted Steels and Iron.* Mat. Sci. Eng. 1985, v. **69**: p. 531-537.

43. Reuther, H., Rauschenbach, B., and Richter, E., *Ion Implantation in Metals - Structure Investigations and Applications.* Vacuum. 1988, v. **38**(11): p. 967-971.

44. Piette, M., Terwagne, G., Möller, W., and Bodart, F., *Nitrogen Implantation into Metals: a Numerical Model to Explain the High Temperature Shape of the Nitrogen Depth Profile.* Mat. Sci. Eng. 1989, v. **B2**: p. 189-194.

45. Terwagne, G., Lucas, S., and Bodart, F., *High Resolution Depth Profiling of Nitrogen in AlN Layers.* Nucl. Instr. Meth. 1992, v. **B66**: p. 262-266.

46. Kopcewicz, M., Jagielski, J., Gawlik, G., and Turos, A., *Phase Diagram of Implanted FeN System.* Nucl. Instr. Meth. 1992, v. **B68**: p. 417-421.

47. Phillips, A. and Seybolt, A.U., *Transmission Electron Microscopy of Some Ion Nitrided Binary Iron Alloys and Steels.* Trans. A.I.M.E. 1968, v. **242**: p. 2415-2422.

48. Fayeulle, S., *These Docteur Ingenieur,* . 1984, Ecole Centrale de Lyon: p. 160-226.

49. Tonghe, Z., Chengzhou, J., Jinghua, S., Ju, C., Fujin, T., and Yuzun, G., *The influence of Ti, N and Ti+N Implantation on Phase Change, Microstructure, Growth of Metallic Compounds and Correlated Effects in Hardness and Wear Resistance in H13 Steel.* Nucl. Inst. Meth. Phys. Res. 1992, v. **B72**: p. 409-420.

50. Easterling, K.E., *Recent developments in quantitative electron microscopy.* Int. Met. Rev. 1977, v. **Review 213**: p. 1-25.

51. Thomas, G., *Electron Microscopy Investigations of Ferrous Martensites.* Metallurgical Trans. 1971, v. **2**: p. 2373-2385.

52. Steel, *XW10 Steel Data Sheet.* 1993, ASSAB steels.

53. Wilson, F.G., *Tempering of Carbon and Low Alloy Steels,* in *Martensite, Fundamentals and Technology,* E.R. Petty, Editor. 1970, Longman: London. p. 137-160.

54. Honeycomb, R.W.K., *Steels: Microstructure and Properties.* 1981, London: Edward Arnold. 244.

55. Pickering, F.B., *Section 7.3: Secondary Hardening Steels,* in *Physical Metallurgy and the design of Steels,* A. Kelly, Editor. 1978, Applied Science Publishers Ltd.: London. p. 133-140.

56. Dahmen, U., Ferguson, P., and Westmacott, K.H., *TEM Study of Fe16N2 and Fe4N Precipitation in Iron-Nitrogen.* Acta Metallurgica. 1987, v. **35**(5): p. 1037-1046.

57. Edington, *Philips monograph No. 3: Interpretation of transmission electron micrographs.* Vol. 3. Philips Technical Library.

58. Stiller, K., Svensson, L.E., Howell, P.R., Rong, W., Andrén, H.O., and Dunlop, G.L., *High Resolution Microanalytical Study of Precipitation in a Powder Metallurgical High Speed Steel.* Acta Metallurgica. 1984, v. **32**: p. 1457-1467.

59. Strid, J. and Easterling, K.E., *On the Chemistry and Stability of Complex Carbides and Nitrides in Microalloyed Steels.* Acta Metallurgica. 1985, v. **33**(11): p. 2057-2074.

60. Lange, W.F., Enomoto, M., and Aaronson, H.I., *Review: Precipitate Nucleation Kinetics at Grain Boundaries.* Int. Mater. Rev. 1989, v. **34**(3): p. 125-150.

61. Somers, M.A.J., Surf. Eng. 1987, v. **3**: p. 123-137.

62. Levy, S.A., Libsch, J.F., and Wood, J.D., *A Study of Fe-C-N Compounds.* Trans. Metall. Soc. of A.I.M.E. 1969, v. **245**: p. 753-758.

63. Biersack, J.P. and Haggmark, L.G., *A Monte Carlo Computer Program for the Transport of Energetic Ions in Amorphous Targets.* Nucl. Instrum. Meth. 1980, v. **174**: p. 257-269.

64. Hill, J.M. and Dewynne, J.N., *Heat Conduction.* Applied Mathematics and Engineering Science Texts, 1987, Oxford: Blackwell Scientific Publs.

65. Robinson and Torrens, Physical Review B. 1974, v. : p. 5008.

66. Möller, W. and Eckstein, W., *Tridyn - A Trim Simulation Code Including Dynamic Composition Changes.* Nucl. Instr. Meth. 1984, v. **B2**: p. 814-818.

67. Koponen, I. and Hautala, M., *The Effect of the Size of Microcrystals on Range Distributions.* Nucl. Instr. Meth. 1988, v. **B33**: p. 112-116.

68. Webb, R.P. and Maydell, E., *Comparisons of Fast Algorithms for Calculation of Range Profiles in Layered Structures.* Nucl. Instr. Meth. 1988, v. **B33**: p. 117-121.

69. Rangaswamy, M., Farkas, D., and Sobel, H.L., *Simulation of High Fluence N Implantation into Fe.* Nucl. Instr. Meth. 1987, v. **B19/20**: p. 196-199.

70. Morral, J.E., Dupen, B.M., and Law, C.C., *Application of Commercial Computer Codes to Modeling the Carburizing Kinetics of Alloy Steels.* Metall. Trans. A. 1992, v. **23A**: p. 2069-2071.

71. Bongartz, K., Quadakkers, W.J., Schulten, R., and Nickel, H., *A Mathematical Model Describing Carburization in Multielement Alloy Systems.* Metall. Trans. A. 1989, v. **20A**: p. 1021-1028.

72. Biersack, J.P., *Three Dimensional Distributions of Ion Range and Damage Including Recoil Transport.* Nucl. Instr. Meth. 1987, v. **B19/20**: p. 32-39.

73. Albaugh, K.B., Puttlitz, and Cade, P.E., *Target heating in ion implantation.* J. Vac. Sci Technol. 1989, v. **B8**: p. 134-135.

74. Klemens, P.G. and Williams, R.K., *Thermal Conductivity of Metals and Alloys.* Int. Metals Rev. 1986, v. **31**(5): p. 197-215.

75. Wrobel, L.C. and Brebbia, C.A., *Boundary Elements in Thermal Problems,* in *Numerical Methods in Heat Transfer,* R.W. Lewis Morgan, K. and Zienkiewicz, O.C., Editor. 1981, John Wiley & Sons Ltd: p. 91-113.

76. Stanley, J.T., *The Effect of Irradiation on Precipitation of Nitrides in Iron.,* in *Diffusion in Body Centered Cubic Metals.* 1965, ASM: Metals Park, OH, USA. p. 349-356.

77. Cottrell, A.H., *An Introduction to Metallurgy.* 1967, London: Edward Arnold Ltd. 548.

78. Kirkaldy, J.S. and Young, D.J., *Diffusion in the Condensed State.* 1987, London: The Institute of Metals.

79. Peterson, N.L., *Grain boundary diffusion in metals.* International Metals Reviews. 1983, v. **28**: p. 65-91.

80. Christian, J.W., *The Theory of Transformations in Metals and Alloys.* 1965, Oxford: Pergamon Press.

81. Ramachandran, P.A., *Application of the boundary element method to non-linear diffusion with reaction problems.* Int. J. Numer. Meth. Eng. 1990, v. **29**: p. 1021-1031.

82. Field, B.W., *Progress towards an Electric Sheep-Shearing Handpiece.* Mech. Eng. Trans., The Institution of Engineers, Australia. 1985, v. **1985**: p. 258-265.

83. Perrott, C.M. and Muller, J.P. *Improved Comb and Cutter Grinding Procedures.* in *2nd National Conference on Wool Harvesting Research and Development.* 1980. Sydney.

84. Perrott, C.M. and Muller, J.P. *Fibre Severance Phenomena and Wear Studies for Reciprocating and Rotary Cutters.* in *2nd National Conference on Wool Harvesting Research and Development.* 1980. Sydney.

85. Seabrook, T.D., *Studies of the Interaction of Sheep Shearing Combs and Cutters.* 1984, CSIRO, Division of Manufacturing Technology, Adelaide.

86. Smith, M.J., *Final Report on Alternative Materials for Combs and Cutters.* 1991, Clayton, Victoria, Australian Wool Corporation.

87. Mair, R.H., Berndt, C.C., Hudson, P.R.W., Edwards, G.H., and Field, B.W., *Wear Resistant Coatings for Wool Severing Applications.* 1992, Clayton, Victoria: Australian Wool Corporation.

88. Field, B.W., *The production of D-gun coated combs.* 1983, Melbourne University, Australia.

89. Field, B.W., Mackenzie, A.J., and Amery, M.I. *Physical Characteristics of Wool Shearing Actions.* in *2nd National Conference on Wool Harvesting Research and Development.* 1980. Sydney, Australian Wool Corporation.

90. Lim, S.C. and Ashby, M.F., *Wear mechanism maps.* Acta Metall. 1987, v. **35**: p. 1-24.

91. Dennis, R.A. *A Test Rig for Investigating the Performance of Sheep Shearing Mechanisms.* in *2nd National Conference on Wool Harvesting Research and Development.* 1980. Sydney:

92. Waterson, P.A., *Child-Langmiur sheath structure around wedge-shaped cathodes.* J.Phys., D:Appl.Phys.1989, v. **22**: p 1300-1307.

93. Holman, J.P., *Heat Transfer.* 5th Ed., McGraw-Hill.1981.